High-throughput Transgenic Mouse Phenotyping Using Microscopic-MRI

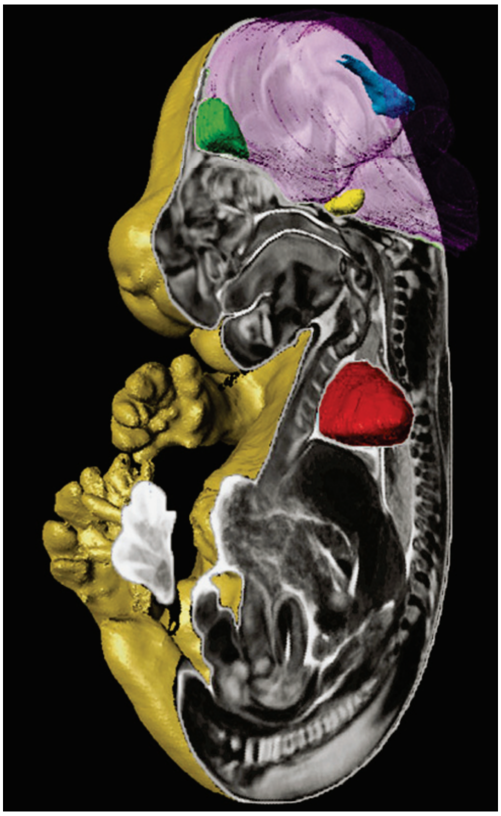

A volume rendering of a segmented atlas image of nineteen 15.5dpc mouse embryos

Jon Orlando Sollas Hawke Cleary
Centre for Advanced Biomedical Imaging

Division of Medicine
& Department of Medical Physics and Bioengineering
University College London
July 2011
MPhil/PhD

Supervisors: *Dr. Mark Lythgoe*
Prof. Roger Ordidge
Dr. Anthony Price

This thesis is submitted as partial fulfilment of requirements for the degree of Doctor of Philosophy

“Always remember that this whole thing started with a dream and a mouse.”

-Walt Disney

I, Jon O. S. H. Cleary, confirm that the work presented in this thesis is my own work except where acknowledged in the text. This work is based on research that was undertaken by me at University College London during the period 26th September 2006 to 30th August 2010.

Signed …………………………………………

Abstract

With the completion of the human genome sequence in 2003, efforts have shifted towards elucidating gene function. Such phenotypic investigations are aided by advances in techniques for genetic modification of mice, with whom we share ~99% of genes. Mice are key models for both examination of basic gene function and translational study of human conditions. Furthering these efforts, ambitious programmes are underway to produce knockout mice for the ~25,000 mouse genes. In the coming years, methods to rapidly phenotype mouse morphology will be in great demand.

This thesis demonstrates the development of non-invasive microscopic magnetic resonance imaging (μMRI) methods for high-resolution *ex-vivo* phenotyping of mouse embryo and mouse brain morphology. It then goes on to show the application of computational atlasing techniques to these datasets, enabling automated analysis of phenotype.

First, the issue of image quality in high-throughput embryo MRI was addressed. After investigating preparation and imaging parameters, substantial gains in signal- and contrast-to-noise were achieved. This protocol was applied to a study of *Chd7*$^{+/-}$ mice (a model of CHARGE syndrome), identifying cardiac defects. Combining this protocol with automated segmentation-propagation techniques, phenotypic differences were shown between three groups of mice in a volumetric analysis involving a number of organ systems.

Focussing on the mouse brain, the optimal preparation and imaging parameters to maximise image quality and structural contrast were investigated, producing a high-resolution in-skull imaging protocol. Enhanced delineation of hippocampal and cerebellar structures was observed, correlating well to detailed histological comparisons. Subsequently this protocol was applied to a phenotypic investigation of the Tc1 model of Down syndrome. Using both visual inspection and automated, tensor based morphometry, novel phenotypic findings were identified in brain and inner ear structures.

It is hoped that a combination of μMRI with computational analysis techniques, as presented in this work, may help ease the burden of current phenotyping efforts.

Acknowledgements

For their enthusiasm and support over the past 4 years I am indebted to my supervisors Mark Lythgoe, Roger Ordidge and Anthony Price. This work has taken me on an intellectual journey that I will be forever grateful to Mark and Roger for starting me on.

I am also tremendously grateful for the support of my friends and collaborators listed below:

Current and former members of CABI:
ManKin Choy, Jack Wells, Bernard Siow, Francesca Norris, Panos Kyrtatos, Ken Cheung, Tanja Holand, Rachael Dobson, Johannes Riegler

Advanced MRI Lab, Queen Square:
David Carmichael, David Thomas, Harry Parkes

Radiology & Physics ICH:
David Gadian, Sally Dowsett, Martin King, Isky Gordon

CMIC:
Marc Modat, Sébastien Ourselin, Benjamin Sinclair, Jorge Cardoso, Pankaj Daga

MMU ICH:
Pete Scambler, Karen McCue, Vanessa Kyriakopoulou

IoN:
Frances Wiseman, Elizabeth Fisher, Sebastian Brandner

NDU ICH
Nick Greene, Juan Pedro Martinez-Barbera, Su Jayakody

I thank the Department of Medical Physics, especially Jem Hebden and Andrew Todd-Pokropek, for their encouragement during my B.Sc. year. The warm reception from the Department convinced me to stay on a bit longer!

In the Division of Medicine: Lucie Clapp and Patrick Maxwell for their continued support during my Ph.D.

I dedicate this work to my parents, Dinah and Alan Cleary, and godfather Clive Jones who have supported me throughout my endeavours so far.

Publications Arising from this Thesis

Peer-Reviewed Publications

Cardiac phenotyping in ex vivo murine embryos using microMRI
Cleary JO, Price AN, Thomas DL, Scambler PJ, Kyriakopoulou V, McCue K, Schneider JE, Ordidge RJ, Lythgoe MF.
NMR in Biomedicine 2009 Oct; 22(8): p857-66.

Magnetic resonance virtual histology for embryos: 3D atlases for automated high-throughput phenotyping
Cleary JO, Modat M, Norris FC, Price AN, Jayakody SA, Martinez-Barbera JP, Greene ND, Hawkes DJ, Ordidge RJ, Scambler PJ, Ourselin S, Lythgoe MF.
NeuroImage. 2011 Jan 15; 54(2): p769-78.

Structural correlates of active-staining following magnetic resonance microscopy in the mouse brain
Cleary JO, Wiseman FK, Norris FC, Price AN, Choy M, Tybulewicz VLJ, Ordidge RJ, Brandner S, Fisher EMC, Lythgoe MF. NeuroImage 2011 (In Press)

Reviews

Cardiovascular Magnetic Resonance Imaging in Experimental Models
Price AN, Cheung KK, **Cleary JO**, Campbell AE, Riegler J, Lythgoe MF
The Open Cardiovascular Medicine Journal 2010 Nov; 4: p278-292

Conference Abstracts

Mouse Embryo Phenotyping with Contrast-enhanced micro-Diffusion Tensor Imaging
Cleary JO, Siow B, Greene NDE, Daga P, Modat M, Ordidge RJ, Ourselin S, Alexander DC, Lythgoe MF,
International Society for Magnetic Resonance in Medicine (ISMRM), 19th Annual Meeting, Montreal 2011

Contrast-enhanced micro-Diffusion Tensor Imaging for Mouse Embryo Phenotyping
Cleary JO, Siow B, Greene NDE, Daga P, Modat M, Ordidge RJ, Ourselin S, Alexander DC, Lythgoe MF,
British Chapter of ISMRM, 16th Annual Meeting, Nottingham 2010

Optimised μMRI for Phenotyping the Tc1 Model of Down Syndrome
Cleary JO, Norris FC, Wiseman FK, Price AN, Choy M, Tybulewicz VL, Ordidge RJ, Fisher EM, Lythgoe MF.
International Society for Magnetic Resonance in Medicine, 18th Annual Meeting, Stockholm 2010
In *Proc. Intl. Soc. Mag. Reson. Med.* 18 (2010) #1044

Phenotyping a Novel Mouse Model of Congenital Heart Disease using µMRI
Cleary JO, Norris FC, McCue K, Price AN, Beddow S, Ordidge RJ, Scambler PJ, Lythgoe MF
International Society for Magnetic Resonance in Medicine,
18th Annual Meeting, Stockholm 2010
In *Proc. Intl. Soc. Mag. Reson. Med.* 18 (2010) #1044

Micro-MRI phenotyping of a novel double-knockout mouse model of congenital heart disease
Cleary JO, McCue K, Price AN, Beddow S, Ordidge RJ, Scambler PJ, Lythgoe MF
Society for Cardiovascular Magnetic Resonance,
13th Annual Scientific Meeting, Phoenix AZ 2010
in *Journal of Cardiovascular Magnetic Resonance* 2010, **12**(Suppl 1)**:**P1

Towards 3D virtual histology using high-field magnetic resonance imaging insights into the pathophysiology of development and disease.
Cleary J, Price A, Thayyil S, Scambler P, Fisher E, Tybulewicz V, Taylor A, Ordidge R, Lythgoe M
British Association of Clinical Anatomists, Winter Meeting,
Southampton 2009
In *Clinical Anatomy*, 23: 352–362 (2010),

Mouse Embryo Phenotyping Using a µMRI Atlas
Cleary JO, Modat M, Price AN, Greene ND, Thomas DL, Scambler PJ, Ordidge RJ, Ourselin S, Lythgoe MF
British Chapter of ISMRM, 15th Annual Meeting, Cardiff 2009

Phenotyping in the Mouse Embryo Using a µMRI Atlas
Cleary JO, Modat M, Price AN, Greene ND, Thomas DL, Scambler PJ, Ordidge RJ, Ourselin S, Lythgoe MF
International Society for Magnetic Resonance in Medicine,
17th Annual Meeting, Hawaii 2009
In *Proc. Intl. Soc. Mag. Reson. Med.* 17 (2009) #825

µMRI Optimisation for Phenotyping the Embryo Mouse Heart
Cleary JO, Price AN, Thomas DL, Scambler PJ, Kyriakopoulou V, Ordidge RJ, Lythgoe MF
International Society for Magnetic Resonance in Medicine,
17th Annual Meeting, Hawaii 2009
In *Proc. Intl. Soc. Mag. Reson. Med.* 17 (2009) #2482

Novel phenotyping methods using microMRI.
Cleary JO, Price AN, Modat M, Thomas DL, Scambler PJ, Kyriakopoulu V, Ordidge RJ, Ourselin S, Lythgoe MF,
Mammalian Genetics and Development Workshop 2009
In *Genetics Research*, 91 (2) #138

Contrast Optimisation in Mouse Embryo microMRI
Cleary JO, Price AN, Thomas DL, Scambler PJ, Kyriakopoulou V, Ordidge RJ, Lythgoe MF
British Chapter of the ISMRM, 14th Annual Meeting, Newcastle 2008

Table of Contents

Index of Figures

Index of Tables

Organisation of Chapters

This thesis is comprised of three introductory chapters, four experimental chapters and a final discussion and summary.

Chapter 1 is an overview of the creation of genetically modified mice and introduction to the imaging techniques other than magnetic resonance imaging that may be used to phenotype them. Specific examples are used to illustrate models where non-invasive imaging may be useful in cardiac and neuroanatomical applications.

Chapter 2 provides an outline to the basic principles of MRI, the background of MRI contrast agents and an overview and examples of the use of microscopic MRI (μMRI) in mouse phenotyping applications.

Chapter 3 outlines some of the basic concepts in image analysis techniques, as applied to current animal and human phenotyping studies, going on to describe some current applications of automated, morphometric to research, particularly in the field of neuroscience.

Chapter 4 is the first experimental chapter, describing the preparation and measurement of tissue parameters relevant to cardiac phenotyping in the mouse embryo and the utilisation of these parameters to provide improved signal and contrast-to-noise in the visualisation of subtle cardiac defects.

Chapter 5 is the second experimental chapter. This applies the embryo μMRI protocol (developed in chapter 4) to imaging of the embryo CNS, demonstrating delineation of subtle structural definition in anatomical imaging of the phenotyping of mutant. This work is then extended through the application of non-linear image registration to create an embryo atlas comprised of multiple subjects. Using this atlas protocol segmentation-propagation is then used to compare phenotype in a number of body structures in three groups of mice with different genetic backgrounds.

Chapter 6 is the third experimental chapter. In this chapter, further to the investigation of the mouse embryo, a contrast-enhanced μMRI protocol is developed to produce high-resolution images of the adult mouse brain. Detailed optimisations allow improved visualisation of substructures of the brain, such as in the thalamus and hippocampus.

Chapter 7 is the fourth experimental chapter. Using the contrast enhanced micro-MRI protocol developed in Chapter 6, visual inspection and image registration techniques are applied in a morphometric analysis of the transchromosomic Tc1 model of Down syndrome, where novel brain phenotypes are identified.

Chapter 8 discusses the key findings of this thesis and provides a final summary and conclusion.

List of Abbreviations

3D: three-dimensional
ATP: adenosine triphosphate
BAC: bacterial artificial chromosome
CHARGE: Coloboma of the eye, Heart defects, Atresia of the nasal choanae, Retardation of growth and/or development, Genital and/or urinary abnormalities, Ear abnormalities and deafness
CHD: congenital heart defect/disease
Chd7: chromodomain helicase binding protein 7
CNR: contrast-to-noise ratio
CNS: central nervous system
Cre: Causes recombination
DNA: deoxyribonucleic acid
dpc: days post coitum
DS: Down syndrome
DSCR: Down syndrome critical region
DTI: diffusion tensor imaging
ENU: *N*-ethyl-*N*-nitrosourea
ES cell: embryonic stem cell
ER: oestrogen receptor
FA: flip angle
FDR: false discovery rate
FIAU: Fialuridine
FID: free induction decay
FSE: fast spin echo
Gd-DTPA: gadolinium-diethylene-triamine-pentaacetic acid
GLM: general linear model
GE: gradient echo
H&E: haematoxylin and eosin
Hesx1: Homeobox expressed in ES cells 1
Hsa: *Homo sapiens*
KO: knockout
μCT: microscopic computed tomography

MRI**:** magnetic resonance imaging
μMRI: microscopic magnetic resonance imaging
Mmu: *Mus musculus*
NMI: normalised mutual information
NSA: number of signal averages
OPT: optical projection tomography
SE: spin echo
SNR: signal-to-noise ratio
SOD: septo-optic dysplasia
SPM: statistical parametric maps/mapping
TBM: tensor-based morphometry
Tc1: transchromosomic 1
TE: echo time
TR: repetition time
VBM: voxel-based morphometry
YAC: yeast artificial chromosome

Introduction

The first three chapters introduce the main topics discussed in this thesis: (1) the need and methods for the creation of genetically modified mice and a discussion of current methods of morphological phenotyping methods; (2) a background to magnetic resonance imaging (MRI), specifically microscopic MRI (µMRI) and the theory behind its application to phenotyping; (3) a discussion of the issues involved in data analysis and an introduction to automated image analysis methods. I aim to provide an overview of the literature, highlight important themes discussed in research chapters and set the context within which the research in subsequent chapters is formulated.

Chapter 1:

Genetically Modified Mice: Models and Morphometric Phenotyping

1.1 Overview: the Mouse as a Model for Studying the Genetic Basis of Human Disease

The humble mouse is a highly relevant model to the study of the basis of human disease, as we share mammalian development, biochemistry and physiology. The key unifying element between the two species, which comprises all these aspects, is the commonality of the mammalian genome. The announcement of the completion of the first draft of the mouse genome in 2002 (Mouse Genome Sequencing Consortium et al., 2002) and the increased sophistication of genomic analysis over the past two decades, have strengthened the evidence of similarity. For example, 99% of mouse genes have a human homologue (Rosenthal and Brown, 2007). In addition, the products of these genes such as proteins and biochemical pathways, also demonstrate strong similarities. This common physiology, coupled with a rapid gestation (~20 days (Otis and Brent, 1954)) and short time to breeding age, has led to the emergence of established techniques to manipulate its genome and cemented the mouse as a key model with which to study genetic influences on disease and physiology. While modified mouse models may not exactly replicate human conditions, they can lead to new insights into the mechanisms of disease. So far several thousand mouse mutants have been produced (Capecchi, 2001), with a number of these models created to allow the direct investigation of a host of human conditions in a variety of systems, as diverse as Down syndrome (O'Doherty et al., 2005), Huntington’s disease (Phillips et al., 2005), diabetes (Pechhold et al., 2007) and cancer (Jahid and Lipkin, 2010).

This chapter will provide an outline of the history and creation of mutant mice, as well as a discussion of non-invasive methods to aid their phenotyping. Finally, as a background to later experimental chapters, subsequent sections will focus in greater detail on specific genetic mutations involved with congenital heart disease and examine the role of genetics on neurodegenerative disease, looking in particular at mouse models of Down syndrome.

1.2 Historical Perspectives on Mouse Genetic Research

Although the earliest mention of the use of mice for general scientific research is in 1664, as part of Boyle and Hooke's investigations on the need for air by living organisms (Beck et al., 2000), the use of mice as a model organism for genetic investigations of heredity beginning in the early part of the 20th Century was pioneered by William Castle working at the Bussey Institution at Harvard (Rader, 2001).

The majority of the common mouse lines in use today can trace their origins to the Victorian commercial breeders needing to satisfy the demand for 'fancy mice' as household pets. In particular, the efforts of one breeder, Abbie Lathrop, contributed several specific lineages for scientific research, derivatives of which are used in the present day. The work of Castle formed the basis for modern mouse studies dependent on highly inbred mouse strains – created by performing a large number of brother-sister matings or other close relatives. With each successive generation of such matings, the gene-pool reduces considerably, resulting in mice with background homozygous for most gene loci[1], which may then be defined and characterised. This led to the creation in the 1910s of inbred strains, such as C57BL, C3H, CBA and BALB/c mice, all of which continue to be in common use today. In 1929, a student of Castle, Clarence Cook Little, continued the formal study, maintenance and storage of mouse lines, founding the Roscoe B. Jackson Memorial Laboratory, now a specialist institution well known today for its mouse research.

1.3 Generation of Genetically Modified Mice

Until the investigation of germ-cell mutagens in the mid-20th Century, new mouse mutants were often discovered after chance observations of unusual phenotypes often caused by spontaneous mutations. An early example is a line of mice commonly used

---

[1] A locus is the specific location of a gene or DNA sequence in a chromosome

by early researchers known as Japanese 'waltzing' mice for their repetitive circling behaviour that persisted with each new generation (Gates, 1925). These mice were later suspected of possessing a homozygous gene mutation that caused inner ear defects, affecting functioning of the vestibular system (Nagy, 2003). A similar example is the ob/ob (obese) mouse line (Ingalls et al., 1950), which first appeared in a mouse litter at the Jackson Laboratories in 1950. These mice are now an accepted model of type II diabetes, becoming obese due to disinhibition of feeding behaviour. Although in use as a model for a number of years, the exact cause of the phenotype was only elucidated in 1994 and was found to be due to a defect in the gene for the hormone leptin (Zhang et al., 1994), which plays a key role in appetite regulation and satiety.

Today, there are broadly two approaches for disrupting gene function in the mouse. The first is a gene-focussed approach to examine or target specific genes, usually where an *a priori* hypothesis prompts the manipulation of specific gene(s). Given the size of the mouse genome –~25,000 genes, of which the function of the majority has not been ascertained – this approach may not be suitable for the rapid creation of novel mutants. Therefore a second approach is to disrupt genes over the entire genome at random, in the hope that new genes may be identified on the basis that a random mutation might produce a novel phenotype in an existing mouse. These and associated genes may then become suitable candidates for more targeted investigations.

Employing these complementary strategies enables researchers to produce a range of new mutations and manipulate the entire mouse genome with relative ease.

1.3.1 Approaches for Investigating and Targeting Specific Genes

1.3.1.1 Transgenesis

The first technique involves transgenesis, where material foreign to the natural genome of the mouse, i.e. exogenously-produced DNA sequences (such as copies of human genes), is added during development. Two methods are used to achieve this result. The earliest technique is pronuclear microinjection, where the foreign DNA is simply injected directly into an embryo before the first cleavage (Gordon et al., 1980).

An alternative approach is to perform microinjections into mouse embryonic stem (ES) cells (Yutzey and Robbins, 2007). Successfully modified ES cells can then be genotyped and selected before implantation into a blastocyst, allowing more control over the quality of the procedure.

Although conceptually simple and relatively fast to perform, allowing creation of models in as little as a few weeks (Yutzey and Robbins, 2007), transgenic methods have the disadvantage that there is often no control over the precise number of additional copies of a gene which will be added to the genome, and the number of gene integrations arising from transgenesis causes variability in the final dosage of gene-products to the organism. Conventional transgenic models may have multiple copies of the exogenous sequence resulting in dosages typically unseen physiologically, even in disease states. Therefore, while these models may give useful insights into the mechanisms governing a disease, some caution must be observed in generalising experimental findings to the actual disease state.

It should be also noted that the wide adoption of mice as genetic models is partly due to the continued viability of mouse embryos despite invasive manipulation. In the rat for example, while also commonly used as a research model, techniques such as pronuclear microinjection have been less successful and therefore relatively few transgenic rat lines exist.

1.3.1.2 Gene-targeting

Also commonly used are gene-targeted mice (often referred to as ‘knockout’ or ‘knock-in’ mouse models) (Capecchi, 2001). This powerful approach was pioneered in the early work of Capecci, Evans and Smithees, and recognised by the Nobel Prize in 2007. In this method a DNA construct is produced that is homologous to the gene of interest, consisting of a null gene (in the case of knockout mice) and, usually, a reporter. By removing an early-stage embryonic stem cell (ES cell) and using a technique to open the plasma membrane, such as electroporation (Neumann et al., 1982), the construct can then be introduced into the ES cell.

As the cell undergoes division, a recombination event substitutes the construct for the gene of interest in the desired chromosome. Once confirmed, this ES cell is removed and injected into a developing blastocyst from a mouse with a contrasting coat colour, and placed in a surrogate mother to develop (Figure 1.1). The resulting offspring will be chimeric, that is having varying contributions of cells from differing stem cells. The vast majority of gene targeting is carried out in ES cells from variants of the 129 mouse strain which has an agouti coat colour. These cells may then be introduced into the blastocyst of a mouse with a black coat colour, typically the C57BL/6, which go on to divide and produce a chimeric mouse. If offspring show the agouti coat colour in addition to black, the modified ES cell has been successfully integrated and indicates the presence of the modified allele.

[Figure removed due to copyright]

Figure 1.1: *Schematic diagram showing an outline of the creation of gene-targeted mice. a) Cultured mouse embryonic stem cells from a mouse with agouti coat colour are electroporated and the targeted gene-construct is introduced. The gene-construct confers resistance to cytotoxic agents e.g. G418 (a glycoside antibiotic, similar to neomycin) or FIAU (Fialuridine, a nucleoside analogue). b) The targeted ES cells are re-introduced into an early-stage blastocyst and implanted into a surrogate mother. Successful creation of chimeric offspring is easily identified by coat colour. Adapted from (Capecchi, 2001).*

Although gene-targeting represents a powerful tool for the creation of new mutants, this is an intrinsically low yield technique due to the infrequent nature of an homologous recombination event (only 1 in 1000 injections of the vector into ES cells will be successful (Capecchi, 2001)).

Additionally, the 129 background is not suitable for many types of study, particularly behavioural work (which will be discussed further in a later section). It is therefore desirable to backcross[2] the chimera with a more suitable strain, such as C57BL/6. Initial generations of offspring with have a mixture of 129 and C57BL/6 alleles. In order to produce mice with a defined background, a large number of backcrosses are

---

[2] Backcross: Where an F1 hybrid is crossed with one of its parents, or with an individual genetically identical to one of its parents

needed to further reduce the remaining fraction of 129 alleles. This process can be lengthy, taking up to 2 years or more, it is common to see studies in the literature performed on mice with a less-defined, mixed genetic background, with some residual 129 genes (this is illustrated in Figure 1.2). After 12 backcrosses to a C57BL/6 mouse, approximately 1% of the genome would be 129 in origin, mostly centred around the mutant allele (Gerlai, 1996).

[Figure removed due to copyright]

Figure 1.2: *After insertion of the gene-targeted construct, indicated by the white line, the new allele is moved on to an inbred background of choice, in this case C57BL/6. In the* F_2 *generation, the genetic background of resulting mice will still have a strong 129 genotype. Selecting mice with the construct and with successive backcrosses to C57BL/6, the proportion of 129 alleles will reduce considerably. Adapted from (Gerlai, 1996).*

Although often used for producing KO models, any homologous gene construct may be substituted. Therefore using a working allele, recombination events are able to replace or introduce additional genes in the mouse genome, creating a 'knock-in' model.

Although such gene-targeted mice have contributed to nearly 10% of models so far, mutations in particular genes (~15% of the genome) can result in embryonic lethality in resulting offspring, making adult study impossible. As a result, it is now increasingly common to use a selective or inducible system that performs gene-targeting in only specific tissues or at a desired timepoint.

The main system of this type in current use is the Cre-loxP system, which was first described by Sauer in the late 1980s (Sauer and Henderson, 1988). The bacteriophage P1 was found to carry an enzyme (Causes recombination or Cre) that was able to trigger a recombination event in a gene flanked by loxP ('locus of X-over P1', a 35 base-pair sequence) sites (termed a 'floxed' gene). This system is easily adapted for use in the mouse (Sauer, 1998).

First, the mouse genome in an ES cell may be modified by conventional gene targeting to replace a normal gene with a floxed equivalent. This mouse is then mated with another mouse that contains the Cre gene. The resulting offspring now contain both the Cre and the floxed gene.

The use of Cre offers a sophisticated mechanism for controlling gene recombination. For example it can be made to initiate only in specific tissues during development by association with a specific promoter, for example an association with *Nkx-2.5* (a gene with an integral role in heart development expressed in developing myocytes (Lints et al., 1993) would cause Cre expression and thus Cre-medicated gene recombination in heart tissue only. The timing of Cre activation can also be made arbitrary to any point during development, including adulthood, using an *inducible* Cre system. In such a system the Cre promoter is activated by a specific external stimulus such as an activated receptor. One commonly used is the oestrogen receptor (Cre-ER) (Feil et al., 1997). Administration of the oestrogen analogue tamoxifen to the animal, causes activation of the receptor and the downstream Cre, resulting in the gene of interest being excised through recombination.

1.3.1.3 RNA Interference

In addition to these approaches, more recently, so-called ‘knock-down’ models have been developed. These use a phenomenon known as RNA interference, where administration of either double-strand or short interfering RNA (dsRNA and siRNA) sequences can silence the effect of transcribed RNA from an homologous gene (Caplen et al., 2001; Elbashir et al., 2001). These models are otherwise genetically normal, but the administration of RNA is able to silence particular gene products thus producing effects similar to an inducible Cre knockout for a short period.

1.3.2 Non-specific Gene Mutation

Although it is desirable to specifically target genes in order to investigate function, in recent years an attempt to speed up the isolation and discovery of relevant and novel genes has lead to a more functional, *phenotype-driven* approach to genomic study. In this approach mutants are created using protocols that produce random changes in the genome, which disrupt normal gene function.

1.3.2.1 Irradiation

One of the first approaches developed for the creation of mouse mutants was the use of ionising radiation. In this method, male mice are exposed to high X-ray dosages (typically a single fraction of ~600R) (Ehling, 1966) and as such their resulting sperm may contain gene mutations which are passed to subsequent generations.

1.3.2.2 ENU Mutagenesis

In the 1970s, the non-specific mutagen *N*-ethyl-*N*-nitrosourea (ENU) was found to introduce random point mutations in the DNA of murine sperm with a 5 times greater frequency than radiation (Russell et al., 1979). When male mouse germ cells are exposed to the agent, a relatively high number of point mutations are created (typically ~1 per locus per 1000 gametes (Brown, 1998)). These point mutations may cause gene disruption in subsequent generations. The affected locus may then be identified.

[Figure removed due to copyright]

Figure 1.3: *Simplified outline of the use of ENU for the creation of new dominant mutations. After injection of ENU into male mice, point mutations occur in sperm. After mating with wild-type mice, mutant alleles may be present in resulting progeny. Adapted from (Acevedo-Arozena et al., 2008)*

1.3.2.3 Gene trapping

Gene trapping involves the random insertion of a DNA (gene trap) cassette throughout the genome in an ES-cell line. Such gene trap vectors consist of a gene trapping cassette comprised of a promoterless reporter gene and/or selectable genetic marker. In addition there is a downstream termination sequence (polyadenylation sequence). When the cassette integrates in the middle of a gene sequence, typically in an intron region, upon gene transcription the polyadenylation site causes abrupt termination of transcription, resulting in an abnormal mRNA transcript and resulting protein. The presence of these two gene products, may then be used to assess the efficacy of a gene trapping experiment.

[Figure removed due to copyright]

Figure 1.4: *Outline of gene trap mutation. The gene trap construct is transfected into an ES cell and integrates randomly into the genome. The vector may integrate between gene exons resulting in an abrupt termination during mRNA translation due to the polyA sequence. Adapted from (Castrop, 2010).*

1.4 The Effect of Genetic Background on Phenotype

As previously discussed, most mice used in genetic studies will be in-bred, and therefore homozygous at most loci, with alleles specific to one mouse line. As a consequence, background may have a strong effect on observed phenotype in mutant mice, representing a possible confounder to the characterisation of gene function. For example, a review of mice in neurobehavioural studies found that the 129sv background was generally considered a poor choice for Morris water maze testing (Crawley et al., 1997) although this may be improved by environmental enrichment (Kempermann et al., 1998). Mice from the 129 background in general, appear to present with a higher frequency of structural brain changes such as agenesis of the corpus callosum (Livy and Wahlsten, 1991). As some techniques such as gene-targeting require the use of specific strains, these 'innate' phenotypes must be borne in mind when beginning studies and deciding on the eventual background.

1.5 High-throughput Mutagenesis Programmes

Large-scale programmes, utilising targeted mutations (such as the International Knockout Mouse Project) and random mutagenesis techniques, such as ENU, are underway to systematically create transgenic knockout models for each of the approximately 25,000 mouse genes (International Mouse Knockout Consortium et al., 2007). The results of these efforts should greatly increase the understanding of the significance of genes on the phenotype of systems across the whole animal, as these mice are comprehensively analysed in the coming years.

1.6 Mouse Phenotyping Screens

Phenotype is often difficult to assess, as a mutation in a single gene may have effects in multiple organ systems, a situation known as pleiotropy. Effective general phenotyping depends on the use of a battery of screening tests to identify the changes. Two main paradigms exist for such approaches. Genotype-driven screens seek to determine the function of a specifically targeted gene, using information from previous genetic studies to thoroughly determine the probable effect and system(s) affected. More widely used are so-called phenotype driven screens in which mice are tested with more general, basic examinations and no underlying assumptions are made as to the gene's probable effect.

1.6.1 Current Techniques in High-throughput Phenotype-driven Screens

The worldwide consortia producing novel mouse mutants generate large numbers of new mutants annually (1000s). The dissemination of the phenotype of these mice is thus a high priority. To this end, they have actively developed strategies for screening pathways to enable the rapid identification of candidate mutants.

For example the current ENU mutagenesis programmes depend upon phenotype driven screens due to the random nature of mutant produced (Brown, 1998). A standardised sequence of biochemical, physiological and morphological screens are now in place, ranging from blood testing to behavioural studies and bone density scans. The aim of this so-called primary screening is to determine which areas of physiology and organ systems deviate from baseline measurements established in wild-type animals. After this assessment is made, the mutant of interest can then be sent to a specialist secondary centre for a secondary phenotypic analysis (Brown et al., 2005; de Angelis et al., 2006).

An example of a primary screen, are the two phenotyping pipelines used and developed by members of the European Mouse Disease Clinic (EUMODIC) programme known as EMPReSSslim. This utilises a small number of mutants typically ~10, which are then placed through a series of behavioural, biochemical, imaging studies. Incorporated into these may also be system challenges in the form of short hearing, nociception tests and immune system challenges. Results from these tests are captured, analysed and placed into an on-line portal (Morgan et al., 2010) for wide dissemination.

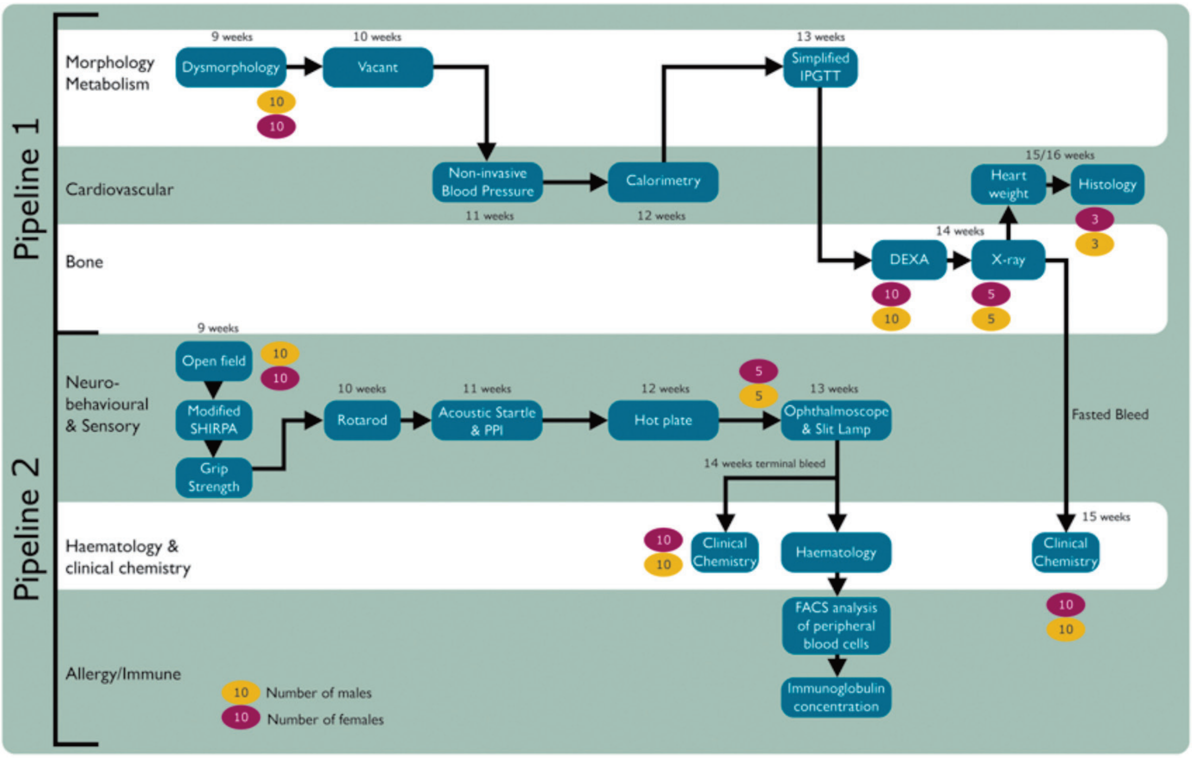

Figure 1.5: *Schematic outline of the two-pipeline primary organ systems screen (EMPReSSslim) devised by the EUMODIC phenotyping programme.*

As seen in Figure 1.5, while there is a comprehensive assortment of testing procedures for primary screening for common phenotypic features, the end point for morphological assessment remains histology, which presents a bottleneck in the throughput in the identification of novel phenotypes. The current high-throughput mutagenesis programmes acknowledge that there is key a role for fast, non-invasive imaging methods to be integrated as either primary or secondary screens.

1.7 Methods of Morphological Mouse Phenotyping

Over the subsequent introductory and study chapters MRI methods for *ex-vivo* phenotyping in the mouse will be discussed. The following sections outline the main histological and alternative imaging methods for phenotyping in the mouse embryo and the adult mouse brain.

1.7.1 Morphological Phenotyping in the Developing Mouse Embryo

Morphological analysis of anatomy is an important part of both phenotype and genotype driven screens. Conventionally this is done *ex-vivo* by microscopic examination with histology. In this method embryos are ethanol-dehydrated, embedded in paraffin wax and thinly sectioned into 2-8µm slices (Kaufman, 1992). This provides high-resolution 2D data and sections that may also be stained for gene and protein expression.

[Figure removed due to copyright]

Figure 1.6: *Example of a haematoxylin and eosin-stained histology image from an E13.5 mouse embryo heart.* ***A:*** *illustration of anatomy, arrow indicates the conal septum separating the two ventricular outflow tracts (MB=major bronchus, Dao=descending aorta, PT=pulmonary trunk, PA=pulmonary artery, LSV=left superior vena cava, RSV=right superior vena cava, E=oespohagus.* ***B:*** *Higher power image from the conal septum clearly showing the areas of apoptosis (arrows indicating apoptotic debris, small dots) and mitosis (black triangle indicating a dividing cell). Adapted from (Savolainen et al., 2009).*

A recent refinement of this process is episcopic imaging, where the autofluorescence of each histology section can be photographed and combined computationally to generate high resolution 3D volume datasets (typically 1-2µm isotropic resolution) (Weninger and Mohun, 2002). However these histological approaches are time-consuming and do not lend themselves readily to rapid screening as only one embryo may be imaged at a time.

[Figure removed due to copyright]

Figure 1.7: *Axial slice through a 3D episcopic fluorescence image capture (EFIC) dataset, showing the heart, great vessels and lungs of a 16 days-post-coitum embryo. RA = right atrium, LA=left atrium, LV=left ventricle, RV=right ventricle, CV=left superior vena cava. In-plane resolution 2.32µm x 2.32 µm. Adapted from (Weninger and Mohun, 2002).*

A further complication is that a phenotype may be largely unknown (21) or incompletely penetrant, meaning that a particular genotype does not necessarily lead to a phenotypic effect. Therefore relatively large numbers (10s to 100s) of embryos are sometimes needed to gain a good measure of the prevalence of the phenotype in a population (22).

Compounding this, due to the numbers of lines being generated, the IKMC and ENU mutagenesis programmes also may experience a histological bottleneck due to large numbers of embryos. In the case of ENU programmes, although 7-10 mutants are typically phenotyped in a primary screen, their aim is to process up to several hundred mouse lines annually. Thus a high-throughput phenotyping technique is essential to meet the demands of modern molecular medicine.

1.7.2 The Role of Non-invasive Imaging in Mouse Embryo Phenotyping

Due to the low volume of embryos that may be phenotyped with conventional histology together with its destructive effects on tissue morphology, there is interest in utilising non-invasive imaging methods for morphological screening. These methods, such as magnetic resonance imaging (MRI), have the potential to offer large time saving advantages and are increasingly becoming used as an adjunct to histology in the examination of embryo phenotype.

While most non-invasive methods are able to provide both *in-vivo* and *ex-vivo* imaging assessments of phenotype, the most successful approach for anatomical phenotyping is *ex-vivo*. This allows high-resolution scans to be performed, as sample movement is greatly reduced and the lack of animal anaesthetic and monitoring requirements enables long scan times.

μMRI is one such imaging method, allowing assessments of both embryo development (Petiet et al., 2008) and phenotype (Bamforth et al., 2004; Goddeeris et al., 2008). High-throughput screening can be achieved with multiple mid-gestation embryos (typically up to 32 simultaneously) in a single 12-hour scan at ~25μm resolution (Schneider et al., 2003c; Schneider et al., 2004). Full 3D datasets for all embryos are created, allowing structures to be visualised relative to one another. In this method, embryos are fixed in a gadolinium-chelate contrast agent in order to improve signal to noise and image quality. μMRI techniques will be the focus and expanded upon in later chapters.

Other whole embryo imaging modalities are available and have been successfully used to phenotype transgenic mice. The two main alternatives are photon projection techniques, which depend on differences in the photon attenuation properties of tissue for contrast. This contrasts with MRI where signal is intrinsically generated within the tissue itself.

Microscopic computed tomography (μCT) (Johnson et al., 2006) uses x-rays to image tissue and also allows high-throughput imaging. High resolution 3D scans are possible, with a single embryo at an 8μm isotropic resolution being acquired in a 12-hour scan time or 27μm in 2-hours. μCT is ideally suited to imaging dense structures such as bone (Oest et al., 2008) but the technique suffers conventionally from the limited range of linear attenuation coefficients in soft tissue, leading to similar signal intensities for most organ structures, and impairing detailed visualisation (Takeda et al., 2000). However, recent innovations in the use of dense radiopaque tissue stains such as osmium tetroxide and iodine have gone some way to improve the visibility of soft tissue and internal contrast (Degenhardt et al., 2010; Johnson et al., 2006) (Figure 1.8).

[Figure removed due to copyright]

Figure 1.8: *Example slices through a μCT dataset, showing sagittal (A), coronal (B) and axial (C) views through a wild-type 12.5dpc embryo after staining with osmium tetroxide. The resolution is 27μm isotropic. (a, cardiac atrium; cc, central canal of the neural tube; fl, forelimb; sc, semicircular canal; v, cardiac ventricle). Adapted from (Johnson et al., 2006).*

Optical projection tomography (OPT) (Sharpe et al., 2002) is also a 3D projection-reconstruction modality but uses photons in the visible spectrum. As an optical technique this can provide detailed images of tissue structures through autofluorescence but also gene and protein expression using conventional fluorophores. High resolutions are achieved (typically down to 5μm (Walls et al., 2008)). However the technique requires translucent skin tissue, in order for light to penetrate and thus its use in older embryos (>13.5dpc) that are more opaque is more limited (Schneider and Bhattacharya, 2004). Examples of both raw projection and reconstructed data are shown in Figure 1.9.

[Figure removed due to copyright]

Figure 1.9: *Example slices through an OPT dataset of a 10.5dpc mouse embryo. Showing: (A) a typical image from raw autofluorescence data as acquired. (B) Coronal section through the embryo after 3D reconstruction processing. (C) Raw OPT projection data with fluorescence data from double-antibody staining for HNF3β (green) and neurofilament (blue). (D) Coronal slice through dataset as in (C) after 3D reconstruction. Adapted from (Sharpe et al., 2002).*

An additional technique for both structural and functional imaging in the developing mouse is ultrasound biomicroscopy (UBM). UBM uses high-frequency ultrasound, operating a greater frequency than conventional clinical ultrasound systems (typically 30-60MHz (Henkelman, 2010)) achieving resolutions in the 10s of microns (Phoon and Turnbull, 2003). Furthermore, UBM is able to produce high-resolution images of developing mice *in-utero.* Imaging is relatively straightforward with the application of an acoustic probehead close to the body, and images are immediately viewable. Ultrasound images may be difficult to plan and interpret, as it is unlike the previous modalities which produce a true 3D reconstruction across a defined tissue volume, the picture is created by an acoustic array, typically producing a fan beam whose resolution reduces considerably with increasing depth. Contrast is dependent on the properties of tissues to reflect acoustic waves, which can appear similar throughout most tissues but tissue boundaries provide the most apparent contrast. A key application of UBM is in the imaging of vascular structures in the heart and brain as these structures are more easily delineated and amenable to Doppler imaging, where the frequency shift of moving blood can be measured and quantitative, directional flow-rates easily calculated. Examples of vascular imaging in the developing embryo are shown in Figure 1.10:

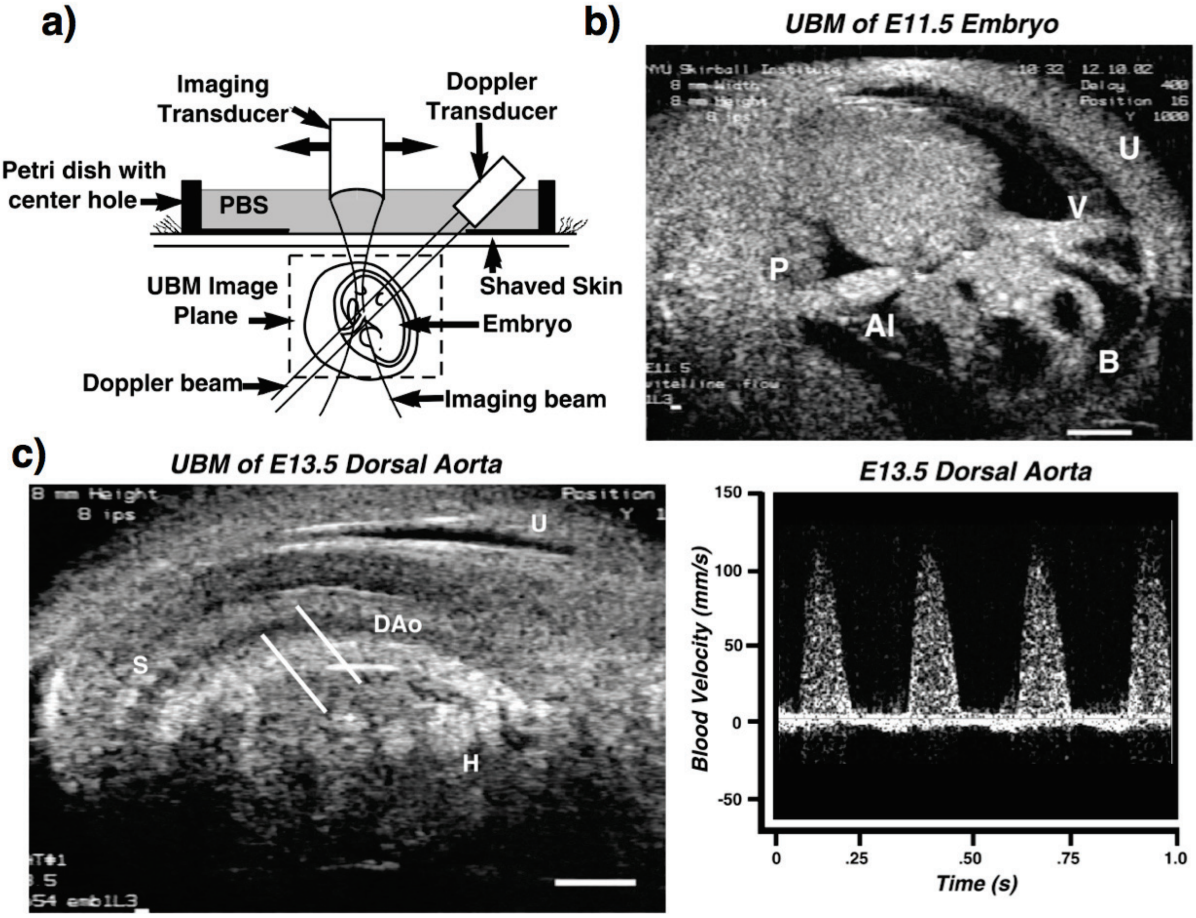

Figure 1.10: ***a)*** *shows the typical arrangement of ultrasound transducers in-utero imaging.* ***b)*** *UBM image of an 11.5dpc embryo (P=placenta, U=uterus, Al=alantois, V=vitelline arteries, B=brain).* ***c)*** *An example of Doppler flow imaging: after identification of the aorta (DAo) on an anatomical scan (H=head, S=spine), a Doppler transducer may be oriented perpendicularly to obtain haemodynamic information from the vessel. Adapted from (Phoon and Turnbull, 2003).*

1.7.3 Morphological Phenotyping in the Adult Mouse Brain

As may be expected, even small genomic manipulations in the mouse are able to have considerable and complex effects on the brain, in terms of physical structure, organisation of connectivity, physiology and behaviour. These may manifest themselves early, indicating a failure in normal neurogenesis or presenting later in adult life indicating a neurodegenerative effect. It is perhaps surprising to note that ~90% of neurological conditions with a brain phenotype will result in an observed structural change. Therefore the morphological phenotyping is a key investigation for mouse phenotyping.

As with the embryo, in the adult mouse brain, high-resolution phenotyping is typically carried out by histological sectioning either through paraffin embedding as discussed previously or cryosectioning to create thin sections. The choice of technique is usually determined by the stains needed, with cryosectioning being more suitable for fresh tissue and may enable a greater preservation of intact proteins for immunohistochemistry. However, due to the distinct number of brain structures, which differentiate into glial and neuronal cell-types with defined receptor profiles, expression profiles of interest, specialised stains and immunohistochemistry are best able to delineate these subtle regional and functional domains However, extraction and preparation effects (such as shrinkage) that occur in tissue, in addition to large numbers of sections produced, make volumetric measurements challenging as well as accurate visual assessments of morphology, particularly of small or easily damaged structures such as the pituitary or olfactory bulbs.

Histological approaches have the advantage of highlighting cell and region-specific changes with great sensitivity and with a resolution capable of identifying individual cells and axonal connections. One example where this has been used to great effect is in the production of so-called ‘brainbow’ images of the mouse brain where individual cells and axons may be identified and traced using fluorescence microscopy (Livet et al., 2007). This is shown in Figure 1.11.

[Figure removed due to copyright]

Figure 1.11: *Fluorescence microscopy using an inducible Cre-Lox system in the Brainbow transgenic mouse. Upon activation of Cre in these granule cells of the cerebellum, differing combinations of fluorescent marker proteins are expressed depending on cell-type* ***(a)****. The connectivity of cells and corresponding axons may then be traced by these specific colours* ***(b)****. Adapted from (Livet et al., 2007).*

However as in the embryo, any full characterisation is extremely time-consuming if sectioning and staining are performed manually. Histological characterisation studies in a population have been attempted in the both the mouse and human brain, although this has required the development of highly automated sectioning methods and semi-automated histological classification techniques which still require many months for comprehensive categorisation of histological structures in the thousands of sections of a single brain (Amunts et al., 2000). In addition, if accurate 3D reconstruction of histology is required, a high-resolution reference MRI scan is also required and sections are aligned (registered) to this dataset in an attempt to correct for geometric distortions (Lebenberg et al., 2010; Purger et al., 2009).

1.7.4 The role of Non-invasive Imaging Techniques in Mouse CNS Phenotyping

In the case of conditions resulting in gene-related atrophy, non-invasive, longitudinal imaging studies offer a powerful method for accurately measuring volume-change and determining the precise location of atrophy.

In addition to MRI, which is discussed fully in subsequent chapters, microscopic computed tomography (μCT) can also produce non-invasive images of the brain. However, as in the embryo, without CT contrast enhancement its use is best suited to bony structures, such as the skull, a highly dense structure that results in low radiation transmission, and therefore high signal on CT images. An example of the use of μCT for adult mouse craniofacial phenotyping is shown in Figure 1.12.

[Figure removed due to copyright]

Figure 1.12: *Comparison of μCT skull data from population averaged datasets of 5 wild-type* ***(A)*** *and* ***(B)*** *5 novel connexin43 ENU mutants (*$Gja1^{Jrt}$*). The overall size of the skull in the mutant rendering can be seen to be reduced, with notable differences in lower jaw morphology. Adapted from (Nieman et al., 2006)*

More recently, structural brain imaging using μCT has been optimised to produce high-resolution images of *ex-vivo* brain tissue (9μm isotropic resolution), which has been successfully used to identify pathological changes in cancer models (Prajapati et al., 2010). However the x-ray dosages required for such resolution are extremely high and incompatible with *in-vivo* imaging (Boone et al., 2004).

[Figure removed due to copyright]

Figure 1.13: *Sagittal, axial and coronal views through a MicroCT dataset without contrast enhancement (9µm isotropic) of an ex-vivo wild-type mouse brain at postnatal day 43. Adapted from (Prajapati et al., 2010)*

Applications to Cardiac and Neuroscience Research

The following two sections will focus on specific areas and models where non-invasive imaging approaches may be especially useful, namely in the characterisation of phenotype.

1.8 Specific Application of Mouse Models to Cardiac Research

The use of mouse models in cardiac research in particular is now routine, due in part to the high degree of correspondence with human anatomy. The mouse heart is four-chambered and the basic developmental and regulatory genetic networks are well-conserved between mice and humans, making mice ideal for investigating the role of genes on cardiovascular dysfunction through transgenic and knockout models (Yutzey and Robbins, 2007).

The use of the mouse embryo is essential for examining the effects of genes on development and congenital disease. They may be of particular use in determining the cause and features for a knockout resulting in embryonic lethality or postnatal mortality. Given their small size (typically 1-2cm at mid-gestation) and the difficulties of *in-vivo* experiments, examination of phenotype is usually achieved by examining *ex-vivo* morphology and gene expression profiles.

The study of the effect of genes on mouse embryo development is particularly applicable to the investigation of congenital heart defects (CHDs). These are a group of conditions which affect over 1% of live births and are responsible for complications immediately from birth through to later adult life (Hoffman and Kaplan, 2002). Inheritable gene mutations and chromosomal effects are the direct cause of nearly 20% of CHDs. While the basis of remaining so-called sporadic conditions is uncertain, epidemiological studies demonstrate an increased risk of

CHDs in siblings and offspring of those affected. This illustrates there is potential genetic involvement even in these cases (Bentham and Bhattacharya, 2008).

1.8.1 Genetic Aspects of Heart Development

The heart is formed early on in development, initially consisting of a single heart tube that undergoes several stages of folding, initially to form two chambers, which will become the atria and ventricles. These structures will also septate further to form the left and right chambers. Complex, timed genetic networks are responsible for initiation and completion of heart processes. With striking similarity to CHDs seen in humans, failure in the correct functioning of these networks during development commonly involves one or more of the following: the simple gross enlargement of the heart and surrounding vessels; effects on atrial and ventricular septa (thinning and/or absence); enlargement or stenosis of great vessels (such as in tetraology of Fallot); and defects in endocardial cushion development affecting valve development. As may be expected from the large number of genes implicated in CHDs gene dysfunction results in a spectrum of severity and highly dependent on the gene and corresponding pathways involved. A summary of genes with known involvement in CHD and an indication of their severity is shown in Table 1.1.

[Figure removed due to copyright]

Table 1.1: *Table showing genes identified from the online Mouse Genome Informatics database that may be implicated in CHD. Each gene is ranked by pleiotropy score, indicating the number of heart structures affected, with a score of 1 indicating one structure, a score of 5 indicating five structures. Adapted from (Bentham and Bhattacharya, 2008)*

1.8.1.1 Hypotheses of gene involvement on CHDs

A number of different genetic events may lead to a similar cardiac phenotype and hypotheses have been generated to explain the mechanisms behind both the spontaneous mutations and Mendelian-inherited alleles. While specific to CHDs, these concepts may also be generically applicable to the phenotypes observed other organ systems.

1.8.1.1.1 Allelic Heterogeneity

As CHD has a ~60% infant morality when untreated, reproductive fitness will tend to remove highly penetrant alleles from the population. Therefore cases are often the result of new spontaneous mutation, usually specific to that individual, causing a CHD phenotype.

1.8.1.1.2 Gene Copy-number Variation

A change in normal the number of genes is strongly linked to the development of CHDs. For example, the phenotypes seen in DiGeorge syndrome are the result of a deletion (at 22q11.2), whereas those of Down syndrome (trisomy 21) and trisomy 18, which also result in CHDs, are caused by an *increase* in gene dosage.

1.8.1.1.3 Buffering Capacity and Mutational Load of Genetic Networks.

As heart development is governed by the interplay of complex genetic networks, a single gene mutation is unlikely to affect the process and other networks may be able to buffer the system. However, in patients with a high mutational load, the capacity of networks to compensate may break down, resulting in CHD.

1.8.1.1.4 Gene-environment Factors

The environmental conditions encountered by the foetus may have an impact on the correct function of a specific allele and thus CHD occurrence. For example, the maternal methylene tetrahydrofolate reductase alleles known as 677CT and 677TT are associated with a threefold and six-fold increase in the risk of CHD risk to their children. A clinical study of the effect of folate administration on CHD development (Czeizel et al., 2004) found a reduced odds-ratio (0.6) of CHDs in these individuals. This shows how genetic and environmental influences can interact in the pathogenesis of CHD. Importantly, environmental factors, such as maternal diabetes and obesity, also may disrupt buffering mechanisms and result in CHD.

The ultimate goal from the study of these models is to gain an understanding of the effect and role of genes in CHDs as a basis of identifying possible targets for therapeutic compounds. This approach would aim to parallel the large reductions seen in neural tube defects after the identification of the necessity for folate during pregnancy (MRC Vitamin Study Research Group, 1991). The following section introduces a specific gene whose absence results in CHDs in mouse models: *CHD7*.

1.8.2 CHARGE Syndrome and CHD7

Chromodomain helicase DNA-binding protein 7 (*CHD7*) is a gene located on human chromosome 8, mutations in which strongly correlate to instances of the human condition CHARGE syndrome. Children born with this condition show abnormalities in a number of organ systems, which were previously used to define the condition. Coloboma of the eye, Heart defects, Atresia of the chonae, Retardation of growth, Ear abnormalities and/or deafness. The condition affects an estimated 1 in 10,000 in newborns and defects in the *CHD7* gene specifically (heterozygosity for nonsense, deletion, or missense mutations) are thought to be responsible for ~67% of these cases. The clinical features of CHARGE in humans and mice are highly variable and incompletely penetrant. From reports of *CHD7* mutation positive CHARGE individuals, the most commonly affected organ in humans with *CHD7* mutations is the ear. Ear defects in CHARGE include temporal bone abnormalities, external ear malformations, and hearing loss. Although olfactory function is less commonly analysed, a majority of CHARGE patients analyzed have some form of olfactory defect including olfactory bulb hypoplasia and/or aplasia and impaired olfaction ranging from mild hyposmia to anosmia. The variability in CHARGE features suggests that mutations in *CHD7* lead to pleiotropic developmental defects; however, the mechanisms underlying these defects have not yet been determined.

CHD proteins are a part of the large group of adenosine triphosphate (ATP)-dependent chromatin remodelers. The mammalian genome encodes approximately 30 such genes that appear to be vital for normal embryonic development. Many ATP-dependent chromatin remodelling genes show haploinsufficiency, indicating that their products may be involved in rate-limiting steps during development. *CHD7* is one of nine ATP-dependent chromatin remodelling enzymes, which are broadly classified into three subfamilies based upon their amino acid sequence and functional protein domains. *CHD7* and the other eight CHD proteins are a class of ATP-dependent chromatin remodelers with unique protein motifs that are incompletely characterized.

To date, *CHD7* is the only member of this class of proteins for which mutations have been associated with a well-described human syndrome (Layman et al., 2010).

1.8.3 Cardiac Phenotypes in the Adult Mouse

This thesis partly focuses on heart development in the embryonic mouse. In the *in-utero* conditions the developing mouse is not reliant on functioning left-right heart separation for delivery of oxygenated blood. Therefore mutant mice with more severe morphological abnormalities may persist until birth.

Gene knockouts compatible with postnatal life while non-lethal, may still have notable effects on the phenotype of adult mice. The adult mouse is more amenable than the embryo to *in-vivo* investigations, allowing a dynamic assessment of cardiac function, using techniques such as ultrasound, ECG and electrophysiology testing and *in-vivo* MRI.

Although these mice will often show normal physiology in the resting state, they may demonstrate heart dysfunction after being subject to pharmacological or interventional challenges. For example, the agent dobutamine may be used to simulate the effect of exercise on the heart. Interventions such as aortic banding or simulation of myocardial infarction through ligation of coronary arteries may also expose phenotypic differences such as in functional parameters such as ejection fraction and volumetric measurements of the extent of infarction.

1.9 Applications of Mouse Models to Neuroscience Research

In recent years increasing evidence has accumulated for an underlying genetic component in a number of neurological conditions. Genomic and phenotyping studies have opened the way for understanding the underlying pathology of many neurological disorders. The outcome of current intense research into the genetics of neurological disorders will hopefully be the introduction of new diagnostic tools and the discovery of potential targets for new and more effective medications and preventive measures.

The mouse shares the principal cell-types and functional brain domains common to human development. As with applications to heart research, genetically manipulated mouse models may be used to understand the fundamental pathways for brain development and maintenance through single-gene disruption or through transgenesis methods.

Genetic factors make a significant contribution to neurological conditions. The process of neurogenesis pathways may also be disrupted through genetic manipulation, leading to new insights into these mechanisms of proliferation and growth. In addition to neurogenesis, genetic factors also play a strong role in the support and maintenance of developed cells and failure of these pathways may lead to premature cell-death and atrophy. These are a hallmark of a number of neurodegenerative conditions.

Common mouse models of neurological disease now include Alzheimer's, Huntington's and Parkinson's diseases; amyotrophic lateral sclerosis (ALS or motor neurone disease), epilepsy and certain cancers.

The following sections outline two conditions which will be examined further in later chapters: i) septo-optic dysplasia – a developmental abnormality – and ii) Down syndrome.

1.9.1 A Gene for Optic Nerve and Pituitary Development: HESX1

HESX1 is a homeobox gene that has been implicated in certain forms of the human condition septo-optic dysplasia (SOD). Clinically, children with this condition are characterised by hypopituitarism. Additionally there may be malformation of eyes, optic nerves and optic chiasm leading to blindness in a number of cases. Embryonic mouse models by have been produced with gene-knockouts and commonly seen clinical alleles of the condition have been shown to demonstrate similar phenotypes to the human form (Dattani et al., 1999) by the age of 18.5dpc.

SOD is a rare condition, which was first described by Reeves in a 7-month-old baby and is sometimes known as de Morsier syndrome. The phenotype is highly variable, and may include any two of the three classical features. Pituitary hypoplasia may manifest as endocrine deficits, varying from isolated growth-hormone deficiency to panhypopituitarism. Either sexual precocity or the failure to develop in puberty may occur. Abnormal hypothalamic neuroanatomy or function may also be a feature. Several aetiologies have been proposed to account for the sporadic occurrence of SOD, such as viral infections, environmental teratogens and vascular or degenerative damage. Familial cases of SOD are rare, and may be associated with an autosomal recessive inheritance. In the light of the phenotype demonstrated in *Hesx1* null mutant mice, Dattani *et al.* examined patients with SOD for mutations in *HESX1*. A homozygous missense mutation in the homeobox of *HESX1* was found in two siblings with optic nerve hypoplasia, absence of the corpus callosum, and hypoplasia of the pituitary gland with panhypopituitarism born to a highly consanguineous family. Heterozygotes for this particular mutation were phenotypically normal.

Additionally, in view of the occasional heterozygous phenotypic manifestation in the murine *Hesx1* null mutants, Dattani *et al.* also went on to screen DNA samples from a number of patients with sporadic SOD and other pituitary disorders also identified heterozygous mutations of *HESX1* similar to the mouse model with variable penetrance.

1.9.2 Genetic Mouse Models for the Investigation of Down Syndrome

A particular application of transgenic technology has been to the human condition Down syndrome (DS). As first identified by Jérôme Lejeune in 1959 (Lejeune et al., 1959), this condition results in a non-disjunctive germline transmission of all or part of an additional chromosome 21 (Hsa21), resulting in a theoretical 50% increase in gene dosage. There is a typical incidence of 1 in 700 live births, although the risk of an affected pregnancy greatly increases with maternal age.

Children are often born with congenital heart defects. A characteristic behavioural phenotype in infants is a hypotonic demeanour. Craniofacial abnormalities are also a feature of these patients. The structural consequences to brain anatomy in DS are known from studies and case-reports of MRI findings in the literature. These include: overall smaller brain-volume and reduced cerebellar size (Beacher et al., 2010).

In older subjects, ventricular enlargement may be common, as well as early-onset

Alzheimer's Disease which may be related to the increased gene dosage of the amyloid precursor protein (APP).

Although there are instances of transmission of part of Hsa21, 95% of DS affected individuals carry a complete copy of chromosome 21. Although the smallest of human chromosomes, Hsa21 still houses a large number of genes, which initial estimates put at ~230 (Hattori et al., 2000), although recent advances in the detection of non-protein coding RNA put this figure as high as ~400 (Gardiner and Costa, 2006).

With such a large number of genes, the effect of this increased dosage is wide-ranging. The additional copy of Hsa21 results in elevated expression of many of the genes encoded on this chromosome, with varying expression levels in different tissues. The increased dosage of Hsa21 genes, and the dosage imbalance between Hsa21 and non-Hsa21 genes has been proposed to cause the plethora of phenotypic alterations that characterize DS.

Although Hsa21 represents a large number of genes, much past work has focussed on a small region – the Down Syndrome Critical Region (DSCR) – a distal section of 33 genes, thought to be responsible for the majority of phenotyping features in DS. However, recent investigations comparing mouse models of Mmu16 trisomy and DSCR alone, suggests that DSCR alone may not be sufficient to cause the characteristic phenotypes of DS, and moreover restoration of normal DSCR gene dosage does not rescue cardiac and craniofacial developmental defects (Lange et al., 2005; Olson et al., 2007). This accumulating evidence points against a single DSCR. Current data suggests that a number of 'susceptibility regions' located on Hsa21, which are modified by other loci on Hsa21 and elsewhere in the genome, increasing the risk of developing specific DS associated phenotypes.

Work has also focused on the gene DYRK1A, a kinase that appears to be critical biochemical step in the development for a number of aspects of the DS phenotype. A summary of DYRK1A phosphorylation targets are shown in Figure 1.14.

[Figure removed due to copyright]

Figure 1.14: *The Hsa21-encoded kinase DYRK1A has been shown to phosphorylate a multitude of targets, which have been implicated in a number of biological processes and DS-associated phenotypes, including endocytosis and AD. Adapted from (Wiseman et al., 2009).*

Mouse models of DS are instrumental in identifying which genes contribute to DS phenotypes, and unravelling the mechanisms by which these phenotypes arise.

Hsa21 is syntenic to three regions of the mouse genome. Most of the genes on Hsa21 have homologous genes on mouse chromosome 16 (Mmu16), but two smaller gene rich regions have syntenic portions on Mmu10 and Mmu17. The majority of mouse models used for DS research are either trisomic for large regions of Mmu16, 10, 17 or are transgenic animals used to investigate overexpression of a single gene, such as DYRK1A.

One of the most well-characterised models so far has been the Ts65Dn mouse (Reeves et al., 1995). As the result of an induced translocation, it has partial trisomy of Mmu16 and a small part of Mmu17, in total carrying an additional copy of 132 genes syntenic with Hsa21. This particular mouse demonstrates symptoms similar to human DS, including altered facial characteristics, memory and learning problems and age-related changes in the forebrain.

Another model of DS that has been of great interest in recent years has been the transchromosomic (Tc1) mouse, produced as part of efforts beginning in the late 1980s, culminating in an initial characterisation reported in 2005 (Hernandez et al., 1999; O'Doherty et al., 2005). In this mouse an additional, largely complete form of Hsa21 has been introduced, with the aim of examining the effects in the mouse but using human genetic material to perhaps offer a more translational model of the condition. This also opens the possibility to monitor the affects in future drug treatments to specifically modulate the human gene and protein expression in an animal model.

A summary comparison of regions coded by a number of current models of Down syndrome, including Tc1 and Ts65Dn mice is shown in Figure 1.15.

[Figure removed due to copyright]

Figure 1.15: *Top: comparison of syntenic regions in human and mouse. Middle: Comparison of syntenic regions from the Tc1 mouse (human genes) and common mouse DS models. Although the Ts65Dn model is largely trisomic for Mmu16, it also contains a small portion of Mmu17 (not shown). Bottom: The regions associated with some monosomic models are also illustrated. Adapted from (Wiseman et al., 2009).*

As has been outlined in the preceding sections, through the use of a number of mutants to model DS, spanning from single genes to the length of Hsa21, the key genes that control the condition are slowly beginning to be identified. This characterisation of Hsa21 should enable the discovery of new pharmacological targets and one day even allow the possibility of DNA-based therapies for the condition.

1.10 Summary

In this chapter, the rationale and methods for the creation of genetically modified mice were outlined and discussed. The use of a variety of novel imaging modalities was also introduced, in the context of the morphological phenotyping of these new mice. In the following chapter, a background to magnetic resonance imaging and examples of applications will be discussed.

Chapter 2:

Magnetic Resonance Imaging

This chapter aims to outline the basic theory behind magnetic resonance imaging and introduce some of the practical uses of MRI as applied to mouse phenotyping studies.

2.1 Overview

Magnetic resonance imaging is a non-invasive imaging method, well established in human and small-animal imaging. It utilises non-ionising radiation and is capable of generating high-resolution 2D and 3D images with excellent soft-tissue discrimination both *in-vivo* and *ex-vivo*. An illustration of the quality of images now obtainable in a high-field human system *in-vivo* is shown in Figure 2.1.

[Figure removed due to copyright]

Figure 2.1: *Left: example axial MR image of a human subject in a 7 Tesla MRI system. Right: enlarged section, showing the detail of structures visible in and around the central sulcus of the brain. Image voxel resolution: 214x214µm in-plane, 1mm slice thickness. Adapted from (Li et al., 2006).*

2.2 Generation of the Magnetic Resonance Signal

In simple terms, MRI exploits a phenomenon known as nuclear magnetic resonance (NMR) to create an image. This is now a well-studied physical phenomenon that has resulted in some of the most seminal work in physics throughout the 20th Century.

An inherent property of atomic nuclei is a nuclear spin, a form of angular momentum. MRI is able to detect information about the quantity and local environment of nuclear spins present in elements with an unbalanced number of protons, such as hydrogen nuclei (^1H) found in tissue water molecules.

Atomic nuclei have magnetic moments that are proportional to their spin, I. In the case of certain nuclei, this spin is nonzero. ^1H for example, has two possible spin states, either +½ or -½. When these protons are placed in an external magnetic field

(**B_0**) the magnetic moments thus become aligned either parallel (+½) or anti-parallel (-½) with the main magnetic field. The parallel state is the lower energy of the two and a slightly higher proportion of protons (~4×10^{-4}%) exist in this state (Figure 2.2).

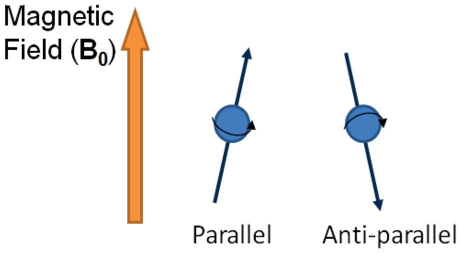

Figure 2.2: *Illustration of the two possible orientations of magnetic moments after protons have entered an external magnetic field (**B_0**)*

The proportion in both states may be determined by the relationship shown in Eq. 2.1:

(Eq. 2.1)
$$\frac{N_{anti-parallel}}{N_{parallel}} = e^{\left(\frac{-\Delta\varepsilon}{k_B T}\right)}$$

(where k_B is the Boltzmann constant, 1.38×10^{-23} JK^{-1}, $\Delta\varepsilon$ is the energy difference between the two states and T is the temperature in Kelvin)

This imbalance, with a greater number in the parallel state, creates a net magnetisation in the tissue, in the direction of the applied field (**M_0**).

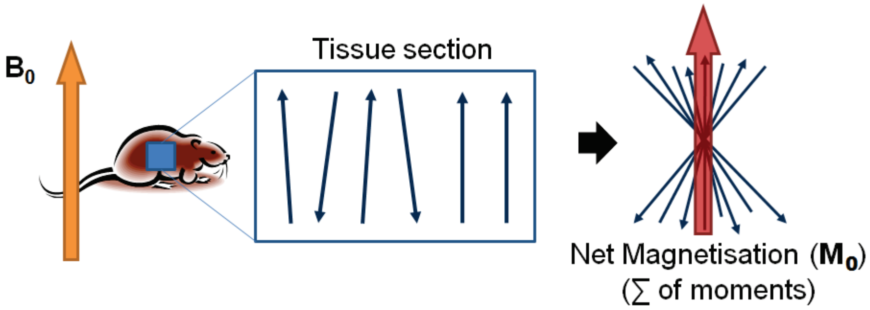

Figure 2.3: *Illustration of the summation of magnetic moments in a sample in a magnetic field leading to the net magnetisation (**M_0**)*

At the same time, these spins precess about an axis parallel to the field lines of the applied magnetic field. The frequency of precession – known as the Larmor frequency ω_L– is proportional and particular to the field-strength used.

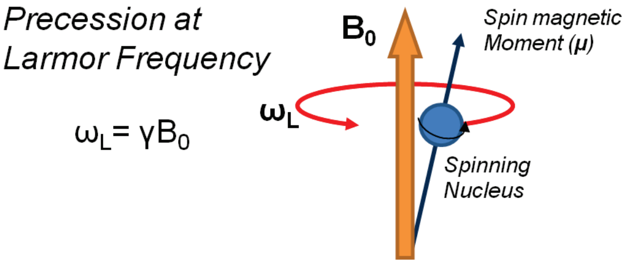

Figure 2.4: *Schematic showing an outline of spin precession (where γ is the gyromagnetic ratio)*

The magnetisation created in the tissue is also very small (of the order of microTesla) compared to the main magnetic field. As it is also aligned with the main field, it first must be brought out of this alignment before it can be measured. This is achieved by the input of energy into the tissue in order to create a transition of protons from the lower to the higher energy spin state. The energy needed for this is defined in equation shown in Eq. 2.2.

(Eq. 2.2)
$$E = h\nu = \frac{\gamma h B_0}{2\pi}$$

(where E=energy to cause a spin-state transition, h=Planck's constant, B_0=field strength of the external magnetic field and γ=gyromagnetic ratio)

This relationship suggests that a high gyromagnetic ratio and a high external magnetic field would give the highest degree of energy change and thus signal. This is one reason for the use of ^{1}H (the nucleus with the second highest magnetogyric ratio) for MRI and the continual push for the use of higher and higher field strengths for imaging magnets. Additionally, most tissues contain an approximately 90M concentration of water hydrogen and this abundance makes it especially useful in MRI studies.

Applying this energy as a radiofrequency (RF) pulse at the Larmor frequency, perpendicular to B_0, causes the transition of spins to the higher energy level before returning to the ground state. This has the effect of unbalancing the net magnetisation **M,** moving it into an angle with the main field. The extent of deviation – the flip angle (α) – is determined by the duration and magnitude of the RF-pulse used. After the application of the RF-pulse, the net magnetisation then returns parallel to the magnetic field. This process is illustrated in Figure 2.5.

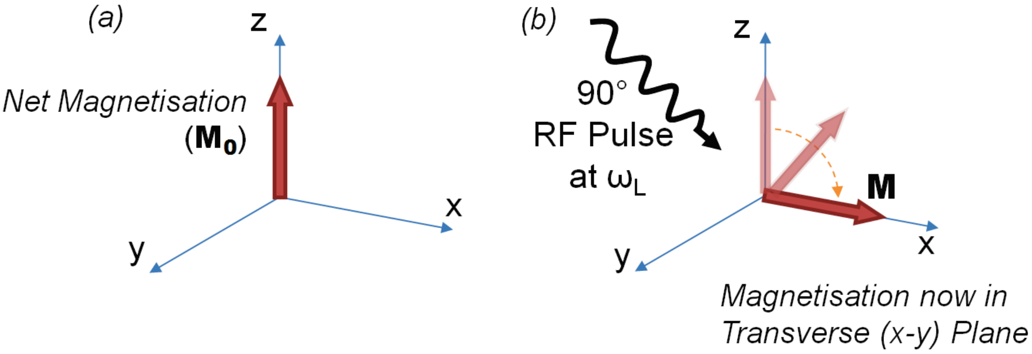

Figure 2.5: *Illustration of the effect of an RF pulse on the magnetisation. After being at equilibrium and aligned with the main magnetic field (a), after application of a 90° RF the magnetisation (*$\mathbf{M_0}$*) is tipped into the transverse plane (b) giving a new vector (**M**).*

The precession of the magnetisation in the transverse plane, in combination with its decay, creates an induced, sinusoidal current in a receiver coil near the sample, producing the characteristic NMR signal known as the free induction decay (FID).

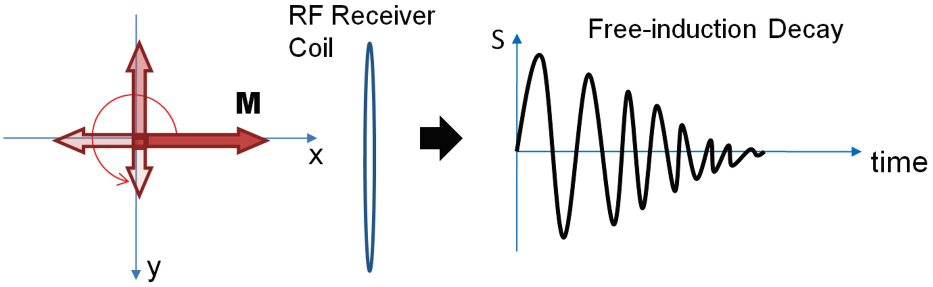

Figure 2.6: *FID Generation: The combined rotation and decay of the transverse magnetisation is detected by a receiver coil (left). The induced electromagnetic current is known as the free induction decay (FID) (right).*

2.2.1 MR Signal Characteristics

This return, or *relaxation* of magnetisation to equilibrium, is governed by two concurrent processes: spin-lattice relaxation (the longitudinal, z-component of magnetisation: also known as T_1) and spin-spin relaxation (the transverse, x-y component: known as T_2).

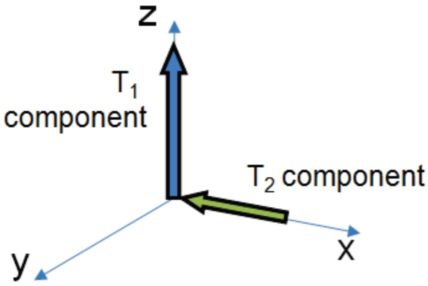

Figure 2.7: *Outline of the overall path of spin relaxation as seen from the laboratory reference frame. The individual contributions of T_1 and T_2 relaxation processes during this process are shown by the arrows, with T_1 acting longitudinally and T_2 transversely in the x-y plane.*

2.2.2 T_1 Relaxation

Spin-lattice or T_1 relaxation – is the gradual loss of energy from excited spins back to the main lattice of the sample and is the longitudinal (z) component of the total relaxing magnetisation as it returns to the equilibrium position. Spins are unlikely to spontaneously return to the lower energy state and instead rely on stimulated emission of energy through dipole-dipole interactions with their surroundings. This is brought about by the tumbling motion of surrounding dipoles. For a transition to take place between spin states, interactions need to take place at near the Larmor frequency. Fast tumbling media, such as free protons in liquids, tend to have very long T_1 relaxation times as the fluctuating magnetic field varies faster than the Larmor frequency minimising its effect. Similarly, bound protons tend to have slow rates of tumbling and so also have a long T_1. The ideal environment is among intermediately bound protons, which tumble at the Larmor frequency, resulting in a greater number of spin transitions per unit time and thus the shortest T_1.

2.2.3 Measurement of Tissue Parameters: T_1

The gold-standard for T_1 measurement is a technique known as inversion-recovery. In this method, spins are initially inverted in the Z direction yielding a magnetisation of $-M_0$.

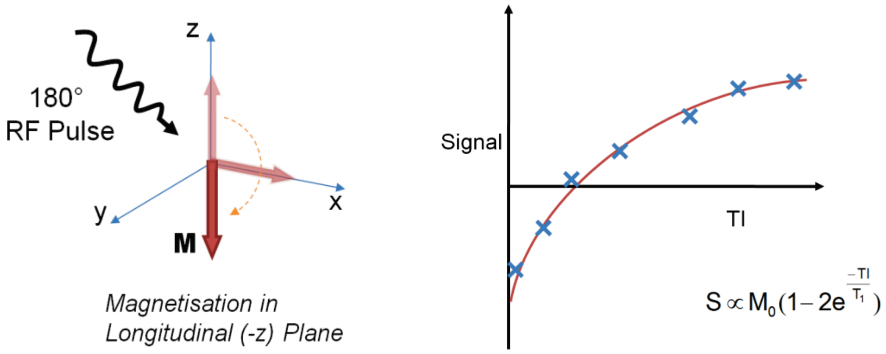

Figure 2.8: *Illustration of* T_1 *measurement in a sample. Spins are initially inverted by a 180° pulse (shown left). The remaining signal after a number of inversions is shown in the right graph. A curve corresponding to the recovery may then be fitted to these points yielding the value of* T_1

After a certain delay time – the inversion time (TI) – the remaining M_z magnetisation can be recorded. Sampling at multiple inversion times builds up the full recovery curve, allowing the tissue T_1 to be calculated. The T_1 value for a specific tissue is the time needed for the longitudinal magnetisation to return to 63% of M_0. The full recovery curve during inversion-recovery is defined by the following equation:

(Eq. 2.3)
$$S \propto M_0(1 - 2e^{-\frac{TI}{T_1}})$$

The repetition time between inversion experiments (TR) is typically five times T_1 in order to ensure full longitudinal relaxation of the tissue at each stage (Pykett et al., 1983). An adiabatic inversion pulse will often be used, as this ensures spins are exactly inverted by 180°. Otherwise variations in the RF power delivered by the scanner may lead to flip angles more or less that the desired amount if a conventional pulse is used, leading to inaccurate T_1 values.

2.2.4 Measurement of Tissue Parameters: T_2

Spin-spin or T_2 relaxation occurs in the x-y plane and is characterised by the gradual dephasing of the spins which are initially coherent after the 90° RF pulse. As two neighbouring protons (in the same molecular environment and at the same precessional frequency) come close together, energy is readily exchanged between each other. Inter- and intramolecular interactions can also cause fluctuations in the rates of precession. Both processes lead to the loss of initial coherence as these energy exchanges take place and spins dephase with each other. This has the effect of reducing the transverse magnetisation with time. This is shown schematically in Figure 2.9 below.

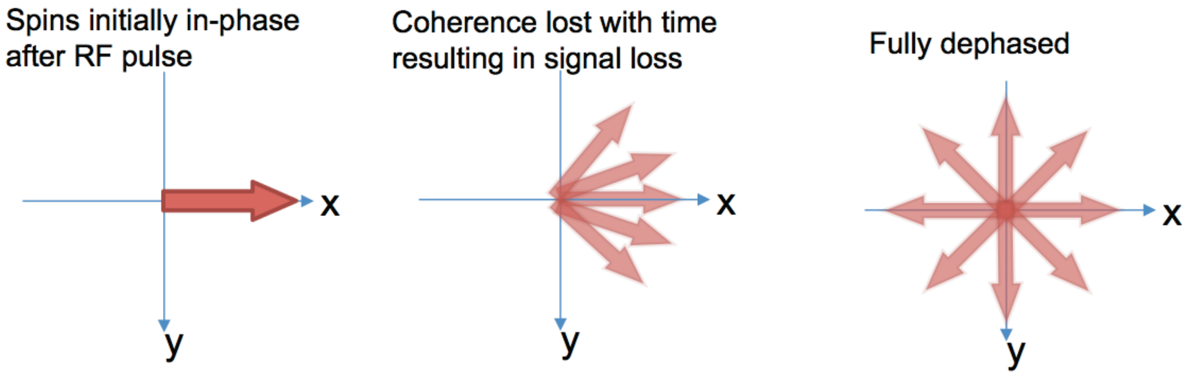

Figure 2.9: *Illustration of the loss of phase coherence of spins in the transverse x-y plane. After the initial 90° RF pulse (left), spins are initially in phase with each other, resulting in a high received signal. After a short amount of time (~ms) spins begin precessing at slightly different rates, becoming out of phase (middle), resulting in a reduction in net signal. After complete* T_2 *relaxation (right), spins are fully dephased resulting in zero net signal.*

Solids tend to possess a broader range of precessing frequencies, as bound protons tumble slowly and behave more like a static inhomogeneity. Thus T_2 decay is fast in this case. Fluids have a narrower range of B_0 frequencies as their fast tumbling results in a fluctuating magnetic field that averages to near zero. This leads to a fairly homogenous local field and a slower rate of T_2 decay. In contrast to T_1 relaxation, while there is interaction and energy exchanged between spins, no net energy is lost.

It is possible to measure the relaxation time of the transverse magnetisation component. The general equation for remaining MR signal at a certain echo time, due to T_2 decay is:

(Eq. 2.4)

$$S \propto M_0 e^{-\frac{TE}{T_2}}$$

The value of T_2 is the time after which the signal due to transverse magnetisation will be 37% of M_0. To calculate T_2, results of a series of MR experiments are plotted with the signal intensity against increasing echo time. A curve fit to this data allows T_2 to be accurately determined.

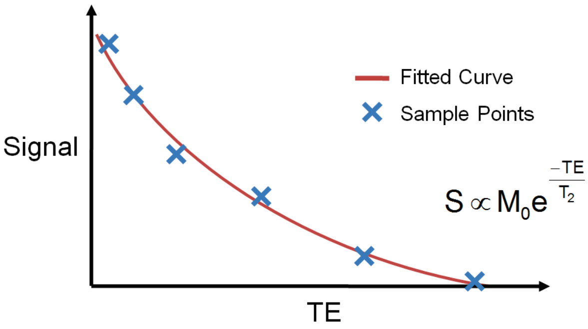

Figure 2.10: *Illustration of T_2 measurement in a sample. The remaining signal after a number of echo times is shown. A decay curve may then be fitted to these points giving the value of T_2.*

2.2.5 MR Image Generation and Contrast

The free-induction decay itself is rarely used directly in an image acquisition – an ‘echo’ is usually created and acquired. As spins begin to dephase at the end of the FID, an echo can be generated by bringing dephasing spins back into coherence. Building up successive echoes across a volume allows the raw frequency information to be obtained and taking the Fourier transform of this data produces the MR image.

There are broadly two subtly different methods of producing an echo and these define two basic MR imaging sequences known as gradient-echo and spin-echo.

2.2.5.1 Gradient-echo Imaging

Gradient echo imaging uses a magnetic field gradient across the sample to rapidly dephase spins. Reversing the sign of the gradient causes spins to rephase and form an echo. The time taken before creating the echo is known as the echo time (TE). Gradient echo allows short echo times, as only one RF pulse is needed in one TR.

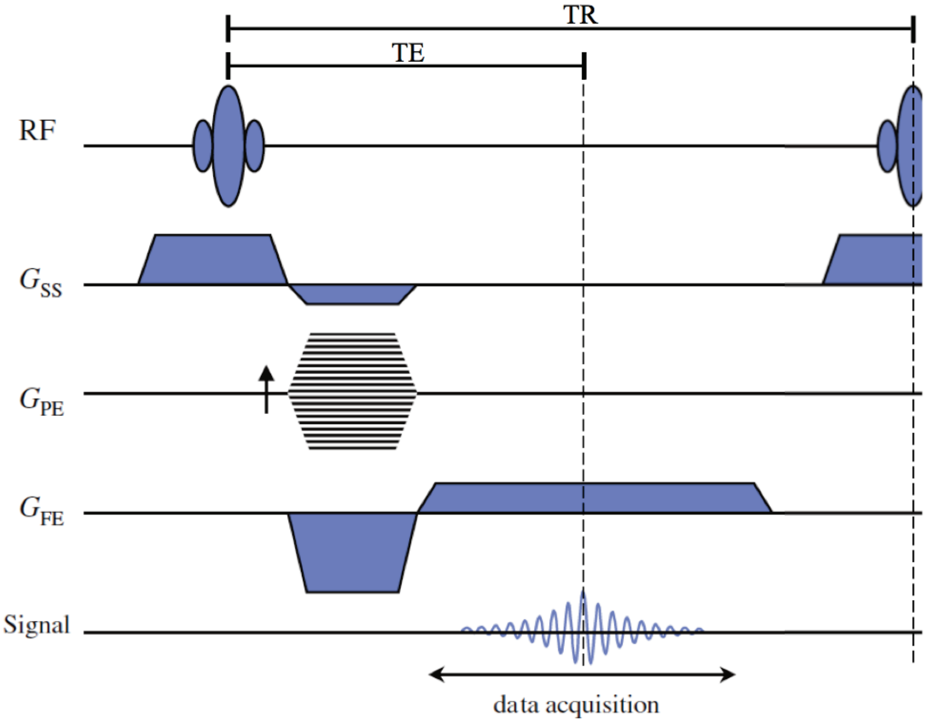

Figure 2.11: *Basic pulse sequence diagram of a slice-selective gradient-echo sequence. G_{ss}=slice selection gradient, G_{PE}=phase encoding gradient, G_{FE}=frequency encoding gradient, TE=echo time, TR=repetition time. Adapted from (McRobbie et al., 2003).*

However, true T_2 relaxation is rarely encountered in gradient echo sequences, as the transverse relaxation of the remaining magnetisation is susceptible to inhomogeneities in the main magnetic field which are not corrected as the gradient refocuses the spins. These local differences cause spins to dephase more quickly than would be expected in T_2-decay, resulting in shorter, composite relaxation known as T_2*. This is dependent on the extent of the local field inhomogeneities in both the main magnet and the sample (ΔB_0) and may be defined by equation 2.5:

(Eq. 2.5) $$\frac{1}{T_{2^*}} = \frac{1}{T_2} + \gamma \Delta B_0$$

It is possible to minimise some of this change and additional 'shim' coils cited around the main magnet can improve the uniformity of the field, reducing ΔB_0.

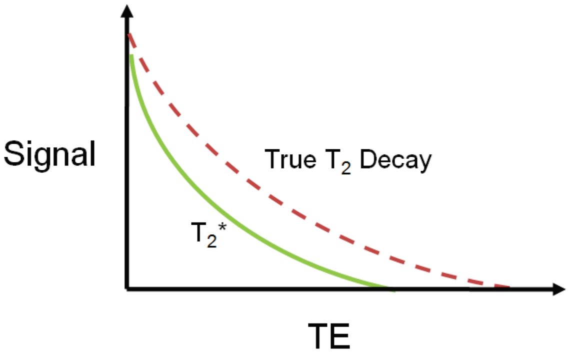

Figure 2.12: *Graph illustrating the effect of magnetic field inhomogeneities on* T_2 *decay in a sample. These result in faster dephasing and a composite* T_2** *decay.***

A common problem with gradient echo-sequences is the build-up of residual transverse magnetisation (Epstein et al., 1996), which may lead to image artefacts. Additional 'spoiler' gradients and RF pulses may be used as part of the pulse sequence in order to remove any residual magnetisation. Thus a commonly used sequence is so-called RF-spoiled gradient echo.

2.2.5.2 Spin-echo Imaging

The spin echo imaging sequence gives high SNR images and is less susceptible to magnetic field inhomogeneties. Spin-echo imaging uses a 180° refocusing RF pulse to create the signal echo, instead of a magnetic field gradient. The 180° has the effect of reversing the direction of the dephasing spins, causing them to now rephase. An advantage of spin echo is that inhomogeneities in the main B_0 field are also corrected after the application of the 180° pulse, producing an echo that follows true T_2 decay and not T_2*.

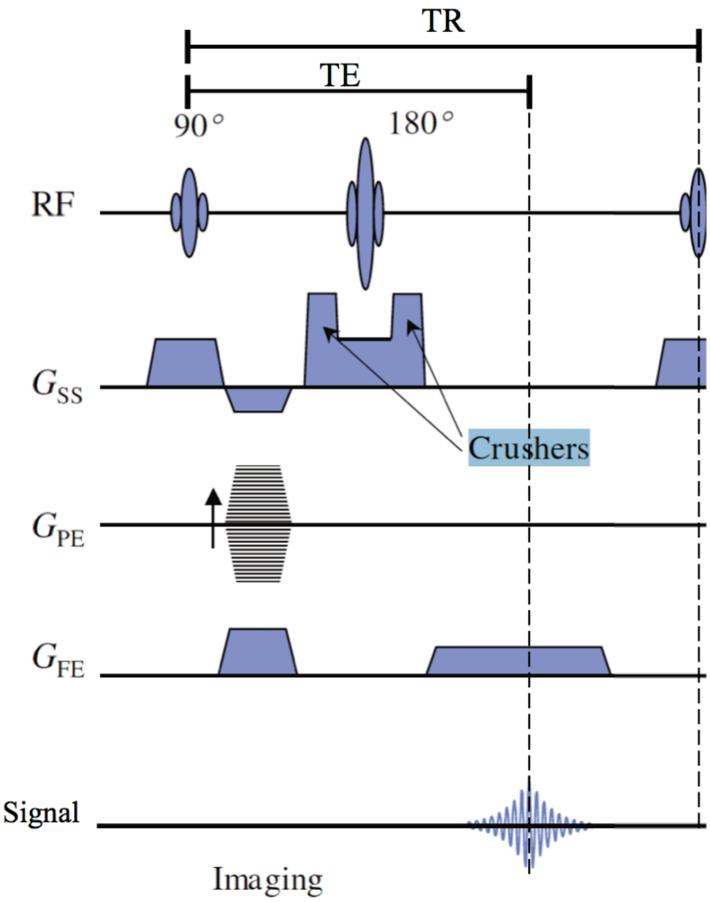

Figure 2.13: *Pulse sequence diagram of a basic spin-echo sequence. Also shown are crusher gradients about the 180° pulse which remove any residual FID prior to acquisition due to imperfections in the pulse. Adapted from (McRobbie et al., 2003).*

2.2.6 k-space and the Fourier Transform

With the advent of Fourier-imaging through the use of imaging gradients, MRI data is acquired in the frequency domain. This may be represented as a 2D or 3D space known as k-space. In k-space, the imaging data with each successive phase-encoding step is acquired during each phase-encoding line is placed into a row in the k-space matrix. After acquiring all k-space data in the 2D plane or 3D volume, performing successive Fourier transforms in x, y and (if applicable) z-directions and taking the absolute value, will then reconstruct the magnitude image data.

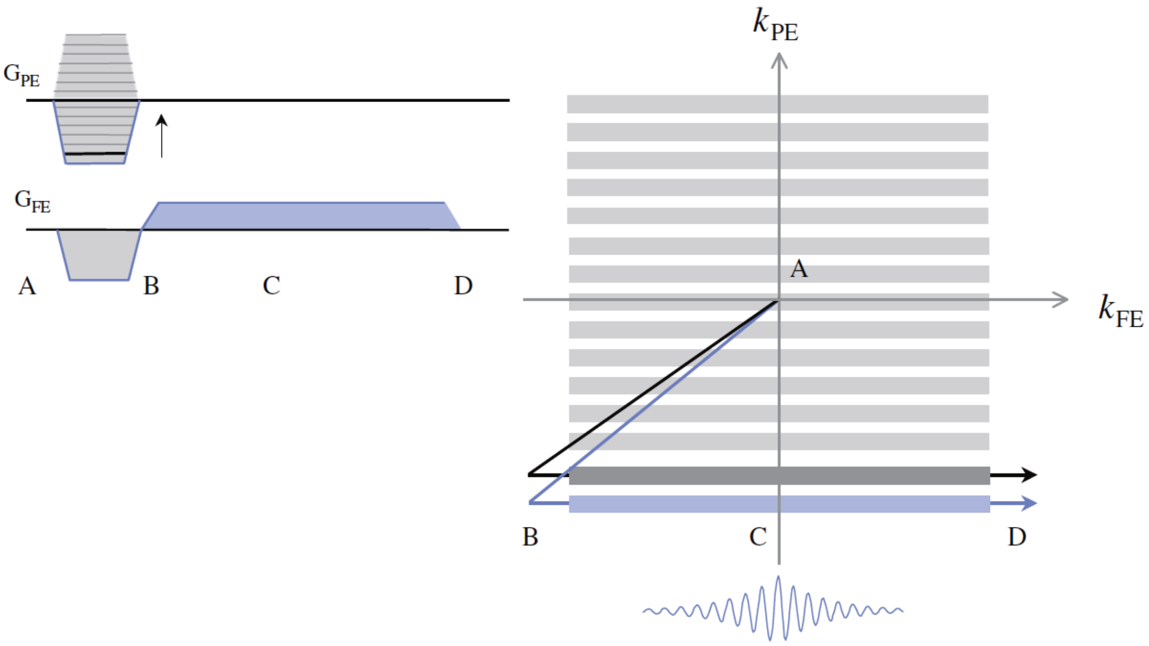

Figure 2.14: *Illustration of echo placement into k-space in a 2D image. The measured echo during each successive increment of the phase-encoding gradient (G_{PE}) is placed in a new k-space line (right), building up the complete range of spatial frequency information needed to create an image. Taking the absolute value of the 2D Fourier transform of the k-space data will yield a magnitude image. Adapted from (McRobbie et al., 2003).*

2.2.7 Image Contrast in MRI

The contrast between structures seen in an MR image is determined by a number of factors, namely the density of protons in the tissue (which determines the magnitude of M_0), tissue relaxation parameters (T_1, T_2 and T_2*) and the choice of MR sequence timings. A specific tissue will have a unique combination of these parameters based on structure and the local proton environment. To exploit differences between tissues one can alter MR scan parameters (such as TR and TE) in the imaging sequence. An example is shown in Figure 2.15.

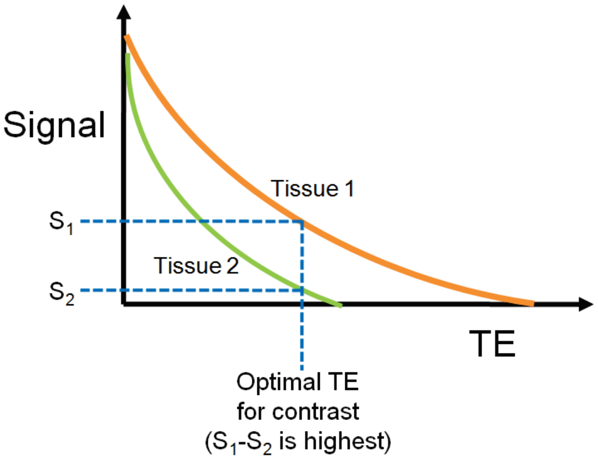

Figure 2.15: *Example of the effect of sequence parameters on contrast showing the difference for two tissues, in this instance varying TE to give* T_2 *or* T_2** *contrast. Maximum contrast* (S_1-S_2) *is achieved when signal difference is at its highest. From this graph it is apparent that Tissue 1 has a longer* T_2 *than Tissue 2.*

If the precise values are known for the tissues of interest one can go further and mathematically model the signal intensity and relative contrast produced in an image in order to determine the optimum for distinguishing two tissues. This is achieved by inserting experimental values into a theoretical signal intensity equation for a given MR imaging sequence. Contrast may then be determined for a variety of sequence parameters, giving the optimum TR and TE.

2.3 Microscopic MRI (μMRI)

From the initial description of MRI by Lauterbur in the early 1970s, it was conceived that the technique could be capable of producing images at near microscopic resolutions. This has led to the emergence of the field of microscopic magnetic resonance imaging or μMRI – which is typically defined as image acquisition at an isotropic voxel resolution of less than 100μm (Benveniste and Blackband, 2006).

The need for a separate term for imaging on this scale arises from the challenges in imaging objects at such small voxel sizes. The foremost concern is that that sufficient MR signal obtained during imaging this is directly proportional to the voxel volume. Thus a 3D dataset with voxel dimensions of 100μm in all directions (termed 100μm isotropic) will have 1/1000 the signal-to-noise ratio (SNR) per unit time of a 1mm isotropic dataset.

There are a number of engineering strategies for improving SNR at microscopic resolutions. The use of a high field spectrometers (with a field strength >7 Tesla) is important as this increases the detectable tissue magnetisation, giving rise to the approximately linear relationship between SNR and field strength (Edelstein et al., 1986). Signal may also be gained through the use of smaller imaging coils, as receiver coil sensitivity is inversely proportional to coil diameter. Specialised types of imaging coils have also been developed for µMRI use, such as those utilising cryogen cooling (Wright et al., 2000) (which reduces coil resistance and improves thermal noise). Increasing scan time by combining longer repetition times (which allows more T_1 recovery, boosting signal) and an increased number of signal averages (NSA) will also improve SNR. The acquisition bandwidth (BW) – the range of frequencies sampled by the receiver during the application of the frequency encoding gradient – can also affect SNR. A higher bandwidth will increase the range of frequencies sampled, and as noise is constant over the frequency spectrum, more noise will be incorporated into an image. A summary of the relationship between SNR and some of these dependencies (excluding T_1 and T_2) is shown in equation 2.6 (Kale et al., 2009):

(Eq. 2.6)

$$SNR \propto \Delta x \Delta y \Delta z \sqrt{NSA} \frac{1}{\sqrt{BW}}$$

(where x, y and z represent voxel dimensions, NSA the number of signal averages and BW the bandwidth)

It should be noted from that increasing signal averaging alone is a particularly time-expensive method of increasing SNR. For example, if the voxel size is doubled in all directions, the number of averages and thus the time needed will increase by 64-fold. Thus one must generally look to the choice and optimisation of the MRI sequence parameters and sample preparation to in order to improve SNR.

To produce high-resolution 3D datasets and mitigate potentially long scan times, ‘fast’ 3D imaging sequences are used in µMRI. Two sequences in particular are commonly used: gradient echo, which generally offers T_1 contrast with a short TR

(~30ms) or fast spin-echo offering T_2 contrast can acquire multiple echoes per phase-encoding step. Partial-Fourier techniques may also be used to reduce time (Petiet et al., 2008), where a portion (typically ~75%) of k-space data in the two phase encoding directions are acquired, reducing the number of TRs needed. While the phenomenon of k-space symmetry may be employed to allow final image reconstruction, there is loss of SNR due to this undersampling (McRobbie et al., 2003).

Choice of receiver bandwidth is particularly important in μMRI as this has an impact on the resolution of structural detail. The bandwidth of the system should be sufficient to resolve the full range of frequencies corresponding to a particular voxel. Too low a receiver bandwidth results in blurring and poor edge discrimination. This is a matter of balance however, as a higher bandwidth will lead to an increase in noise and reduced SNR. The minimum bandwidth needed for a given tissue may be defined in terms of its T_2*:

(Eq. 2.7) $$N\frac{1}{\pi T_2^*} = BW$$

(where N is the number of points in the frequency encoding direction)

The amounts of data created in μMRI acquisitions can pose challenges during reconstruction and analysis, given the use of large matrix arrays (typically 512^3 or higher) for multiple subjects (leading to datasets of several gigabytes) (Petiet et al., 2008). However the progressive rise in processing power and storage capacity of personal computers, coupled with the introduction of 64-bit architectures has made working with larger matrix sizes more practical.

2.4 MR Contrast Agents

MR contrast agents are compounds that have the ability to alter the intrinsic MRI contrast properties of tissue and are used clinically for angiography and enhancing areas of pathology such as brain tumours or an area of myocardial infarction in the heart (Mathur-De Vré and Lemort, 1995). In recent years these agents have also found a use as so-called ‘active-stains’ for *ex-vivo* tissue (Johnson et al., 2002b). In contrast to the engineering and pulse sequence strategies previously discussed that facilitate μMRI, this offers a method of manipulating the MR properties of tissue, further boosting the SNR obtainable.

MR contrast agents fall into two categories: positive contrast agents based on paramagnetic metals (such as gadolinium or manganese) which generally cause an increase in signal; and negative contrast agents, consisting of superparamagetic compounds (typically iron oxide based agents) that create signal voids on an MR image. The physical mechanisms of these agents are quite different.

2.4.1 Paramagnetic MR Contrast Agents

Paramagnetic agents act to reduce tissue relaxation times at short distances (Caravan, 2007) and protons need to be either in direct contact with the complex or close in the local environment. Gadolinium-chelate compounds are the most commonly used paramagnetic agents and generally provide positive contrast. They reduce both T_1 and T_2 relaxation times but at typical clinical concentrations the T_1 effect is most apparent. This reduction is due to the compound's structure: gadolinium has seven unpaired electrons in its outer shell. These electrons have a very high magnetic moment compared to a proton (~658 times larger) and hence can create strong local effects. In the case of T_1, strong dipole-dipole interaction leads to a greater number of spin transitions in the tissue and thus a shortening of the observed tissue T_1. Also at relatively high concentrations, the agent will behave as a local inhomogeneity and cause higher dephasing of spins and a shortening of T_2.

The chelate component of Gd complexes has two functions. It first acts as a protective agent for *in-vivo* use, as gadolinium, in common with other heavy metals, is highly toxic. It also reduces the number of water binding sites on the Gd^{3+} ion, making the relaxation effect highly local and primarily dependent on water protons interacting with the molecule itself. A common paramagnetic MR contrast agent is the compound gadolinium-diethyl-triamine-penta-acetic acid (Gd-DTPA, tradename Magnevist) whose structure is shown below. In this instance, the DTPA component in the molecule reduces the number of water coordination sites on the Gd^{3+} ion from 9 to 1.

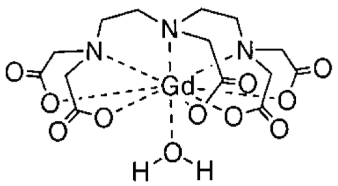

$[Gd(DTPA)(H_2O)]^{2-}$ (Magnevist™)

Figure 2.16: *The physical structure of the molecule Gd-DTPA, showing a single coordinated water molecule in the inner sphere. Adapted from (Caravan, 2007).*

There are a number of features of paramagnetic agents that affect their relaxation enhancement. An illustration of some of these features and molecular interactions are shown in Figure 2.17 below.

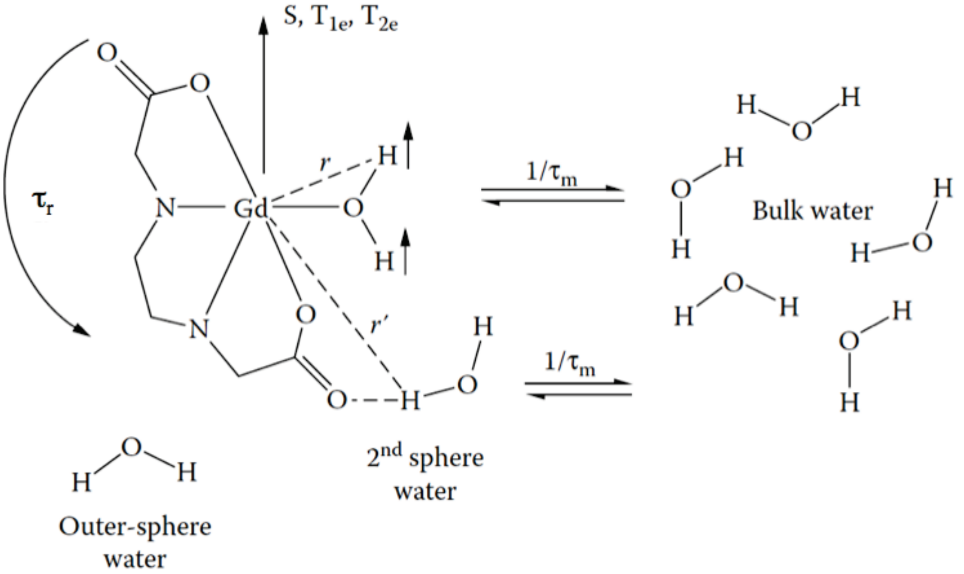

Figure 2.17: *Types of interaction of water proton interactions with Gd-DTPA and molecular parameters that affect relaxation. Such protons may undergo relaxation enhancement through the inner sphere, 2^{nd} sphere or outer sphere relaxation mechanisms. Molecular parameters shown include: τ_r= rotation time of the complex, τ_m=residence time of the water molecule in the complex, r=the distance of the proton from the paramagnetic ion, T_{1e}=electronic T_1 relaxation time, T_{2e}=electronic T_2 relaxation time, S=spin quantum number: 7/2 for Gd^{3+}. Adapted from (Caravan, 2007).*

The relaxation of water molecules surrounding the Gd-chelate is dependent on encountering a locally fluctuating magnetic field. A number of characteristics of the agent enable this. First, the properties of electrons in the Gd ion promote relaxation, such as the high spin number (S=7/2) and slow electronic relaxation rates (T_{1e} and T_{2e}). Second, are properties of the complex that enable interactions with water optimal for relaxation. Although there is only one coordination site, the coordinating water is in rapid chemical exchange with the surrounding bulk water (10^6 exchanges per second) and this also results in efficient inner sphere relaxation. τ_m represents this residence time of water in the inner sphere, which should be short in order to allow the greatest number of water molecules to undergo inner sphere relaxation from the surrounding bulk water. Additionally, while not interacting directly with the Gd ion, surrounding bulk water molecules may also undergo some relaxation in 2nd sphere and outer sphere environments. τ_r represents the rotation time of the contrast agent molecule, which should be relatively slow in order to allow time for immediately surrounding water to coordinate in the inner sphere.

An overall measure of the interaction between two species (Gd and water protons) is the correlation time (τ_c) which encompasses some of the parameters discussed (Eq. 2.8 below), including the water residence time, molecular rotation time and electronic T_1. Ideally the reciprocal of this quantity should be close to the Larmour frequency in order to ensure efficient T_1 relaxation.

(Eq. 2.8) $$1/\tau_c = 1/\tau_r + 1/T_{1e} + 1/\tau_m$$

This study of paramagnetic MR contrast agents was begun fairly early on in the development of MR and is formally described in the work of Solomon (Solomon, 1955) and Bloembergen (Bloembergen, 1957). This has resulted in the construction of a simple relationship to determine a measure of the relative efficacy of a contrast agent in altering T_1 and T_2 relaxation times, known as the relaxivity (R), and may be defined in relation to T_1, T_2 or T_2* as Eq. 2.9.

(Eq. 2.9) $$\frac{1}{T_{total}} = R[CA] + \frac{1}{T_{tissue}}$$

(where T_{total} is the observed relaxation time, [CA] is the agent concentration and T_{tissue} is the relaxation time in the absence of agent)

From this equation, an effective agent would be expected to produce a high degree of relaxation with a small concentration and therefore possess a high relaxivity value. This is a characteristic of Gd-based agents. Relaxivity values are specific to a particular relaxation mechanism (T_1 or T_2) and depend on the medium where the agent is present. While paramagnetic agents act to reduce both T_1 and T_2 relaxation times, at the concentrations typically used both clinically and active-staining applications, the predominant effect is that of an increase in signal due to T_1 reduction.

2.4.2 Superparamagnetic Agents

While future chapters of this thesis will concentrate on paramagnetic agents, which produce local, positive contrast that is most useful in high-resolution imaging studies, another major class of compounds – superparamagnetic agents – are also in common use. These are generally composed of crystalline particles of iron oxide (e.g. ferrite, Fe_3O_4). A large ferrite crystal containing a large number of spins can, through quantum interactions, result in a very large total spin and thus a very high magnetic susceptibility. This phenomenon is known as ferromagnetism and the material's magnetism continues even after removal from the external magnetic field. If small, sub-micron, iron oxide particles are used instead of a large crystal, the result is a material that exhibits a weaker form of susceptibility known as superparamagnetism (termed superparamagnetic iron oxide particles or SPIOs). In contrast to ferromagnets, such materials do not remain magnetic after removal from an external magnetic field.

As with the paramagnetic agents, high concentrations of iron can be highly toxic in biological systems and so for clinical use, particles are coated with a biochemical wrapper. One example of an SPIO agent is ferumoxide (tradename Endorem) which has a dextran coating to ensure biocompatibility. In contrast to paramagnetic agents, these particles result in image hypointensity due to T_2 reduction, majority of effects from these particles. Behaving like an inhomogeneity in the magnetic field these agents are able to produce negative contrast (signal voids) on MR images. A clinical use of these agents is in hepatic tumour imaging, as the particles are most easily taken up by functioning phagocytic Kuppfer cells of the liver, allowing the delineation of tumour cells that do not. A further application in pre-clinical studies has been the use of SPIO agents for stem cell tracking. Cells are able to take up SPIO particles which then appear as small hypointensities when introduced into tissue. The movement and division of these cells may then be monitored over time to determine their effect in regions such as the brain (Panizzo et al., 2009) or the heart (Stuckey et al., 2006).

2.5 Tissue 'Active-staining' for μMRI

While MRI is usually considered as an *in-vivo* technique, it has been frequently applied to the imaging of post-mortem (Thayyil et al., 2009) and delicate tissue samples (Null et al., 2008; Ullmann et al., 2010), where non-invasive examination of the intact structure is important and provides a useful adjunct to conventional, destructive histology. However, imaging of normal fresh or fixed tissue is constrained by the intrinsically long T_1 (of the order of seconds) leading to long scan times in order to achieve acceptable SNR with high resolution.

An innovation initially described by Johnson *et al.* (Johnson et al., 2002a) has been the use of Gd-based MRI contrast agents as so-called active-stains for tissue. Similar to histological staining, the use of the contrast agent enables firstly more rapid μMRI of tissues and secondly may modify the MR properties to reveal structural detail. The initial use of active staining was for the former, to enable sufficient signal-to-noise for μMRI, due to predominant T_1 reduction properties of paramagnetic agents as previously discussed.

With their predominantly local mechanism of action, which leads to positive contrast and increased signal, gadolinium chelates in particular, are the agent of choice for active stains in *ex-vivo* tissue. Given their good relaxivity properties, only small quantities are needed: immersing tissue in mM concentrations shortens T_1 (typically from ~2 sec to <100ms). This causes a great improvement in the signal available due to faster recovery of longitudinal magnetisation. μMRI can then be performed with greatly reduced scan-times, decreasing from the order of days to hours for a typical 3D scan.

So far a number of Gd-chelate agents at a variety of concentrations, in combination with both spin- and gradient-echo sequences, have been used for active-staining in *ex-vivo* mouse imaging. Standardised preparation protocol has yet to be agreed upon for either embryo or brain tissue. The two most commonly used agents are Gd-DTPA and gadoteridol (tradename ProHance) used for doping solutions of formaldehyde fixatives. While their molecular structures are somewhat different, using different chelates, gadoteridol has very similar relaxivity properties to Gd-DTPA in solution. The two main approaches employed are either a high concentration of agent (typically ~45mM) in the initial fixation of tissues (over the first few hours) or immersion with a lower concentration (2-8mM) over at least several days.

The consequences of the addition of MR contrast agent to fixative are a dramatic reduction and compression of the range of T_1s and T_2s from normal values (as illustrated in Figure 2.18). Thus imaging parameters that are conventionally used in the *in-vivo* setting or in ordinary fixed tissue will not be appropriate may need to be adjusted for the particular concentrations, immersion durations and for the specific structural contrast.

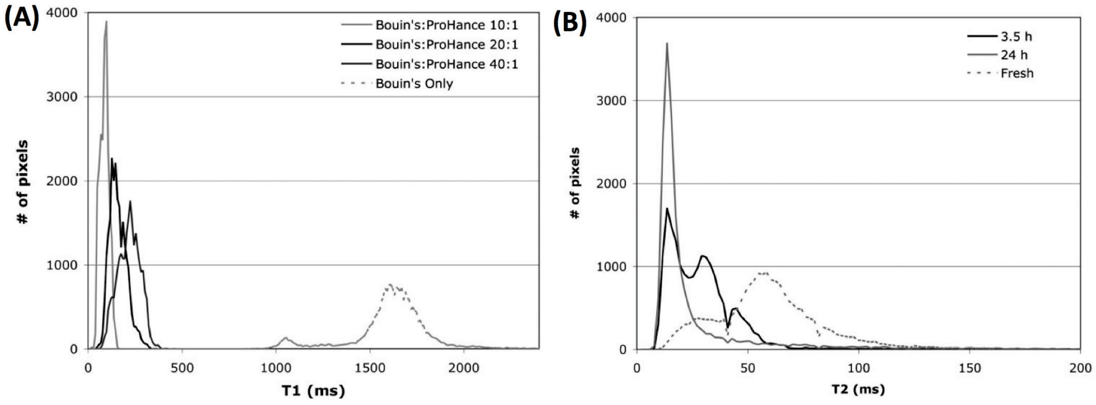

Figure 2.18: *Examples of compression of* T_1 *and* T_2 *values in 18.5dpc rat foetuses. (A) Shows a histogram of* T_1 *values after fixation for 3.5 hours in Bouin's fixative solution doped with increasing concentrations (12, 24 and 45mM) of the Gd contrast agent gadoteridol. (B) Histogram of* T_2 *values in a rat foetus after immersion in Bouin's fixative doped with 24mM gadoteridol, after initial, 3.5 and 24 hours immersion-fixation. Adapted from (Petiet et al., 2007)***.**

While Gd-based chelates are the predominant agent used for µMRI studies, the use of other paramagnetic agents such as manganese chloride, as alternative active-stains are also being investigated. $MnCl_2$ becomes Mn^{2+} in solution and is thought to behave as an analogue of Ca^{2+} *in-vivo*. A large number of *in-vivo* MR studies use Mn^{2+} as a positive contrast agent, as it can lead to signal hyperintensity in tissues where it is taken up (Silva et al., 2008) providing an indication of function. Preliminary work in *ex-vivo* mouse brains as an alternative active-stain appears promising, suggesting the use of Mn^{2+} may give specific contrast by binding to tissue in the manner of conventional histology stains (Huang et al., 2009), although signal and contrast to noise may not be as high as Gd-agents due to the short T_2 of Mn-stained tissue.

2.5.1 Applications of MR to Mouse Embryo Phenotyping

As discussed in the previous chapter, due to the generally low volumes of embryos that may be phenotyped with conventional histology and its destructive effects on tissue morphology, there is interest in utilising non-invasive imaging methods for morphological screening. µMRI is one such imaging method, allowing assessments of both embryo development (Petiet et al., 2008) and phenotype (Bamforth et al., 2004; Goddeeris et al., 2008).

The use of high-resolution µMRI for cardiovascular phenotyping was initiated in the 1990s by Smith and colleagues (Smith et al., 1994; Smith et al., 1996), where they developed a technique to image embryo vasculature. Individual embryos are dissected and perfused through umbilical vessels with an MR contrast agent (bovine serum albumin-Gd-DTPA) dissolved in gelatin. Some time after perfusion, the gelatin hardens causing the agent to remain in the vessel lumen. A high-resolution 3D MRI then enables the visualisation of individual vessels in the embryo similar to an MR angiogram. This technique has been successfully used for vascular phenotyping studies (Berrios-Otero et al., 2009). A disadvantage of this method is the complexity and operator dependency of the embryo preparation, with only a small numbers (1 to 4) able to be imaged at once.

[Figure removed due to copyright]

Figure 2.19: *Maximum intensity projection image of the vasculature of a 16.5dpc mouse embryo prepared using the BSA-Gd-DTPA injection technique. Adapted from (Berrios-Otero et al., 2009)***.**

Later, Jacobs and colleagues produced high resolution MR images of single embryos (Dhenain et al., 2001), with the goal of creating 3D anatomical atlases as an advance over the 2D histology-based atlases (Kaufman, 1992) commonly used, although this involved imaging single embryos with very long scan-times – up to 37 hours per embryo (Dhenain et al., 2001).

The use of active staining in embryos, primarily as a method of T_1 reduction was initiated by Schneider et al. (Schneider et al., 2003b), enabling high-throughput embryo phenotyping studies through the use of large volume coils in conjunction with a gradient-echo sequence with a short TR (Schneider et al., 2004).

This work has recently been extended by Petiet *et al.* who developed an immersion-fixation protocol using Bouin's fixative doped with gadoteridol, in combination with 3D spin-echo imaging. The same group went on to produced an annotated database of embryonic, neonatal and adult mice imaged at a number of developmental timepoints (Petiet et al., 2008) and also to characterise heart phenotypes in mid-gestation embryos (Goddeeris et al., 2008). Their methodology has also been used recently for a manual volumetric study to determine the effects of embryonic brain development after ethanol administration (Parnell et al., 2009).

2.5.2 Embryo Imaging with MR, *In-utero*

The studies mentioned above have all been performed in *ex-vivo* embryos which offer the advantages of highly-controlled sample preparation and the imaging of subjects with little or no movement, easily achieving sub-100μm image resolutions. However, a goal of embryo MRI would be to ultimately develop a high-resolution *in-vivo* imaging, *in-utero*, in order to perform longitudinal and functional studies. Work on this front has slowly progressed over the past decade.

In the *in-utero* setting there are a number of challenges, particularly that of respiratory motion of the mother and movements of individual embryos, which can rapidly degrade image quality. Previous work has attempted to use relatively fast T_2-weighted, multi-slice acquisitions (5-9 slices, 0.8-1mm thick, 234x234μm in-plane resolution, scan time 4-6.5mins). However this need for a rapid acquisition, to minimise the effects of embryo motion typically results in relatively poor spatial resolution due to a limited number of phase-encoding steps and relatively thick image slices (Chapon et al., 2002).

[Figure removed due to copyright]

Figure 2.20: *In-utero images of 18/19dpc embryos showing visible anatomy. In-plane resolution = 234x234µm^2 Scale bar = 5mm. Adapted from (Chapon et al., 2002)*

More recent studies have used Mn^{2+} to improve SNR during imaging, as Mn^{2+} is readily taken up by tissues with a high Ca^{2+} turnover. This leads to signal enhancement especially in CNS structures, which in conjunction with retrospective respiratory gating to the mother's breathing, can produce good quality 3D images (Deans et al., 2008).

MR-based motion correction techniques such as navigator echoes may also be used to characterise and reduce motion (Ordidge et al., 1994). In embryo heart imaging there are particular difficulties in obtaining an ECG signals in order to gate the acquisition of k-space lines to specific heart phases. Access, the presence of multiple of embryos and the maternal heartbeat makes the use of conventional electrode ECG gating difficult. A technique called cardiac self-gating, has been used to address this, where a small amount of low resolution data is acquired just prior to image acquisition. This data can then used to identify the heart movements that relate to the phases of the cardiac cycle in a specific embryo. A self-gated sequence and imaging protocol has been successfully used to produce 3D images in 17dpc embryo hearts (Nieman et al., 2009).

[Figure removed due to copyright]

Figure 2.21: *In-vivo black-blood images and volume rendering of a 17dpc embryo heart at diastole (left) and systole (right). Images were acquired using a self-gated MRI technique. Adapted from (Nieman et al., 2009)*

2.6 Applications of MR to Adult Mouse Brain Phenotyping

Phenotyping in the adult mouse brain is also a key application of MRI and is able to produce excellent contrast between, grey and white matter, and the CSF present in ventricular structures. Conventionally, *in-vivo*, a number of image weightings (such as T_1, T_2 and Proton Density) are available to generate contrast through the relevant intrinsic properties of the three classes (grey matter, white matter and CSF) of brain tissues. In addition, tissues may be delineated through other more specialised contrast mechanisms such as magnetisation transfer (Natt et al., 2003) and diffusion imaging techniques.

Although this thesis focuses on methods of *ex-vivo* brain imaging, which provides the highest spatial resolution and visualisation of the greatest number of structures, an important use of MRI is its ability to conduct *in-vivo* imaging studies. Such studies enable the same subjects to be tracked over time, allowing the direct characterisation of anatomical or functional change with age or disease. For example, previous work in adult mice has used MR to characterise mouse models of neurodegeneration (for example, models of Alzheimer's disease) and the consequences of interventional models such as stroke. Changes in the volumes and signal intensity change in tissues may be observed. Additionally, neuropathological changes seen in these models may have additional MR-contrast that may be used as a biomarker to indicate the presence and severity of pathology. For example, in stroke models, infarcted tissue over the initial hours post-occlusion, will show a progressive increase in T_2, resulting in hyperintensity on T_2-weighted images. Also amyloid plaques in mouse models of Alzheimer's disease may have an increased iron content leading to a local T_2 reduction and a hypointensity in an image, allowing the plaque to be visualised.

[Figure removed due to copyright]

Figure 2.22: *Example 2D multi-slice MR images from individuals in a longitudinal study of structural brain changes in the R6/2 transgenic mouse model of Huntington's disease. Imaging was performed from postnatal day 21 to day 84. Potential cortex and hippocampal atrophy was seen in transgenic mice and are indicated by white and black arrows respectively. Dashed lines indicate structural boundaries identified on control brains at P21. Structural labels: 3V=third ventricle, CX=cortex, H=hippocampus, LV=lateral ventricles, S=striatum and T=thalamus. Adapted from (Zhang et al., 2010a)*

[Figure removed due to copyright]

Figure 2.23: *Visualisation of amyloid-β plaques in an APP/PS1 transgenic mouse by MRI. a&b:* T_2*-weighted in-vivo images of specific numbered plaques identified in a typical individual. c&d: similar* T_2*-weighted images in the same animal ex-vivo. e&f, g&h: images of the same numbered plaques in a similar histological sections after Thioflavin S amyloid, and Prussian blue-diaminobenzidine-enhanced iron stains respectively. Adapted from (Wengenack et al., 2008).*

However a disadvantage of *in-vivo* work is a limited scan-time, as an animal can only be under anaesthesia for a few hours in each scan session to ensure successful recovery, without lasting physiological effects. Also, as with embryo imaging, even slight movement may result in blurring of the image. This combination has the effect of limiting the achievable resolution to typically 100µm for 3D isotropic acquisitions (Bock et al., 2006), or for 2D multi-slice acquisitions, ~30µm in-plane with a 300µm slice thickness (Boretius et al., 2009). This relatively coarse resolution, compared to *ex-vivo* studies may affect the sensitivity of *in-vivo* MRI to detect very subtle phenotypic effects.

[Figure removed due to copyright]

Figure 2.24: *Illustration of the histological detail in cortical layers obtainable in the mouse brain by in-vivo MRI in combination with a specially designed mouse-holder to reduce subject motion during acquisition. (30x30µm in-plane resolution, 300µm slice thickness). Adapted from (Boretius et al., 2009).*

Ex-vivo imaging in contrast, although preventing longitudinal studies, enables high-resolution imaging as longer imaging times (usually several hours or more) are possible, and firm positioning of samples results in very little movement during acquisition. The resolutions of acquired images are typically as low as 20µm isotropic, thus approaching conventional light microscopy. With such high-resolution available, the applications of the technique are generally anatomical, such as MR atlases of single (Johnson et al., 2010) and multiple subjects (Dorr et al., 2008), in addition to mutant mouse phenotyping studies (Sawiak et al., 2009a).

[Figure removed due to copyright]

Figure 2.25: *Example axial image slices from a 'canonical' individual imaged at high resolution as part of a mouse brain segmentation and anatomical atlas project. (a) Monochrome Nissl stained histology section from a reconstructed 3D brain volume. (b) Similar* T_2** MR image slice from the same brain for comparison (c) Overlaid, coloured structure labels as identified from histology and registered to the MR image volume. Adapted from (Johnson et al., 2010).*

[Figure removed due to copyright]

Figure 2.26: *Coronal and sagittal* T_2*-weighted μMR brain images of typical wild-type (WT) and transgenic individuals from the R6/2 model of Huntington's disease. In the R6/2 mouse, the lateral ventricles appear enlarged compared to WT, indicating neurodegeneration. Images are full 3D volumes with 70μm isotropic resolution. Adapted from (Sawiak et al., 2009a).*

With such high-resolutions available, one would expect the sensitivity to the detection of subtle phenotypic changes in anatomy to be higher than *in-vivo* imaging. Although again, as in the embryo, datasets may be extremely large (e.g. 1 brain consisting of approximately 500 coronal slices at 40μm isotropic resolution) making manual inspection and volume analysis difficult. Here there is also a need for automated methods for automated identification of phenotype and background to the methods for the analysis of these large datasets will be introduced in the next chapter.

2.7 Diffusion Tensor Imaging

Diffusion tensor imaging (DTI) is another MR technique often applied to *ex-vivo* phenotyping studies. It utilises additional imaging gradients to explore the degree and direction that water can diffuse in tissue. In the mouse brain, DTI studies have been successfully used to investigate brain development (Baloch et al., 2009) and also to identify phenotype (Tyszka et al., 2006). The technique is particularly successful in allowing the visualisation of axonal white-matter tracts in the adult brain resulting in tractography maps (seen in Figure 2.7 below). However, a key factor limiting the use of DTI is the scan time needed to achieve <100μm isotropic datasets (e.g. ~24 hours per brain for <50μm resolution) and at least 7 complete image volumes also need to be acquired in order to give sufficient directional information to create the diffusion tensor map.

[Figure removed due to copyright]

Figure 2.27: *Example side (a) and bottom views (b) of white-matter tractography seen in a C57BL/6 mouse brain. Structures are: corpus callosum (red, enlarged in (d)), cingulum (cyan), anterior commissure (blue, enlarged in (c)), fimbria (white, enlarged in (e)), optic tract (green), and habenular commissure (pink, enlarged in (c)). Transparent regions shown for reference: olfactory bulbs (light blue), anterior commissure (purple), fimbria (green), hippocampus (yellow), septal nuclei (brown) and cortex (dark blue). (DTI data resolution 43μm isotropic, 6-directions+b0, scan time 28 hours). Adapted from (Jiang and Johnson, 2010).*

2.6 Conclusion

In this chapter, the basic principles of MRI were outlined, with a discussion on the mechanism of MR contrast agents and their use in μMRI, along with specific applications. The datasets produced by μMRI techniques, while detailed, are often large, presenting a challenge to an individual observer analysing multiple subjects. In the next chapter the use of automated image analysis techniques is discussed, which can greatly ease the burden of μMRI study analysis.

Chapter 3:

Image Analysis in Mouse Phenotyping

As seen in previous chapters, the completion of human and mouse genome sequences has resulted in a shift of research from genotype to phenotype. This study of mutant mice has the potential to make significant advances in the understanding of human disease processes, which may lead to new screens and therapies. However, with the ambitious scale of current international projects, significant challenges remain in the sheer quantity of data that will be acquired for phenotypic analysis of the many thousands of mouse lines generated in the coming years.

The previous chapter outlined the role of μMRI techniques in non-invasive mouse phenotyping, which offer high-quality 3D images with high signal and contrast-to-noise, giving typical isotropic resolutions of 20-50μm. However the resulting 3D dataset for a single mouse brain or embryo will typically consist of many hundreds of image slices. Over a number of subjects and mouse lines this quickly becomes a very large quantity of data.

While an individual could visually inspect each dataset, in a similar manner to a radiologist giving a report of findings, (comparable to the typical use of histology in mouse studies), this restricts the use of the 3D data to a simple description and provides limited quantitative information. Thus there is a need for objective, numeric measures of phenotypic structural change, which is one role of image analysis.

Additionally, while visual inspection may be a possibility for single or small groups of mutant mice, particularly those with obvious structural deformities, the sheer quantity of data may make such interpretation time-consuming and labour-intensive when many mice are imaged. Thus there is additionally a need for automated methods of image analysis to ease this burden.

This chapter will outline some of the basic principles behind image analysis, giving an overview of some commonly used manual and more recent, automated methods.

It should be noted that the application of automated methods to the analysis of preclinical MRI data is still at a relatively early stage of development with the first morphometric studies in the adult mouse reported only a few years ago. Use of such analysis in human studies is more established. Examples from both the human and mouse brain literature will therefore be described in this chapter. Additionally, the analysis of mouse embryo datasets is in the preliminary stages of development (Zamyadi et al., 2010), with our contribution (Cleary et al., 2010) discussed later in chapter 6.

3.1 Manual Analysis

The simplest way of analysing data is through a form of manual analysis. At the most basic level, this involves visual assessment of images for pathology by an experienced observer, similar to the way a radiologist would view and interpret data in the clinical setting. In phenotyping studies, the presence or absence of a particular structure may be tallied (and noted in a table) to give a measure of the incidence and penetrance of the phenotype in that population (such as in (Bamforth et al., 2004)).

A more quantitative approach would be make measurements of structures of interest. With 3D imaging volumes, such as those produced by μMRI, one could measure volumes of specific of organ structures. Typically these regions are drawn by hand on each slice in turn in a dataset, by loading the dataset into an image analysis package (one well-known example is ImageJ, a public domain, Java-based image processing program) which has specific tools for this purpose. The subsequent regions may then be used to generate data on a number of phenotypic parameters, such as shape, volume or average signal intensity in the image. While this may be conceptually simple, in the case of μMRI datasets, hand drawing of structures in several, often complex regions of interest may take many hours and in less-sophisticated programs, the task of keeping track of the large number of regions in an animal may not be straightforward (a example of a manually segmented mouse embryo is shown below in Figure 3.1 (Dhenain et al., 2001)).

[Figure removed due to copyright]

Figure 3.1: *An example of manual segmentation of structures in a 3D µMRI dataset of a 13.5dpc mouse embryo. A) Single axial slice of the original MRI dataset, B) Outline of manually segmented regions, C) Resulting coloured labels delineating structures such as brain (pink), ventricles (light blue) and spinal cord (white). Adapted from (Dhenain et al., 2001)***.**

An additional problem with this type of manual regional analysis, particularly in larger studies, is the possibility of inconsistencies in the segmentation of structures (Riegler et al., 2010) either through errors by a single or multiple observers. Structures may be segmented differently by the same observer in the same dataset (resulting in so-called intra-observer variability) and or two observers may segment a particular structure differently (resulting in inter-observer variability). Regions with a small volume or those that are poorly visualised due to low SNR or limited contrast boundaries may be particularly affected.

3.2 Semi-automated Segmentation Methods

Given the time-consuming nature of manual analysis, many image analysis tools now offer additional options to assist manual segmentation. For example, by using image contrast and regional signal intensity, one may be able to demarcate structures on the basis of similar signal intensity between adjacent voxels. Simple algorithms based on signal intensity such as flood-filling, may be used to identify regions: starting from a selected ‘seed’ voxel and then selecting an area up to a surrounding contrast boundary. These are most effective when initiated within an enclosed tissue of interest with a relatively homogenous signal intensity range. After building up a series of 2D segmentations over a number of slices, a 3D interpolation scheme, such as marching cubes, can then generate a 3D reconstruction of the volume. Examples of such segmentation and reconstruction are shown in Figure 3.2 below. However, as may be seen in the figure, these methods are highly dependent on a well-defined contrast boundary surrounding the structure and manual correction is often required to give a truly accurate result.

[Figure removed due to copyright]

Figure 3.2: *Examples of a surface and volume rendering based on the selection of an area based on MR signal intensity. In A, the approximate exterior surface of mouse embryo has been readily segmented by this approach. Similarly, in figure B, the high signal intensity of the brain and spinal cord relative to surrounding tissue has allowed segmentation of the CNS. While the both embryo and CNS structures are selected, in both images there is evidence of the limitations of a simple intensity algorithm: in A, a small area at the top of the head of the embryo remains unselected; in B, the contours of brain are not well-defined due to erroneous inclusion of surrounding voxels with a similar signal intensity. Adapted from (Schneider et al., 2003c).*

3.3 Automated Methods of Analysis

As seen in the previous section, manual and semi-automated approaches may have limitations, particularly in the ability of a single operator to reproducibly delineate a large number of anatomical structures in a reasonable amount of time and in the many subjects needed for a complete study. Thus a more automated approach to data analysis is vital to increase throughput.

The field of human brain research was one of the earliest to adopt computational morphometric techniques for identifying anatomical differences in a population. This has transformed research in the neuroimaging field, which accordingly has become the driving force for development of these automated methods. While initiated in human research, these methods are being increasingly applied to MRI datasets of the mouse brain (Carroll et al., 2011; Ellegood et al., 2010a; Kovacević et al., 2005; Lerch et al., 2010).

The following sections aim to provide an overview of some of the automated image analysis techniques currently in use in preclinical imaging, going on to give examples of current applications, particularly in neuroscience.

3.4 The "Atlas": an Overview

Automated morphometric techniques for examining imaging data rely largely on image processing and statistical techniques but a central theme in their use is the notion of an 'atlas'.

The term has acquired a number of meanings throughout the years in the field of image analysis. In its traditional sense it may refer to an anatomical reference work mapping structure, typically comprising a high-quality series of images with descriptive labels. Alternatively this term has more recently been used to describe a (usually digitised) high-quality image of an organ or body structure, such as the brain, contained in a fixed conceptual 3D space defined by coordinates that mark key reference structures. Furthermore, this atlas may be based on characterisation of images from the anatomy of a single individual or a composite of a multiple subjects.

Since the time of Brodmann who produced his seminal work detailing the functional brain regions by detailed histological analyses to demarcate cytoarchitecturally distinct areas (Brodmann, 1909) there has been a strong desire to create a formal taxonomy of brain regions (Zilles and Amunts, 2010). An extension of this is the Talairach brain atlas, which was initially created to provide a stereotactic framework for neurosurgery.

Conceived by Jean Talairach in the 1960s, the Talairach atlas was the documentation of a histological analysis of a 60 year-old female brain (Talairach and Tourneaux, 1988), identifying specific brain regions in a stereotactic coordinate system, defined by a line drawn between anterior and posterior commissures. The atlas was originally intended as useful guidance for surgery and surgical planning, as functional regions may then be avoided, for example in the surgical approach taken for excision of a brain tumour.

[Figure removed due to copyright]

Figure 3.3: *Coronal section from the Talairach atlas showing an example of its use in treatment planning. Coloured and numbered regions show brain structures as identified from histology, with numbers corresponding to Brodmann areas. The green circle on the right, indicates a hypothetical lesion near the corpus callosum (purple). The arrows indicate two possible approaches, the first through Brodmann area 6, the second though area 24. (Adapted from (Talairach and Tourneaux, 1988))*

In the early 1990s, a perceived crisis in the slow development of brain mapping techniques lead to a call for new investigational tools, particularly those using the emerging field of MRI (Crick and Jones, 1993). This lead to the adaptation of Talairach's work to further the goal of a defined anatomical system for non-invasive brain imaging studies. In the wake of these demands, brain atlases using MRI were also constructed, resulting in a number that are still in current use, such as those developed by the Montreal Neuroimaging Institute (MNI). Their initial datasets had a specified coordinate system (MNI coordinates, which while not identical is readily converted to Talairach coordinates – seen in Figure 3.4 below) and comprised two datasets. The first is a high quality dataset of a single subject, scanned repeatedly and averaged and the second is a composite of many subjects and both sexes (Figure 3.4). A population atlas is necessary, given the brain is a complex and convoluted structure resulting in numerous subtle differences between individuals of both sexes. This makes a single subject atlas alone highly subjective in reporting findings and is also needed to determine normal anatomical variation.

This use of a common coordinate space for images is an important concept in modern neuroscience. It allows the findings of studies to be reported in a common image space. For example, regions of activation in functional MRI studies are often reported in terms of MNI coordinates so researchers worldwide may then identify the exact location on a corresponding histological and multimodal atlases. An ideal scenario in preclinical studies would be to emulate this with a standardised reporting structure in order to ease interpretation of phenotypic differences identified amongst the many groups of researchers worldwide.

As has been stated, defining anatomy from a single subject may be misleading due to the high degree of natural anatomical variation, especially in the brain. This has led to an increase in the use of population brain atlases where variations in the population may be taken into account in the dataset.

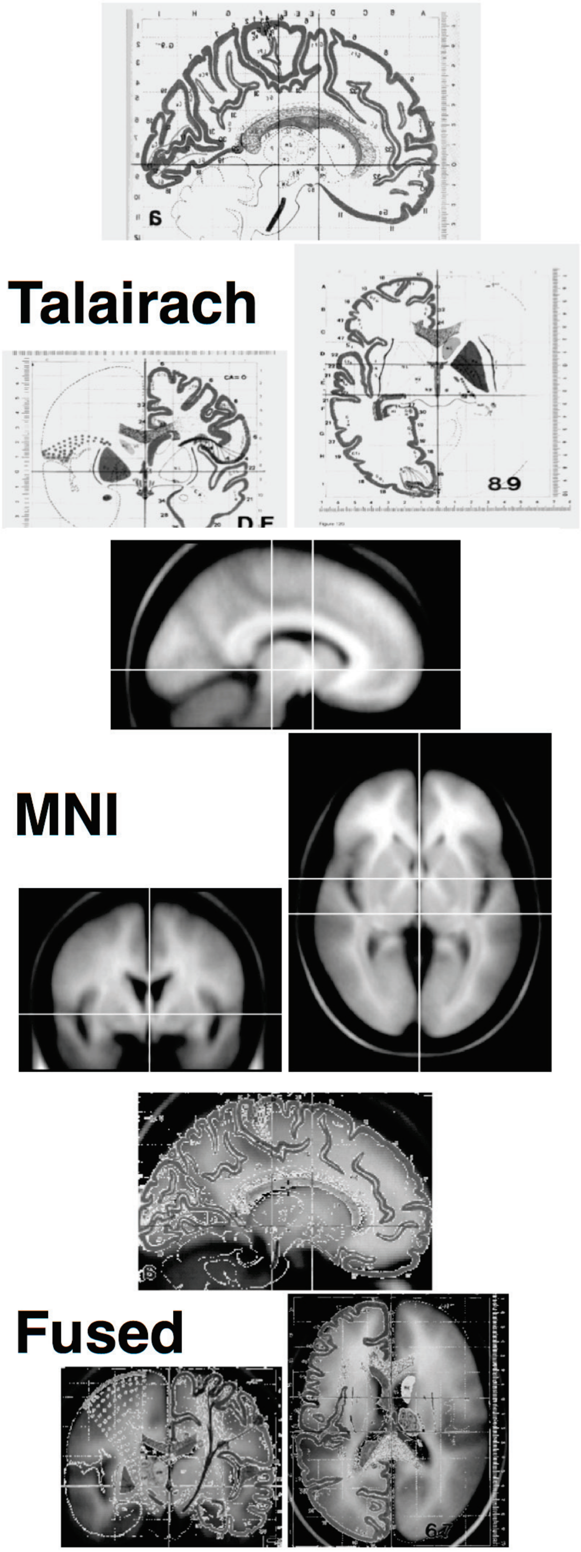

Figure 3.4: *Illustration of the correspondence of equivalent images from the Talairach Atlas (top), an average image of an atlas comprised of 305 subjects in MNI space (middle). Images from both atlases overlaid illustrating the possibility of conversion between them. Adapted from (Collins, 1994).*

3.5 Atlas Space in Preclinical Studies

As has been seen in the previous sections, atlas space is a volume with a defined coordinate system that study datasets will become aligned in. Atlases are particularly useful in population studies and they may be used to define several modalities into the same space.

Much work in recent years has been towards the goal development of equivalent histological, registration and atlas tools for use in preclinical imaging, with a number proposals suggested by groups worldwide. For example, most recently Johnson *et al.* proposed a new mouse atlas environment – termed Waxholm space (Johnson et al., 2010) – as an equivalent to Talairach space for mouse neuroscience studies. This is comprised of high-resolution multimodal datasets (~20μm isotropic resolution), regional volume segmentations and a registered histological volume, all from the same individual brain.

3.5.1 Registration

In order for these atlases to be produced, image registration techniques are necessary to computationally combine images from multiple subjects or modalities. More recently improvements in image registration and advances in computing hardware have enabled the registration of large μMRI datasets and thus the creation of high resolution atlases in the preclinical field. It is registration that also enables the automated methods of morphometric image analysis, which will be discussed later in this chapter.

Image registration is the technique of spatially transforming an image in order to align it exactly with another. In a typical patient study, the goal is usually to align single or multimodal images of the same subject. In population studies, such as those performed in phenotyping studies, *multiple* subjects are registered together in order for anatomy to be easily compared. This is a more complex problem due to anatomical variation in a population.

More formally, registration can be described as an algorithm that computes a transform (**T**) that specifies the mapping needed to align voxels in one image (usually termed the source image) to another (usually called the target image). This is illustrated graphically in Figure 3.5 below.

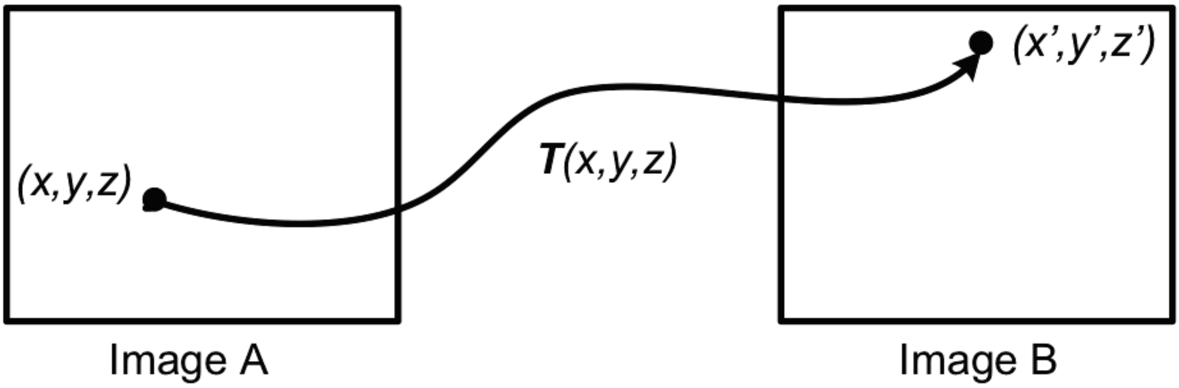

Figure 3.5: *Schematic illustration of the simplified intended result of image registration: computation of an appropriate transform T that best maps the voxels in Image A to those in Image B.*

Such algorithms are usually iterative, with the process of determining the correct transform requiring a series of small changes to the transform used on the source image to produce increasingly accurate estimates of alignment until an adequate match with the target is reached.

The registration of two individual images is a relatively straightforward process, however, the process when registering multiple subjects, although similar, is computationally more complex. One such methodology is known as groupwise registration and is the approach used in the later chapters of this thesis. This method has the advantage of avoiding the use of one target image, which may introduce bias into the final result.

In groupwise registration, an average is taken of all images, which becomes the target image. After an initial registration is attempted (with all starting images now source images), the average is then regenerated and used as the new target. This process continues indefinitely until convergence of the transformed datasets – i.e. there is now little change in the transformations after each successive iteration. One guide to the quality of groupwise registration is to look at the average of all transformed images in the group after registration. This will be initially very blurred (reflecting an average of misaligned images) but after successive iterations will become sharper and no longer change visually with each iteration, indicating that convergence has been reached. A similar, but more objective measure, is to examine the coefficient of variation of voxel signal intensity over all voxels in an image between all subjects which will be low when images are well aligned.

Four key processes are needed at each stage of the registration process (taken from (Crum et al., 2003):

1. A similarity or error measure describing the "goodness" of the match
2. A transformation model
3. An interpolation strategy to convert the new image to the defined grid of voxels that make up an image.
4. A way of finding the transformation parameters that maximises the similarity measure.

These processes will be discussed in greater detail in the sections below.

3.5.2 Similarity measures

In order to identify that a good correspondence has been achieved in the registration of one's images, a similarly measure that indicates the correspondence must be calculated.

At a basic level image registration is the activity of maximising similarity between two sets of images. One way of achieving this is to maximise the shared information between the two. If one were to combine a set of perfectly aligned images it would be conceivable that such a combined image would look similar to the source images with every structure in precise overlap. Conversely a poorly aligned image will have very little overlap. If one were to subtract images, in the first instance there will be very little residual 'information', in the second there is a great deal. Maximising this 'mutual information' between the source and target images that allows its use as a similarity measure. A similarity measure regarded as particularly robust and is often used for intra-subject, multimodal registration is known as normalised mutual information (NMI) (Studholme et al., 1999). NMI relies on a concept known as joint entropy. In simple terms, this is a quantity that is an expression of the probability of finding the same number of voxels with a certain signal intensity range in one image as compared to the other. This is calculated from a joint histogram (which plots voxel signal intensity in two images against each other for a particular voxel coordinate). Intuitively, a focused, near-linear relationship would be expected for two intra-modal images that were well-aligned (as voxels for a given (x,y,z) coordinate in both images will have the same signal intensity).

3.5.3 Registration: the Transformation Model

In the creation of a population atlas, there are 3 parts to the registration process, involving 2 global registrations: initial spatial alignment using rigid registration and affine registration; and finally the third local, non-linear registration.

3.5.3.1 Rigid

The first part of any registration protocol is rigid registration. The goal of rigid registration is to redefine all datasets into a common space and remove any large spatial differences. One aspect of the registration procedure is that any initial bias between subjects due to alignment is removed before future registration steps that will go on to assess size differences. Usually a particular subject is chosen as the target image for the registration.

Rigid registration optimises two parameters: rotation and translation (giving 6 degrees of freedom) to produce the optimal alignment.

3.5.3.2 Affine

Affine registration continues the registration process after the spatial normalisation achieved with rigid registration. In addition to translation and rotation, shear and linear scaling of the datasets are now optimised, resulting in 12 degrees of freedom**.**

3.5.3.3 Non-linear

Once the global registration using rigid and affine registration is complete, and any large differences between images removed, a non-linear transformation model is then used which registers the images locally (at a voxel level). This has the effect of aligning fine structural details in the images together.

Non-linear (also known as non-rigid) registration is the most complex of the 3 registration stages as deformations across the whole image need to calculated and optimised, and as a result is very sensitive to the algorithm being applied. An example of a successful algorithm is recent years is that of free form deformation (FFD) (Rueckert et al., 1999).

The basis of FFD and similar algorithms is the optimisation of a 3D grid of local control points over the image. Manipulating a control point warps voxels in its controlled area, allowing local features in the image to be aligned between subjects. After making a number of small adjustments to control points across the image, the of NMI value between the image and the average is then assessed. This process is then repeated until NMI is maximal.

The large number of control points spread over a number of subjects in large MRI datasets representing many millions of degrees of freedom. However, recent advances in cluster computing and graphics processing units (GPUs) have finally enabled implementations of these algorithms which have reduced the required processing times down from many days to a few hours (Modat et al., 2010). Importantly, it is from this registration process that parameters will be acquired that will be used in subsequent morphometric analyses. Thus, it is vitally important that the registration is accurate. A summary of the registration process in creating an example average atlas of 3 mouse embryos after registration is shown in the figure below:

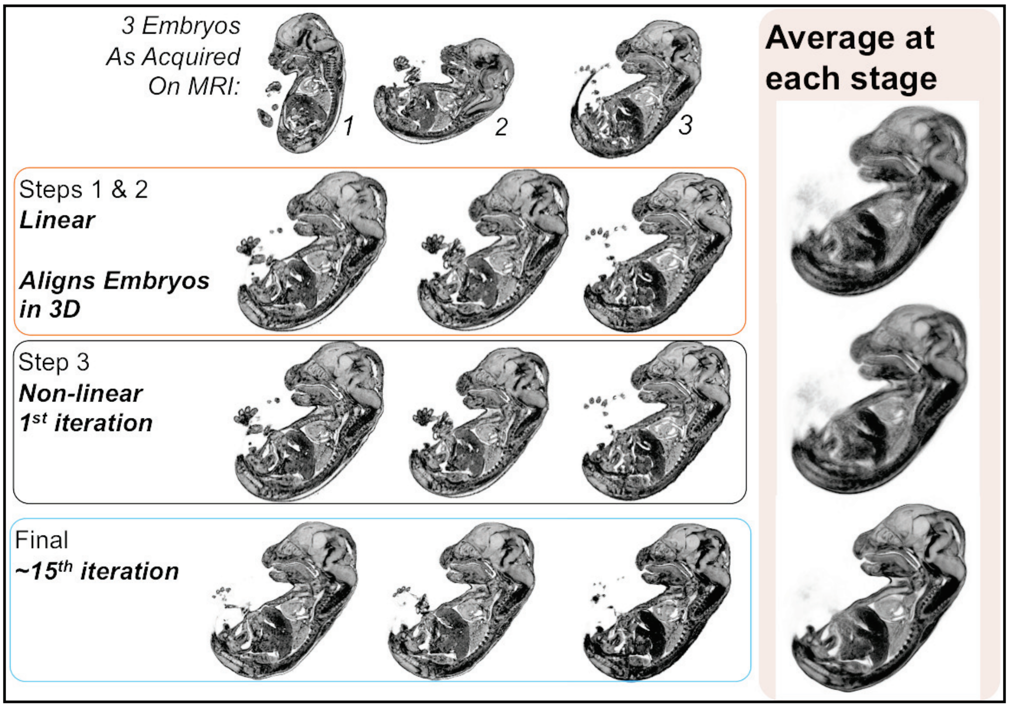

Figure 3.6: *Demonstration of stages during registration of 3 embryos to create an atlas. As seen in the top row, embryos are acquired in differing orientations in the MRI scanner. First these global differences are corrected using linear, i.e. rigid and affine models (orange box, second row). As each stage progresses, the average of all embryos becomes progressively sharper, with the non-linear registration allowing the most accurate mapping of local anatomy by the 15th iteration and producing the sharpest average atlas.*

3.5.4 Interpolation

One problem with image registration is that the calculated transformation, such as in the case of a rotation or a scale term will require manipulation of the image in order to often calculate at a sub-voxel scale in order to appropriately align the two datasets. This causes difficulties in that the resulting transformed image must be represented in the defined voxel matrix of the original target image. For example, if a linear rotation is applied to an image, it is likely that voxels in the transformed source image will fall between existing voxels in the target. Interpolation is then needed to determine the value of the new voxel value at this point. A number of schemes are in use, of varying complexity such as nearest neighbour (the simplest), linear interpolation, sinc functions and splines. The scheme used is dependent on the application, need for resulting smoothness and limitations of processing time/complexity.

3.5.5 Final Transform and Deformation Field

After the optimisation of all 3 stages in the registration process, the matrices describing each individual's image voxels and their mapping on to the calculated average image are saved in the form of a 3D deformation field. This specifies how each voxel in the original image has been to be manipulated in order to map to the average atlas of all images.

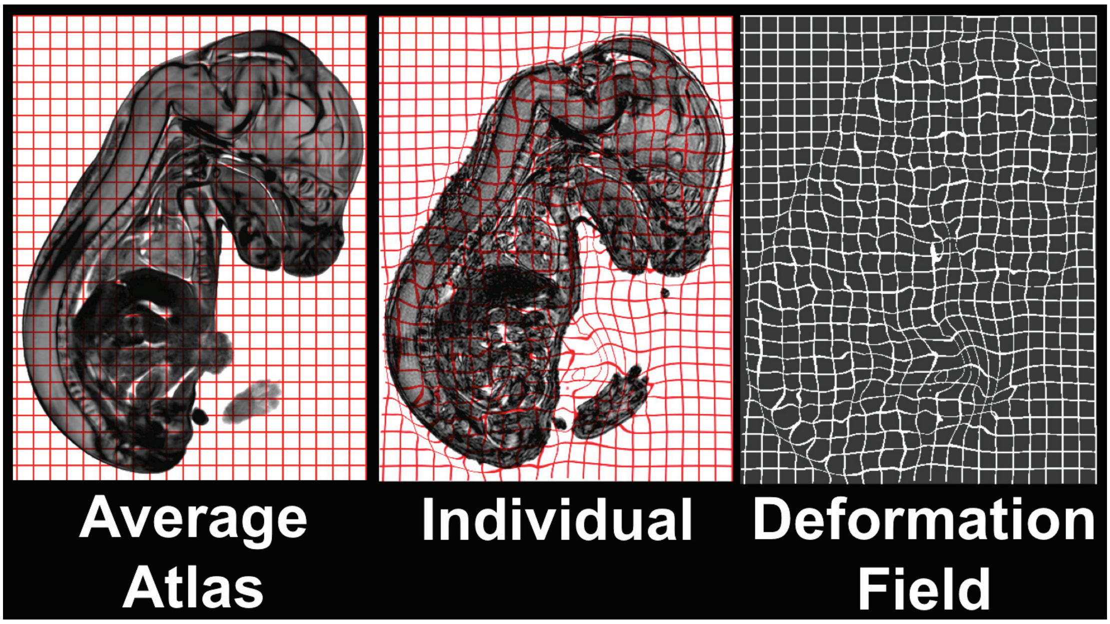

Figure 3.7: *Illustration of the deformations calculated in image registration. In the leftmost image, the average of a number of mouse embryos after non-linear registration is seen. An arbitrary grid has been placed over the average image. In the individual image and associated deformation field, the deformations that have been calculated by non-linear registration algorithm needed to warp the individual embryo image to that of the average atlas of all subjects are shown.*

3.6 Applications in MRI: Image Quality Improvement

One basic application of image registration is its ability to improve image quality, through the combination of multiple images of the same subject. As previously discussed, once a coil, preparation protocol and a fixed TR has been chosen, SNR improvement in MRI is generally only possible through the averaging of multiple image datasets to reduce the effect of noise.

Images of a single brain from multiple acquisition sessions have been registered in this manner in order to produce a high-quality 3D image for the construction of a mouse brain atlas for anatomical use ((Keller et al., 2010), Figure 3.8). This follows earlier work in human studies, such as the commonly-used MNI dataset, *colin27,* which is a single subject scanned multiple times and the acquisitions registered in order to provide a high-quality anatomical image for structural correlation (Holmes et al., 1998). The improvement in image quality with multiple images is shown in Figure 3.9.

[Figure removed due to copyright]

Figure 3.8: *Composite images and segmentation of cerebellar lobules and dorsal hippocampus of a mouse brain dataset acquired as part of an MRI anatomical atlas project. Images are registered average of 8 separate 3D acquisitions of the same mouse brain acquired on a 16 Tesla system. Adapted from (Keller et al., 2010).*

[Figure removed due to copyright]

Figure 3.9: *Example of the improvement in image quality seen after the use of image registration to average multiple MR acquisitions of a human subject. A & B:* T_1*-weighted Images of an individual after a single multi-slice acquisition at 0.7mm and 1mm slice thickness respectively. C & D: Corresponding images (0.7mm and 1mm slice thickness) after registration and averaging of 27 separate acquisitions. Adapted from (Holmes et al., 1998)*

3.7 Multiple Subject Atlases and Segmentation-propagation

Registration of multiple subjects also enables the use of the average atlas image as a high-resolution population atlas (Dorr et al., 2008). As this average is also a composite of multiple acquisitions, image SNR is greatly increased in the regions common to all subjects.

Additionally, as affine and voxelwise mappings are available for all individuals in the dataset, segmenting the atlas into regions of interest, allows a measure of the volumetric variation of structures in the population to be readily available. This is known as segmentation-propagation.

As has been seen previously, manual quantification of structure volumes is a useful, although time-consuming measure of phenotype in MRI data. However the technique of segmentation-propagation uses registration to greatly speed up the process. In this method, a number of segmentations are drawn on the high-quality average atlas (Calmon and Roberts, 2000; Dorr et al., 2008). As the transformation and Jacobian values are known which give a 1:1 mapping of regions on the average image and equivalent areas on the individual subjects' datasets, this then allows volumes to be measured in all individuals automatically. An example of a comprehensive mouse brain atlas comprised of multiple subjects is shown in Figure 3.10 below. This consists of 40 C57BL6/J individuals (20 male and 20 female) and 62 segmented regions.

[Figure removed due to copyright]

Figure 3.10: *An example of the segmented regions in a C57BL6/J mouse brain atlas comprised of 20 males and 20 females. 3D volume rendering image (A), coronal (B), sagittal (C), axial (D) and 3D inferior views (E).*

Once an atlas brain has been segmented in this manner, similar datasets from a new study may then be registered to it, allowing the reporting of volumes in those new datasets and identification of structures. To this end, a number of segmented brain atlases are freely available online (Dorr et al., 2008; Johnson et al., 2007; MacKenzie-Graham et al., 2004).

3.8 Use of the Deformation Field for Morphometric Studies

While a number of MRI studies have demonstrated gross anatomical changes in neuroanatomical mouse models, showing features such as ventricular enlargement, indicating atrophy and volume loss is taking place in the brain. Automated imaging analysis techniques may go a step further to identify the specific areas elsewhere in the brain that are reducing in volume.

An early use of deformation fields in human studies has been in the examination of local, progressive structural brain changes, for example in the tracking of longitudinal changes in patients with Alzheimer's disease (Figure 3.11, (Fox et al., 2001).

[Figure removed due to copyright]

Figure 3.11: *Coronal MRI slices showing regions of relative compression or expansion after registration of serial images after an interval of 11 months (control subject) and 14 months (patient with Alzheimer's disease). In the patient, the expansion of ventricles and contraction of cortical regions may be readily visualized. Adapted from (Fox et al., 2001).*

3.9 Tensor-based Morphometry

Going a step further than intrasubject comparison, the deformation fields may be used to make comparisons between groups of subjects, on a voxelwise basis. This type of statistical morphometric analysis is termed tensor-based morphometry (TBM).

TBM offers unbiased approach, as only the final local deformation field, generated automatically by the non-rigid registration process, is typically used for the statistical analysis, without any human intervention. A simplified diagram of the process is shown in Figure 3.12.

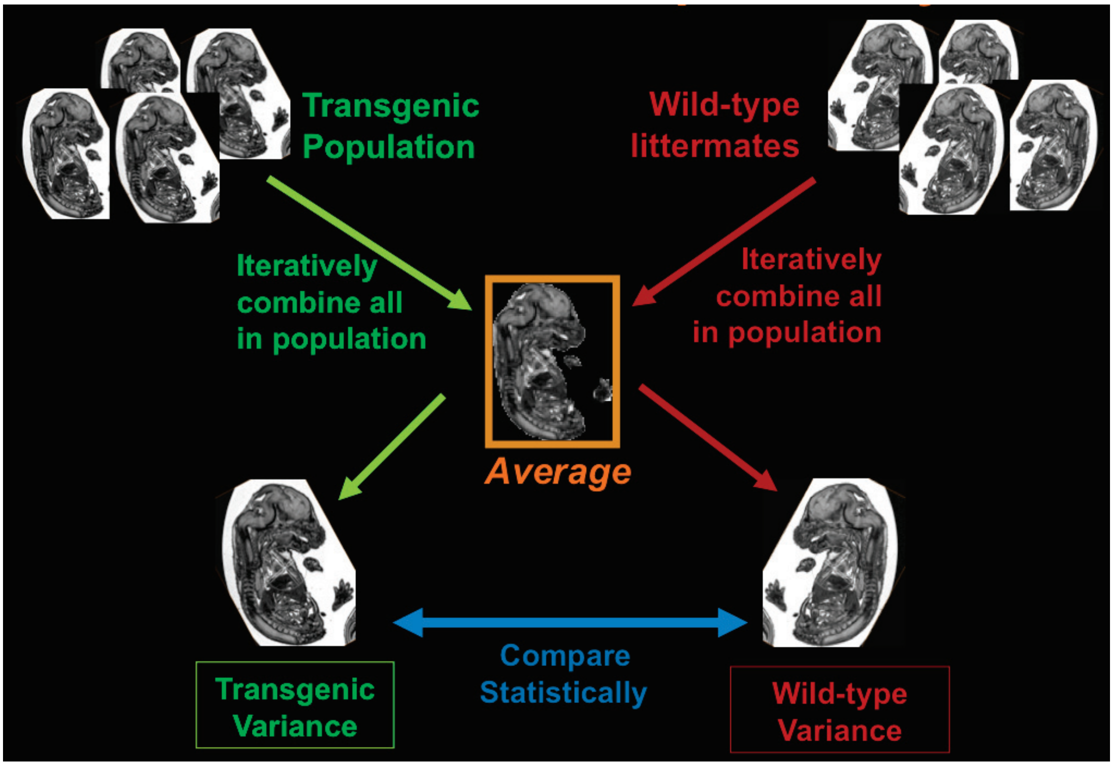

Figure 3.12: *Simplified schematic flow diagram of a TBM study comparing two groups of embryos. Initially, images from both groups are registered using iterative registration, as has been described in previous sections, into an average atlas. Deformation fields are saved for each individual. Morphometric information from the fields can then be compared between populations in order to look for significant structural differences.*

Tensor-based morphometry relies on the local deformation field acquired during non-rigid registration. More specifically, from these a numerical value expressing compression or expansion at a particular voxel can be calculated, known as the Jacobian determinant (measures of expansion and contraction over the image) as calculated by the registration transform. By simple *t*-testing, the values of the Jacobian determinant may then be compared between groups.

More formally: for transform (T_1) for a specific point in the image (x,y,z), the Jacobian (J_1) is the first-order differential.

$$T_1(x,y,z) = \begin{bmatrix} T_1^x(x,y,z) \\ T_1^y(x,y,z) \\ T_1^z(x,y,z) \end{bmatrix} \quad J_1(x,y,z) = \begin{bmatrix} \frac{\partial T_1^x}{\partial x} & \frac{\partial T_1^x}{\partial y} & \frac{\partial T_1^x}{\partial z} \\ \frac{\partial T_1^y}{\partial x} & \frac{\partial T_1^y}{\partial y} & \frac{\partial T_1^y}{\partial z} \\ \frac{\partial T_1^z}{\partial x} & \frac{\partial T_1^z}{\partial y} & \frac{\partial T_1^z}{\partial z} \end{bmatrix}$$

Taking the determinant of J_1 (det J_1) gives us a scalar quantity that gives a relative measure of the total volume expansion or contraction experienced by that voxel. A value of <1 indicates contraction of the voxel; >1 indicates. This is graphically illustrated in Figure 3.13 below.

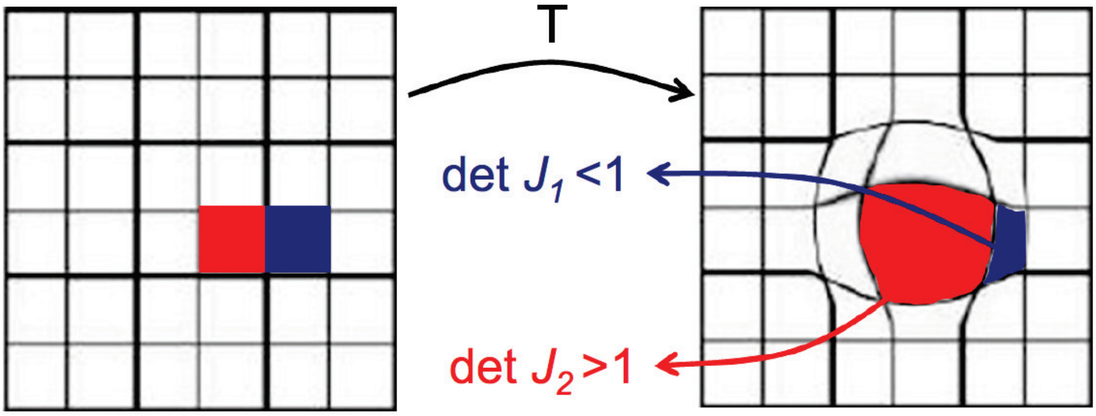

Figure 3.13: *Illustration of the Jacobian determinant (*det *J) after the application of a non-rigid transformation (*T*) to a 6x6 grid of squares. The relative area inside two of the grid squares, before and after transformation, are highlighted in red and blue. In the case of the red square post-transformation, there has been an increase in area relative to its original size, thus the Jacobian of the red square is >1. Conversely the area of the blue square has reduced can be seen to have reduced relative to its original size, resulting in corresponding Jacobian value of <1. Modified from (Zamayadi, 2010)*

Making maps of the Jacobian determinant (commonly referred to as Jacobian maps or simply 'Jacobians') for each individual gives information about local structural differences, at the voxel level, between that subject and the whole population under study.

3.9.1 Analysis and Presentation of Deformation Data

In order to interpret the findings of morphometric studies, a method of representing the regions of significant findings called statistical parametric maps is employed. A piece of software known as Statistical Parametric Mapping (SPM, Functional Imaging Laboratory, UCL) is commonly used for this purpose.

In order to analyse imaging datasets, the SPM software package employs a general linear model (GLM), which has been successfully used in a large number of previous studies. The GLM incorporates a statistical test (such as a conventional *t*-test), but also associated covariates that may change interpretation of the data. For example additional variables, sex and age, may have an effect on the Jacobian determinant seen in an image voxel, in addition to genetic background.

The general form of the GLM is:

$$\textbf{(Eq. 3.1)} \qquad \mathbf{Y}=\mathbf{XB}+\mathbf{U}$$

Where **Y** is a matrix consisting of Jacobian maps from all averaged individuals in the study, **X** is a design matrix for the study (specifying information such as the phenotype or gender of the individual in the corresponding map), **B** is a matrix containing the parameters that are to be estimated and **U** is a matrix containing error or noise data.

After analysis of data, results are then reported pictorially, in the form of a high-quality image of the average atlas with a coloured overlay consisting of regions that are statistically different (volumetrically compressed or expanded) between study groups after accounting for covariates. This is termed a statistical parametric map.

As can be envisaged by the need for parametric testing over Jacobian determinants in all voxels of an image, a significant issue is that of multiple comparisons. A large proportion of these may result in regions of significance at the 5% level due to chance. Corrected p-values are therefore often used in statistical maps, typically using false discovery rate (FDR (Genovese et al., 2002)) which reduces the number of type I errors (the incorrectly rejected null-hypotheses).

3.9.2 Use of Morphometric Techniques in Investigating Anatomical Changes

As the statistical maps are generated over the whole image, the analysis is independent of the research question involved, allowing a wide variety of applications. In human studies differences in behaviour often manifest in a corresponding change in neuroanatomy, and may be detectable on MRI (Nieman et al., 2007). In human MR, statistical studies have allowed the identification of subtle differences, notably showing an increased hippocampal volume in the brains of London taxi drivers (Maguire et al., 2000) compared to control subjects from the general population.

As the current preclinical mouse literature is developing, the adult mouse brain was the first to be analysed by morphometric techniques. Once a data-processing pipeline has become established it is relatively easy to generate experimental paradigms that can then be studied. Recent work have produced new insights into differences in the adult mouse brain including: sex and strain differences (Chen et al., 2006), hemispheric asymmetry (Spring et al., 2010) and phenotyping studies of transgenic and knockout mice (Badea et al., 2009; Ellegood et al., 2010a; Lerch et al., 2008).

Indeed, while this approach is often applied to MRI datasets it should be stated that these techniques are modality independent and may also be applied to other imaging data types such as mouse skull analysis from μCT data (Nieman et al., 2006).

3.9.3 Specific Applications of Morphometric Techniques in Preclinical MRI

As morphometric methods are able to compare the volumetric and signal intensity differences between groups over the many millions of voxels in an image, these analyses have the ability to identify small local neuroanatomical differences.

Given the utility of these approaches in clinical studies, this has more recently been applied to preclinical studies and has led to novel neurological findings in mouse models. For example, recent morphometry studies have shed new light on mouse models of Huntington's disease (HD). While previous studies of HD have utilised MRI, they have used gross measures of phenotypic change, such as ventricular, striatal and total brain volume, as these structures are easily visualised for manual measurements. Using a TBM approach, confirmed by histology, studies by Sawiak *et* *al.* (Sawiak et al., 2009a, b) have been able been able identify regions of significant volume change in *specific* striatal regions that may result in the observed ventricular enlargement (Figure 3.14 below).

[Figure removed due to copyright]

Figure 3.14: *3D reconstructions of the striatum in the R6/2 model of Huntington's Disease after morphometric analysis. Coloured regions show the F-score of volume areas with significant volume differences between groups with the threshold set at p<0.05 (FDR corrected). The 3D striatum is shown superimposed on axial (A) and coronal (B) slices from the atlas. Panel C shows the striatum in a 3D 'glass' brain. Panel D shows magnified views of the left striatum (Str), with significance set at p<0.05, p<0.01 and p<0.0025 respectively. Adapted from (Sawiak et al., 2009b)*

Recent work has also shown the utility of *ex-vivo* morphometric studies in investigations of memory and learning. In one recent study, where mice were given a Morris water maze learning task, TBM was used to identify regions of volume expansion in the hippocampus. This indicates that TBM analysis of high-resolution anatomical MR images may be sensitive enough to detect neuroanatomical changes brought about by learning tasks after only 5 days of training (Lerch et al., 2010).

[Figure removed due to copyright]

Figure 3.15: *Representative coronal slices through a mouse brain after a Morris water maze-training task in the mouse. After 5 days of training, the statistical parametric maps of significant regions after a group ANOVA shows volume increase in a number of structures, and particularly in the hippocampus compared to untrained controls. Adapted from (Lerch et al., 2010).*

3.10 Future Horizons

As has been seen in the previous sections, the application of automated techniques, such as segmentation propagation and tensor-based morphometry to preclinical MRI data, are exciting developments, and have allowed relatively rapid, non-invasive phenotyping in the mouse brain.

3.10.1 Mouse Brain

However although MNI coordinate space has now become the *de facto* standard for the reporting of human MRI studies and the framework for new histological atlases (Amunts et al., 2000) there has yet to be a standardised atlas system for the adult mouse brain. As shown previously, a number of groups have suggested frameworks based on the volume segmentation of single brains (Johnson et al., 2010) with histological correlation, while others have performed detailed segmentations of average datasets of multiple subjects (Dorr et al., 2008). As mouse phenotyping is an international endeavour, a standardised system of reporting and analysis would be advantageous. Which atlas becomes the standard will be of some debate in future but as with the MNI atlas, a detailed histological correlate (giving a mouse equivalent of Talairach) may be the most compelling factor.

3.10.2 Mouse Embryo

A digital stereotactic framework for analyses of the mouse embryo are very much in the preliminary stage, with only two papers demonstrating the feasibility of computational techniques to these datasets so far. With the continued interest in the study of development and the basis of congenital disease, this unmet need will no doubt make this a fertile area of research in coming years.

Chapter 4:

Optimisation of High-Throughput Cardiac μMRI in Ex-vivo Murine Embryos

4.1 Chapter Outline

As stated in previous chapters, in recent years MRI has become increasingly used for phenotyping mouse embryos, especially in cardiovascular disease models. However, there have so far been very few studies that investigate the optimal preparation and scanning parameters required for heart imaging using contrast-enhanced μMRI.

This chapter is a study to determine the optimal preparation and scanning parameters for gradient-echo imaging of transgenic mice, in order to improve the sensitivity to subtle anatomical defects.

4.2 Introduction

The mouse is a key model for research into human disease and is ideally suited to genetic study, as the genome (Mouse Genome Sequencing Consortium et al., 2002) and techniques for manipulating its sequence are readily available (Balling, 2001; Capecchi, 2001). A number of large-scale programmes are underway to create transgenic knockout models for each of the approximately 25,000 mouse genes (International Mouse Knockout Consortium et al., 2007). This increasing use of genetically modified mice has highlighted the need for techniques to rapidly characterise the new morphological phenotypes presented in these models.

Congenital heart defects (CHDs) are a group of conditions amenable to such genetic study. They affect over 1% of live births and are responsible for complications immediately from birth through to later adult life (Hoffman and Kaplan, 2002). Inheritable gene mutations and chromosomal effects are the direct cause of nearly 20% of CHDs. While the basis of remaining so-called sporadic conditions is uncertain, epidemiological studies demonstrate an increased risk of CHDs in siblings and offspring of those affected. This illustrates there is potential genetic involvement even in these cases (Bentham and Bhattacharya, 2008).

Modified-mouse embryos are an ideal way of studying these types of disease during development. Given the high number of potential mouse variations in the future, effective methods of phenotyping embryos are essential. Conventionally this is done *ex-vivo* by microscopic examination with histology, where embryos are dehydrated, wax embedded and thinly sectioned (2-8μm) (Kaufman, 1992). This provides high-resolution 2D data and sections that may also be stained for gene and protein expression. Episcopic imaging is a refinement of this process, where autofluorescence of each tissue slice can be photographed and combined to generate high-resolution 3D volume datasets (1-2μm isotropic resolution) (Weninger et al., 2006; Weninger and Mohun, 2002). However these histological approaches are time-consuming and do not lend themselves readily to rapid screening as only one embryo may be imaged at a time.

A further complication is that a phenotype may be largely unknown (Nolan et al., 2000) or incompletely penetrant, meaning that a particular genotype does not necessarily lead to a phenotypic effect. Therefore relatively large numbers (10s to 100s) of embryos are sometimes needed to gain a good measure of the prevalence of the phenotype in a population (Schneider and Bhattacharya, 2004). Thus a high-throughput phenotyping technique is essential to meet the demands of modern molecular medicine.

Microscopic MRI (μMRI) – high-resolution imaging at an isotropic resolution of <100μm (Kim et al., 2009) – is powerful technique allowing assessments of both embryo development (Petiet et al., 2008) and phenotype (Goddeeris et al., 2008). High-throughput, μMRI screening can be achieved with multiple mid-gestation embryos (up to 32 simultaneously) in a single 12-hour scan at a ~25μm resolution (Schneider et al., 2003c; Schneider et al., 2004). Full 3D datasets for all embryos are created allowing structures to be visualised relative to one another. In this method, embryos are fixed in MRI contrast agent, improving signal to noise and thus image quality. Other methods of whole embryo imaging include microscopic computed tomography (μCT) (Holdsworth and Thornton, 2002; Johnson et al., 2006) and optical projection tomography (OPT) (Sharpe, 2003). μCT allows high throughput but suffers conventionally from the limited range of linear attenuation coefficients in soft tissue, impairing detailed visualisation (Takeda et al., 2000). OPT can provide detailed images of gene expression, but requires translucent skin tissue and its use in older embryos (>13.5dpc) that are more opaque is limited (Schneider and Bhattacharya, 2004).

Furthermore, it has been shown that heart development is complete only after this stage, with septation occurring by 15.5dpc (Kaufman, 1992; Schneider et al., 2003b).

High throughput MRI screening is a new and improving technique, yet there is limited information on the optimal MR and preparation parameters for embryo studies. The few previous studies have investigated either qualitative optimisation of MR parameters or embryo preparation in isolation (Petiet et al., 2007; Schneider et al., 2003c). Here described are the results of a combined study, assessing the effect of contrast agent concentration, fixation time and MR acquisition parameters for imaging the embryo heart. These parameters then used to identify abnormalities in a preliminary MRI screen of mouse embryos heterozygous for the gene *Chd7*, a transcription factor implicated in CHARGE syndrome (Bosman et al., 2005) – a group of associated congenital abnormalities affecting approximately 1 in 10,000 human live births (Blake and Prasad, 2006). The syndrome is characterised by defects in a number of organs including the cardiovascular, eye and vestibular systems. The *Chd7* embryos used were created using gene trapping, a method not previously reported for this disease model.

4.3 Materials and Methods

4.3.1 Animal Preparation

All parts of this study were carried out in accordance with the UK Animals (Scientific Procedures) Act, 1986. Successfully plugged pregnant female mice were sacrificed by cervical dislocation at 15.5dpc. The embryos were removed from the mother and placed in 37°C Hanks (Sigma-Aldrich Company Ltd., Gillingham, UK) solution and bled out after cutting the umbilical cord. Care was taken to avoid blood clots in the umbilical vessels. The embryos were then immersed in ice-cold 4% paraformaldehyde solution (Sigma-Aldrich Company Ltd., Gillingham, UK), doped with gadolinium-diethylene triamine pentaacetic acid (Gd-DTPA, [Magnevist], Bayer-Schering, Newbury, UK) and placed on a rotator. After a period of time, the embryos were removed and embedded in a 1% agarose gel – doped with identical concentration of Gd-DTPA to fixation – in a 50ml centrifuge tube. The tube diameter at the widest point was 31mm.

<u>*For MRI optimisation:*</u> Six groups of CD-1 embryos fixed for 3-days (in 2 and 4mM Gd-DTPA) or 2-weeks (at 2, 4, 8 and 16mM). Six embryos were used for each fixation-time/concentration per tube.

<u>*Transgenic screening:*</u> 13 transgenic *Chd7* embryos (n=5 +/+, n=8 +/-) at 15.5dpc were then prepared in an identical fashion to the CD-1 embryos but fixed and embedded in media containing 8mM Gd-DTPA (2 week fixation period). The *Chd7* gene in these mice was inactivated using a gene trap method (International Mouse Knockout Consortium et al., 2007). Mice were maintained on a C57BL/6 background and were backcrossed to this background for at least 5 generations. Any embryo subsequently identified with heart abnormalities was wax-embedded and sectioned into 10µm axial slices. Heart slices were then stained with haematoxylin and eosin (H&E).

4.3.2 MR Acquisition

Embryos were scanned using a Varian 9.4T VNMRS 20cm horizontal-bore system (Varian Inc. Palo Alto, CA, USA), using 40G/cm imaging gradients. A 39mm quadrature birdcage coil (RAPID Biomedical GmbH, Würzburg, Germany), was used for both volume transmit and receive. Tuning and matching of the coil was performed manually; flip angle and shim were automatically calibrated but both parameters were checked for consistency between experiments. Sample temperature (measured during a full 10-hour 3D gradient-echo scan) was 22.5±1.0°C.

4.3.3 Measurement of Tissue Parameters

To provide tissue information for the optimisation, T_1 and T_2* maps were created using a single sagittal slice (FOV 27 x 27mm, 256^2 matrix size, 0.5mm thickness). For T_1 mapping, inversion-recovery spin-echo with a global adiabatic pulse was used. T_2*

mapping was performed with a standard 2D gradient echo sequence with each TE acquired as a separate acquisition.

For the 3-day-fixed embryos, parameters were: T_1 mapping: 10 TIs, range 20-2700 ms, TE=11.75ms, TR=5000ms, NSA=2. T_2* mapping: 10 TEs, range 20-120ms, TR=5000ms, NSA=2

For 2-week data: T_1: 13 TIs, range 6-450 ms, NSA=7; T_2*: 13 TEs, range 3.5-40ms, TR=750-1000ms, NSA=7.

TI and TE spacing was adjusted slightly for each concentration to counter reductions in T_1 and T_2* with contrast agent, especially at higher concentrations. TR was chosen to be at least 5x T_1.

T_1 and T_2* maps were created by a pixel-by-pixel, least-squares fit of the resulting data using in-house C-programs. Image pixels were assigned a zero value when the tissue signal to noise was similar to background, or when the range of TI times (optimised for the heart) was inappropriate for the tissue $T_{1,}$ resulting in occasional dark pixels in the T_1 maps (Figure 4.1).

Given the potential for partial volume in the maps of the chamber lumen (due to small heart size), background agarose was used as a surrogate for extracellular/interstitial fluid. This assumes that the penetration of the contrast agent in the fluid regions in the heart was similar to background at the time of image acquisition.

Proton density mapping (M_0) was carried out on the 2-week-fixed embryos, 2mM concentration, using a single-slice spin-echo with multiple TE acquisitions (TR=1000ms, 10 TEs, range 6-80ms, NSA=2). Signal intensities from heart (n=3) and agarose regions of interest were fitted against an exponential to determine the signal at TE=0ms. This was used to produce a ratio of M_0 between agarose and heart tissue.

Calculation of Linewidth

Linewidth was calculated from T_2* values using (25):

(Eq 4.1) $$Linewidth = \frac{1}{\pi T_2^*}$$

Relaxivity Calculation

Tissue-specific relaxivity of Gd-DTPA (R) was determined by fitting mean values of T_1 and T_2* in agarose and heart regions of interest to a linear model, at 2-weeks fixation, in accordance with (Stanisz and Henkelman, 2000):

(Eq. 4.2)

$$\frac{1}{T_{total}} = R[Gd] + \frac{1}{T_{tissue}}$$

4.3.4 Contrast Optimisation by Computer Simulation

The 2-week-fixed embryos at four Gd-DTPA concentrations were used for contrast optimisation between embryo heart and chamber lumen.

To determine contrast between the heart muscle and chamber, the signal equation for spoiled-gradient echo imaging (Pelc, 1993) (Eq. 4.3) was used as part of a Matlab (Mathworks Inc., Natick, MA, USA) script to calculate theoretical signal.

(Eq. 4.3)

$$Signal \propto M_0 \frac{\sin a \cdot (1-e^{\frac{-TR}{T_1}})}{1-(\cos a \cdot e^{\frac{-TR}{T_1}})} \cdot e^{\frac{-TE}{T_2^*}}$$

α is the excitation pulse flip angle. T_1, T_2* values were measured at each concentration and inserted into the equation as constants. 7 different TRs, with an appropriate number of signal averages (NSA), were trialled. These ranged from TR=20ms (with 7 averages) to TR=137ms (1 average). These values gave an overall scan time of 10 hours in each case (given a 512^3 matrix size).

Assuming √NSA increase in signal-to-noise ratio (SNR) with NSA averages, Eq. 4.3 can be extended to:

(Eq. 4.4)

$$'SNR' \propto M_0 \frac{\sin a \cdot (1-e^{\frac{-TR}{T_1}})}{1-(\cos a \cdot e^{\frac{-TR}{T_1}})} \cdot e^{\frac{-TE}{T_2^*}} \cdot \sqrt{NSA}$$

The noise level was assumed to be constant throughout the acquisition. At these 7 fixed TRs, CNR and SNR were calculated for heart muscle and chamber over a range of TEs (permitted by the system, typically 5-25ms) and flip angles (0-90°) for a fixed bandwidth. The maximum CNR was defined as the greatest SNR difference between the two tissues ($SNR_{chamber}$–SNR_{heart}) occurring over the range of scan parameters.

4.3.5 Volume Imaging

All embryo volumes were scanned using an RF-spoiled 3D gradient echo sequence. Field of view was $27x27x27mm^3$ with a matrix size of 512^3, giving an isotropic resolution of 52x52x52µm per voxel. A hard RF pulse (duration 100µs) was used for excitation and receiver bandwidth was fixed at 130Hz per pixel. Imaging time in all cases was a maximum of 10 hours.

An initial 3-day, 4mM Gd-DTPA dataset was scanned with unoptimised parameters (TR=30ms, α=90°, NSA=4, TE=7ms) for general assessment of embryo contrast and anatomy.

All concentrations of 2-week fixed embryos were scanned using parameters produced after contrast simulation. Embryos at 2mM concentration were additionally scanned with parameters – optimised for global embryo contrast – from previous studies in the literature (Schneider et al., 2003c) (TR=30ms, TE=10ms, α =90°, NSA=4) for comparison.

4.3.6 Image Processing

The 512^3 3D volume images were reconstructed on the console (VnmrJ v2.3, Varian Inc., Palo Alto CA, USA) and converted to Analyze format, using a custom C-program, for review in ImageJ (National Institutes of Health, Bethesda, MD, USA). SNR and CNR were measured in a number of organs by taking the ratio of average signal in a whole-organ volume of interest (VOI) and the standard deviation in a region of background noise:

$$\textbf{(Eq. 4.5)} \qquad SNR = \frac{Signal}{Noise\ SD} \qquad CNR = \frac{Signal_1 - Signal_2}{Noise\ SD}$$

4.4 Results

Initially, the effect of Gd-DTPA concentration and fixation time on heart T_1 and T_2* values was assessed. This enabled image contrast simulations to maximise CNR in the embryo heart. The parameters for optimum CNR were then applied to investigate heart defects in transgenic *Chd7* embryos.

4.4.1 Assessment of Concentration and Fixation Time

To compare embryos prepared at two Gd-DTPA concentrations (2 and 4mM) and two fixation times (3-days and 2-weeks), T_1 and T_2* were measured in two regions of interest – embryo heart tissue and background agarose – from a sagittal-slice through three embryos. Figure 4.1 and Table 4.1 show T_1 and T_2* maps and values for each concentration and fixation time from the two regions of interest (heart and agarose).

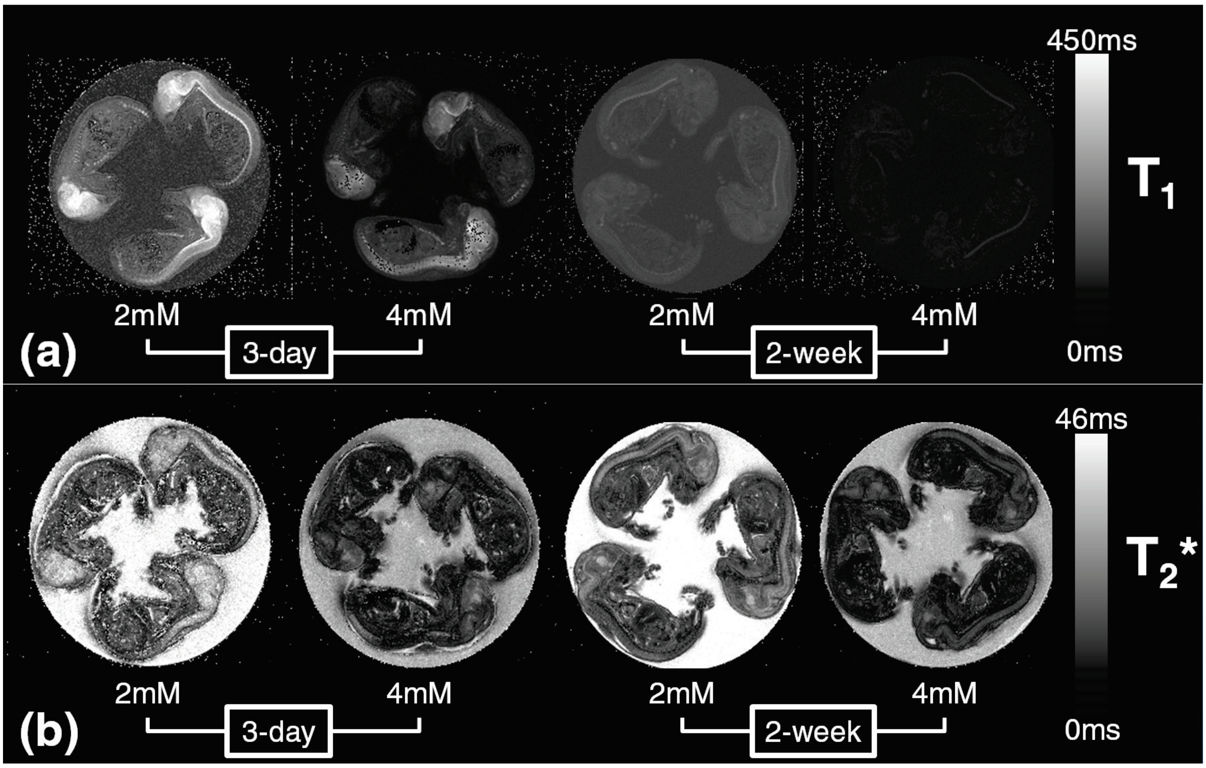

Figure 4.1: *Single slice T_1 and T_2* maps for the two concentrations (2mM & 4mM) and two fixation times (3-days and 2-weeks).*

	Fixation Timepoint and Concentration				
Tissue Type **(mean ±1SD, n=3)**	**3-Day 2mM**	**3-Day 4mM**	**2-Week 2mM**	**2-Week 4mM**	**ANOVA p-values for Concentration and Fixation Time Effects:**
Agarose *T_1 (ms)*	123.8 ±3.7	58.2 ±3.8	121.0 ±0.2	63.9 ±0.3	Fixation on T1: NS Conc. on T_1: $p<0.0001$
T_2 (ms)*	43.0 ±2.1	28.2 ±0.5	44.6 ±1.0	29.2 ±0.2	Fixation on T_2*: NS Conc. on T_2*: $p<0.0001$
Heart ROI *T_1 (ms)*	172.0 ±5.3	98.2 ±9.9	136.2 ±2.7	72.3 ±0.8	Fixation on T_1: $p<0.0001$ Conc. on T_1: $p<0.0001$
T_2 (ms)*	17.9 ±2.3	11.2 ±0.5	16.7 ±2.1	11.4 ±0.3	Fixation on T_2*: NS Conc. on T_2*: $p=0.0002$

Table 4.1: *Summary of measured parameters in regions of interest (ROIs) in embryo T_1 and T_2* maps*

4.4.1.1 Effect of fixation time:

The length of fixation time affected heart tissue by reducing T_1 at both concentrations. For example, at 2mM T_1 reduced from 172ms at 3-days to 136ms at 2-weeks ($p<0.0001$). A reduction was also seen in T_2* in the heart for the 2mM groups, although this was less than the change in T_1. No significant T_2* change was detected between the 4mM heart groups (3-days and 2-weeks). Agarose T_1 did not significantly change with fixation time, which is expected as agarose preparation was independent of embryo fixation, using fixed Gd-DTPA concentrations. Figure 4.2 shows a comparison of 3-day and 2-week fixed embryos at 4mM concentration. The contrast between heart and chamber is clearly improved (Figure 4.2b), as the signal intensity increased in the chamber at 2 weeks (chamber:background signal intensity ratio 3-day = 0.58; 2-weeks = 0.96), due to the penetration of Gd-DTPA into the embryo, shortening T_1.

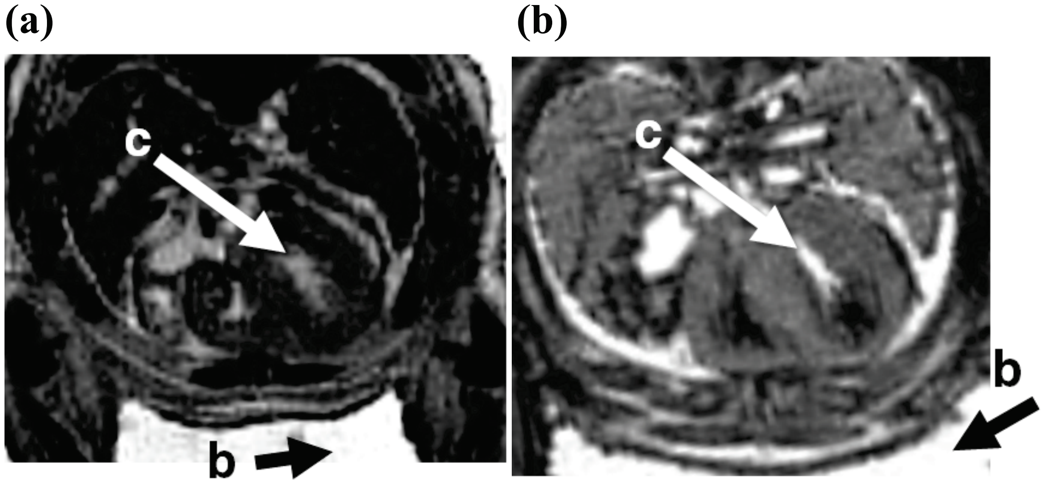

Figure 4.2: **(a):** *Axial slice through a 4mM embryo fixed for 3-days. Arrows indicate heart chamber (c) and background agarose (b). (Signal intensity ratio (chamber:background) 0.58)*
(b): *Axial slice through a 4mM embryo fixed for 2-weeks. Arrows indicate heart chamber (c) and background agarose (b). (Signal intensity ratio 0.96)*

4.4.1.2 Effect of Gd-DTPA concentration

In the heart, there was a significant reduction in T_1 with increasing concentration; for example, reducing from 172ms (2mM) to 98ms (4mM) ($p<0.0001$) for the 3-day fixation period. The decrease in T_2* was also significant.

It was observed that both concentration and fixation time have an impact on heart T_1. Although the effect of fixation time was less (21% T_1 reduction) than for concentration (43% reduction), it does have a noticeable effect on resulting gradient-echo images in embryos at the same concentration. Further optimisation continued using the 2 week fixation time, in the light of the improvements seen in contrast agent penetration.

4.4.2 Tissue Parameter Measurements at 2-week Fixation

Subsequently, the T_1 and T_2* for tissues at all four different concentrations of Gd-DTPA with 2-week fixation were measured, to provide input values for the later contrast simulation. Table 4.2 shows a summary of T_1 and T_2* values for each concentration in the two regions of interest (agarose, heart). With the addition of higher Gd-DTPA concentrations there was still a significant decrease in T_1 with concentration: in the heart, mean T_1 reduced from 136.2 (2mM) to 16.7ms (16mM) ($p<0.0001$). T_2* reduction was also significant ($p<0.0001$) and notably by 8 and 16mM, values had become particularly short (heart 8mM: 6.3ms, 16mM: 3.6ms). The corresponding linewidths – calculated from T_2* values – increased with concentration. In the heart, the linewidth increased from 22Hz (at 2mM) to 97Hz (at 16mM).

Tissue Type **(mean ±1SD, n=3)**	**2mM**	**4mM**	**8mM**	**16mM**
Agarose *T_1 (ms)*	121.0 ±0.2	63.9 ±0.3	31.0 ±0.1	16.0 ±0.1
T_2 (ms)*	44.6 ±1.0	29.2 ±0.2	16.6 ±0.5	9.5 ±0.2
Max. Linewidth (Hz)	7	11	20	34
Heart ROI *T_1 (ms)*	136.2 ±2.7	72.3 ±0.8	34.9 ±0.5	16.7 ±0.5
T_2 (ms)*	16.7 ±2.1	11.4 ±0.3	6.3 ±0.8	3.6 ±0.3
Max. Linewidth (Hz)	22	29	57	97

One-way ANOVA for concentration effect: $p<0.0001$ for all tissues

Table 4.2: *Summary of measured embryo tissue parameters for four different Gd-DTPA concentrations at 2-week fixation.*

4.4.2.1 Relaxivity Calculation

Using the measured T_1 and T_2* values to investigate relaxivity at 2-weeks (shown in Figure 4.3), it was noted that R_1-relaxivity in the heart (3.8 $mM^{-1}s^{-1}$) was similar to agarose (3.9 $mM^{-1}s^{-1}$). However there was a larger difference in the R_2* constant (heart: 15.9 $mM^{-1}s^{-1}$, agarose: 5.9 $mM^{-1}s^{-1}$) suggesting that T_2* will decrease more rapidly in heart tissue than in agarose.

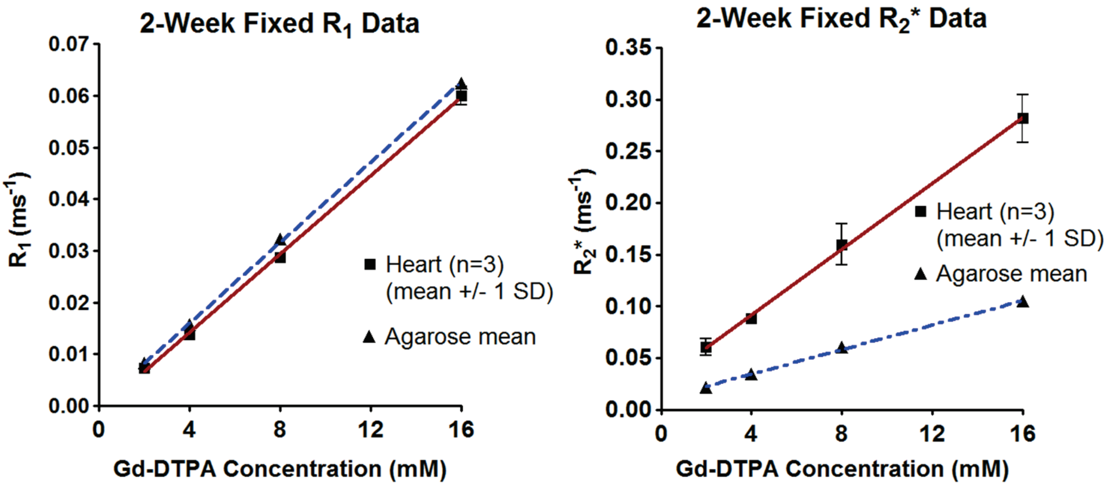

Figure 4.3: *Effect of Gd-DTPA concentration on R_1 and R_2* in agarose and heart ROIs.* ***Agarose R_1/R_2*-Relaxivity: 3.9±0.5/5.9±0.2; Heart: 3.8±0.7/15.9±0.4 $mM^{-1}s^{-1}$***

4.4.2.2 Estimation of Proton Density (M_0)

To estimate proton density, the lowest concentration embryos (2mM) were scanned with multiple echo times and fitted to find signal intensity at TE=0ms for regions of interest in the heart tissue and agarose. The mean ratio of M_0 values from the fit tissues (agarose:heart) was 1.

4.4.2.3 Scan Parameter Determination

After measuring the tissue parameters (T_1, T_2*) for the 2-week data, these values were input into the Matlab program to yield the estimated scan parameters giving maximum contrast for each concentration. The results are summarised in Table 4.3.

Concentration	**Optimum-Contrast Parameters**
2mM	TE=22ms, TR=28ms, α=39°, NSA=5
4mM	TE=16ms, TR=28ms, α=52°, NSA=5
8mM	TE=9ms, TR=20ms, α=60°, NSA=7
16mM	TE=6ms, TR=20ms, α=74°, NSA=7

Table 4.3: *Summary of optimum parameters for heart/agarose contrast from the simulation.*

4.4.3 Assessment of High-Resolution Embryo Images

For each concentration, 3D gradient echo datasets were created using estimated parameters from the simulation. SNR and CNR were measured in heart, chamber and background volumes in each embryo in each dataset. A summary is shown in Table 4.4.

Gd-DTPA Concentration and Parameters (mean ±1SD)	**SNR Heart (n=6)**	**SNR Chambers (n=6)**	**SNR Agarose**	**CNR Agarose-Heart**	**CNR Chamber-Heart**
(Globally-optimised Parameters) ***2mM*** *TE=10ms, TR=30ms* *α=90°, NSA=4*	11.2 ±1.1	16.2 ±2.2	15.9	4.7 ±1.1	5.1 ±1.1
2mM ***[Shim LW=45Hz]*** *TE=22ms, TR=28ms* *α=39°, NSA=5*	14.1 ±1.4	28.0 ±0.7	28.3	14.2 ±1.4	13.9 ±1.1
4mM ***[Shim LW=55Hz]*** *TE=16ms, TR=28ms* *α=52°, NSA=5*	14.6 ±0.9	34.7 ±2.1	35.0	20.4 ±0.9	20.0 ±2.0
8mM ***[Shim LW=77Hz]*** *TE=9ms, TR=20ms* *α=60°, NSA=7*	23.2 ±1.0	**(2-tailed t-test: NS difference)** 50.3 ±1.4	48.6	25.5 ±1.0	27.1 ±1.6
16mM ***[Shim LW=135Hz]*** *TE=6ms, TR=20ms* *α=74°, NSA=7*	23.0 ±1.5	59.2 ±2.7	60.1	37.0 ±1.5	36.1 ±2.3

Table 4.4: *Summary of SNR and CNR values in volumes of interest (VOIs) over whole-embryos for the 4 Gd-DTPA concentrations at 2-weeks fixation.1-way ANOVA of SNR and CNR change with concentration, for each VOI: $p<0.0001$*

There is a marked SNR difference between the 2mM images at initial starting values (Schneider et al., 2003b) and optimised scan parameters – best illustrated by the signal intensity increase seen in Figure 4.4. The image using optimised parameters at 2mM shows improved heart and chamber SNR (heart SNR: 11 to 14 $p<0.003$, chamber: 16 to 28 $p<0.0001$). Fluid/tissue contrast is also superior in the optimised image (heart-chamber CNR: 5 to 14, $p<0.0001$).

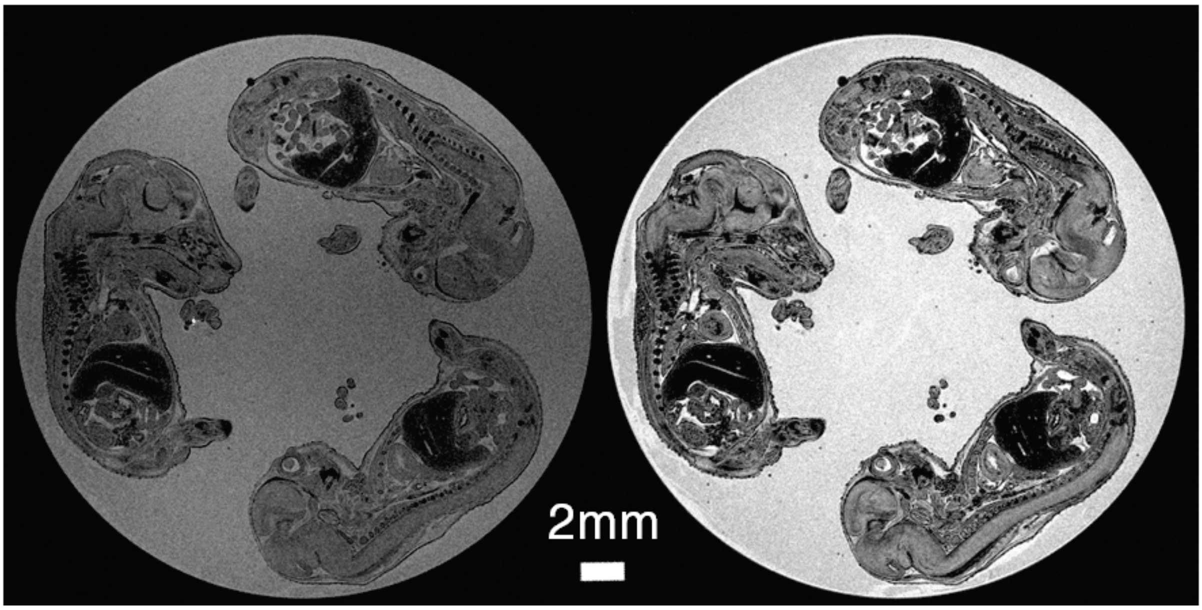

Figure 4.4: *2mM embryos. Left: scanned with initial parameters found in the literature (TE=10ms, TR=30ms, α=90°, NSA=4); right: with optimum contrast parameters produced by simulation (TE=22ms, TR=28ms, α=39°, NSA=5). Images identically scaled.*

As seen in Table 4.4 and Figure 4.5, increasing Gd-DTPA concentration initially leads to a rise in SNR in the heart, with SNR increasing from 14 (2mM) to 23 (8mM) ($p<0.0001$). A signal increase is also seen in the chamber: 2mM SNR: 28, 16mM SNR: 59 ($p<0.0001$). SNR at 2mM using initial globally-optimised parameters (2 g opt/2mM* in Figure 4.5) (Schneider et al., 2003b) was measured for comparison and found to be 11 (heart) and 16 (chamber).

However, a plateau can be seen (Figure 4.5) where mean heart SNR does not increase after 8mM (8mM mean 23.2; 16mM: 23.0). By 16mM, shim linewidth has also become high (135Hz, previously 77Hz at 8mM) indicating a shortening in global T_2*. Therefore 8mM appears to be the optimum concentration, with a balance of good contrast in the heart and improved resolution and SNR. This is also shown in the degradation of image quality in embryo heart and body at 16mM (Figure 4.5).

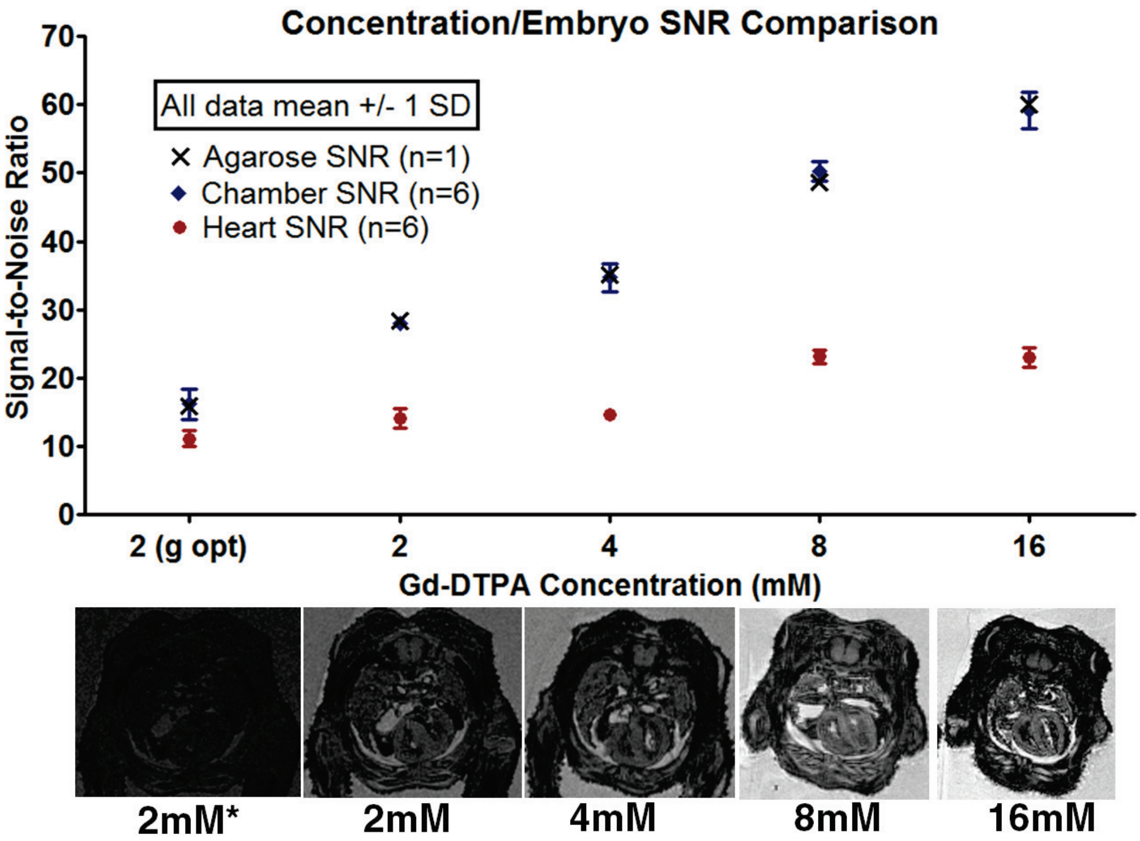

Figure 4.5: *SNR values of whole-embryo organ volumes at calculated optimum MR parameters for each concentration. 2 (g opt) represents SNR measurements on the 2mM data using globally-optimised parameters. Below: comparison of identically scaled images of an axial section through an embryo at optimum MR parameters. A scan at global-optimum parameters (2mM*) is included for comparison. Overall SNR can be seen to increase with increasing Gd-concentration.*

This is supported by Figure 4.6, which shows the excellent signal and contrast to noise in resulting images at 8mM (heart SNR: 23, CNR heart-chamber: 27). At this concentration, major anatomical features were easily identified.

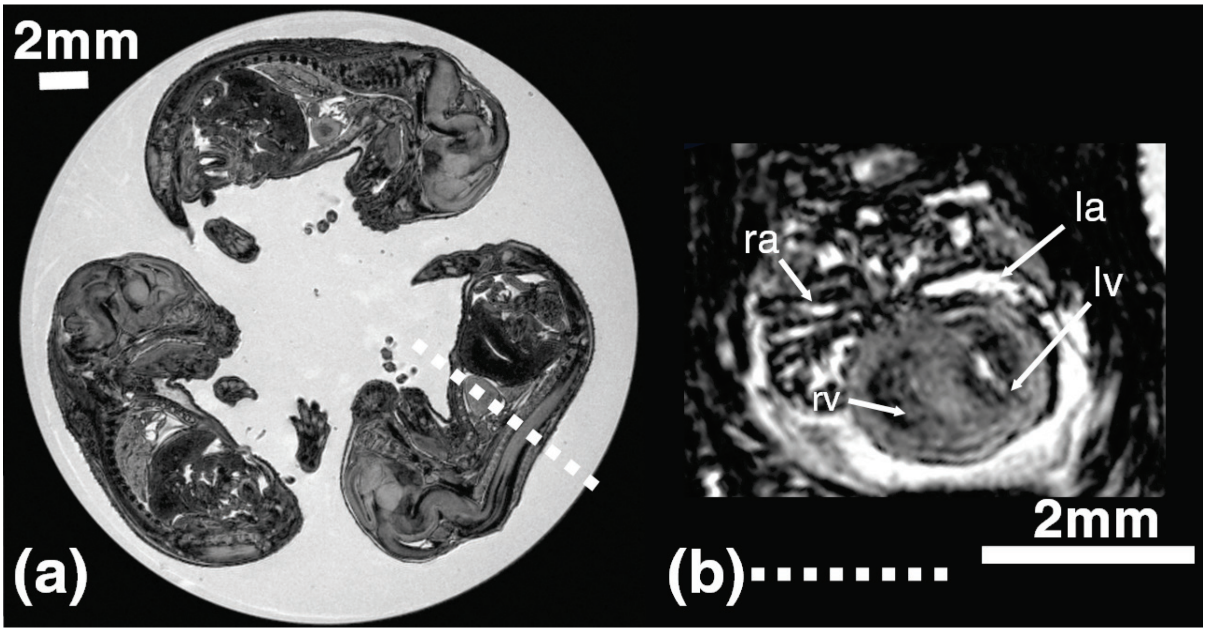

Figure 4.6: *Example images from an 8mM 3D gradient-echo dataset at optimum parameters. Excellent contrast over the whole embryos can be observed (a) as well as heart chambers (b). (ra=right atrium, la=left atrium, lv=left ventricle, rv=right ventricle)*

4.4.4 Validation of Simulations

In order to compare the signal predictions made by the simulation to experimental data, linear regression was performed to examine the relationship between measured SNR and simulated values. SNR was measured in heart and agarose VOIs in the gradient-echo data sets that corresponded to region-volumes in slices used for the initial T_1 and T_2* measurements.

As seen in Figure 4.7, there is excellent agreement between simulated and measured SNR values in both the agarose (r^2=0.998) and heart (r^2=0.993) regions of interest, indicating that the simulation is adequately predicting signal intensity values for tissue and thus also for contrast optimisation.

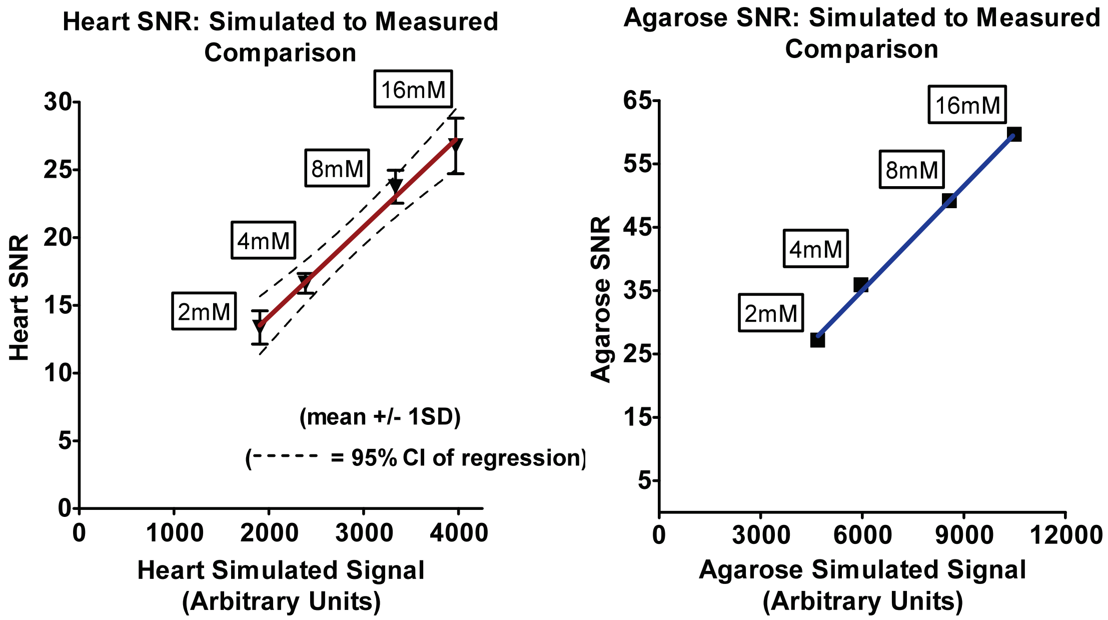

Figure 4.7: *Graphs comparing the simulated and experimental values.* ***(a)*** *Regression plot of experimental heart data against simulated signal values* ***(**r^2 **=0.993).*** ***(b)*** *Regression plot of experimental agarose data against simulated signal values (*r^2*=0.998)*

4.4.5 Transgenic Screen

Using this optimum preparation (8mM Gd-DTPA, 2-weeks fixation) and MR scan parameters, 13 embryos (*Chd7*$^{+/+}$ or $^{+/-}$) were then screened for heart defects. Of the 8 embryos heterozygous for *Chd7*, 1 was identified as having a ventricular septal defect (VSD). This is illustrated in Figure 4.8a and b where hearts from both hetero- and homozygote are shown. There is a clear difference between the ventricle septal walls – patent in the heterozygous embryo. This was later confirmed by H&E sectioning of the embryo (Figure 4.8c) where the VSD was also seen.

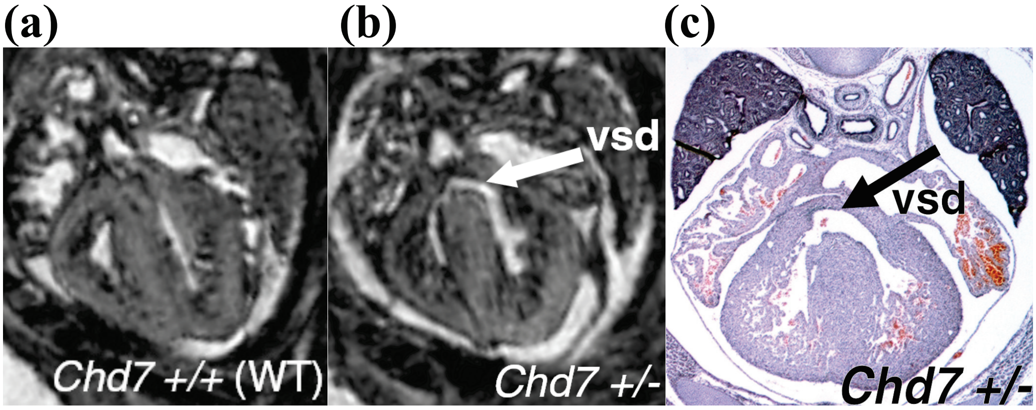

Figure 4.8: *Images of Chd7 wild-type and mutant embryo hearts.* ***(a)*** *Detail of normal heart in a wild-type littermate.* ***(b)*** *Detail of a ventricular septal defect in an embryo heterozygous for the Chd7 gene.* ***(c)*** *Subsequent axial H&E section, from the same animal, confirming the defect.*

4.5 Discussion

This study presents the results of an optimisation with the aim of improving detection of heart and vascular defects in high-throughput MRI embryo screens.

In the initial part of this study the effects of Gd-DTPA concentration and fixation time on T_1 and T_2* values of the embryo heart were assessed, to determine the best preparation method for imaging. To date, there has been very limited work investigating the effect of MRI contrast agent concentration and fixation time on mouse embryo imaging. Work by Schneider *et al.* reported an initial investigation of embryo contrast at 2mM by altering MR scanning parameters (Schneider et al., 2003c) to perform non organ-specific contrast optimisation. A study by Petiet and colleagues (Petiet et al., 2007) in 18.5dpc rat embryos, demonstrated the impact of contrast agent concentration and fixation time on tissue $T_{1,}$ using the Gd contrast agent gadoteridol (an agent with slightly reduced T_1-relaxivity than Gd-DTPA but a higher viscosity (Bellin, 2006; Tweedle, 1997)). Four concentrations – 0, 12, 24 & 46mM (assuming a standard 0.5M solution) – and two timepoints (3.5 & 24 hours) were reported. After 3.5 hours fixation, mean whole-embryo T_1 varied from 1570ms (0mM) to 266 (12mM), 115 (24mM) and 74ms (46mM) respectively, demonstrating a reduction in T_1 as concentration increases. Increasing fixation time also showed a reduction in T_1 (24mM concentration), where T_1 decreased from 3140ms (fresh) to

14ms (24 hours). In addition, T_2 also reduced with an increase in fixation time. The authors conclude that a 3-6 hour fixation was optimum in terms of T_1 and T_2 reduction, deciding on a 5 hour fixation time at 24mM.

In the study it was also observed that there was a decrease in T_1 with increasing concentration and with fixation time. The fixation time dependency was probably due to changes in skin permeability with gestational age (Petiet et al., 2007). It is known that skin stratification occurs by 14dpc, and development of full barrier-function at 16dpc (Hardman et al., 1998). Thus 15.5dpc embryos are likely to have impeded movement of Gd-DTPA into body tissues which may account for our findings.

Short TR sequences can be used to minimise scan times in high resolution embryo datasets and active staining methods thus rely on shortening T_1 to recover tissue SNR (Johnson et al., 2002b). From our results, ignoring any T_2* effects, increasing fixation time and Gd-DTPA concentration would contribute to an increase in SNR per unit time and therefore benefit acquisition. In the heart, limited change was seen in T_2* for either concentration when fixation time was increased from 3 days to 2 weeks indicating that there is no effect of T_2*-signal loss at the longer fixation time.

In the study by Petiet (Petiet et al., 2007), the intention was to have an initial high concentration of agent that could reduce tissue T_1 to the desired level (<100ms) in a short fixation time. Given the effect seen in the heart, where the Gd-DTPA has less penetration (T_1 values are elevated compared to heart tissue at 3 days but have reduced by 2-weeks), a 2 week fixation time was chosen to continue the optimisation. At two weeks, concentration of Gd-DTPA and thus T_1 in the whole embryo will have tended toward equilibrium with its surroundings. In addition, if repeat imaging is needed, then more stable T_1 and T_2* values in the embryo increases the likelihood that optimised scanning parameters will remain valid in the future.

Calculated from the 2-week multiple concentration data, R_1-relaxivity in the heart (3.8 $mM^{-1}s^{-1}$) was similar to agarose (3.9$mM^{-1}s^{-1}$, in-line with a previously recorded value of 3.9 $mM^{-1}s^{-1}$for Gd-DTPA saline solutions at 8.45T (Donahue et al., 1994)). R_2*-relaxivity in the heart, however, was >2.5 times higher than agarose (15.9 vs. 5.9 mM^{-}

$^{1}s^{-1}$) illustrating that Gd-DTPA has a particular impact on reducing tissue T_2* regardless of concentration.

The final part of the study was to determine the optimum parameters in the heart for maximum contrast between heart wall and chambers. A range of possible MR parameters, to identify the maximum signal difference were investigated, using an approach commonly used to optimise flip angle for gradient echo imaging (Pelc, 1993). It was noted that there was no unique set of parameters for any one concentration and the calculated parameters varied markedly between concentrations. One question that was specifically addressed was whether an increase in TR would be more beneficial for SNR as opposed to increasing the number of averages. It was found that increased averaging with short TRs (relative to T_1) was favoured, with 5 averages/28ms TR (2 and 4mM concentrations) and 7 averages/20ms TR (8 and 16mM) giving the highest contrast to noise. Although an odd number of averages could compromise some of the benefits of pulse sequence phase cycling (Kingsley, 1995), this may be outweighed by the need for the highest contrast to noise per unit time obtainable, especially at such small voxel sizes.

Thus an advantage of higher Gd-DTPA concentration, which reduces T_1 further, is that TR may be reduced, allowing a shorter acquisition time or the opportunity to increase signal averages. While this approach also has the potential to reduce signal due to T_2* decay, our measurements show that heart and chamber SNRs consistently increased from 2 to 8mM concentrations. For these concentrations the benefits of a shorter T_1 on signal outweighed T_2* losses. At 16mM, the short tissue T_2* measured (~3ms) was probably responsible for the lack of change seen in heart SNR compared to 8mM, as well as impaired resolution of structure.

In the embryo heart, SNR improved with the optimised scan parameters resulting in a marked increase in contrast between heart wall and chamber (heart SNR increased from 11 to 14; chamber SNR from 16 to 28). Subsequent Gd-DTPA concentrations also showed improvements in organ SNR and heart-chamber contrast above that of 2mM up to the 16mM concentration. While a contrast improvement was seen at 16mM, this was mostly due to an increase in chamber signal alone – mean heart SNR remained similar to 8mM.

When scanning each concentration at simulation-derived optimum MR settings, measured global shim linewidth increased with Gd-DTPA concentration (2mM: 45Hz, 4mM: 55Hz) reaching a maximum at 16mM (135Hz). This reinforces the notion that global T_2* is particularly short at 16mM. As this linewidth exceeds the bandwidth of 130Hz per pixel, there would be concern about susceptibility effects and blurring due to the wide point spread function (Callaghan et al., 1994; Choi et al., 1997), affecting image discrimination and contrast over the whole embryo. The chosen 8mM concentration had a linewidth of 77Hz, well within bandwidth. This trend was also shown by the calculated maximum linewidths in the heart specifically, where the value increased markedly with concentration. The combination of these factors led us to determine that 8mM, when imaged at the optimal parameters, showed the greatest balance of heart contrast, image resolution and overall embryo SNR for phenotyping.

There was no difference between the SNRs of agarose and heart chamber in 8mM optimum images. This indicates that the composition of the 1% agarose background was similar enough to the heart chamber at 2-weeks to be used as a surrogate when making T_1 and T_2* measurements. This is supported by a previous study suggesting that for Gd-DTPA solutions with a small macromolecule content, T_1-relaxivity should remain similar(Stanisz and Henkelman, 2000).

Our method of contrast optimisation was also validated, as linear fits of simulated to measured signal intensity values showed excellent agreement with experimental data (Figure 4.7).

It is understood that tissue parameters are affected by magnetic field strength, with a longer T_1 and shorter T_2 as field increases (Bottomley et al., 1984). A recent *in vivo* rat brain study (de Graaf et al., 2006) compared relaxation times in a number of brain regions at three field strengths (4.0, 9.4 and 11.7T). Although significant T_1 increase/T_2 reduction was seen as field strength increased, the change in tissue parameters was less dramatic between 9.4 and 11.7T (e.g. mean cortex T_1 1948 vs. 2073ms) compared to 4.0 and 9.4T (1285 vs. 1948ms). As our embryos are contrast-enhanced, the measured T_1 and T_2* are dominated by the relaxation characteristics of the Gd-DTPA. Previous work (Donahue et al., 1994) with Gd-DTPA saline solutions (at field strengths of 1.0, 4.7 and 8.45T) showed that for T_1, Gd-DTPA relaxivity was not significantly different between 4.7 and 8.45T (4.02 vs. 3.87mM^{-1}s^{-1}). These studies indicate that, given the dominant effect of the contrast agent, our optimised scan parameters may be broadly applicable, particularly to the higher field strengths generally used for μMRI.

From our measurements of chamber SNR with Gd-DTPA concentration, there is the suggestion that vascular signal can be emphasised with progressively higher amounts of Gd-DTPA and/or longer echo-times if structural anatomy is not specifically desired. This parallels the early attempts at vascular phenotyping by Smith and colleagues (Smith et al., 1994), where a solution of BSA-Gd-DTPA was directly injected into embryo vasculature, producing MRA-like images of the vascular tree.

Using the optimal preparation for improved SNR and contrast, an initial screen of 13 *Chd7*$^{+/+}$ and $^{+/-}$ embryos for heart defects was performed, using 8mM Gd-DTPA with 2-weeks fixation and corresponding MR scan parameters. With this relatively simple preparation and single acquisition of the multiple embryos, a ventricular septal defect was easily identified in a heterozygote (see Figure 4.8b) and later verified by histology (Figure 4.8c). This confirms that the gene trap generated *Chd7* mutant produces a heart phenotype, consistent with expected findings (Bosman et al., 2005) and is the first demonstration of this cardiac abnormality by MRI in this transgenic model.

4.6 Conclusion

In this chapter optimised preparation and scan parameters for heart imaging in 15.5dpc mouse embryos were presented. Fixation for 2-weeks provides a gain in SNR due to T_1 reduction, as does increasing Gd-DTPA contrast agent concentration. It was found that the best balance of heart CNR and muscle SNR was achieved at 8mM. Using gradient-echo simulations with measured T_1 and T_2* values, the optimum scanning parameters were determined and verified. These parameters were then used to identify a heart defect in *Chd7*$^{+/-}$ mice. This optimisation should allow better determination of heart and vascular anatomy in a variety of transgenic embryos, enabling greater sensitivity in detection of defects.

Chapter 5:

Magnetic Resonance Virtual Histology for Embryos: 3D Atlases for Automated High-throughput Phenotyping

5.1 Chapter Outline

The previous chapter outlined an optimised preparation and scanning protocol for the enhanced SNR and CNR to enable cardiac phenotyping in mid-gestation mouse embryos. In this chapter, this work is extended to show that the protocol may also be successfully applied to the visualisation and examination of CNS phenotypes, using the *Hesx1* model of septo-optic dysplasia as an example.

While µMRI phenotyping is possible through the examination and segmentation of images by an experienced observer, this can become time-consuming and labour-intensive. This chapter further expands previous work, resulting in a novel application of image registration and atlas techniques in order to produce an automated, high throughput method of analysing phenotypic differences between mice with differing genetic backgrounds.

This work was a collaboration with Marc Modat, UCL Centre for Medical Image Computing, who developed and modified the non-linear registration software for use with large embryo datasets. Additionally, histological sectioning and staining of embryos was performed by Sujatha Jayakody and Sandra De Castro, of the Neural Development Unit UCL Institute of Child Health.

5.2 Introduction

In the wake of the first draft of the full mouse genome sequence (Mouse Genome Sequencing Consortium, 2002), large-scale mutagenesis programmes are underway (International Mouse Knockout Consortium, 2007) that will produce mice with gene knockouts for each of the approximately 25,000 genes in the mouse genome. Analysis of these mice in coming years will give new insights into the genetic basis of human disease, as novel genes are identified that impact upon mammalian physiology and morphology. Mouse embryos in particular may be studied to determine the role of genes on development and congenital abnormalities. With an increasing number of new mutants, effective methods of identifying novel phenotypes in these embryos will be crucial.

Current phenotyping of embryo morphology is generally achieved by histological examination using microscopy. Specimens are dehydrated, wax embedded and thinly sectioned (2-8µm) (Kaufman, 1992), providing high resolution 2D data and tissue sections that may also be stained for gene and protein expression. Episcopic imaging is a development of this process, where autofluorescence of each tissue slice can be photographed and combined to generate high resolution 3D volume datasets (1-2µm isotropic resolution) (Weninger and Mohun, 2002). However these histological approaches are time-consuming, introduce distortions into final 3D image due to the sectioning process and do not readily enable rapid screening as only one embryo may be imaged at a time.

MRI is now an established method for non-invasive embryo imaging, beginning with the early work of Smith and colleagues (Smith et al., 1994). High-resolution 3D datasets with isotropic resolutions of down to 12µm are created (Smith et al., 1996) with excellent soft tissue contrast, allowing the visualisation and segmentation of individual organ structures (Dhenain et al., 2001). MRI is also capable of high-throughput screening of multiple *ex-vivo* embryos (up to 32 in a single overnight scan) with the combination of a large volume imaging coil (Schneider et al., 2004) and fixation in an MR contrast agent (Cleary et al., 2009). Diffusion-tensor imaging (DTI) – an alternative MRI technique – has also been used to investigate the structure of embryo CNS by exploring the degree and direction water is able to diffuse along neuronal axons (Zhang et al., 2003). Although this technique is ideal for investigating white matter, it is impractical for high-throughput imaging, as many hours are needed to generate connectivity maps in a single brain.

Other imaging methods such as optical projection tomography (OPT) and micro-computed tomography (µCT) are also able to non-destructively produce 3D datasets.

OPT can create images of embryos that combine both anatomical structure and gene expression with conventional fluorophores, at high resolution (5-10μm) (Johnson et al., 2006; Sharpe, 2004). However the technique requires embryos which are partially transparent thereby making its use challenging in older subjects (>13.5 days post coitum, dpc) (Schneider and Bhattacharya, 2004). μCT is also capable of acquiring high-resolution datasets (typically less than 27μm) in a short scan-time (~2 hours) (Johnson et al., 2006). Although conventionally μCT has difficulty in distinguishing soft tissues, which have inherently low contrast due to a narrow range of CT numbers (Holdsworth and Thornton, 2002), the use of CT contrast agents as tissue stains, such as osmium tetroxide (Johnson et al., 2006) and potassium triiodide (Degenhardt et al., 2010), have improved its ability to discriminate tissues. μCT is also particularly suited to skeletal studies, as it can produce excellent images of dense radiopaque structures such as bone (Oest et al., 2008).

Despite the availability of these advanced imaging techniques, any embryo dataset must still be manually assessed through inspection by a trained observer. As high-throughput analysis is increasingly demanded, conventional visual assessment for abnormalities is likely to become labour-intensive and insensitive.

Advanced computational techniques such as segmentation-propagation and voxel-based morphometry (VBM) have been used to investigate populations in both clinical and adult mouse MRI studies (Ashburner and Friston, 2000; Calmon and Roberts, 2000; Lerch et al., 2008; Sawiak et al., 2009b). These methods enable anatomical differences between groups to be identified with little manual intervention or visual assessment. Integral to these techniques is the use of an *atlas*, a spatial average image of the whole population (Ashburner and Friston, 2000; Calmon and Roberts, 2000) created by finely warping individual subject images together to locally align anatomical features. Segmentation-propagation is a quantitative method for making volumetric measurements. After segmenting a volume of interest on the atlas image, such as the brain or heart, differences may then be identified between groups in the population by propagating the segmented volume to all individuals, thus providing the group mean and standard deviation from a single volume of interest on the atlas image. However, while average images of registered wild-type embryos have been reported previously (Zamyadi, 2008), there has so far been no application of atlas methods for phenotypic assessment. It is envisaged that a combination of multiple whole-embryo imaging with image processing techniques would allow the creation of an average embryo atlas from a population and enable automated phenotypic comparisons between transgenic and wild-type littermates.

In this study there were three stages to the investigation of the embryo atlas. This started with addressing the lack of brain tissue contrast on MR images. Initially a contrast enhanced MR technique was developed to produce structural detail in the embryo CNS. This was assessed in *Hesx1*$^{-/-}$ and *Hesx1*$^{\mathrm{I126T/I126T}}$ mice, models of septo-optic dysplasia (SOD) (Dattani et al., 1998; Sajedi et al., 2008). These models typically give rise to a dysmorphic pituitary gland. However, the small size of the gland and its protected location often results in preparation artefacts and damage during histological sectioning. Thus a non-invasive approach may facilitate phenotyping morphology in this region. Combining the contrast enhanced protocol with computational methods, an MRI atlas was generated for a population of CD-1 embryos and compared against histology. Finally, this enabled the use of a segmentation-propagation technique to assess brain and cardiac phenotypic differences between CD-1, C57BL/6 strains and *Chd7*$^{+/-}$ knockout mice (a model of the condition CHARGE syndrome) (Bosman et al., 2005; Randall et al., 2009) based on a novel population atlas.

5.3 Materials and Methods

5.3.1 Animal Preparation

All parts of this study were carried out in accordance with the UK Animals (Scientific Procedures) Act, 1986. Pregnant female mice were sacrificed by cervical dislocation. Embryos were then dissected from the mother and transferred to warm Hanks solution. Their umbilical cords were cut and the embryos were allowed to bleed out into the solution. The embryos were then fixed in a solution of 4% formaldehyde and Magnevist MR contrast (Gadolinium-DTPA, Bayer-Schering Pharma, Newbury, UK) and left on a rotator. The embryos were removed and embedded in a 50ml centrifuge tube using 1% agarose gel doped with an identical concentration of Magnevist to initial fixation. After comparing Gd-DTPA concentrations (2, 4, 8 & 16mM) in groups of CD-1 embryos over two fixation durations (three days and two weeks), it was determined that fixing embryos with 8mM Gd-DTPA for at least two weeks produced the greatest SNR and brain contrast without major susceptibility artefacts. Three groups of mice were imaged at 15.5dpc: outbred CD-1 mice from an established colony at UCL, and *Chd7* wild-type and heterozygous gene trap mice (C57BL/6 background). Also *Hesx1*$^{-/-}$, *Hesx1*$^{\mathrm{I26T/I26T}}$ and wild-type embryos at 18.5dpc.

5.3.2 Imaging

Embryos were imaged on a Varian VNMRS 9.4 Tesla MRI system (Varian Inc., Palo Alto CA, USA) using a 33mm quadrature birdcage volume coil (RAPID Biomedical GmbH, Würzburg, Germany). Maps of T_1 and T_2* in tissue were created using a single sagittal slice field of view=27x27 mm^2, 256^2 matrix size, 0.5 mm thickness). For 3D imaging a gradient-echo sequence was used, TR=20 ms, 7 averages, flip angle=60°. Field of view=27x27x27 mm^3, matrix size=512^3, zero-filled to 1024^3 on the console to a voxel-size of 26x26x26 µm^3. Echo-time (TE) was 9 ms for 15.5dpc embryos; 5 ms for 18.5dpc embryos to enable better visualisation of the bone structures of the cranial floor.

5.3.3 Image Registration

Embryos were first semi-automatically extracted from the dataset and group-wise registration, using global and local transformations, was performed to create an average image atlas. The obtained deformation parameters from each individual to the template were then used to propagate the different regions of interest to each embryo.

5.3.3.1 Digital Extraction

The embryos were extracted from the acquisition volumes using simple operators such as Gaussian smoothing, thresholding and mathematical morphology (erosion, dilation and selection of connected components).

5.3.3.2 Registration and Atlas Average Creation

The intensity ranges of the embryos were first normalised prior to registration. One embryo was selected and taken as the reference, with all further processing performed in its image-space. The others were first spatially normalised using a rigid registration algorithm consisting of 6 global degrees of freedom (DOF): 3 translation and 3 rotation parameters, in order to correct the differing orientations of each embryo in the acquired images. All resulting images were then averaged into a new blurry reference image. This initial registration step, due to the rigid transformation, did not affect the geometry of the embryos. Thus the average image was not biased toward the selected embryo's geometry. The embryos were then aligned using affine registration (12 global DOF: 3 translations, 3 rotations, 3 scales and 3 shears) to the previously created average image. Rigid and affine registration was performed using a block-matching technique (Ourselin et al., 2001). 5 iterations were performed using the affine algorithm. After each iteration the resulting average image was updated (an example of the result after affine registration is shown in Figure 5.5A). A non-linear registration algorithm, Free-Form Deformation (FFD) (Rueckert et al., 1999) was then used to locally align the embryos to the reference average image. Control point positions were optimised in order to locally deform each image to the target reference image. The degree of alignment was evaluated using Normalised Mutual Information (NMI) (Studholme et al., 1999). 18 iterations of non-linear registration were performed, using a coarse-to-fine approach where the control point spacing was gradually reduced to 5 voxels width (130 μm) overlaid on the full resolution images. After each non-linear registration step, it was ensured the average image was geometrically in the middle of all input images by the subtraction of the mean total displacement from each deformation field before resampling the embryo images to produce the average atlas. All non-linear registration steps were performed using a parallel implementation (Modat et al., 2010) of the FFD algorithm on a computing cluster, which allowed them to run concurrently within each step. A cluster with approximately 1000 CPU cores was used.

5.3.4 Volume Segmentation, Rendering and Propagation

Regions of interest were semi-automatically segmented and rendered using Amira visualisation software (v5.2.2, Visage Imaging Inc., Andover MA, USA). As the result of the group-wise registration consists of an atlas average image and a set of deformation fields, there is direct spatial correspondence between every voxel in the average image and their corresponding positions in each single embryo. Using this set of deformation fields, segmented regions of interest were propagated from the atlas into the original image space of each embryo.

5.3.5 Signal-to-Noise Measurements

Signal-to-noise (SNR) in raw image data was calculated by taking the mean signal in a volume of interest and dividing by the standard deviation of the signal in a region of background noise.

5.3.6 Statistical Analysis

Analysis of volume data was performed in Prism v5.00 (GraphPad Software, San Diego CA USA) using one-way ANOVA with Tukey testing for multiple comparisons (propagated volumes) and the Kruskal-Wallis test with Dunn's test for multiple comparisons (normalised volume data).

5.4 Results

5.4.1 Micro-MRI for the Investigation of Embryo Brain Anatomy in 3D

15.5dpc CD-1 embryos were fixed in 4% formaldehyde solution (Sigma-Aldrich Company Ltd., Gillingham, UK) with a gadolinium-chelate contrast agent (Gd-DTPA) and imaged at 52µm resolution, interpolated to 26µm by zero-filling. Obtaining tissue contrast, particularly in brain structures is often difficult in embryo imaging. Images of the embryo CNS acquired from specimens fixed in four contrast agent concentrations (2 to 16mM) and two fixation durations (three days and two weeks) were evaluated to determine optimal preparation. Two weeks fixation resulted in better penetration of the agent into brain structures compared to 3 days, as determined by reduced tissue T_1 (e.g. 179 to 80ms, 4mM). It was determined that embryos fixed in 8mM Gd-DTPA for two weeks, produced images with the highest brain contrast-to-noise (CNR=8.0, 8mM vs. CNR=5.7, 4mM, between external capsule and basal ganglia regions), without major artefacts. Images also showed excellent tissue contrast throughout the entire embryo. White-matter tracts and developing layers of the cortex were clearly visualised (Figure 5.1), which was due to the selection of MRI parameters; a relatively long 9ms echo time compared to the 6ms T_2* of the CNS (mean T_1=38ms) giving T_2*-weighted images. Using this imaging protocol, multiple subjects may then be imaged (up to 40; using a 35mm diameter volume imaging coil, with a 60mm z-profile) in a single 10-hour overnight scan with high SNR (~23 over the whole embryo).

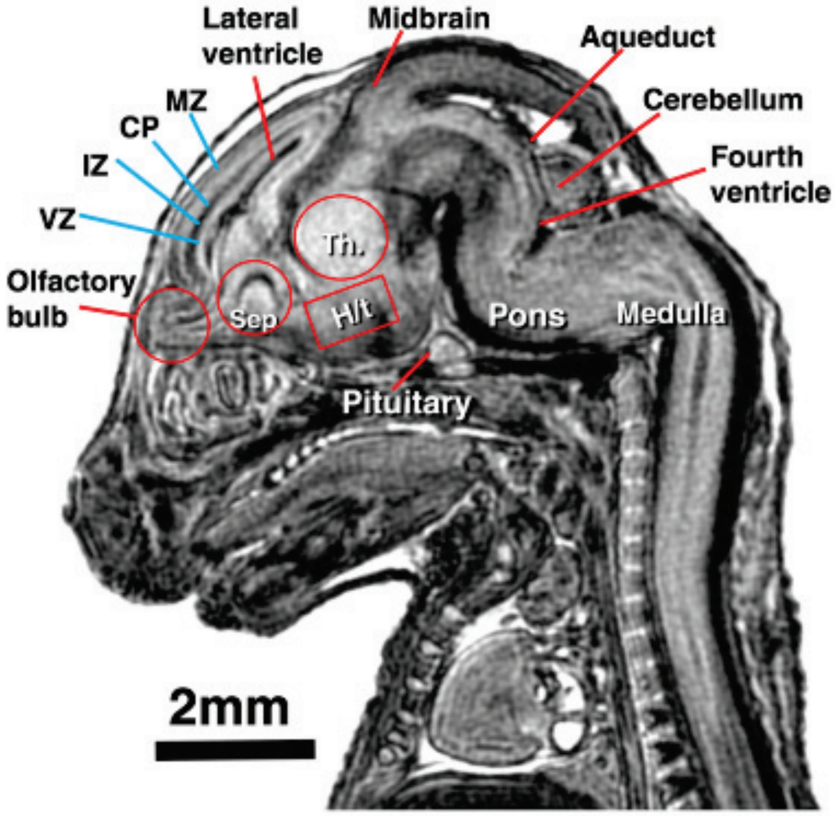

Figure 5.1: *Sagittal section through an example 3D embryo dataset showing CNS structures in the brain. Structures of the cortex can be seen, including cortical plate (CP), ventricular (VZ), intermediate (IZ) and marginal zones (MZ) (blue labels). Also thalamus (Th.), hypothalamus (H/t) and ventricular septum (Sep.).*

Following this preliminary investigation, the imaging protocol was applied to a phenotyping study of 18.5dpc embryo mice (*Hesx1*$^{-/-}$, *Hesx1*$^{I126T/I126T}$ and wild-type) for CNS and pituitary defects. *Hesx1*-deficient embryos showed hypoplasia of the left olfactory bulb and telencephalic vesicles (Figure 5.2). Eyes were absent with no sign of optic nerve development. Close examination revealed an apparent hyperplasia of the pituitary gland with an outgrowth of closely associated mucosal tissue, which has not been previously described (Dattani et al., 1998) (Figure 5.2A) in *Hesx1*$^{-/-}$ mutants. Tissue contrast was readily apparent between both parts of the gland in wild-type embryos, which enabled segmentation of the individual lobes (Figure 5.2B). The *Hesx1*$^{I126T/I126T}$ embryo showed milder forebrain defects with normal corpus callosum and olfactory bulbs, but eyes were also absent. This particular specimen showed a distinct phenotype in which the anterior and posterior pituitary lobes could not be identified, but there was a tissue mass invading the oropharyngeal cavity. Although ectopic oral pituitary tissue has been inferred from histological analysis, it has not been shown so evidently as in Figure 5.2B. The mid-coronal MRI shows an obvious cranial shift of the left anterior hypothalamic area as a result of the malformation of the pituitary gland (bottom of Figure 5.2A, red arrow). These MR findings were all confirmed on subsequent histology (Figure 5.2A).

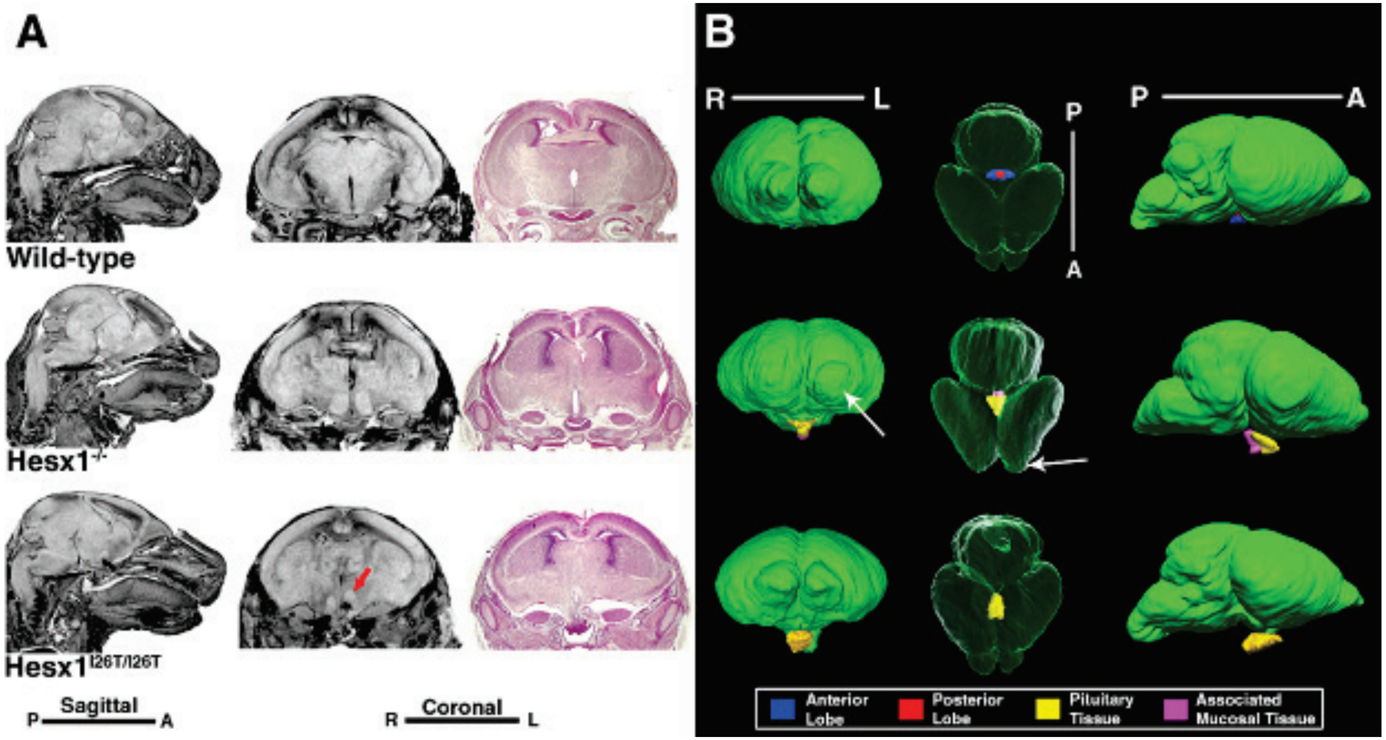

Figure 5.2: *Images of Hesx1 mutant and wild-type embryos. (A) Sagittal and coronal MR images of 18.5dpc wild-type, Hesx1*$^{-/-}$ *and Hesx1*$^{I26T/I26T}$ *18.5dpc mice at the levels showing greatest changes in structure. Similar histology views from the same embryo are also shown. The pituitary gland is also visibly enlarged and penetrates the oropharyngeal cavity (Hesx1*$^{-/-}$ *sagittal view, middle-left). In the Hesx1*$^{I26T/I26T}$ *mutant, in addition to an enlarged pituitary gland, structures of the left hypothalamic area can be seen to be upwardly shifted (red arrow). (B) 3D volume rendering of whole-brain and pituitary structures. In the Hesx1*$^{-/-}$ *mutant, the gland is visibly dysmorphic and enlarged compared to wild-type, with a large amount of associated mucosal soft tissue posterior. The rendering also shows an underdeveloped left olfactory bulb (white arrows). The gland in the Hesx1*$^{I26T/I26T}$ *mutant (bottom) is highly dysmorphic compared to wild-type.*

5.4.2 Generation of an MRI Embryo Population Atlas

Conventionally, embryo atlases use single subjects at a given developmental timepoint to illustrate representative anatomy. In this study an average atlas of a population of mid-gestation embryos was generated. Using computational methods combining 3-stages of image registration – rigid, affine and non-linear registration –6 CD-1 embryos were warped into a single average image.

Figure 5.3 demonstrates that the atlas reinforces structures common to all, whilst reducing the effect of imaging or preparation artefacts present in individual embryos. Combining images from multiple subjects also increases image signal-to-noise. Comparing our images to histology, it was observed that hypointense regions on the MR images, enhanced in the composite atlas, correlate well to large fibre structures in the developing CNS such as internal (Figure 5.3, blue triangles) and external capsule (Figure 5.3, red arrows). It is notable that the anatomical detail has been preserved during atlas formation and SNR is improved and as such, the atlas is ideally suited to a host of image processing techniques such as brain volume segmentation-propagation, which will be explored in the following section.

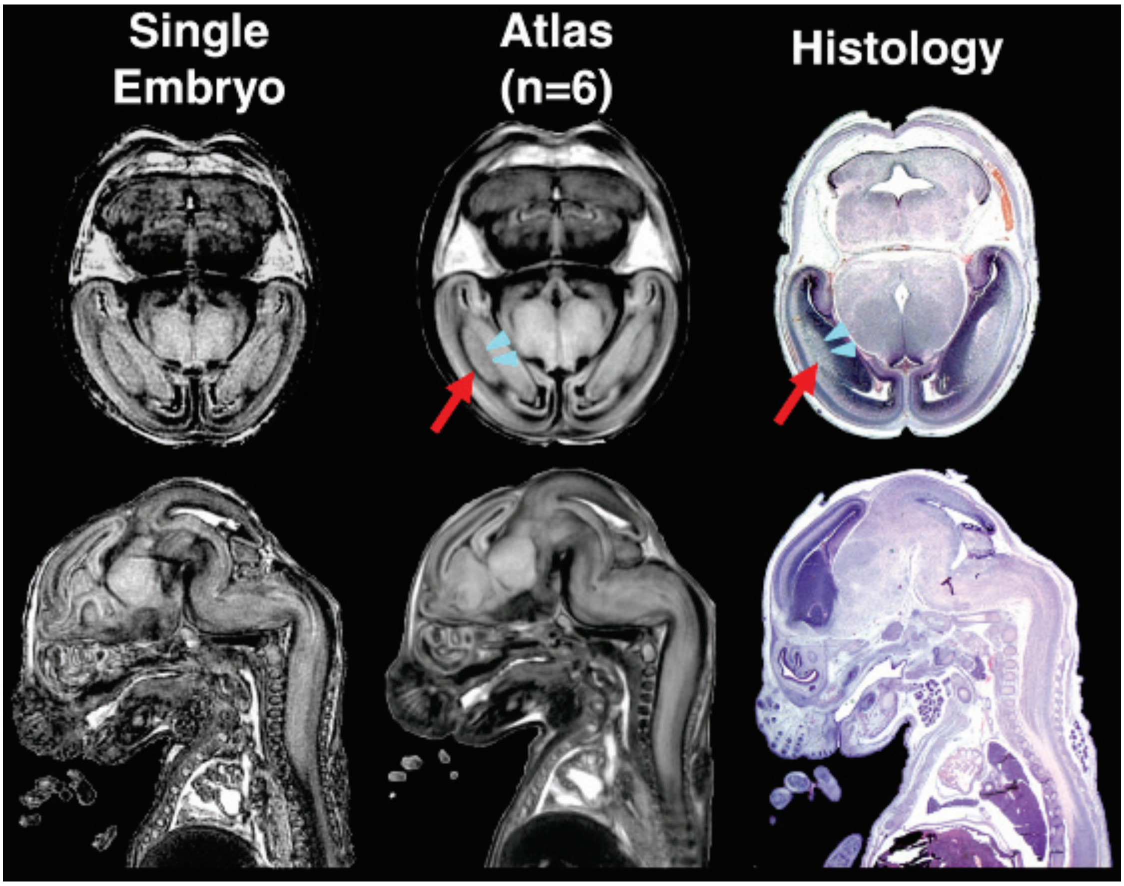

Figure 5.3: *Similar axial and sagittal images comparing single embryo, atlas and equivalent histology sections. Even with six embryos, there is a noticeable improvement in signal-to-noise. Structural details common to all embryos appear enhanced in the atlas image and correspond well to histology, such as internal (blue triangles) and external capsule (red arrows).*

5.4.3 Unsupervised Generation of Quantitative Tissue Volumes in a Whole Population

Figure 5.4 shows the steps in the segmentation-propagation process of an MRI embryo atlas. This allows regional segmentation from a single average image to be mapped onto the original individuals for calculation of tissue volumes. The utility of the atlas segmentation in automatically identifying volume differences between two groups of mice with differing backgrounds: outbred CD-1 (n=6) and C57BL/6 mice (n=13) was examined. The C57BL/6 mice were further subdivided into wild-types and *Chd7*$^{+/-}$ gene trap mice (n=5 and n=8 respectively).

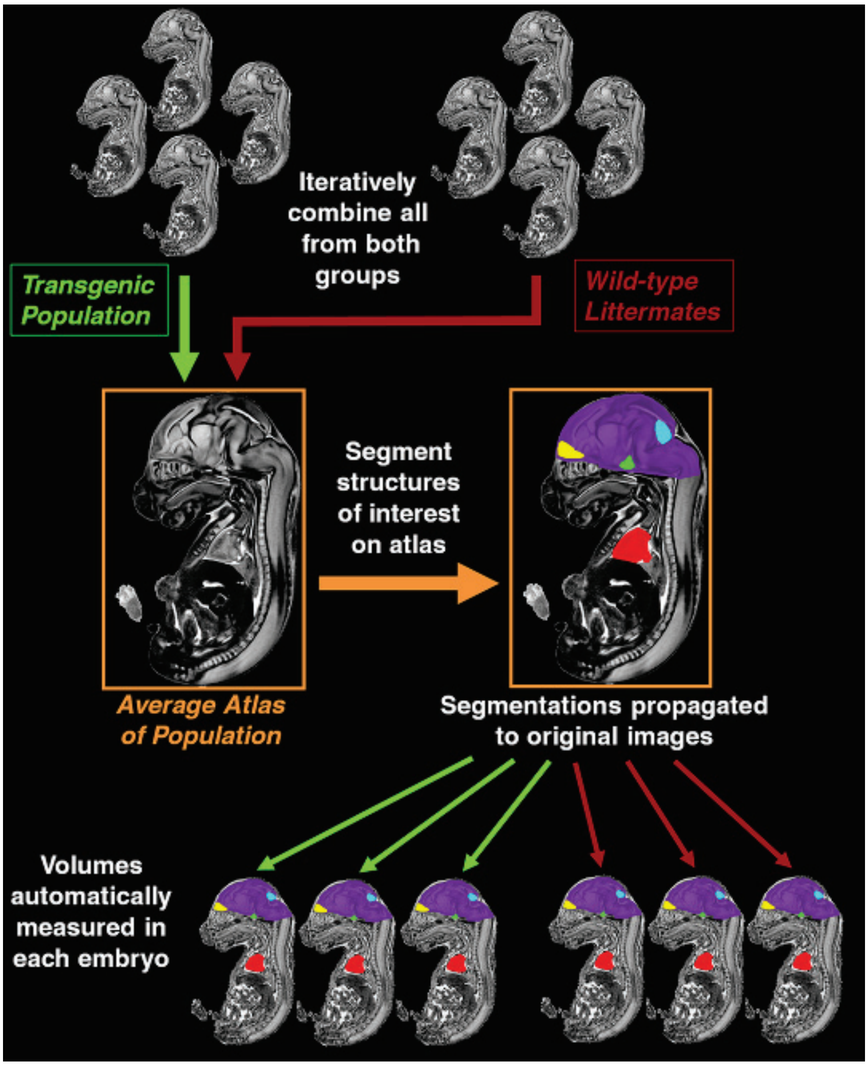

Figure 5.4: *Schematic diagram outlining the segmentation-propagation process. Following the initial non-linear registration of all images in the study population, an average atlas is created. The transforms used to warp the images to create the average image are recorded at all points in 3D across the dataset. Applying the inverse transform to regions segmented on the atlas allows volumes of structures to be measured in individual subjects. A similar method has been used previously for volume measurements in adult mouse brains (Bock et al., 2006).*

First, an MRI atlas of these 19 individuals was created using the registration techniques described previously. The improvement in the average image after 18 iterations of non-linear, compared to initial affine registration, is shown in Figure 5.5.

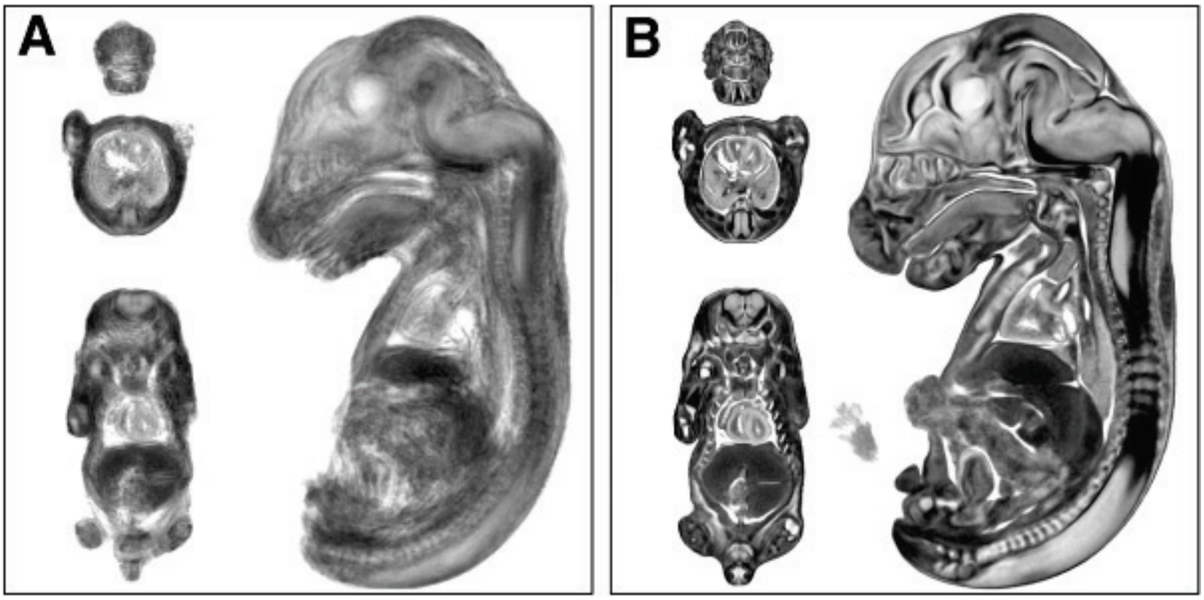

Figure 5.5: *Overview of average images produced during the registration process: (A) average image of the 19-embryo dataset after global alignment (affine registration). (B) Final average image after multiple iterations of the local deformation algorithm. The sharpness of the non-linear registration result as seen in image (B) indicates good alignment of structure.*

The resulting average atlas was then manually segmented (Figure 5.6) into left olfactory bulb (coloured green), pituitary (yellow), mesencephalic vesicle (blue), whole-brain (purple) and whole-body (tan) volumes. Heart ventricles (red) were also segmented for comparison. Volumes from the atlas segmentation were then automatically measured for each individual through propagation.

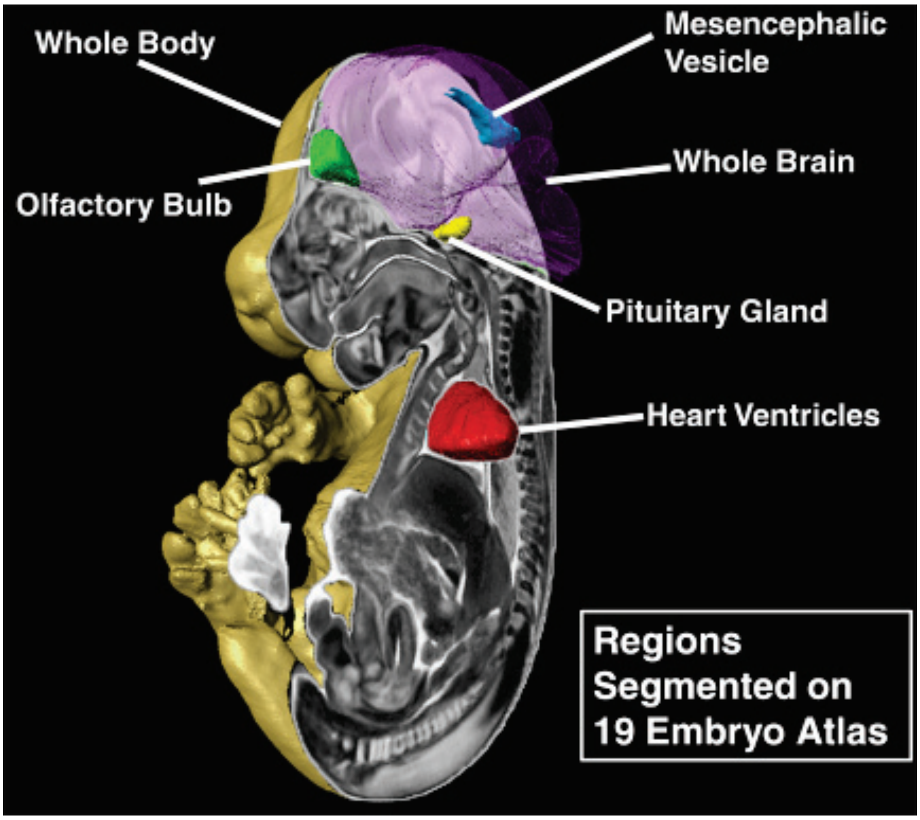

Figure 5.6: *3D volume rendering of the atlas of 19 subjects indicating the volumes of interest drawn for segmentation-propagation volume measurement.*

As shown in Figure 5.7, there was good anatomical agreement between the areas segmented on the atlas with resulting propagation on the original individual dataset. Furthermore, propagated volumes compared favourably against manually segmentation from 6 CD-1 embryos. Using the established Dice similarity measure of spatial agreement (Dice, 1945) (where a value of 1 represents full spatial overlap and 0 is none) there was a mean correspondence between manual and propagated whole-brain volumes of 0.95±<0.01. The propagated volumes measured in the three groups are summarised in Table 5.1.

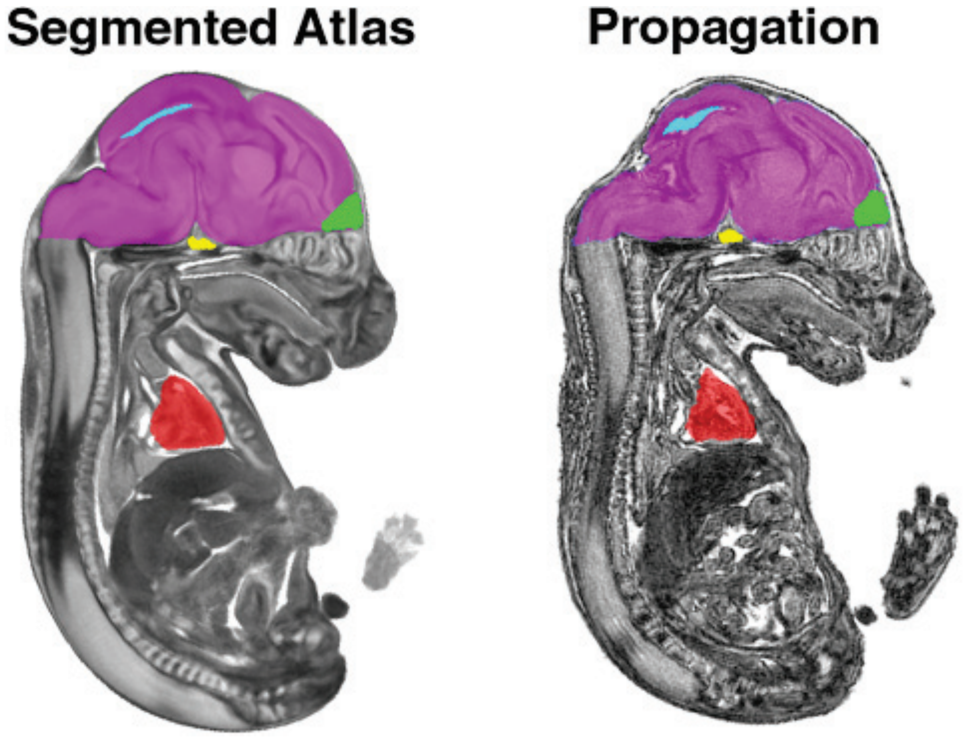

Figure 5.7: *Similar sagittal slices through our 19 embryo atlas (left) and a single CD-1 embryo (right) illustrating the good correspondence of segmented regions propagated from the atlas to individual datasets. (Red: heart ventricles, yellow: pituitary gland, green: olfactory bulb, purple: whole brain, blue: mesencephalic vesicle.)*

Region Volume (mm^3)	**CD-1 (n=6)**	**SD (% mean)**	***Chd7* WT (n=5)**	**SD (% mean)**	***Chd7*$^{+/-}$ (n=8)**	**SD (% mean)**
Whole Body	388	6.9	322	10.6	312	4.7
Whole Brain	45.7	2.6	42.5	6.2	39.2	4.3
Olfactory Bulb	0.3	6.2	0.3	15.4	0.2	15.1
Vesicle	0.2	11.0	0.2	38.1	0.2	47.7
Pituitary	0.1	7.3	0.1	13.3	0.1	8.8
Heart Ventricles	2.4	12.8	2.2	14.3	2.0	7.4

Table 5.1: *Summary of propagated volumes for our three groups of embryos.*

Analysing the propagated volumes, significant differences were found in the absolute overall brain volume between the three groups ($p<0.05$, Figure 5.8B), with the smallest mean brain volume (39.2mm^3) observed in the *Chd7*$^{+/-}$ mice. Significant differences were found between CD-1 and *Chd7* wild-type embryos in propagated volumes of the whole embryo and olfactory bulb (0.323 vs. 0.258 mm^3, $p<0.05$, Figure 5.8B & C).

In an attempt to account for developmental differences between embryos the data was also normalised to embryo body volume. After normalisation, significant differences were observed between strains in brain and pituitary volumes (both $p<0.01$, Figure 5.8D & E).

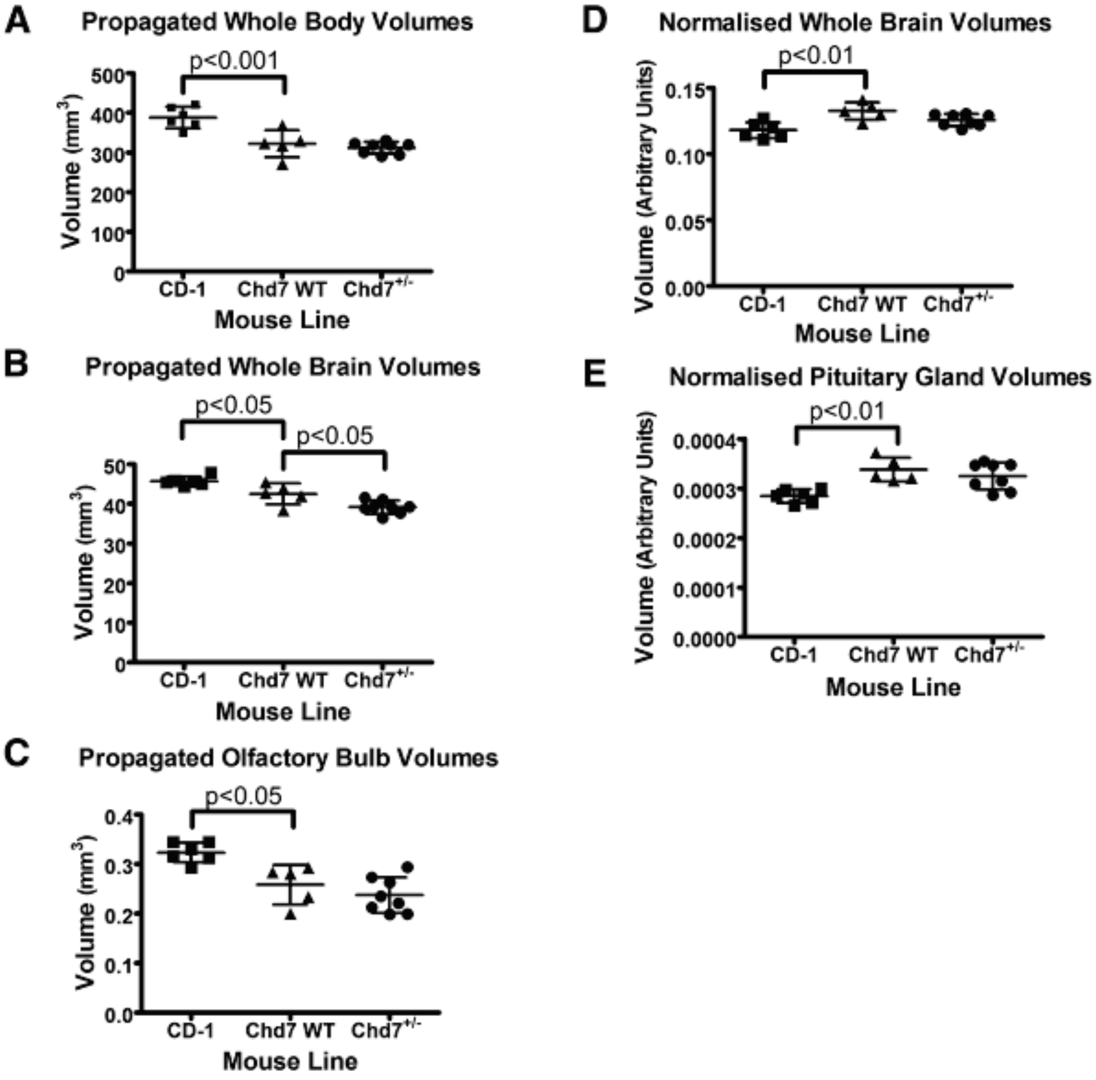

Figure 5.8: ***(A)-(C):*** *Graphs showing propagated volume differences in brain and pituitary regions between groups.* ***(D)-(E):*** *Graphs showing volume differences in brain and pituitary regions between strains after normalisation of data to embryo whole-body volumes.*

5.5 Discussion

The main findings of this study were: i) development of embryo-specific MR methods and contrast agent protocols enabled high-resolution structural imaging with enhanced anatomical detail in the CNS; ii) using these methods, the structural consequences in *Hesx1*$^{-/-}$ and *Hesx1*$^{\mathrm{I126T/I126T}}$ mouse mutants were identified; iii) a composite whole-embryo atlas using computational methods was generated with excellent anatomical tissue contrast, and finally iv) a novel application is presented of a technique to generate a composite atlas from three groups of embryos, allowing automated high-throughput investigation of phenotype, through volume analysis by segmentation-propagation.

5.5.1 Phenotyping the Developing Brain Using MRI

This study demonstrates that through our preparation of 15.5dpc embryos, which combines fixation in a relatively high concentration of MR contrast agent (8mM) and sufficient fixation time (>2 weeks) enabling the agent to fully penetrate into the CNS, one is able to visualise small brain structures. Image signal-to-noise is high, as brain T_1 is now short and uniform across the brain (reduced to ~38ms).

Previous embryo MRI phenotyping studies have largely concentrated on the heart (Fischer et al., 2007; Petiet et al., 2008; Schneider et al., 2003b), although some have investigated gross changes in the developing brain and other organs (Schneider et al., 2003a). The images acquired in these cases have generally been optimised to give high overall signal from tissue, resulting in proton density (Jacobs et al., 1999) or predominantly T_1-weighted MR images (Petiet et al., 2007; Schneider et al., 2003c). Although the use of the gadolinium-chelate active-stains improves signal-to-noise, the narrow range of tissue T_1s (Petiet et al., 2007) after staining limits the scope for T_1-weighted contrast, producing a generally uniform appearance of the embryo brain. Given the short T_1 of our embryos, the brain contrast observed in our images was unlikely to be due to the chosen MR repetition time (TR). It is likely that the short T_2* observed in the embryos (~6ms) enabled CNS tissue contrast to be generated through the choice of echo time (TE), resulting in the well-delineated structures seen in the images acquired.

Typically MRI methods are able to produce images with the greatest degree of intrinsic CNS contrast (white-grey matter) when axons are fully myelinated (Miot-Noirault et al., 1997). In the developing embryo, while distinct myelinated brain structures are beginning to form, contrast on MR images is generally limited, as T_1 and T_2 differences are small in these young brains (Mori et al., 2001), making visualisation of brain structures difficult. Some of this structure has been seen without contrast enhancement, as part of a wider DTI study (Mori et al., 2001). However our technique allows a reduced scan time together with higher resolution (10 hours for up to 40 whole embryos at 52μm isotropic compared to 13 hours for a single extracted brain), indicating that high throughput is possible while still maintaining good brain tissue contrast.

Beyond preparation optimisation, further improvements in SNR could be made with the adoption of multiple solenoid imaging coils as opposed to the single, large volume coil used in this study. A recent investigation showed a greater than threefold increase in SNR is achievable but this typically requires a large number of receive channels (16), which are currently uncommon on most preclinical MR systems (Zhang et al., 2010b).

Our methods were used to phenotype *Hesx1* embryos, which demonstrated novel phenotypic defects showing hyperplasia of the pituitary gland and closely associated mucosal tissue penetrating into the oropharyngeal cavity. The presence of pituitary tissue in this area may also explain the perinatal lethality observed in these embryos (Dattani et al., 1998), as the pups suffer from respiratory difficulties. Furthermore, a previously unrecognised cranial shift in the anterior hypothalamus was also observed. Symptoms such as obesity and circadian rhythm defects are often associated with human SOD (Rivkees, 2003), which suggest a hypothalamic contribution to the disease. Our findings in the mouse model provide supporting evidence for this hypothesis.

5.5.2 Population Atlases for Anatomical use

In this study, multiple embryo MRI and image registration were combined to produce an MRI atlas that allows a number of white matter and other structures to be readily identified. Previous MRI-based anatomical studies of the embryo (Jacobs et al., 1999;

Petiet et al., 2008) have consisted of single subjects that are imaged at a particular timepoint. This single subject may not represent the true population average due to normal variations in development and may also have been affected by the preparation and the imaging process. An averaged dataset thus reduces the contribution of preparation and imaging effects from individual images not common to the whole population. Previously, wild-type population atlases have concentrated on characterising the adult mouse brain (Dorr et al., 2008; Kovacević et al., 2005; Ma et al., 2005), as anatomical structures are fully developed by this stage and subjects have consistent intrinsic MRI tissue contrast.

The fidelity of the atlasing process in the developing mouse embryo can be seen in the quality of both CD-1 and 3-group average images, indicating good performance of the algorithm in identifying anatomical correspondence between subjects. The image sharpness of a resulting atlas has been shown to be a good indicator of the accuracy of registration (Robbins et al., 2004). It was also noted that in a number of organs other than the brain there was also good registration and enhancement in the average atlas, such as the liver, heart and great vessels.

Having an efficient registration algorithm is essential for registration of large datasets such as presented here. Our non-linear registration algorithm – fast-Free-Form Deformation (F3D) (Modat et al., 2010) – is a new, parallel and scalable implementation of the well-known Free-Form Deformation (FFD) algorithm (Rueckert et al., 1999). Improvements to the registration optimisation process decreases computation time, thus allowing more iterations to be run. For example, registration of a single embryo dataset with ~57 million voxels, represents an optimisation problem with 3 million degrees of freedom. With our algorithm this may be completed in 1 to 2 hours on a standard computer compared to a much longer processing time (many hours to days) with the original FFD implementation. Our method is therefore well-suited to the needs of high-throughput screens, where speed without compromising accuracy and the ability to register large numbers of images is an important consideration.

Phenotyping of the CNS in prenatal mice by MRI has been mostly restricted to those with gross developmental abnormalities, such as a study of *Cited2*$^{-/-}$ mutants which displayed severe exencephaly (Schneider et al., 2003a). In that study, a small number of mutant embryos (n=4) were imaged. The findings of this chapter suggest that high-throughput MRI could now be expanded to visualise and identify more subtle CNS defects through the combination of enhanced MRI contrast and atlasing methods.

5.5.3 Automatic Volume Measurements in an Embryo Study

A mixed average population atlas was used to make regional volume measurements from a single segmentation in the embryo. Previous work on volumetric measurements in the adult mouse brain has allowed the characterisation of wild type brains (Dorr et al., 2008; Kovacević et al., 2005) and also volume differences between mouse strains (Chen et al., 2006), but has not been performed in the embryo. After segmenting five volumes of interest on a mixed atlas of three groups of embryos, significant differences between CD-1 and *Chd7* wild-type embryos were identified in propagated olfactory bulb and body volume. This was attributed to phenotypic differences between CD-1 and C57BL/6 strains at this stage of development, with CD-1s being generally larger. A significant difference between propagated brain volumes of *Chd7* wild-type and *Chd7*$^{+/-}$ mice was also noted, indicating that *Chd7* may be implicated in the process of overall brain development. This would be consistent with recent histological findings of impaired olfactory bulb development (Layman et al., 2009) and previous descriptions of hearing and ear defects (Bosman et al., 2005). After normalising the propagated volumes to whole-body volumes, significant strain differences were seen in whole-brain and pituitary gland volumes.

Both propagated volumes and those normalised to whole-body volumes were presented in this study. Normalisation of data may reduce the effect of non-gene related differences, such as variation in growth-rate, which could affect overall size and thus organ volumes. Both volumes are presented, as normalisation also has the potential to mask phenotypic effects, and as yet there is no accepted standard mode of data presentation. The ability to rapidly generate accurate volumetric data from an imaging modality such as MRI in the embryo is new and further work is required to fully assess the need for data normalisation in phenotypic analysis.

Given the brain volume differences identified between wild-type and the heterozygous *Chd7* embryos (a mean volume difference of ~8%) one hypothesises that this sensitivity would be sufficient when screening the homozygous mutant embryos generally produced by the ENU mutagenesis programmes, which would be expected to exhibit more severe phenotypes.

Our methods could also be used to address mutations with variable expressivity, where a phenotype may be present in one embryo but not others. By comparing embryos on an individual basis to an atlas of wild-types, and performing segmentation-propagation or VBM, outlying, abnormal individuals may then be identified.

5.6 Conclusion

In this chapter, an average atlas generated from high-throughput multi-embryo MRI datasets was presented. The results demonstrated that anatomy is conserved in wild-type CD-1 embryos, enabling the creation of an average embryo atlas that has effectively enhanced anatomical detail. Volumetric analysis of three groups of embryos using segmentation-propagation found significant brain volume differences between CD-1, *Chd7*$^{+/-}$ knockout and wild-type. Significant differences were observed in whole-body and olfactory bulb volumes between CD-1 and *Chd7* wild-types (C57BL/6 background). Normalising propagated volumes to whole-body, significant strain differences were also seen in whole-brain and pituitary gland volumes.

As there is no limit to the number of embryos that may be registered, this technique opens the possibility for quantitative analyses of very large numbers (100s) of embryos with increased statistical power. One hopes this represents a first step towards combining high-throughput MR embryo imaging with high throughput analysis through computational methods.

Chapter 6:

Structural Correlates of Active-Staining Following Magnetic Resonance Microscopy in the Mouse Brain

6.1 Chapter Overview

Chapter 4 described the development of an optimised preparation and scan protocol for high-throughput phenotyping of the mouse embryo. In this chapter, this work is extended by examining optimal preparation and MR parameters to produce detailed images of the adult mouse brain. After optimising the preparation of *ex-vivo in-situ* brains for µMRI, enhanced delineation of subtle structures such as in the thalamus and hippocampus is demonstrated. Detailed histological comparisons of these structures with those seen on MRI are then performed.

This work was produced in collaboration with Dr. Frances Wiseman, UCL Institute of Neurology, who culled and provided the animals used and Prof. Sebastian Brandner, UCL Institute of Neurology, who performed histological sectioning and staining.

6.2 Introduction

An ever-increasing number of mice are being created through genetic manipulation to advance the goal of translational neuroscience to produce and identify mouse models of human conditions. In order to investigate and validate these mouse models, detailed studies must be undertaken of the mouse brain. Phenotyping the brain morphologically conventionally relies on examination of cellular and anatomical structures by histology. While this method is ideal to visualise physiological or pathological changes on a cellular and architectural level, tissue processing artefacts and shrinkage affect the reliability of 3D volumetric assessments. Effective methods for rapid, non-invasive phenotyping are thus needed for the analysis of mouse mutants.

In recent years these efforts have been advanced by the increasing use of microscopic MRI (µMRI) to characterise brain phenotypes of novel mouse mutants. MRI offers a number of advantages over traditional histological sectioning, namely its ability to produce non-invasive datasets, which allow the accurate calculation of volumes without distortion. Morphometric techniques may then be used to allow the identification of novel phenotypes. Work in this field has lead to the creation of non-invasive mouse brain atlases (Dorr et al., 2008; Ma et al., 2005) and has generated new insights into models such as Huntingdon's disease and age-related neurodegeneration (Lerch et al., 2008; Sawiak et al., 2009b; Wetzel et al., 2008).

μMRI produces high resolution datasets of *ex-vivo* tissue with isotropic resolutions of less than 100μm (typically between 21.5-70μm in most brain studies (Badea et al., 2007b; Sawiak et al., 2009a)). This can be technically challenging, with each voxel representing a tissue volume of <1nL, conventionally requiring long scan times to obtain sufficient signal-to-noise (SNR). The innovation of tissue active staining, where gadolinium-chelate MR contrast agents are used during the fixation process to shorten T_1 relaxation, has enabled the acquisition of high SNR 3D datasets with greatly reduced scan times (Johnson et al., 2002a).

The appearance of μMR images acquired in this manner is sensitive to preparation and scan parameters including the contrast agent, fixation concentration and pulse-sequence used (Cleary et al., 2009). It has been recently shown that the use of higher contrast agent concentrations (>5mM Gd-DTPA) as part of the fixation of mouse brains excised from the skull (*ex-situ*), in combination with a 3D gradient-echo sequence, can produce images with high contrast, delineating a number of brain structures seen on conventional histology (Huang et al., 2009; Kim et al., 2009).

The combination of a high contrast agent concentration with *in-situ* preparation may produce enhanced neuroanatomical contrast and allow more detailed and sensitive morphometric atlases, with clearer delineation of regions of phenotypic change. Resulting volume measurements and morphometric analysis may also be less affected by preparation than *ex-situ* brains (Badea et al., 2007a). However, there is little data in the literature comparing *ex-* and *in-situ* brains by MRI. Furthermore, the timecourse for optimal fixation of *in-situ* brains with an MR contrast agent is unknown and a direct histological correlation of brain structures enhanced through gradient-echo imaging together with active-staining has not been performed.

The specific aims of this study were to investigate enhanced tissue contrast using an active-stain µMRI preparation and optimised scanning protocol (Cleary et al., 2009) for imaging adult mouse brains. Specifically the effect of active-staining on perfused- and simple immersion-fixed *ex-situ* brains was assessed and the *in-situ* MR tissue characteristics over a period of 9 weeks were monitored. Furthermore, this study sought to identify the optimal imaging parameters to enable rapid imaging of *in-situ* brains in 3 hours with a standard imaging coil. In particular contrast-enhanced brain structures were assessed via a direct comparison with tissue histology, which may give insights into the cellular distribution and mechanism of MR active-staining.

6.3 Materials and Methods

6.3.1 Animal Preparation:

All parts of this study were carried out in accordance with the UK Animals (Scientific Procedures) Act, 1986. Wild-type mice (n=8) (O'Doherty et al., 2005) were taken from a colony maintained by mating Tc1 females to F1 (129S8 x C57BL/6) males. The mice were culled by an overdose of sodium pentobarbitone administered by injection.

Ex-situ Brain Study: In order to investigate the preparation of excised brains the effects of perfusion-fixation were compared to simple immersion-fixation. 2 of 4 mice were given an initial saline flush (15-20ml of normal saline at a flow rate of 3ml/minute introduced via a needle in the left ventricle) and then perfusion-fixed with 50ml of 4% buffered formol-saline (Pioneer Research Chemicals, Colchester, UK) with 8mM Gd-DTPA (Magnevist, Bayer-Schering Pharma, Newbury, UK) at a flow rate of 3ml/minute; the remaining 2 mice were simply culled. All 4 brains were then carefully extracted from the skull and post-fixed in 4% buffered formol-saline (with 8mM Gd-DTPA) at 4°C.

In-situ Study: For *in-situ* brain MRI, 4 mice were perfusion-fixed as previously described with 2 fixed using formol-saline perfusate alone and 2 with formol-saline with 8mM Gd-DTPA. After this, mice were decapitated and skin, muscle, lower jaw, tongue, nasal bones and zygomatic arches removed, with the remaining intact skulls post-fixed in 4% buffered formol-saline (with 8mM Gd-DTPA) at 4°C.

6.3.2 Imaging:

All imaging was performed on a Varian 9.4T DirectDrive VNMRS system (Varian Inc., Palo Alto CA, USA) with a 26mm quadrature birdcage coil (RAPID Biomedical GmbH, Würzburg, Germany). Samples were removed from fixative and excess solution carefully blotted with a paper towel. They were then immersed in Fomblin perfluoropolyether (type PFS-1, Solvay Solexis S.p.A., Bollate, Italy) in 20ml plastic syringes and immobilised with surgical gauze. Samples were allowed to equilibrate for at least 2 hours at room temperature prior to imaging. Air bubbles in samples were minimised by the equilibration time and gentle agitation of the syringe.

6.3.2.1 Ex-situ Study

T_1, T_2* and 3D gradient-echo images of the 4 *ex-situ* brains were obtained after 7 days fixation. 1 immersion fixed and 1 perfusion-fixed brain were then reimaged after 2 weeks fixation and further T_1, T_2* and 3D gradient-echo images obtained. Parameters: Single sagittal slice (0.5mm thick), matrix=128x64, FOV=18x9mm, NSA=4, TR was at least 5xT_1. *T_1:* Inversion-recovery spin echo, 17 TIs (range 6-400ms), TE=10ms; *T_2*:* Gradient echo, FA=90°, 11 TEs (2.9-14ms). 3D RF-spoiled gradient-echo imaging: FOV=18x18x9mm, TR=20ms, FA=60°, NSA=6, matrix=256x256x128, TE=9 or matrix=450x450x225, TE=6ms.

6.3.2.2 In-situ Study

4 Wild-type Tc1 skulls were fixed and imaged over a 5 week period. T_1 and T_2* maps were obtained at each time point. Parameters: Single sagittal slice (0.5mm thick), matrix=128x85 (reconstructed on the console to 128x128), FOV=19.5x13mm, NSA=4. TR was at least 5xT_1. *T_1:* Inversion-recovery spin echo, 13 TIs (range appropriate for estimated T_1), TE=10ms; *T_2*:* Gradient echo, FA=90°, 8 TEs (range appropriate for estimated T_2*). 40μm isotropic, structural 3D gradient-echo images at unoptimised parameters were also obtained (FOV=20.48x13.04x13.04mm, matrix size=512x326x326, TE/TR/FA=6ms/20ms/60°, NSA=2 or 6). Measured tissue parameter values were input into a Matlab program (The Mathworks Inc., Natick MA, USA) employing the theoretical equation for spoiled gradient echo signal (Eq. 6.1) to

determine the approximate optimal scan parameters for maximal cortex-corpus callosum contrast in a 3 hour scan-time, as described previously (Cleary et al., 2009).

(Eq. 6.1)
$$'SNR' \propto M_0 \frac{\sin a \cdot (1-e^{\frac{-TR}{T_1}})}{1-(\cos a \cdot e^{\frac{-TR}{T_1}})} \cdot e^{\frac{-TE}{T_2^*}} \cdot \sqrt{NSA}$$

The effect of echo time on brain contrast was also investigated experimentally by repeated imaging of one brain at 5 weeks fixation with 5 different echo-times (3.8-7ms).

6.3.3 Delineation of Anatomy on MRI and Histological Correlation

4 additional perfusion-fixed *in-situ* brains were then imaged using our final protocol after 9 weeks fixation (males, ages 18-21 weeks) in 4% buffered formol-saline (with 8mM Gd-DTPA), using an RF-spoiled gradient-echo sequence. Optimised 3D GE scan parameters: FOV=20.48x13.04x13.04mm, matrix size=512x326x326, TE/TR/FA/NSA=4ms/17ms/52°/6.

One brain was carefully extracted from the skull, dehydrated using graded alcohols and xylene, embedded in paraffin, cut into 3-μm sagittal sections and processed for haematoxylin-eosin (H&E) and Luxol Nissl staining. Antibodies or antisera against the following antigens were used: GFAP (DAKO Z0334), MAP-2 (Chemicon MAB3418), Neurofilament 200 (Sigma N5389); Myelin basic protein (SMI94). All immunostaining was carried out using the automated Ventana Benchmark or Discovery (Ventana Medical Systems) automated staining apparatus following the manufacturer's guidelines, using biotinylated secondary antibodies and a horseradish peroxidase-conjugated streptavidin complex and diaminobenzidine as a chromogen. Slides were photographed with a SIS Megaview 3.2 megapixel digital camera mounted on a ZEISS Axioskop.

6.3.4 Image Processing

T_1 and T_2* maps were created by a pixel-by-pixel, least-squares fit of the resulting data using in-house C-programs. The inverse of these were also calculated, using ImageJ (National Institutes of Health, Bethesda MD, USA), producing corresponding maps of R_1 and R_2*. Statistical analysis of map values was performed in Prism v5.00 (GraphPad Software, San Diego CA, USA). 3D volume images were reconstructed and converted to Analyze format using custom Matlab code and reviewed in ImageJ. SNR and CNR was measured in a number of brain regions by taking the ratio of average and signal differences in whole-structure volumes and the standard deviation in a region of background noise (Eq. 6.2):

$$\textbf{(Eq. 6.2)} \qquad SNR = \frac{Signal}{Noise\ SD} \qquad CNR = \frac{Signal_1 - Signal_2}{Noise\ SD}$$

Visualisation of brain structures was performed in Amira software (v5.2.2, Visage Imaging Inc., Andover MA, USA).

6.4 Results

6.4.1 *Ex-situ* Study: Comparison of Immersion and Perfusion-fixed Brains at Two Fixation Durations.

After 7 days immersion in contrast-fixative, there was no significant difference in T_1 and T_2* values between the immersion and perfusion-fixed brains ($p>0.40$ in all comparisons) (Table 6.1).

	Perfusion Fixation (n=2)				**Immersion Fixation (n=2)**		
Region of Interest	Cortex	Cerebellum	Whole-brain		Cortex	Cerebellum	Whole-brain
T_1 (ms)	32.2±0.4	31.8±0	33.2±0.2		33.1±1.3	28.2±6.2	34.2±1.3
T_2* (ms)	4.4±0.6	5.1±0.8	3.7±<0.1		4.4±0.2	5.2±0.2	3.8±0.3

Table 6.1: *Table showing T_1 and T_2* values in brains after 7 days immersion only or with initial perfusion-fixation (mean values ± SD).*

T_1 and T_2* measurements were repeated at 2 weeks (Figure 6.1). A similar change was observed in whole-brain T_1 (perfusion: 33.2 to 31.4 and immersion: 35.1 to 31.7) and T_2* (perfusion: 3.7 to 3.5 and immersion: 3.5 to 3.2) between 7 days and 2 weeks (Figure 6.1).

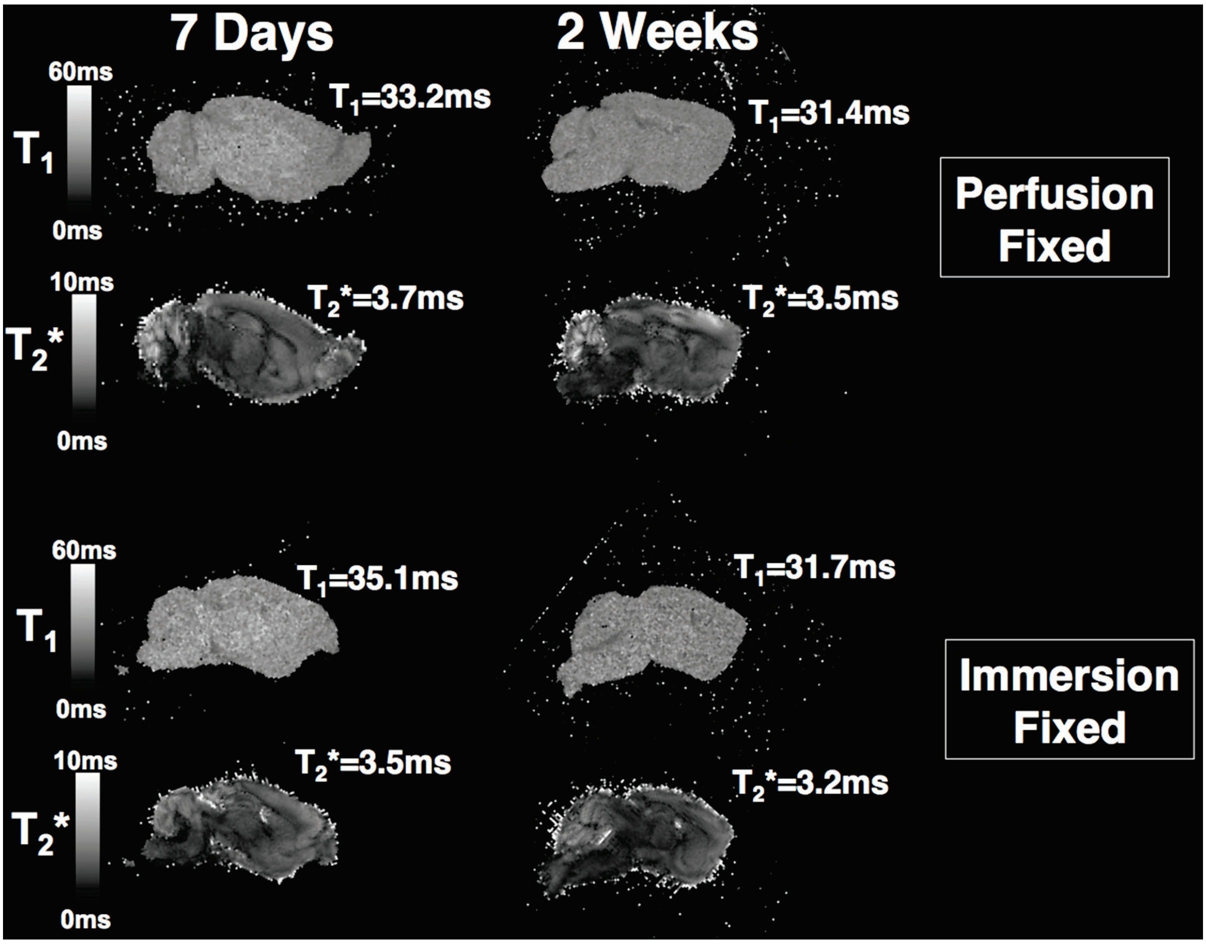

Figure 6.1: *T_1 and T_2* maps showing similar sagittal slices and mean, whole-brain T_1 and T_2* values through representative immersion and perfusion-fixed brains after 7 days and 2 weeks.*

It was noted that the immersion-fixed brains had sustained some additional cortical damage during the extraction process when compared to the perfusion-fixed brain (Figure 6.2). Furthermore, cortical vessels, although present in both immersion and fixed brains, were more apparent in the perfusion-fixed brains, otherwise the brains from the two methods appeared similar. This comparison indicates that the use of simpler immersion-fixation method, where the brain is removed directly from the skull without perfusion-fixation, would facilitate magnetic resonance microscopy techniques, if damage from extraction is not a confounder.

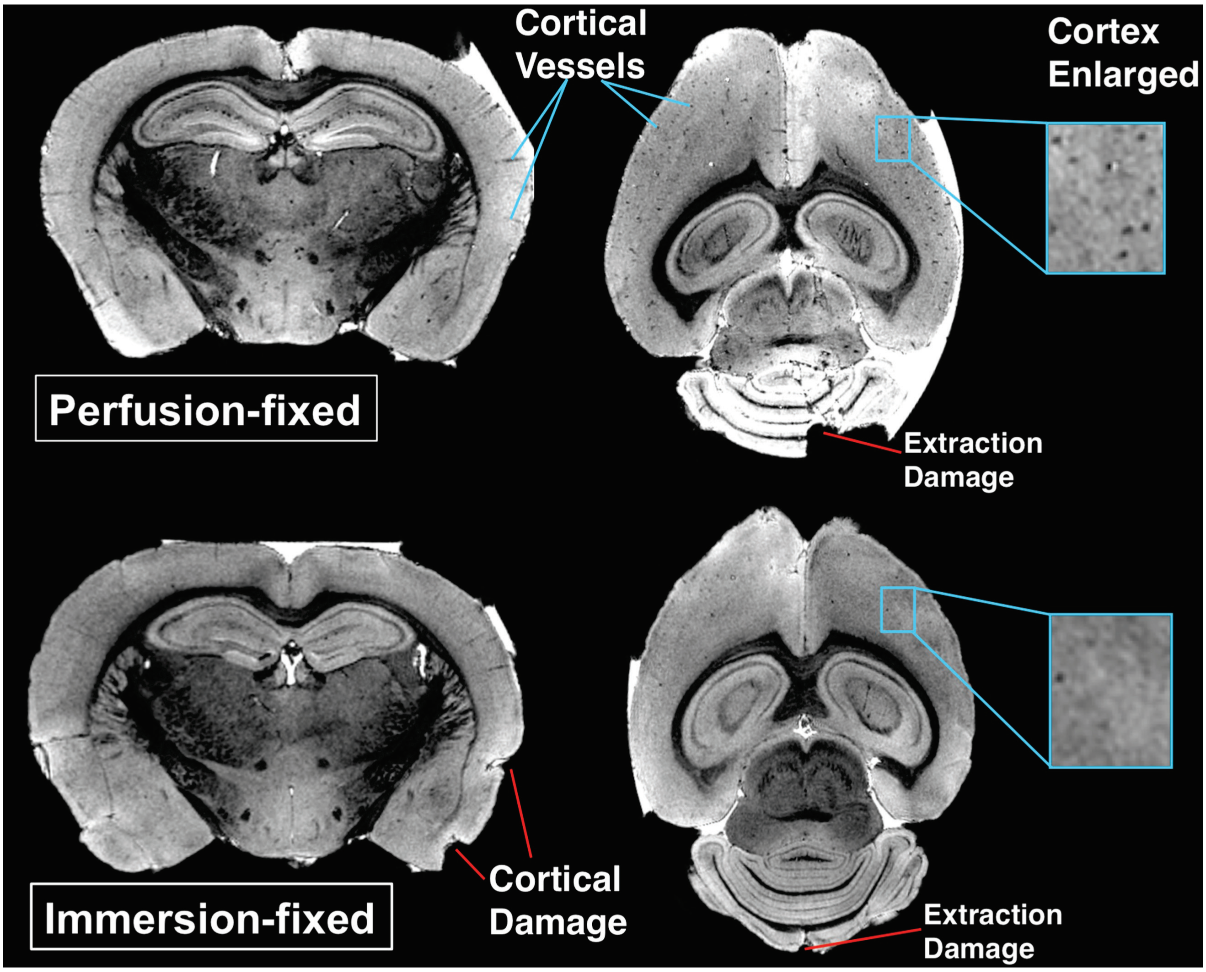

Figure 6.2: *Representative slices through 3D volumes of brains imaged after 2 weeks fixation (40µm isotropic resolution).*

6.4.2 *In-situ* Study

Given that varying degrees of cerebellar and cortical damage was apparent in all brains imaged, the feasibility of contrast-enhanced imaging with the brain *in-situ* was explored. Initially it was investigated whether the addition of 8mM Gd-DTPA in the initial perfusate would improve the rate of T_1 reduction over perfusion fixation and immersion fixation alone. After measurement of T_1 and T_2* values in each group after 1 week fixation, it was apparent that there was no significant difference ($p>0.65$) in T_1 data: therefore all brains were pooled in subsequent analysis. MR parameters were measured over 1, 2, 3, and 5 weeks. Table 6.2 demonstrates that T_2* values were found to reach a minimum at 3 weeks immersion (mean thalamus-midbrain=2.9ms, cortex=3.8ms). In contrast, T_1 values continued to reduce after 3 weeks, approaching uniformity across the brain by the 5 week timepoint (mean thalamus-midbrain region=48±3 ms, cortex=43±2ms, Table 6.2). Figure 6.3 illustrates the corresponding regional R_1 changes occurring over 5 weeks. It was observed that a greater immersion time lead to a lower T_1 (e.g. whole-brain T_1: 1 week 109±53 vs. 5 weeks 44±2ms, $p<0.05$, Table 6.2) and also reduced the magnitude of T_1 difference between cortical and midbrain-thalamus structures deep in the centre of the brain (e.g. mean difference at 1 week=15ms vs. 5 weeks=5ms, Table 6.2).

(n=4)	**T_1 (ms)**			**T_2* (ms)**	
Region of Interest	**Thalamus-Midbrain**	**Cortex**		**Thalamus-Midbrain**	**Cortex**
Immersion Duration					
1 week	113±32	99±23		6.1±1.5	6.3±1.1
2 weeks	67±5	55±4		3.4±0.2	4.3±0.3
3 weeks	61±7	49±3		2.9±0.2	3.6±0.3
5 weeks	48±2	42±2		3.2±0.2	4.0±0.1

Table 6.2: *Table showing T_1 and T_2* values within cortical and central thalamus-midbrain regions of interest over 5 weeks fixation.*

An increase in the conspicuity of white matter structures (such as fibres of the internal capsule) was observed on 3D images with increasing immersion time (Figure 6.3).

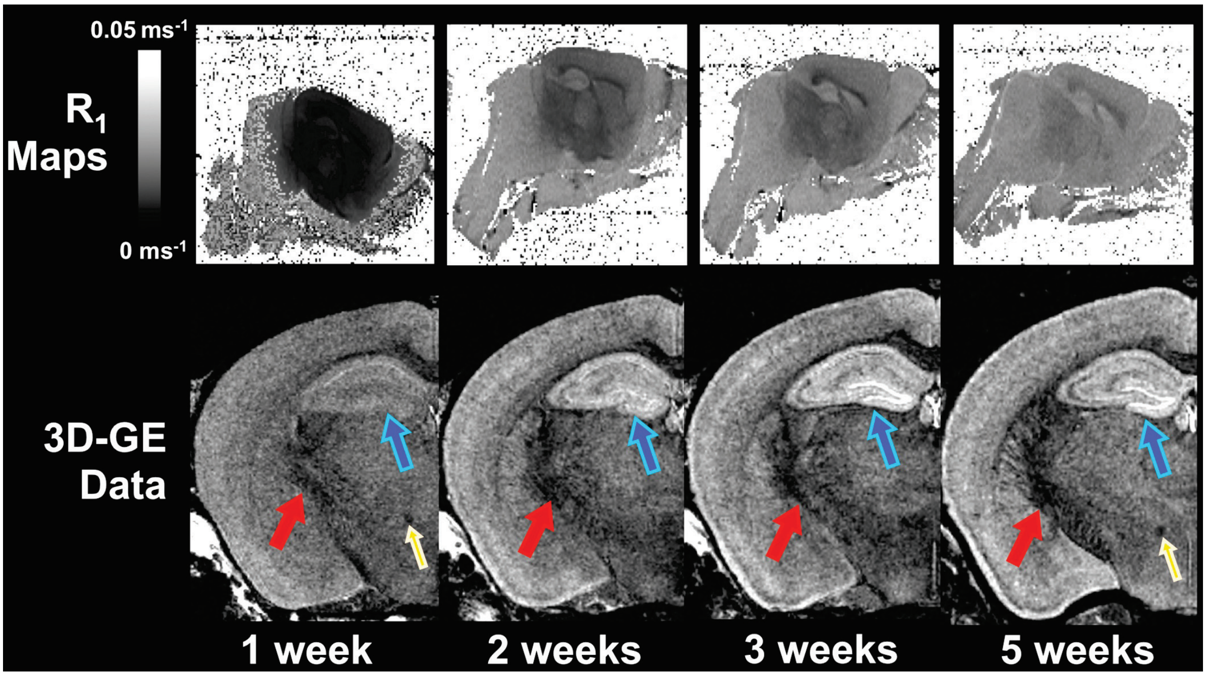

Figure 6.3: *Comparison of representative R_1 maps and similar volume slices from the same in-situ brain over 5 weeks fixation. As seen in R_1 maps (top) a greater amount of time is required for values in the centre of the brain to equilibrate with more cortical regions. Although a modest SNR enhancement may be seen in 3D gradient-echo images after successive weeks (bottom), there is a noticeable improvement in the quality of structural delineation, particularly in the hippocampus (blue-arrows) and white matter structures (e.g. internal capsule, red arrows; mammilothalamic tract, yellow arrows). (Images identically scaled)*

6.4.3 Scan Parameter Optimisation

From calculations using mean T_1 across the whole-brain at 5 weeks immersion, it was determined that parameters of TR=17ms, NSA=6, at the whole-brain Ernst angle (47°) would produce the highest SNR (assuming constant noise), in a 3 hour scan time. From the T_2* data at 1 week the ratio of M_0 in the corpus callosum relative to cortex in the 4 brains was estimated to be 0.96±0.01. Using these estimates and T_2* values from maps at 5 weeks, it was calculated that a TE of approximately ~3.4ms would give optimal cortex/corpus callosum contrast. To ascertain the optimal TE at 5 weeks experimentally, repeated high-resolution scans of a single brain from our dataset were performed, with the calculated TR, NSA and flip angle above. Figure 6.4 shows the effect of varying TE from 3.8ms (the minimum permitted by the system at 100kHz bandwidth) to 7ms. Although SNR in all structures was highest at TE=3.8ms (whole-brain SNR=31.5), cortex-corpus callosum CNR appeared to be maximal at TE=4ms (CNR=7.5, whole-brain SNR=30.3). Interestingly white-grey matter CNR in the cerebellum peaked slightly later at a TE=5ms (CNR=22.4).

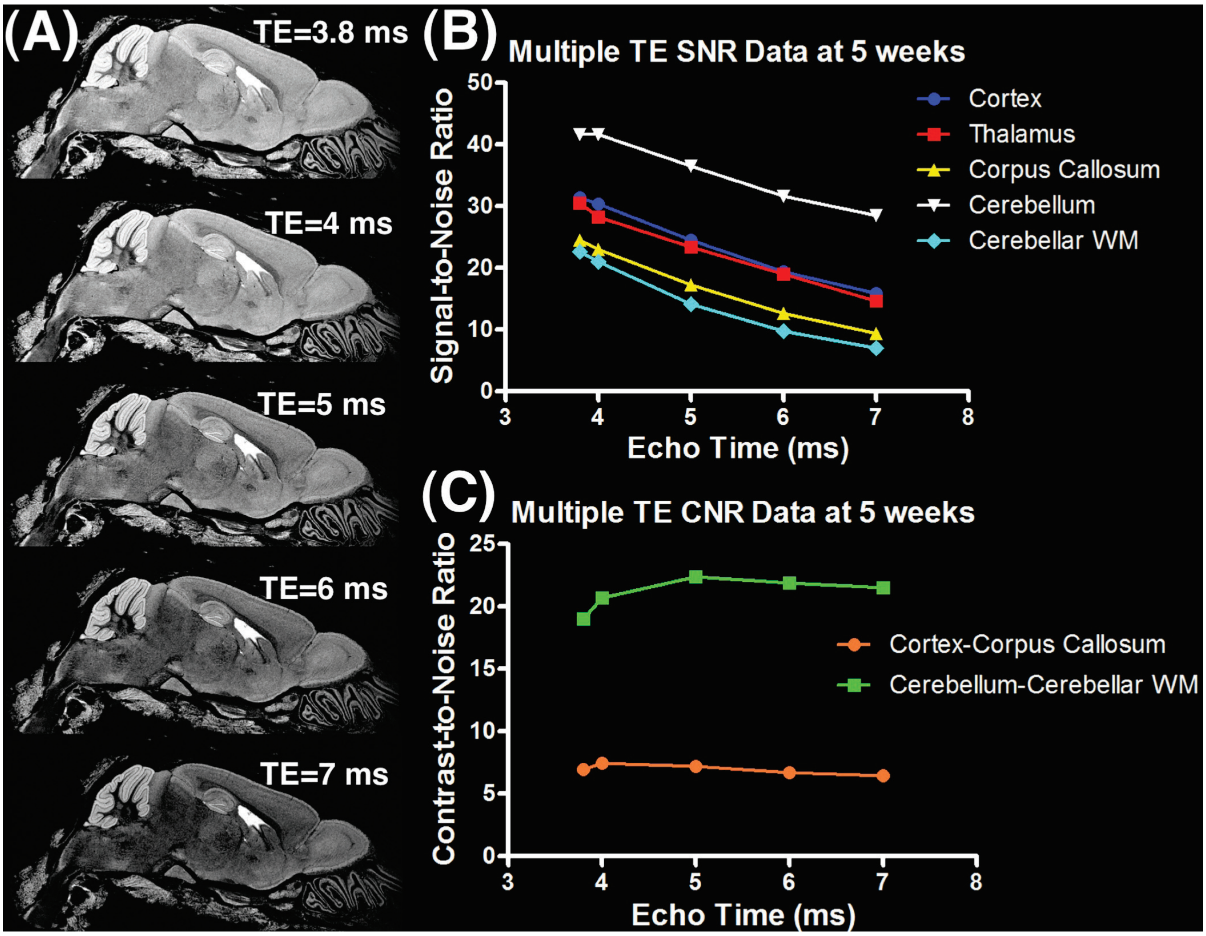

Figure 6.4: *Representative sagittal slice (A) and measured SNR (B) and CNR (C) from 3D volume data of a brain imaged after 5 weeks fixation at five different echo times.*

As indicated in Figure 6.5, it was noted that increasing echo time appeared to enhance the delineation of more subtle structures, such as cortical layers and the layer of Purkinje cells in the cerebellum, indicating a T_2* dependency to this contrast. Opting for a balance of high SNR and high grey-white matter CNR, final parameters of TE=4ms, FA=47° (the Ernst Angle), TR=17ms and NSA=6 averages were chosen for future studies.

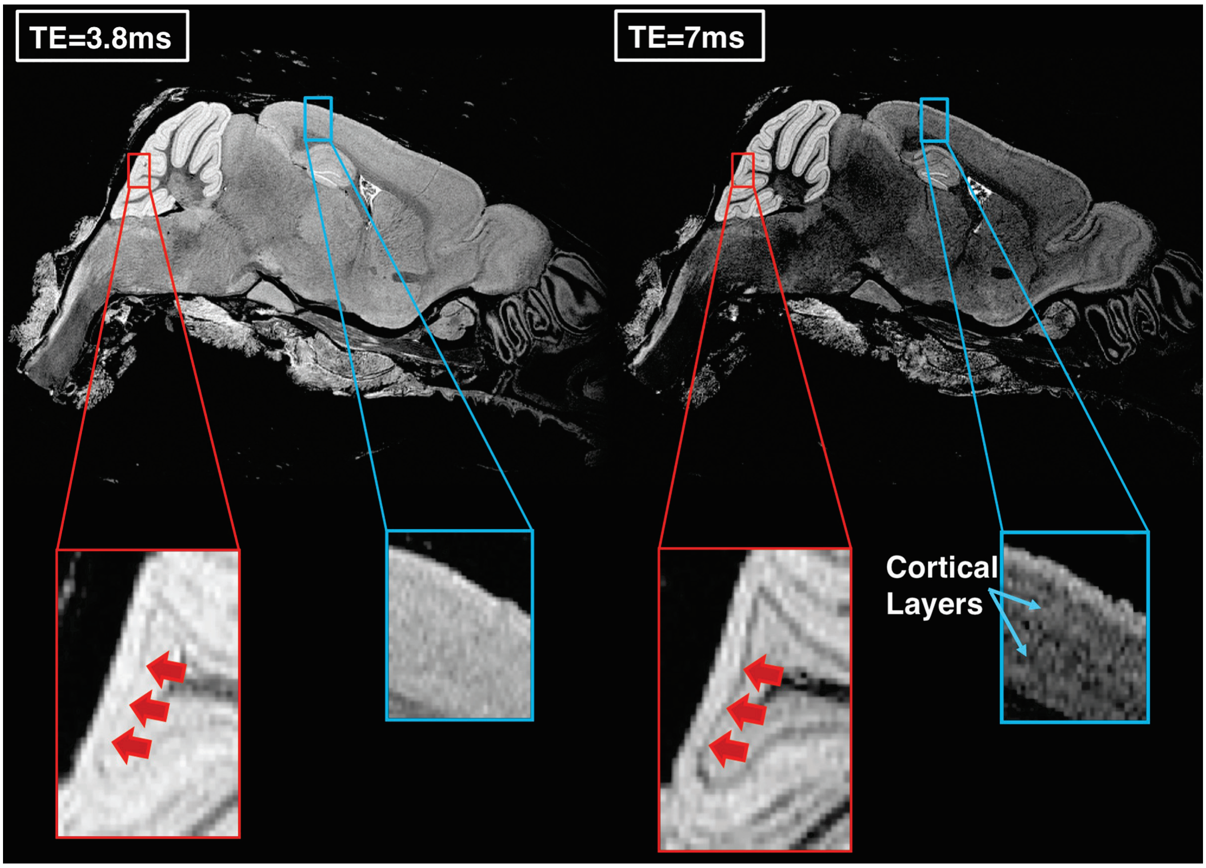

Figure 6.5: *Enlarged sections of cerebellar lobe and cortex showing their appearance at TE=3.8 and 7 ms. Red arrows appear to correlate to the Purkinje layer of the cerebellum and appear to become more defined at a longer TE, as does the visibility of cortical layers. (Images identically scaled)*

6.4.4 Brain MR Parameters at 9 weeks

After identifying the need for a long immersion duration to enable full penetration of contrast agent, the above optimised parameters (FA=52°, appropriate for these T_1s) were applied to a further 4 *in-situ* brains after 9 weeks immersion, acquiring T_1 and T_2* maps and high-resolution 3D volumes. Compared to 5 week data, while R_2* values remained similar in both cortical and thalamus-midbrain regions to our previous brains (Figure 6.6B), R_1 showed a more marked increase (Figure 6.6A), with the corresponding whole-brain T_1 measured as 35±2ms compared to 44±2ms of previous brains at 5 weeks. As seen in a corresponding R_1 map of a sagittal slice through an example brain (bottom right, Figure 6.6), values have a narrow distribution across the brain (SD of T_1 values over whole-brain ROI=3.8±0.1ms, n=4) indicating that 9 weeks immersion may be more suitable. Whole-brain SNR was comparable to previous 5 week data and measured to be ~30.

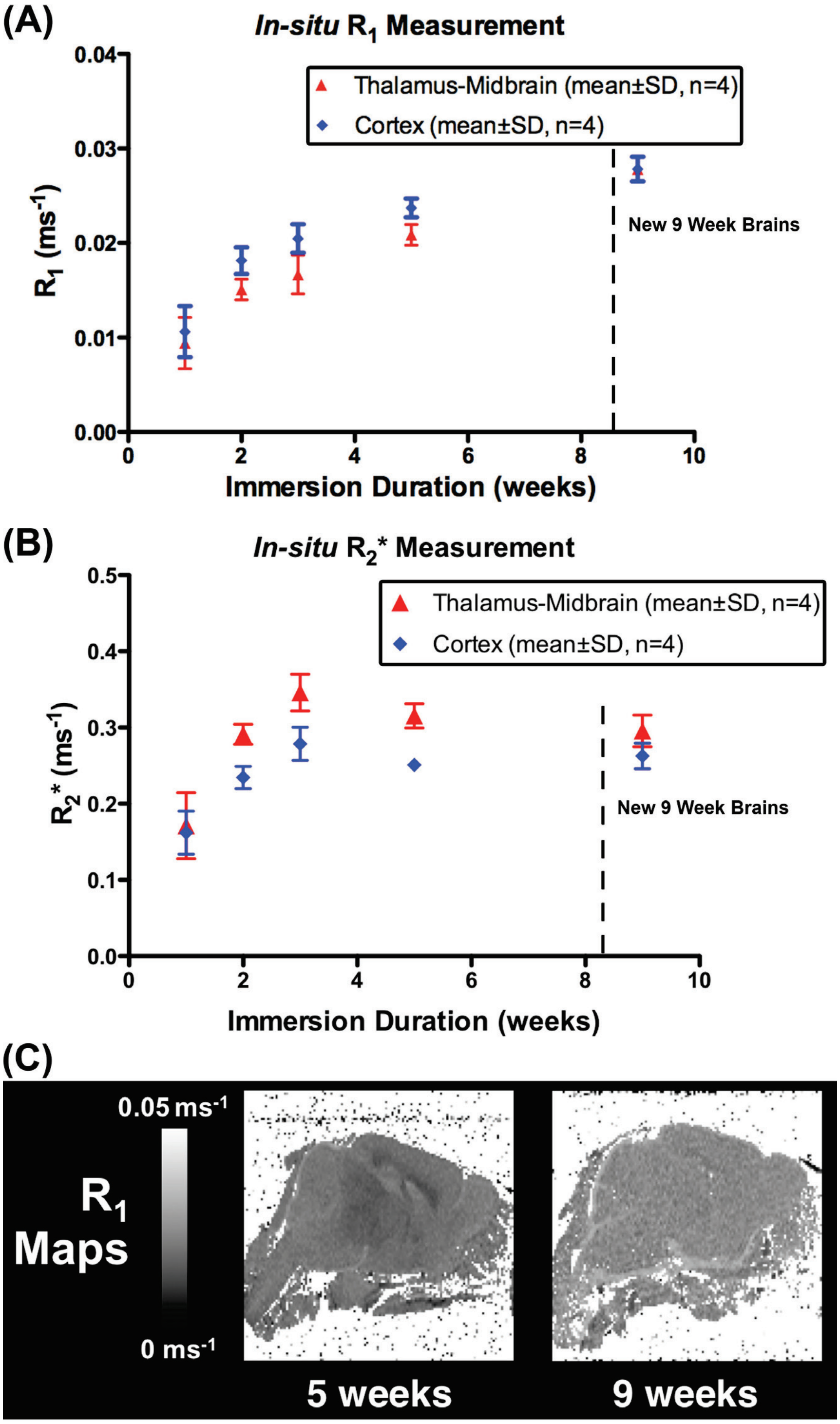

Figure 6.6: *Graph showing the timecourse of R_1 (A) and R_2* change (B) with immersion time in fixative+Gd-DTPA solution, incorporating values from the previous 5 week study and 9 week brains indicating a minima has been reached. Representative R_1 maps from 5 and 9 week brains shown for illustration (C).*

6.4.5 Structural Correlates of Active-Staining in the Brain

The resulting gradient echo images acquired at the selected parameters (TE/TR/FA/NSA=4ms/17ms/52° Ernst angle/6 averages), after 9 weeks in contrast-fixative, demonstrated excellent contrast, enabling the delineation of a number of structures in the cortex, hippocampus, olfactory bulb and cerebellum (Figure 6.7, sagittal image). In the hippocampus, individual layers were clearly visible such as a bright granular cell layer of the dentate gyrus, as well as bright region of the stratum lucidum and dark layer in the region of CA3 (Figure 6.7, coronal view A, blue panel). Individual nuclei were also visible, including medial and lateral habenular nuclei and a number of thalamic nuclei (Figure 6.7, coronal view A, green panel). White-matter tracts were easily visualised, appearing with strong negative contrast on gradient-echo images (Figure 6.7, coronal view B).

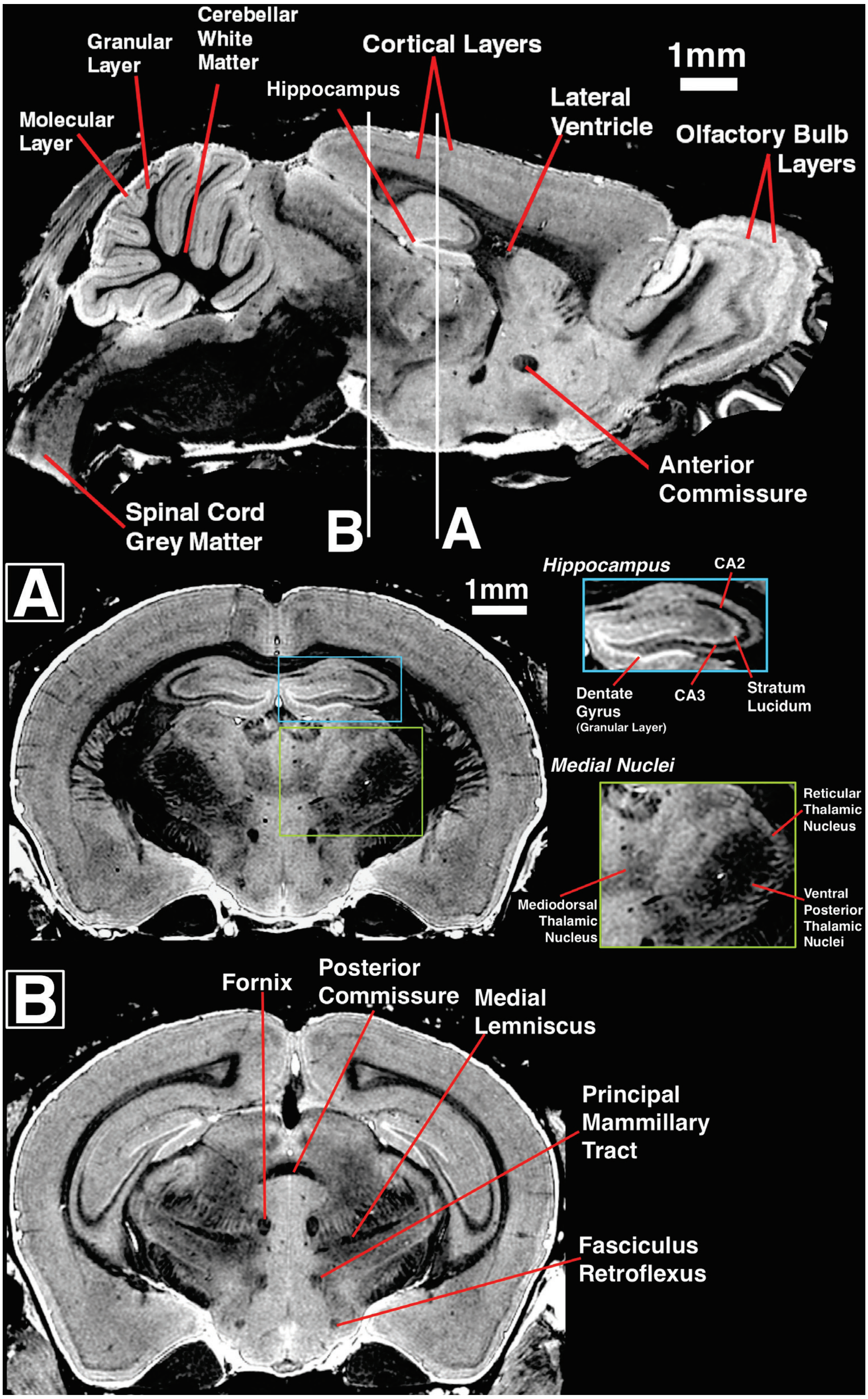

Figure 6.7: *Sagittal and corresponding coronal views through a brain fixed for 9 weeks and imaged at optimised parameters. Sagittal view (top) shows the principal anatomical structures seen. Coronal view (A) shows hippocampal anatomy visible (blue panel) and visible nuclei (green panel). Coronal view (B) shows visible white-matter tracts.*

Sagittal MR images were compared to histology where a good correlation was observed between a number of white matter structures defined on a neurofilament stained section and equivalent dark areas on a similar MR image (Figure 6.8A). Structures such as the anterior commissure, superior colliculus commissure and fasciculus retroflexus were easily visualised.

In the cerebellum, (Figure 6.8B) structures on MR correlated well to those seen on histology, such as the bright outer molecular layer, consisting of mostly Purkinje cell dendrites (seen on calbindin section, Figure 6.8B), a bright granular cell layer and dark Purkinje cell layer (evenly-spaced, large Purkinje cells visible in all sections, Figure 6.8B) and axonal fibre tracts (Figure 6.8B, neurofilament section). While MR signal intensity was high in both molecular and granular layers, the granular layer appeared to be slightly hypointense.

In the olfactory bulb (Figure 6.8C) the main features of mitral, glomerular and external plexiform layers were easily identified in MR images, with these regions correlating well to all stains. Sublayers in the granular cell layer, seen on H&E and calbindin sections (Figure 6.8C), were not readily apparent on MR with images best correlating to the more uniform appearance of the granular cell layer observed in the neurofilament section.

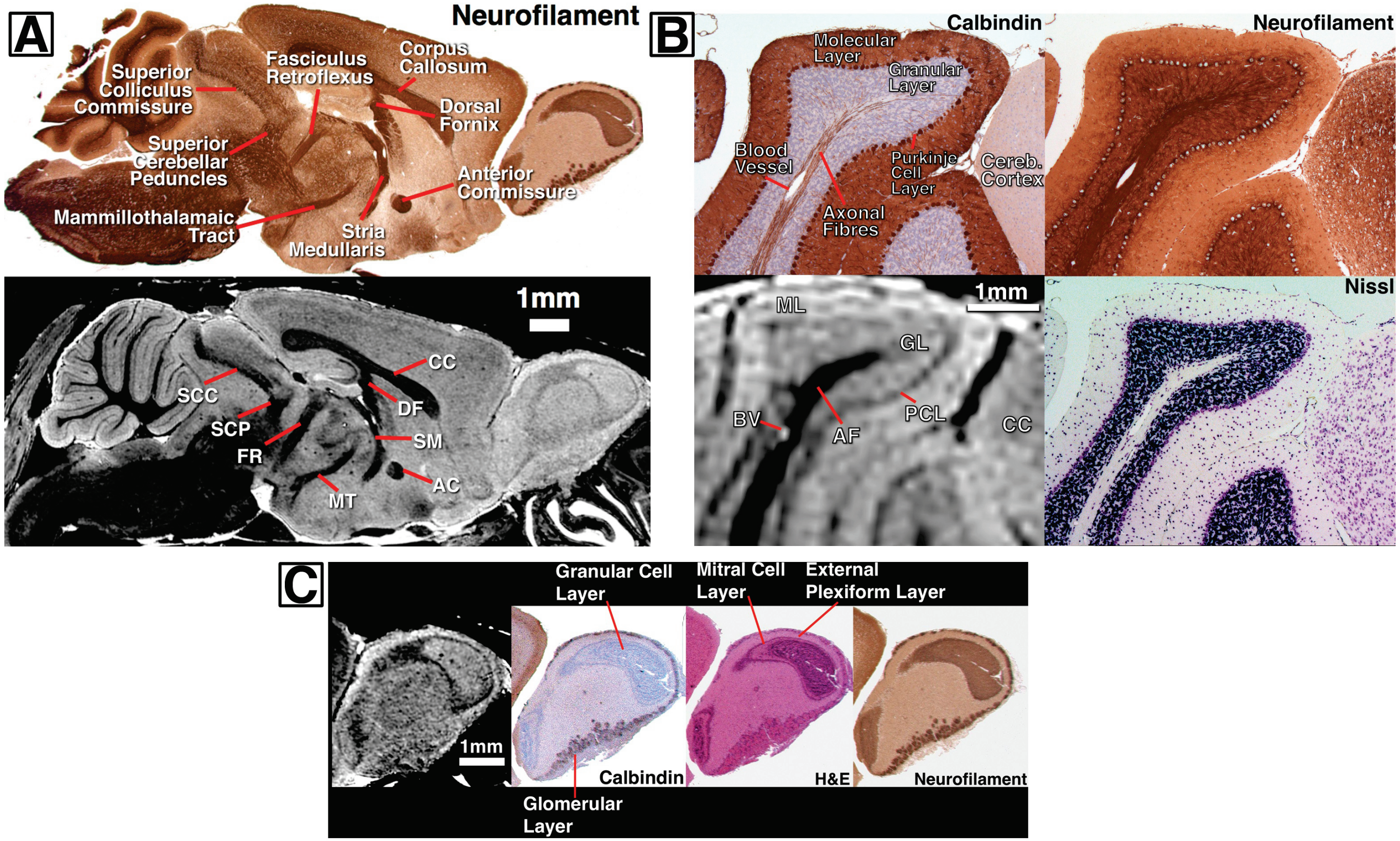

Figure 6.8: *(A) Representative sagittal sections through MRI and a similar neurofilament histology section in the same brain, showing visible white-matter anatomy. (B) Detail through the cerebellum showing the correspondence of structures between histology and MRI such as the granular, molecular and Purkinje layers and axonal fibre tracts. (C) Detail through the olfactory bulb showing layers identified on similar histology sections from the same brain.*

As hippocampal anatomy was especially well defined on MRI, identification of the source of the regional MR contrast was sought by histological comparison. In addition to standard histological stains, the data was also compared to a standard Timm stained section – an established method of visualising the presence of intracellular Zn^{2+} that characterises hippocampal mossy fibres (Haug et al., 1971). Figure 6.9A shows a comparison of hippocampal structures with a similar axial Timm section from a C57BL/6 mouse (Crusio et al., 1986). A conspicuous area of hypointensity in the stratum pyramidale region of CA3 (orange arrows, Figure 6.9A and B) was observed, which correlated with unmyelinated mossy fibres synapsing with pyramidal cells (Figure 6.9A(iv) and 9B, Timm and calbindin sections respectively). Previously, it was observed that hypointensity was associated with myelinated white matter structures (Figure 6.8A), which is not the case in the stratum pyramidale. An area of myelinated fibres in the dentate gyrus molecular layer (Figure 6.9B, blue arrows) did not result in a hypointensity on MRI. Closely associated and lateral to the stratum pyramidale (concave aspect; red arrows) are the suprapyramidal mossy fibres (running in the stratum lucidum) a region of unmyelinated axonal fibres (Figure 6.9A and B, Timm and calbindin sections) that appeared as an area of hyperintensity within CA3. The granular layer of the dentate gyrus (green arrows, Figure 6.9A) was clearly visible as a region of hyperintensity that correlated to a dense area of closely packed cell bodies (Figure 6.9B, H&E and calbindin sections).

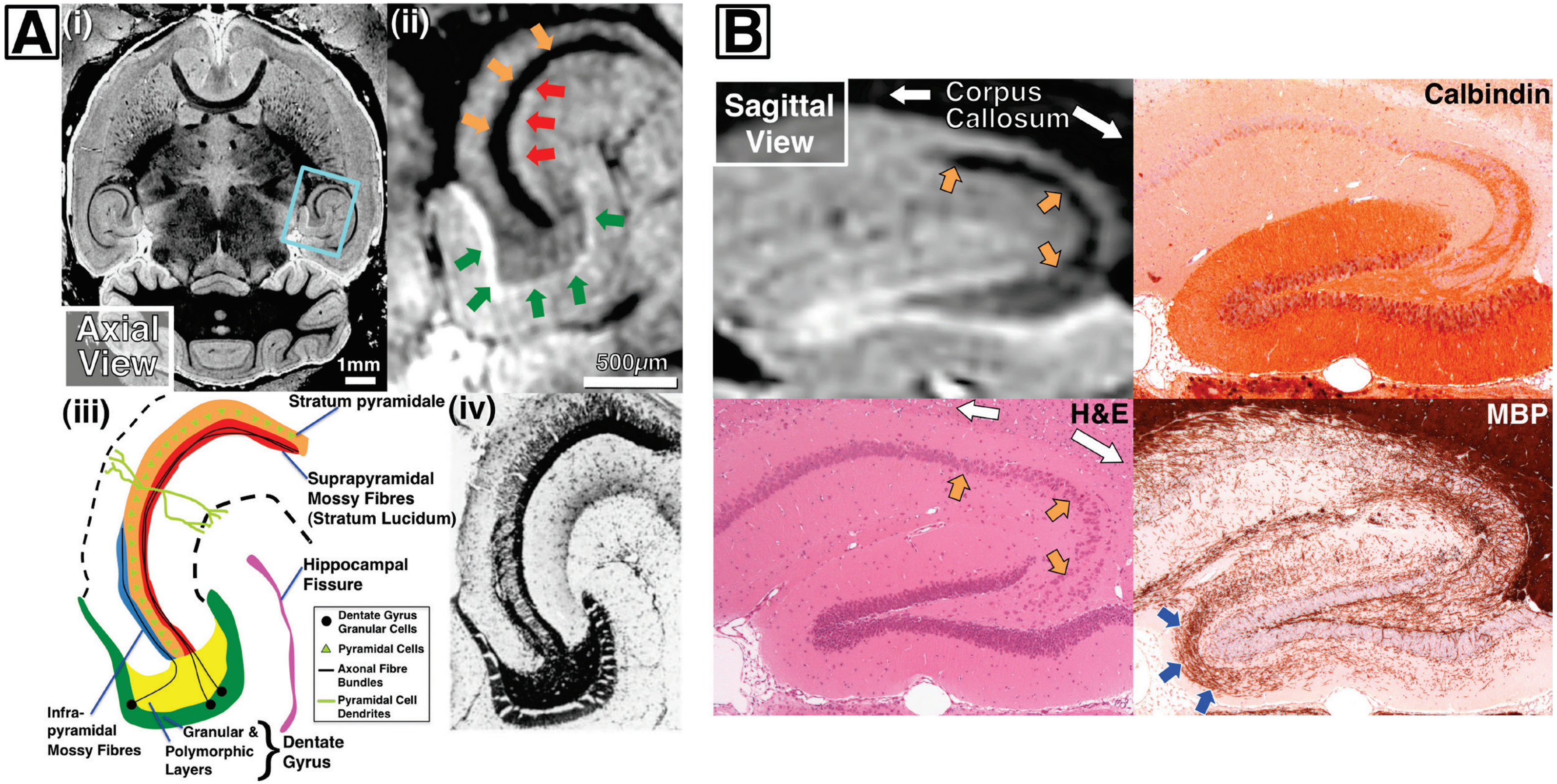

Figure 6.9: *(A) Hippocampal view (ii) from an axial MRI slice (i) compared with a representative section from a C57BL/6 mouse hippocampus stained with Timm silver sulphide stain (iv), showing regions of high ionic zinc concentration, a feature of hippocampal mossy fibres. Red arrows indicate correspondence with mossy-fibre bundles, orange with pyramidal cells, green with the granular layer of the dentate gyrus. (Timm section adapted from (Crusio et al., 1986)) (B) Sagittal view of hippocampal anatomy from a brain fixed for 9 weeks compared with H&E, calbindin and myelin basic protein (MBP) stained sections. Dark regions on MR (orange arrows) appear to correlate with heterogeneous regions containing mossy fibres and pyramidal cells. Corpus callosum (white arrows) indicated for comparison. Blue arrows in the MBP section indicate a diffuse region of myelinated fibres in the molecular layer of the dentate gyrus.*

6.5 Discussion

After an initial study of *ex-situ* brains which showed a high degree of extraction damage, subsequent investigation demonstrated that *in-situ* brains prepared in a solution of 8mM Gd-DTPA and imaged with gradient-echo sequence produced high-resolution (40µm isotropic), high SNR images, with a 3-hour scan time. Additionally, structures delineated on MR were shown to directly correlate to those defined on histology, such as major white matter tracts and layers of the olfactory bulb and hippocampus. This comparison has then enabled us to assess the effects of tissue microstructure on MR contrast of actively-stained tissue.

6.5.1 *Ex-situ* Brain Imaging

Ex-situ brain imaging with a gradient-echo sequence has been reported previously (Huang et al., 2009; Kim et al., 2009) and our ex-situ brains show T_1 and T_2* values are in line with those studies (T_1≈30ms, T_2≈7ms, 10mM Gd-DTPA, after 4 days immersion in contrast-fixative (Kim et al., 2009)) displaying similar image contrast. Additionally our study has shown that these values remain relatively unchanged even after extending the immersion time to two weeks (e.g. mean T_1 perfusion-fixed went from 33 to 31ms) to leave more time for Gd-DTPA penetration. It was demonstrated that brains need not be perfusion-fixed and that simple immersion-fixation produced equivalent image quality, thus enabling magnetic resonance histology in laboratories where perfusion-fixation is not readily available. Imaging of extracted, *ex-situ* brain tissue does have some advantages, in that smaller RF coils can be used, improving SNR and a smaller field of view may improve imaging-time (Kim et al., 2009). However the tissue damage observed in our *ex-situ* brains may compromise their use for automated and quantitative morphometric analyses where accurate anatomical volumes and morphology are essential for sensitivity.

6.5.2 *In-situ* Brain Optimisation

Given the effect of damage in *ex-situ* imaging later parts of this study focussed on *in-situ* brain preparation and MR methods optimisation to produce detailed images of the mouse brain. It was demonstrated that full penetration of Gd-DTPA into brain tissue, as assessed by R_1 values in the cortex and basal ganglia, had equilibrated across the brain by 9 weeks. Indicating that a much greater immersion time is required than in the *ex-situ* brain in order to produce the maximal increase in SNR, and thus image quality, across the brain.

Currently there is no standard protocol for *in-situ* brain preparation and scan parameters, with a number of approaches in current use. A T_2-weighted 3D fast spin-echo sequence (FSE) with brains fixed in 2mM gadoteridol (a non-ionic macrocyclic Gd-chelate) for at least 7 days (Tyszka et al., 2006) is able to produce T_2-weighted images of multiple *in-situ* brains with a 32μm resolution in a 11.3 hour scan, and has been successfully used for morphometric phenotyping (Ellegood et al., 2010a) and atlasing (Dorr et al., 2008) studies. While this can offer good T_2-weighted images with an improved imaging time, the use of an FSE sequence can lead to image blurring and a loss of structural definition (Mulkern et al., 1990).

Partial-Fourier spin-echo has also been successfully used for *in-situ* phenotyping studies giving T_1-weighted images with 21.5μm resolution in a ~2 hour scan time (Badea et al., 2007b). Sharief and Johnson developed an innovative multi-echo T_2 sequence (Sharief and Johnson, 2006) where reconstructed images combine data from a number of echo times. This has the effect of improving contrast, especially in T_2-dependent structures such as in the cortex and brain nuclei. In both these imaging protocols, brains are initially perfusion-fixed with a high concentration (50mM – assuming a standard 0.5M clinical solution) of gadoteridol and fixed overnight 10% formalin prior to imaging.

Our results indicate that, in the *in-situ* brain, such short immersion periods may not be sufficient to give maximal T_1 reduction (and thus SNR gain) over the whole brain. If one assumes that a T_1 of ~31 ms (2-week *ex-situ* data) is a likely minima for values after Gd immersion, this level is nearly achieved after 9 weeks (whole-brain T_1 ~35ms). The need for such an increase in immersion time compared to *ex-situ* brains for Gd penetration is most likely due to the presence of intact meningeal layers and limited entry points for fixative into the skull (e.g. through the foramen magnum and orbits) resulting in a greatly reduced exposed brain tissue surface-area.

Although a virtue of gradient-echo imaging is a short TR and thus reduced acquisition time, this makes it sensitive to T_1 differences. The heterogeneity seen in R_1 maps, corresponding to higher T_1 values in more central structures compared to cortical and cerebellar regions, will thus limit T_1 recovery, causing signal reduction in these portions of the brain. As the majority of these regions, such as basal ganglia and midbrain contain white-matter fibres, there is likely to be an intrinsically lower signal due to the lower T_2 of myelinated structures (Counsell et al., 2003). Thus it is important to ensure there is adequate agent penetration to ensure full T_1 recovery in these regions. Although TR could be increased to compensate, in chapter 4 it was shown that increased signal averaging is generally preferable to small TR increases to boost SNR (Cleary et al., 2009) and is thus not ideal when imaging with a fixed scan time. The benefits of allowing a greater degree of T_1 reduction are readily seen in our gradient-echo images taken over 5 weeks (Figure 6.5), in which structures of the hippocampus and white matter tracts are more conspicuous by the last 5 week timepoint.

Although active-staining primarily acts to reduce tissue T_1 due to administration of contrast agent (Johnson et al., 2002b; Petiet et al., 2007) there is also a corresponding reduction in T_2 (Cleary et al., 2010; Petiet et al., 2007). This may also be exploited to produce image contrast using much shorter TEs than in normal tissue.

In our method, the use of a relatively high contrast agent concentration, leads to a large mean reduction and compression of the whole range of normal tissue T_2 values. For example, as T_2* is now ~3.8ms as measured in the cortex (*in-vivo* $T_2 \approx 45$ms at 9.4T (Uematsu et al., 2007)), our chosen echo-time of 4 ms results in T_2*-weighting in that region, allowing cortical layers to be visualised. Similarly, increased T_2*-weighting, improves visualisation of the Purkinje layer of the cerebellum. Thus an 8mM Gd-DTPA concentration with a gradient-echo sequence with a relatively short TE and TR combines the potential of a short scan time and a high number of signal averages and an optimal T_2* weighting to reveal tissue contrast.

The contrast observed in our gradient echo images may be explained by a combination of intrinsic tissue MR relaxation and effect of contrast agent concentration. For example, myelinated white matter is known to have a lower T_2 than grey matter, due to higher bound water content (Counsell et al., 2003), giving a characteristically darker signal on MR images *in-vivo*, which was also observed in the data. This is probably best explained by the contrast agent reducing T_2 values but still preserving T_2 differences between tissues, which can be exploited by the correct MR parameters. Yet it has also been suggested that distribution of agent itself may be enhancing contrast, particularly in non-myelinated structures (Huang et al., 2009). Although this is unlikely to account for our observed white matter contrast: using R_1 maps as an indication of contrast agent concentration, the lack of regional contrast in maps at 9 weeks does not suggest a selective regional distribution of contrast agent, where higher concentration of contrast agent would be expected to result in area of increased R_1.

Interestingly, negative contrast was also observed in classically unmyelinated regions of the hippocampus that did not appear to depend on the presence of even small traces of myelin (as seen in our MBP-stained section, Figure 6.9B, blue arrows). Previous work in the *ex-situ* mouse brain has suggested that ~23% of brain volume is inaccessible to the Gd-DTPA indicating the agent is not distributed uniformly at a cellular level (Huang et al., 2009). The present study reinforces this view, as the dark appearance of these unmyelinated regions are likely to be due to increased local Gd-DTPA distribution and MR susceptibility at a local level. Thus the choice of a gradient echo sequence is ideally suited to detection of such regions, especially those with subtle T_2* differences.

Both intrinsic contrast and susceptibility could explain the subtly different appearance of molecular and granular layers of the cerebellum on MR. Although the granular layer contains a great number of densely packed cells, as seen on the neurofilament stain, there are still a large number of axonal fibres passing through this region. This could result in the observed hypointensity either through intrinsic relaxation mechanisms where the presence of such myelinated tracts, with a lower T_2*, leads to a partial volume effect with a slight loss in signal, or the regional cytoarchitecture, comprising a mixture of cell bodies and axons, could affect local Gd-DTPA distribution, causing a susceptibility effect.

Similarly an enhancement of the layer of Purkinje cells was observed with increasing echo time. This layer also contains a mixture of large Purkinje cells surrounded by basket cell axons. However a large T_2* dependence on contrast in this region was observed, indicating that susceptibility effects through structural heterogeneity play a greater role, probably due to distribution of contrast agent.

In the olfactory bulb, the observed contrast delineated the mitral and glomerular but not granular layers. In previous *in-vivo* high-resolution T_2-weighted images (Boretius et al., 2009) all of these regions were observed including granular layers. It is conceivable that the more complex cytoarchitecture of both glomerular and mitral layers may explain this observation. Glomeruli are relatively large structures that consist of a number of nerve synapses, surrounded by glial cells (Kosaka et al., 1998); also mitral cells have axonal fibres that contribute to the olfactory tract (Shepherd et al., 2007). In contrast, granule cells possess only dendritic processes and are without axons (Price and Powell, 1970). This more complex structure may lead to greater susceptibility effects in the presence of contrast agent in these regions.

Comparisons with previous diffusion-weighted (Shepherd et al., 2006) and *in-vivo* work (Boretius et al., 2009) may offer some explanation for the enhanced contrast seen in the hippocampus. The area of the stratum lucidum has been seen as hyperintense on diffusion images in the rat (Shepherd et al., 2006) indicating a region of restricted diffusion that may affect the access of Gd-DTPA to the region and thus maintain a longer T_2* than surrounding tissue. Similarly, the dense packing of granular cells in the dentate gyrus may prevent infiltration of contrast into the region and also maintain a long T_2* resulting in its bright appearance.

Previous work (Benveniste et al., 2000) has shown contrast enhancement in the hippocampus on subsequent *ex-vivo* images monitored over a period of 2 to 50 hours after initial *in-vivo* perfusion-fixation with Gd-DTPA. Images acquired at 2 hours post fixation showed a general increase in signal over the whole hippocampus, but the granular layer of the dentate gyrus appeared particularly hyperintense. The stratum pyramidale was visible as a dark band. Over subsequent timepoints, while signal enhancement over the whole hippocampus appeared to be maintained, the conspicuity of both granular layer and stratum pyramidale was greatly reduced. This evolution of contrast was attributed to the vascular nature of this region, with intravascular retention and extravasation of contrast agent leading to the appearance of reduced and increased signal respectively. The initial enhancement seen in the granular layer may indicate that the hippocampus is compartmentalised, possessing regions accessible to contrast agent to a greater or lesser degree. High-resolution *in-vivo* imaging, without contrast, has also demonstrated delineation of hippocampal structures in T_2-weighted images, including the stratum pyramidale, and granular and polymorphic layers of the dentate gyrus (Boretius et al., 2009). In images with strong weighting (TE=82ms), contrast in these regions was markedly different to that of ours as both dentate gyrus and stratum pyramidale appeared hypointense, with the stratum pyramidale visible as a continuous line from CA3 to CA1. Also the granular layer of the dentate gyrus was not easily distinguished from the polymorphic layer. These findings suggest that in certain structures local accumulation of contrast agent can contribute to MR appearance more than intrinsic tissue T_2* contrast. This suggests the exciting possibility that targeting such regions could provide the basis for the investigation of novel MR microscopy stains.

While the presence of contrast agent is likely to contribute most to changes in tissue parameters, an additional consideration is tissue fixation. Aldehyde fixatives cause the cross-linking of proteins (Fraenkel-Conrat and Olcott, 1948), reducing water mobility, resulting in a reduction of tissue MR relaxation times (Dawe et al., 2009). A study in the rat cortical slice model (Shepherd et al., 2009) found T_1 reduced 21% after >10 days fixation, although an 81% T_2 reduction could be reversed after washing out the fixative by immersion in PBS. Timecourse studies in fixed human brain have also shown a progressive decreases in T_1 and T_2, with T_1 change occurring fastest over the initial 1-2 weeks and a slower decline after 5 weeks (Tovi and Ericsson, 1992). Grey and white matter T_1 (Pfefferbaum et al., 2004) and T_2 values (Blamire et al., 1999) also tend to converge with a longer fixation time. There are, however, few studies in the literature assessing the effect of fixation on the use of Gd-chelates. Work in *Xenopus* oocytes (Purea and Webb, 2006) indicates that fixation may alter cell membrane structure, enabling the entry of contrast into the cytoplasm. However, further experiments are needed to examine the role of fixation on contrast in active-stained μMRI of the mouse brain.

The time needed for the penetration of agent in our methodology may be a disadvantage, as histological techniques, especially in light of developments in automatic sectioning systems, can provide more detailed information in a similar amount of time. However, MRI does offer the benefits of non-destructive 3D image acquisition.

6.6 Conclusion

The findings of this chapter show that active-stained μMRI can provide detailed anatomical images of the *in-situ* mouse brain with high resolution and signal-to-noise. Additionally, a variety of stains were used to identify and compare the MRI appearance of brain structures to those defined by histology. Combining this data has highlighted possible mechanisms for the enhanced contrast in these regions, surmising that contrast depends on both preserved, intrinsic T_2* differences as well as regions delineated by distribution of active-stain due to tissue microstructure. This methodology could enable greater sensitivity for the phenotypic characterisation in mutant mouse models and enhance regions of the mouse brain that may be targeted in future transgenic studies.

Chapter 7:

Contrast-enhanced μMRI for High-throughput Phenotyping, as Applied to the Tc1 Model of Down Syndrome

7.1 Chapter Outline

The preceding chapter demonstrated an optimised preparation and scanning protocol for the adult mouse brain. This chapter goes further in applying this protocol to enable a tensor-based morphometry analysis of the Tc1 model of Down syndrome, identifying novel phenotypes.

This work was produced in collaboration with Benjamin Sinclair (CABI/CMIC UCL), who developed and validated the software tools used for the high-throughput TBM analysis of this data. Also Dr. Frances Wiseman (UCL Institute of Neurology) who culled and provided the animals used.

7.2 Introduction

Neurological disease models are a major application of gene-targeted and transgenic mouse technologies. In recent years, there has been a dramatic increase in the production of novel mutant mice in order to develop new and improved models of human conditions.

A particular application of transgenic methods has been to the human condition Down syndrome (DS). In human patients, this condition results in a non-disjunction germline transmission of all or part of an additional copy of chromosome 21 (Hsa21), giving a theoretical 50% increase in gene dosage. The condition is the most common chromosomal disorder of newborns, with a typical incidence of 1 in 700 live births.

The condition affects a number of organ systems but congenital heart defects, neurological and craniofacial malformations are the most common. The structural consequences of brain anatomy in DS typically include an overall smaller brain-volume and reduced cerebellar size (Beacher et al., 2010). In older subjects ventricular enlargement may be common as part of the early-onset dementia associated with DS.

Although there are instances of transmission of part of Hsa21, 95% of DS affected individuals carry a complete copy of chromosome 21. Although the smallest of human chromosomes, Hsa21 still houses a large number of genes. Initial estimates put the total at ~230 (Hattori et al., 2000), although recent advances in the detection of non-protein coding RNA put this figure as high as ~400 (Gardiner and Costa, 2006).

With such a large number of genes, the effect of this increased dosage is wide-ranging. The additional copy of Hsa21 results in elevated expression of many of the genes encoded on this chromosome, with varying expression levels in different tissues. The increased dosage of Hsa21 genes, and the dosage imbalance between Hsa21 and non-Hsa21 genes has been proposed to cause the phenotypic alterations that characterise DS.

Hsa21 is syntenic to three regions of the mouse genome. Most of the genes on Hsa21 have homologous genes on mouse chromosome 16 (Mmu16), but two smaller gene rich regions have synteny on Mmu10 and Mmu17. The majority of mouse models used for DS research are either trisomic for large regions of Mmu16, 10, 17 or are transgenic animals used to investigate overexpression of a single gene, such as DYRK1A.

With the use of a number of mutants to model DS, spanning from single genes to the length of Hsa21, the key genes that control the condition are slowly beginning to be identified. This characterisation of Hsa21 should enable the discovery of new pharmacological targets and one day even allow the possibility of DNA-based therapies for the condition.

A model of DS that has been of great interest in recent years has been the transchromosomic (Tc1) mouse, produced as part of efforts beginning in the late 1980s, culminating in an initial characterisation reported in 2005 (Hernandez et al., 1999; O'Doherty et al., 2005). In this model a near complete form of Hsa21 is introduced into the mouse, with the aim of examining the effects in the mouse but using human genetic material to offer a more translational model of the condition. This also opens the possibility to monitor the effects of future drug treatments in specifically modulating the human gene and protein expression in an animal model. While preliminary measurements of skull morphology, and cerebellar neuronal density have been made in its initial characterisation (O'Doherty et al., 2005), so far no examination of whole-brain anatomy in the Tc1 model has been performed.

Other DS mouse models trisomic for mouse syntenic regions to chromosome 21 have demonstrated altered brain morphometry and reduced cerebellar volume (Aldridge et al., 2007) and also ventricular enlargement (Ishihara et al., 2010).

Brain phenotyping in the mouse is still heavily reliant on conventional histological methods – typically sectioning and microscopic examination. While histology can offer high-resolution datasets that can provide cellular and molecular information using staining techniques such as immunohistochemistry, volumetric morphologic assessment is difficult due to the effects of processing and tissue destruction. It is also a very slow process, often requiring a day or more to section a single brain. This low throughput reduces the utility of histology in providing the screening and analysis needed for high-volume phenotyping studies.

Microscopic MRI (μMRI) is an established, non-invasive method that can produce high-resolution 3D datasets of the mouse brain. Additionally, the digital nature of these datasets allow the use of observer independent, automated analysis techniques such as voxel and tensor-based morphometry (VBM and TBM respectively) (Ashburner and Friston, 2000). These are now standard tools for the groupwise analysis of human brain studies and are increasingly used in preclinical imaging studies (Badea et al., 2007a; Lerch et al., 2008; Sawiak et al., 2009b). A challenge has been the adaptation of existing software tools for the mouse brain, particularly in the complex non-linear image registration that underpins the use of TBM and VBM techniques. Clinical studies often use multislice imaging sequences, with a relatively coarse resolution and slice-thickness. Such scans are fast, well-suited to *in-vivo* studies and result in a relatively small data size (order of ~megabytes). In the mouse brain there is the possibility of high-resolution (~10s of µm), overnight *ex-vivo* acquisitions which can lead to datasets of >100s of megabytes per brain. Only relatively recently, with the development of novel registration implementations that utilise parallel processing (on graphics processing units and computing clusters), have these large datasets been able to be processed and registered in a reasonable amount of time (typically several hours) (Modat et al., 2010).

In this study, a novel, high-resolution µMRI preparation and scanning protocol was used (Cleary et al., 2011) to perform an initial investigation of the Tc1 model of DS. Detailed visual inspection of subjects and automated computational techniques for analysis of the mouse brain (developed by Benjamin Sinclair, CABI/CMIC, UCL) were then combined. These automated approaches may be divided into:

1. 'Global phenotyping', in which a single quantity is measured by which to compare mutant mice to healthy controls, in our case brain size and total intracranial volume (TIV).

2. 'Voxel-wise phenotyping', in which at each region of the brain, as defined by the voxels of a representative atlas, a quantitative measure of the degree of anatomical compression and expansion during image registration (known as the Jacobian determinant) is calculated. Comparison (at each voxel) between groups, yields regions of significant differences between mutants and healthy controls localised to specific regions of the brain.

In the mouse phenotyping field there is currently no agreed standard for the analysis and presentation of voxel-wise data. As a result there are several ways the data may be evaluated. In this study, phenotypic differences based on absolute voxel-wise volume difference and also after normalisation to account for global brain size differences are presented. This normalised analysis may be achieved: (i) numerically, by the omission of the global scaling factor calculated during affine registration, instead relying on local non-linear Jacobian determinant alone or (ii) statistically, based on the use of an anatomical measure (total brain volume) as a covariate for each individual brain. Both these approaches are presented and compared here.

7.3 Materials and Methods

7.3.1 Animal Preparation

All parts of this study were carried out in accordance with the UK Animals (Scientific Procedures) Act, 1986. Mice were bred and provided by Elizabeth Fisher, Frances Wiseman and Victor Tybulewicz at the Department of Neurodegenerative Disease, UCL Institute of Neurology. The imaging cohort consisted of 28 male (14 Hsa21$^+$ transchromosomic, 14 Hsa21$^-$ littermate controls, 129S8 x C57BL/6 background) aged between 18-21 weeks, were culled with an overdose of sodium pentobarbitone and perfusion-fixed with 4% buffered formol-saline (with 8mM Gd-DTPA). They were then left for 9 weeks in 4% buffered formol-saline (with 8mM Gd-DTPA).

Samples were removed from fixative and excess solution carefully blotted with a paper towel, and were immersed in Fomblin perfluoropolyether (type PFS-1, Solvay Solexis S.p.A., Bollate, Italy) in 20ml plastic syringes and immobilised with surgical gauze. Samples were allowed to equilibrate for at least 2 hours at room temperature prior to imaging. Air bubbles in samples were minimised by equilibration and gentle agitation of the syringe.

7.3.2 Imaging

Mouse brains were imaged in a randomised order using a Varian 9.4T VNMRS system using a 3D spoiled-gradient echo (3D GE) sequence. Optimised 3D GE scan parameters: FOV=20.48x13.04x13.04mm, matrix size=512x326x326, TE/TR/FA/NSA=4ms/17ms/52°/6, resulting in a scan-time of 3 hours per brain.

7.3.3 Image Processing and Registration

Raw k-space data was taken from the scanner and Fourier transformed using a custom Matlab script at acquired resolution, giving an isotropic voxel size of 40x40x40μm, and saved in Analyze format. While MRI receiver gain was standardised for all acquisitions, to minimise variations in signal intensity, the intensity range of all images were normalized using the histogram equalisation function in a Matlab script.

As part of the creation of the average atlas for of the population, one image was chosen as the target and initial rigid and affine registration was performed using an iterative block-matching algorithm (Ourselin et al., 2001). Finally, non-linear registration was performed using a fast, parallel implementation (Modat et al., 2010) of the free-form deformation algorithm (Rueckert et al., 1999).

A coarse-to-fine approach was used for the non-linear registration, where the control point spacing was gradually reduced to a width of 5 voxels (200μm) overlaid on the full resolution datasets. Constraints to the algorithm were used such that image folding, indicated by the presence of negative Jacobian determinant values in the deformation fields, was minimised. 10 iterations of the algorithm in total were used to warp images until adequate convergence, as assessed by the visual inspection of the sharpness of aligned brain anatomy in the average atlas image.

The final average image was then used in combination with an expectation-maximisation (EM) approach (Van Leemput et al., 1999) to segment the atlas into grey, white matter and intracranial fluid in order to enable more detailed analysis of total intracranial volume (TIV) and whole-brain volume. Segmentation was carried out using the inbuilt EM algorithm of SPM5 (Functional Imaging Laboratory, UCL) and the *spmmouse* toolkit (Sawiak, 2009), which includes prior probability maps for the mouse brain.

7.3.4 TBM Analysis

Tensor-based morphometry was used to identify regions of significant compression or expansion in images from the Jacobian determinant of the deformation field, where a value >1 indicates an expansion of that region was required in order to align the structure with the average image; <1 indicates a contraction was required. Deformation maps calculated after both affine and non-linear registration were used in subsequent analysis.

Maps of the Jacobian determinant from the deformation fields in each transchromosomic and wild-type brain dataset were then subjected to groupwise comparisons using the general linear model (GLM) of SPM (Functional Imaging Laboratory, UCL). This resulted in statistical parametric maps of *t*-values for both expansion and contraction after multiple two-tailed *t*-tests. Maps were corrected using the false discovery rate (FDR) method (Genovese et al., 2002) and thresholded at a p-value of <0.05, which was taken as significant.

7.3.5 Weight Measurement Study

A separate group of 37 Tc1 animals (15 Hsa21$^+$, 22 Hsa21$^-$) was also monitored over time in order to assess the difference in body weight of these animals from 8 to 20 weeks. This was used as an indicator of overall animal size.

7.4 Results

7.4.1 Visual Inspection

After visual inspection of initial data it was observed that the lateral ventricles were enlarged in 11 Hsa21$^+$ subjects, along with disruption of the choroid plexus. Figure 7.1 shows examples of typical wild-type and Hsa21$^+$ individuals. An absent corpus callosum was also identified in 1 individual (Figure 7.2).

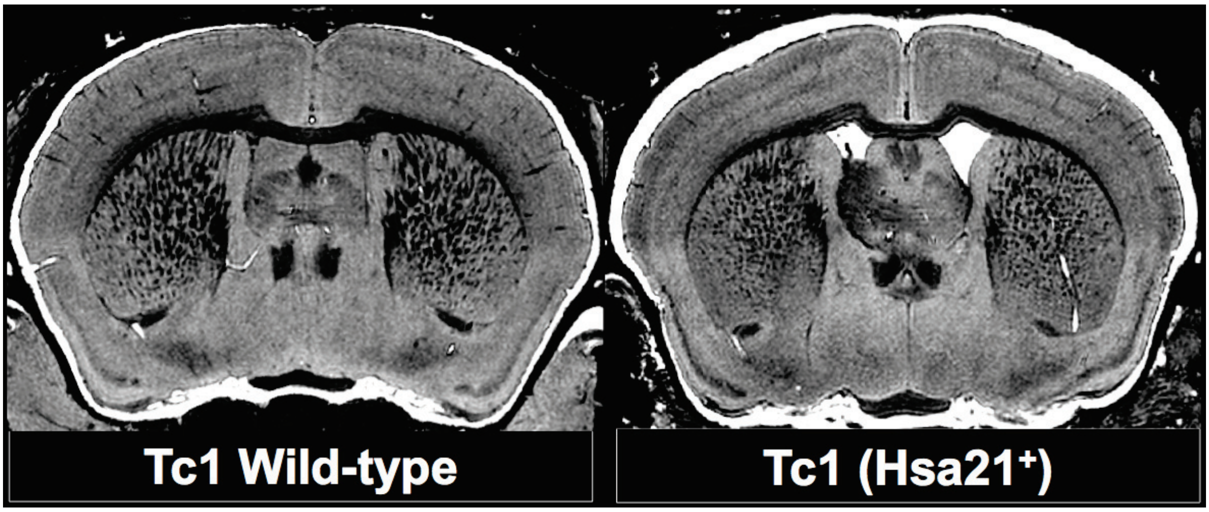

Figure 7.1: *Visual comparison of similar coronal slices from example wild-type and Hsa21$^+$ individuals from our acquired dataset. In the Hsa21$^+$ individual, loss of the choroid plexus and increase in the size of the lateral ventricles may be seen.*

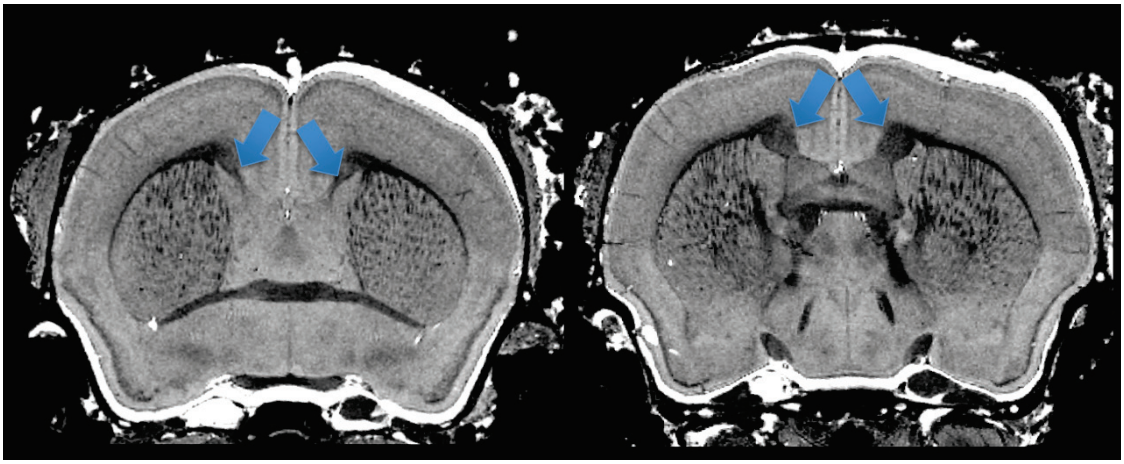

Figure 7.2: *Representative coronal slices through one Hsa21^{+} individual presenting with an absent corpus callosum, blue arrows indicate the residual portions of white-matter that have failed to cross the midline.*

7.4.2 Automated Analysis

7.4.2.1 Atlas Creation

Our datasets were found to be suitable for non-rigid registration, with the average image retaining small anatomical details such as tract and commissural structures and individual regions of the hippocampus. This successful application of the F3D algorithm to our datasets is clearly demonstrated in the quality of the resulting average atlas (Figure 7.3).

Figure 7.3: *Coronal, axial and sagittal views from our average atlas of all 28 subjects in the study. The conspicuity of anatomical features, such as cortical layers, white-matter tracts and hippocampal regions indicates good performance of the registration algorithm.*

7.4.2.2 Global Volume Differences:

After segmentation and categorisation of brain structures using EM, global volume differences were examined. Hsa21^{+} mice were found to have larger mean brain volume than wild-type subjects (mean difference 14%, $p<1x10^{-7}$). A larger corresponding total intracranial volume (TIV, the total of: grey + white matter + intracranial fluid) (17%, $p<1x10^{-6}$) was also observed.

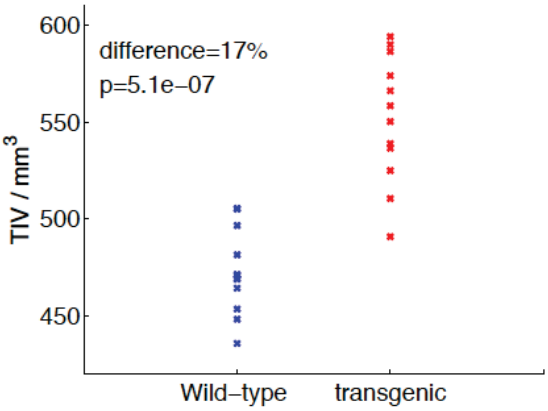

(a) TIV

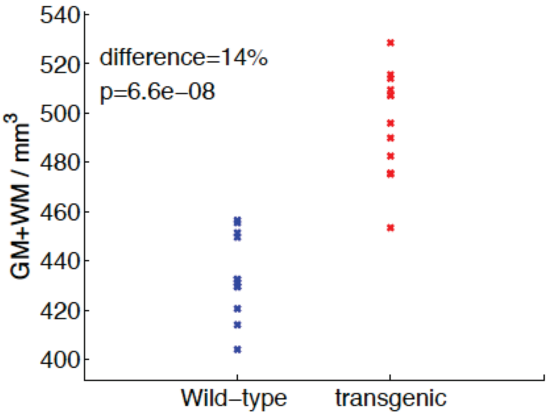

(b) GM+WM

Figure 7.4: *Graphs showing (a) the EM-segmented total intracranial volume (TIV) and (b) segmented grey and white matter tissue volumes of both wild-type and transgenic Tc1 mice.*

7.4.3 Voxel-wise TBM Analysis:

7.4.3.1 *Analysis Based on the Total Affine and Non-linear Jacobian Determinant*

Figure 7.5 shows regions significantly larger and smaller in Tc1 mice based on total volume change over the voxels in each brain. This provides information on regions with an absolute volume difference between groups. As seen in the majority of representative slices, most mid-coronal regions of the brain were significantly larger in Tc1 mice (blue areas Figure 7.5). However a number of cerebellar regions, such as lobule 9 and parafloccular lobules, the forceps major of the corpus callosum, and a large portion of the olfactory bulbs did not show a significant difference between groups. Interestingly, some small bone regions near the inner ear and regions of the trigeminal nerve showed a significant reduction in volume (red regions, Figure 7.5).

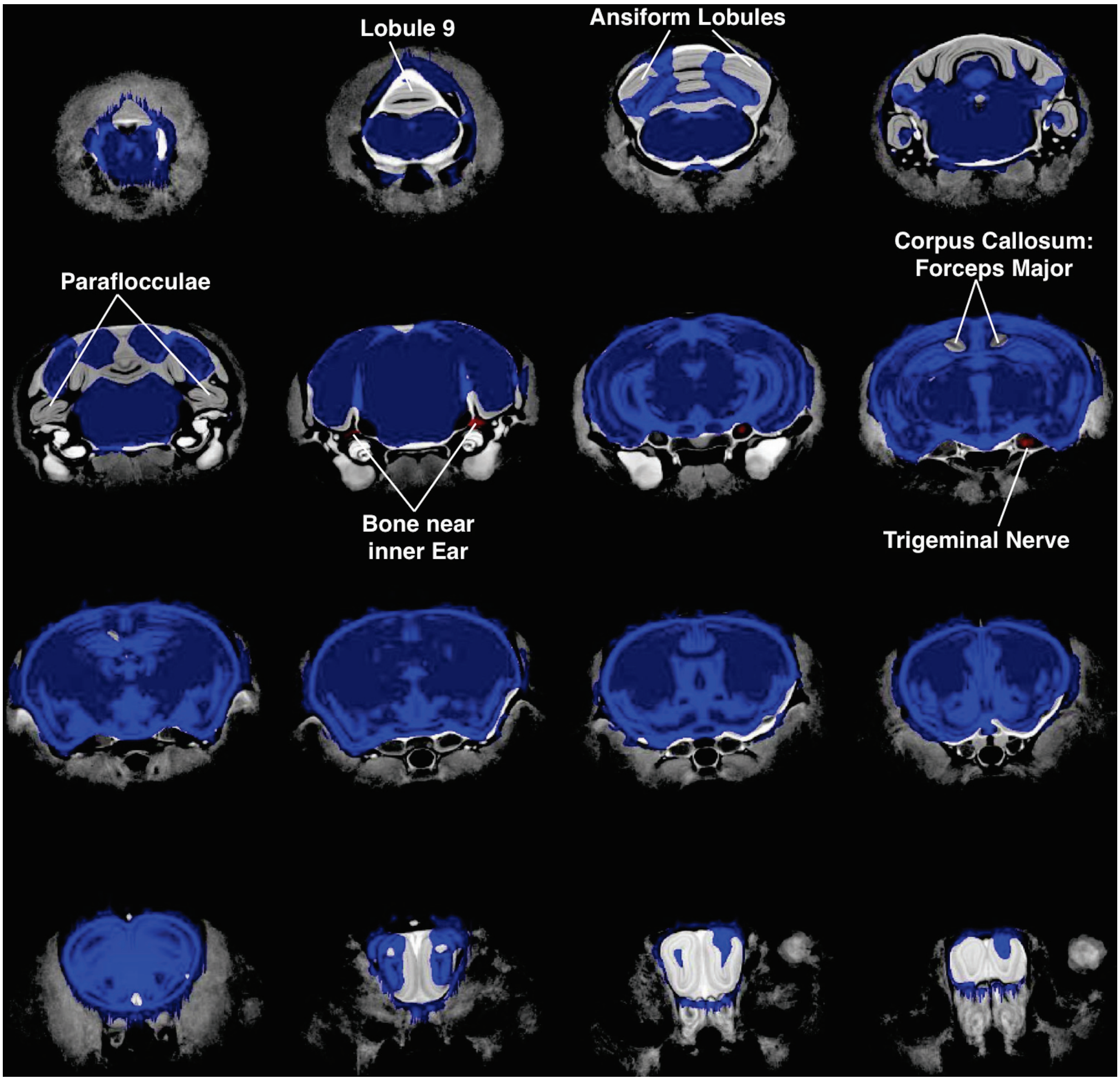

Figure 7.5: *Montage of volume changes identified in 16 representative slices through the average atlas dataset. Coloured regions show areas of significant volume difference overlaid in our cohort of 28 Tc1 mice comparing the pixel-by-pixel, total volume change between groups (global affine + local registration). Blue indicates regions larger in Hsa21^{+} mice; red indicates areas smaller. Labelled structures indicate regions identified in the analysis, including those absent from blue areas (no significant difference) and small regions of global volume decrease in Tc1 mice ($p<0.05$, FDR corrected).*

7.4.3.2 Analysis of Normalised Data

Given the large global change observed in section 7.4.3.1 above, it is useful to examine differences between the groups after correcting for this change, enabling a regional or proportional volume assessment. Data is presented from two methods for achieving this below.

7.4.3.2.1 Analysis of the Non-linear Registration Jacobian Determinant Only

Figure 7.6 shows regions significantly larger and smaller in Tc1 mice based on changes in the Jacobian determinant calculated during the non-linear registration process only and without the affine scaling.

Significant areas of reduced proportional volume were observed in the regions of the cingulum, hippocampal CA1 and the forceps major of the corpus callosum. Also in multiple cerebellar regions, including posterior lobes, ansiform lobules and paraflocculae. Also thalamic nuclei, olfactory bulbs and cortices of the inferior colliculi. Conversely, a number of regions were found to be larger in Hsa21$^+$ mice, including: lateral ventricles, amygdala, hypothalamus, reticular and trigeminal nuclei, CA3 and anterior olfactory area. These are labelled in Figure 7.6 below.

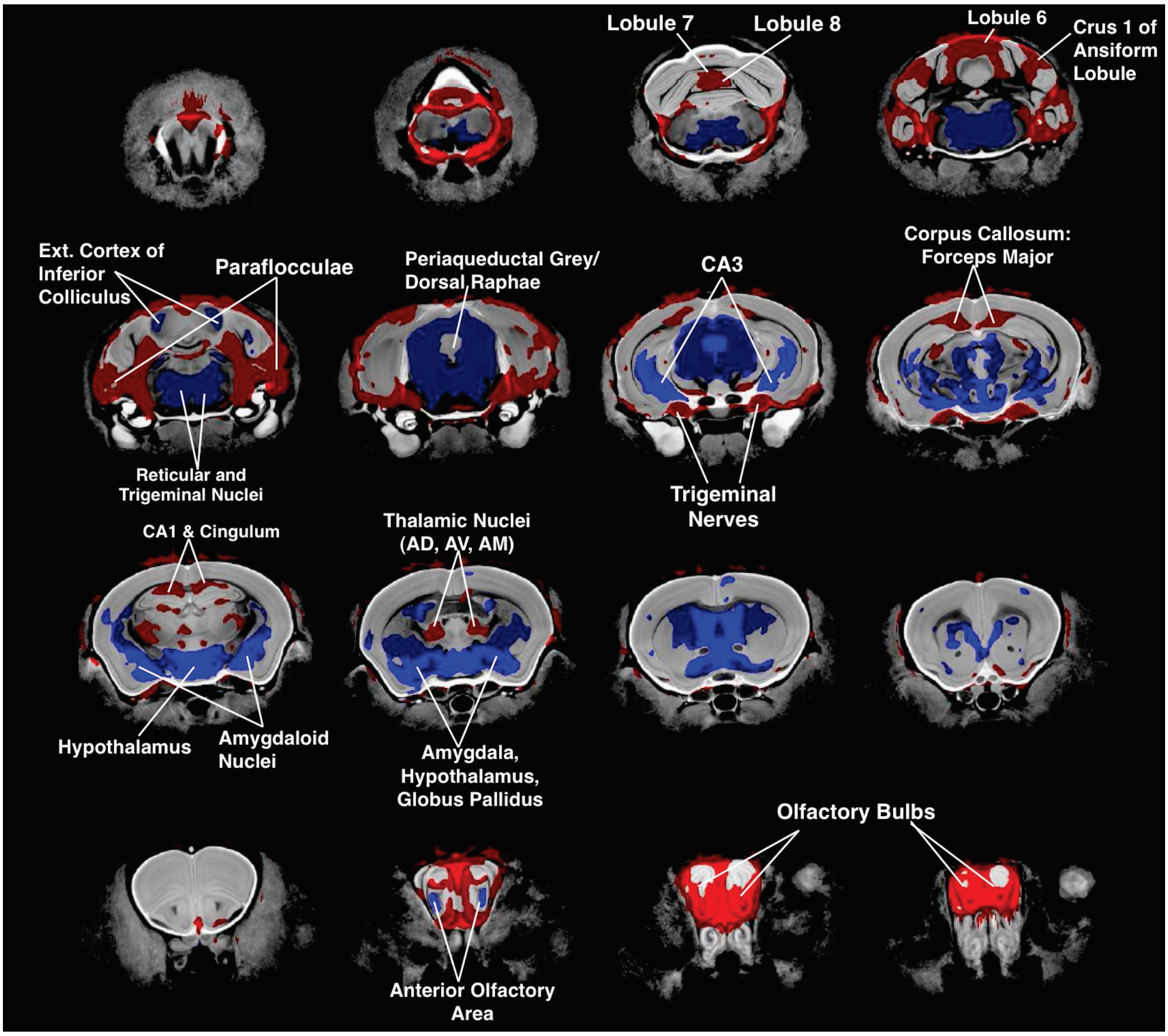

Figure 7.6: *Representative caudal to rostral views showing regions of significant change after correcting for global volume changes from the affine registration. Regions coloured red indicates local volumes are significantly smaller in the Tc1 mice in these regions, blue regions larger (FDR corrected, p<0.05).*

7.4.3.2.2 Total Brain Volume as a Covariate

Correction of data for a large global effect by including the total brain volume (the sum of grey and white matter segmentation) as a covariate in the statistical analysis (Figure 7.7) was also attempted.

By this method, a number of regions were found to be larger in the Hsa21 animals, including: the deep grey of the superior colliculus, and pontine tegmental and reticular nuclei.

Conversely regions found to be smaller included: the vermis of lobule 7, small areas of the ansiform lobule, lobule 2, trigeminal nerves and small regions corresponding to bone above the inner ear. These are labelled in Figure 7.7 below.

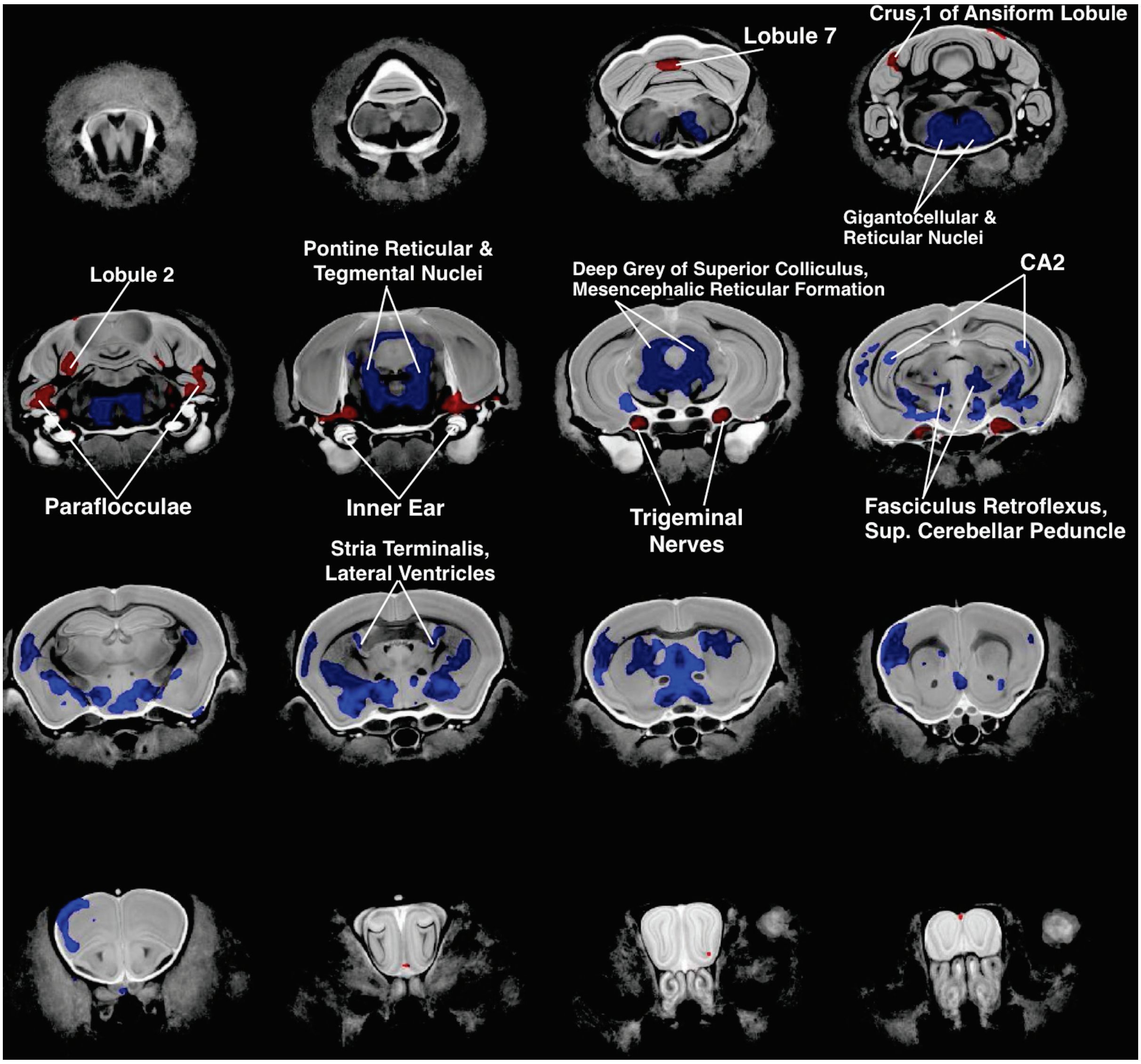

Figure 7.7: *Montage of volume changes identified in 16 representative slices throughout the dataset. Colourmaps indicate regions of significant volumetric changes in the Tc1 mouse brain with correction for total brain volume by its inclusion as a covariate in the groupwise analysis. Blue indicates regions significantly larger in Tc1 mice; red smaller (FDR corrected, $p<0.05$).*

7.4.4 Weight Measurements

In order to ascertain if overall body size correlated with brain volume, the weights of an additional cohort of 37 animals (15 Hsa21$^+$, 22 controls) were measured from 8 to 20 weeks of age, at 4 weekly intervals. While the mean weight of Tc1 mice was significantly less at 12 and 16 weeks ($p<0.05$), by 20 weeks (similar to the age of mice used in the imaging study) no significant difference in weights was observed (Figure 7.8).

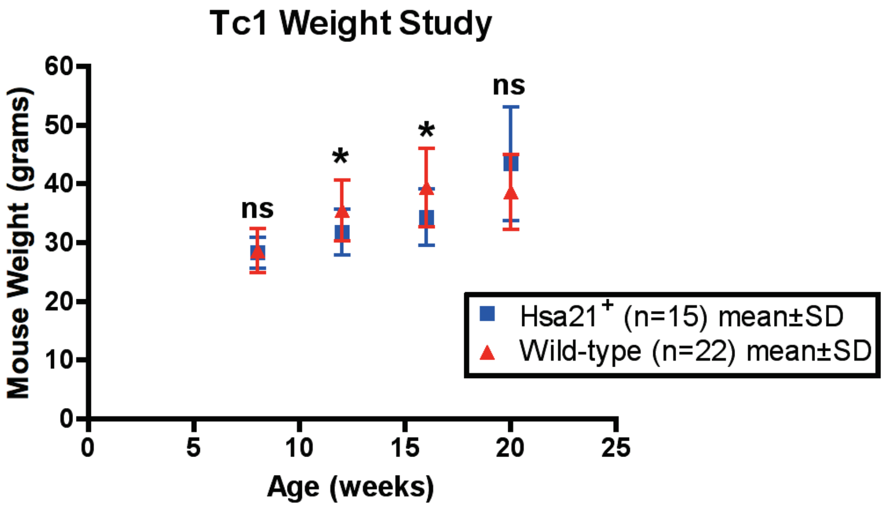

Figure 7.8: *Graph showing the weights of an additional cohort of Tc1 mice (n=37), followed over a 20 week period (* indicates p<0.05).*

7.5 Discussion

This study has phenotyped the Tc1 model of Down syndrome using µMRI for the first time. Both global brain changes and more subtle phenotypic differences between groups have been identified through a combination of visual inspection of the data and tensor-based morphometry methods.

From a methods point of view, it was shown that the image contrast seen in gradient-echo µMRI images is reproducible in a large number of subjects and the anatomical detail visible aids in the identification of fine regions of structural difference. This should enable the broad applicability of the technique to mouse phenotyping studies.

Our contrast-enhanced methodology, in combination with a further novel implementation of the well-known free-form deformation algorithm (Modat et al., 2010), enabled the creation of a high quality average atlas. This indicates that our imaging and tissue preparation protocol is a good foundation for the application of morphometric analysis techniques.

The high quality of the atlas, which retains regional detail in fine brain structures, indicates that the contrast-enhanced μMRI methodology (Cleary et al., 2011) is compatible with non-linear registration. The ability of a non-linear registration algorithm to correctly detect and align anatomy in the underlying datasets is a fundamentally important to the generation of an accurate deformation. Additionally, the enhanced signal to noise seen after averaging of all 28 subjects, may also help more precisely delineate the regions of significant difference between groups, when significant regions are overlaid on to this image.

Ventricular enlargement was seen in 11 Hsa21$^+$ mice, which may indicate a neurodegenerative process in the brain. Recent work in Ts1Cje and Ts2Cje models of DS (models with partial trisomy of mouse chromosome 16) has also shown ventricular enlargement (Ishihara et al., 2010). The individual identified with a corpus callosum deficiency was probably due to mouse background, as absent corpus callosum is often seen in 129 mice (Hof et al., 2000). In the subsequent TBM analysis, blue regions of significant expansion appeared to overlap the lateral ventricle regions in our analysis based on the non-linear Jacobian determinant only.

A continual issue in the presentation of phenotyping studies as discussed in the preceding chapter is the use of normalised data. Given widespread volume increases observed in the Hsa21$^+$, more subtle effects of, for example, the relative distribution of structure volumes may be being masked.

The results show that brains of Hsa21$^+$ mice were significantly larger than those of the wild-type. The assessment of body weight measurements suggests that the brain volume increase observed is not explained by a generally large overall size difference in the Hsa21$^+$ mice. This appears to be due to an underlying genetic mechanism causing brain hypertrophy. A reduced brain volume would be the expected feature, as seen in clinical studies (Pinter et al., 2001). However, brain enlargement has previously been shown in an MRI investigation of a YAC transgenic model of DS (YAC152f7) (Sebrié et al., 2008) which has small gene complement (PIGP, TTC3, DSCR9, DSCR3, DYRK1A) compared to those in the Tc1 model. In that study, the authors suggest that the increased DYRK1A copy-number was probably responsible for the observed increase in brain volume.

In the analysis, the data was corrected by either removing the contribution of the affine registration scale factor (which in effect normalises the data by average skull volume) or through statistical methods by covariating with measured total brain volume. While both approaches produced somewhat similar regions of significance, the maps derived from covariated brain volumes showed greatly reduced regions of significance compared to affine normalised data. This could be due to the fact that the affine registration is aligning all skull structures, including extracranial structures, bone and brain structures. Whereas the covariate analysis is correcting for brain volume only. Therefore both sets of data are presented in this chapter.

The non-linear, non-affine TBM maps, with larger regions of significance, appear to more strongly reflect previous findings in the Tc1 model. Previous histology (O'Doherty et al., 2005) found significant reduction in the granular neuron density in 4 regions of the cerebellum, (16% mean reduction in density, $p<0.003$), including specific samples from lobule 8 in each subject (also 16% mean reduction, $p<0.03$) In TBM maps based on local non-linear volume changes, it was observed that a proportional reduction in volume in a number of cerebellar regions, including lobule 8.

Facial dysmorphia is a common finding in clinical cases of DS and indeed craniofacial changes have been observed previously in the Tc1 mouse through skull measurements using micro-computed tomography (O'Doherty et al., 2005). A significant region of volume reduction was observed in the trigeminal nerve. Differences in facial anatomy may be a cause of this, given its function in providing sensory innervation to the face and whiskers. A change in facial morphology may have a corresponding effect on the degree and development of this innervation. Similarly, regions of significant volume change were noted near the inner ear and in the inferior colliculus, indicating possible effects on the auditory system.

A reduced proportional volume was also seen in the CA1 region of the hippocampus as well as a number of thalamic nuclei.

Previous behavioural studies have demonstrated both motor (Galante et al., 2009) and memory deficits (Morice et al., 2008) in Tc1 mice, supportive of our regional findings. However, further work may be needed to directly confirm the precise sensory, motor and memory changes in these animals suggested by our imaging findings.

Due to time limitations in this study additional histology was unable to be performed to confirm the TBM analysis. In particular, it may have determined the precise nature of the increased brain volume, particularly if this is an increase in neuronal density and if so, whether this represents an increase in all or only specific cell types.

Additionally, the regions identified significant on the basis of the non-linear Jacobian determinants would warrant further investigation to confirm a histological change in that region. However a possible confounding factor in this instance is the global size increase observed in the mouse brains, which may make visualisation of histological changes specifically seen in the normalised regions difficult.

While this may be an issue, a recent study successfully identified subtle cerebellar changes in a mouse model of fragile X syndrome through TBM-guided histology (Ellegood et al., 2010b). The affine-normalised regions identified in that study were smaller than those presented here and differences in cell populations were still identified by subsequent GFAP, NeuN, VGAT, and VGLUT1 immunohistochemistry.

However there may be some drawbacks to the technique. One disadvantage is the application of groupwise statistics to a mosaic model of a condition, where a variable number of constituent cells in the mouse will contain an Hsa21 chromosome. In simple terms, this has the potential effect of giving a broad range of phenotype and it remains to be seen if atlas based analysis will be superior to individual assessment in this scenario. In this model, previous fluorescent in-situ hybridisation studies, demonstrated that ~60-70% of brain nuclei appear to be Hsa21$^+$ (O'Doherty et al., 2005). However this number may vary between animals and could potentially vary between cell populations.

Similarly, a situation where a gene is incompletely penetrant may result in a small number of individuals demonstrating a phenotype. These individuals will then be averaged into their category and the effect masked by the groupwise analysis. This may indicate that manual methods such as visual inspection and the analysis of outliers still have a role to play in the phenotyping of certain mouse models.

As seen previously, despite the size of brain datasets (~400MB per individual), and sheer quantity of data (512 axial slices), our findings demonstrate that tensor-based morphometry is a powerful method to automatically assess the differences in local brain anatomy across two populations.

7.6 Conclusion

In this study, the Tc1 model has been phenotyped for the first time using contrast-enhanced gradient echo μMRI and tensor-based morphometry. The image contrast seen in the μMRI images is reproducible in a large number of subjects, producing a high-quality average atlas after non-linear registration, suggesting the broad applicability of the technique to general brain phenotyping studies. Visual inspection identified lateral ventricle enlargement in a number of the transchromosomic animals. Global segmentation showed that Hsa21^{+} mice had a significantly larger mean total brain volumes (17%), with subsequent voxel-wise analysis on the total Jacobian determinant showing this increase is localised across the majority of brain structures. After normalisation of the data, voxel-wise analysis showed significant proportional volume reductions in the cerebellum, trigeminal nerves, inner ear regions, hippocampal CA1 and a number of trigeminal nuclei. Our findings demonstrate that tensor-based morphometry is a powerful method to automatically assess the differences in local brain anatomy between two populations.

Chapter 8:

General Discussion

The challenge of phenotyping future numbers of modified mouse lines will require robust, large-scale methods for morphological assessments. This thesis demonstrates the utility of an imaging-based approach, integrating both high-throughput imaging and analysis. The use of contrast-enhanced high-resolution μMRI for the investigation of mutant mice in both the embryo and adult mouse brain was explored, which resulted in improved image quality, enabling the delineation of subtle structural features. Additionally, these imaging correlates were compared to histology. This work was extended through the application of automated analysis to this imaging, employing registration techniques such as segmentation-propagation and tensor-based morphometry to successfully identify novel phenotypes.

In chapter 4, the use of an MRI contrast agent (Gd-DTPA) as a tissue active stain for imaging the embryo heart and cardiovascular system was investigated. Optimising preparation and scan parameters for heart imaging in 15.5dpc mouse embryos. It was found that fixation for 2-weeks provided a gain in SNR due to T_1 reduction, as does increasing Gd-DPTA contrast agent concentration. Additionally, it was found that the best balance of heart CNR and muscle SNR was achieved at 8mM. Using gradient-echo simulations with measured T_1 and T_2* values, the optimum scanning parameters were determined and verified. This combination produced a heart-chamber CNR of approximately five times that of previous literature parameters, highlighting the need for preparation and pulse sequence optimisation. These parameters were then used to identify a heart defect in *Chd7*$^{+/-}$ mice. This optimisation should allow better determination of heart and vascular anatomy in a variety of transgenic embryos, enabling greater sensitivity in detection of defects.

Chapter 5 addressed the need for automated image analysis for high-throughput phenotyping of the embryo CNS. The use of individual 3D embryo MRI histology, identified new pituitary phenotypes in *Hesx1* mutant mice, previously difficult to confirm due to the minute size of the gland, which is often destroyed during histological sectioning. Use of embryo atlasing techniques for anatomical studies as the resulting average image is a representation of the true population with high SNR. Subsequently, registration techniques were used to produce a whole-body embryo atlas from 6 CD-1 embryos, creating an average image with greatly enhanced anatomical detail, particularly in CNS structures. This methodology enabled unsupervised assessment of morphological differences between CD-1 embryos and *Chd7* knockout mice, and using a new atlas generated from these three groups, quantitative organ volumes were automatically measured. A difference in mean brain volumes between *Chd7*$^{+/+}$ and *Chd7*$^{+/-}$ mice and differences in whole-body, olfactory and normalised pituitary gland volumes between CD-1 and *Chd7*$^{+/+}$ mice (C57BL/6 background) were demonstrated. This work demonstrates the feasibility of combining high-throughput embryo MRI with automated analysis techniques to distinguish novel mouse phenotypes. As there is no limit to the number of embryos that may be registered, the technique opens the possibility for quantitative analyses of very large numbers (100s) of embryos with increased statistical power.

Chapter 6 investigated the structural correlates of the MRI agent Gd-DTPA, together with the optimal preparation and scan parameters for contrast-enhanced gradient-echo imaging of the adult mouse brain. It was observed that perfuse-fixation of the brain offered no advantage over the simpler preparation of immersion fixation. However, given that damage was observed in all *ex-situ* brains, further work focussed on *in-situ* brain imaging. Optimal fixation time for *in-situ* brains was much longer than in *ex-situ* studies, requiring approximately 9 weeks fixation before reaching similar T_1 values across the brain. From these data, estimates of MR parameters for the optimal cortex-corpus callosum contrast were determined. *In-situ* brains, fixed for 9 weeks with 8mM Gd-DTPA and scanned with calculated parameters (TE/TR/FA/Averages=4ms/17ms/52°/6 averages), produced images with high SNR (~30) and detailed anatomical differentiation. Correlating brain structures directly to histology, our MR images delineated detailed cytoarchitecture in the cortex, cerebellum, olfactory bulb and hippocampus. Neurofilament staining demonstrated that regions of negative MR contrast strongly correlated to myelinated white-matter structures. Many sub-regions were able to be identified, particularly within the hippocampus, such as the unmyelinated mossy fibres (stratum lucidum) and their region of synapse in the stratum pyramidale, together with the granular layer of the dentate gyrus, an area of densely packed cell bodies, which was clearly visible as a region of hyperintensity. This suggests that cellular structure influences the site-specific distribution of the MR contrast agent, resulting in local variations in T_2*, which leads to enhance tissue discrimination. Our results show that μMRI with a relatively high contrast agent concentration (8mM Gd-DTPA) is able to produce high-quality images that delineate a large number of anatomical features as confirmed by histology. Our findings provide insights into the cellular distribution and mechanism of MR active-staining, which enable interpretation of magnetic resonance microscopy brain data and highlight cellular structure for investigation of disease processes.

These results show that active-stained μMRI can provide detailed anatomical images of the *in-situ* mouse brain with high resolution and signal-to-noise. Additionally, a variety of stains were used to identify and compare the MRI appearance of brain structures to those defined by histology. Combining this data highlighted possible mechanisms for the enhanced contrast in these regions, surmising that contrast depends on both preserved, intrinsic T_2* differences as well as regions delineated by distribution of active-stain due to tissue microstructure. This methodology could enable greater sensitivity for the phenotypic characterisation in mutant mouse models and enhance regions of the mouse brain that may be targeted in future transgenic studies.

Chapter 7 presented a study to phenotype the Tc1 model for the first time using contrast-enhanced gradient echo μMRI and tensor-based morphometry. It was shown through this study, that the image contrast seen in our μMRI images is reproducible in a large number of subjects. Similar to the work in the embryo (chapter 6), it was found that applying registration methods to the data resulted in a high-quality average atlas of the subjects in our study population, indicating our datasets were amenable to non-linear registration. This suggests the broad applicability of the technique to general brain phenotyping studies. Visual inspection identified lateral ventricle enlargement in a number of transchromosomic animals. Global segmentation showed that $Hsa21^+$ mice had a significantly larger mean total brain volumes (17%), with subsequent voxel-wise analysis on the total Jacobian determinant showing this increase is localised across the majority of brain structures. After normalisation of the data, voxel-wise analysis showed significant proportional volume reductions in the cerebellum, trigeminal nerves, inner ear regions, hippocampal CA1 and a number of trigeminal nuclei. This study demonstrates that tensor-based morphometry is a powerful method to automatically assess the differences in local brain anatomy between two populations and has identified phenotypic features not easily assessed by visual inspection.

Although this investigation successfully identified group differences, the Tc1 model challenges our current analysis, where there variability in the number of constituent cells containing Hsa21. Further work would seek to refine these methods such as through an integrated approach to the analysis of outliers, which may indicate more extreme phenotypes.

Future directions in the field would aim to develop both MR imaging and analysis. In terms of imaging, as we have seen in our work, the use of paramagnetic contrast agents in conjunction with gradient-echo imaging has produced images with excellent contrast and high resolution. However the precise mechanism and distribution of these agents have yet to be explored. As an adjunct to conventional MR image weightings, a technique such as a susceptibility imaging (Shmueli et al., 2009) may demonstrate a further μMRI contrast mechanism and give clues as to the nature of a contrast agent's distribution. Also an investigation of novel contrast agents, based on other paramagnetic ions and/or chelates may be able to produce alternative contrast in a similar manner to histological stains.

In terms of analysis, as we have discussed previously, standardisation of atlas space in a manner similar to Talairach coordinates (such as in Johnson et al., 2010) is extremely desirable given the international nature of current phenotyping efforts. While we have used the GLM to perform a group analysis, its role in the investigation of outliers should be examined further. Additionally, hypothesis-generation techniques, such as independent component analysis, may have a role, most likely in initial screening. The TBM methodology used in this work could also be expanded to include analysis of the underlying directional vector data that gives rise to the Jacobian determinants. This may allow further insight into the spatial origin of regions of deformational change and enable more intricate studies of brain *shape*.

8.1 Final Conclusion

The burgeoning use of genetically modified mouse models in both the laboratory and large-scale mutagenesis programmes will require novel rapid methodologies for the morphological phenotyping of new mouse lines. This thesis has demonstrated the development of both imaging and analysis techniques, applicable to both embryo and adult mouse data. It is hoped that µMRI in combination with computational analysis will have an increasing role in easing the burden of the identification and characterisation of novel mouse phenotypes in the future.

Appendices

The following appendices introduce two preliminary mouse embryo studies supplementary to the main body of this thesis.

Appendix 1: Overview

In this appendix, a further application of the contrast enhanced embryo imaging protocol is presented, characterising the cardiovascular phenotype of a novel double knockout model of congenital heart disease – *Chd7*$^{+/-}$*Tbx1*$^{+/-}$ mice. *Tbx1* is a gene implicated in the condition DiGeorge syndrome – a condition characterised by aortic arch defects. The possible effect on the gross anatomy of the heart due to interactions between these genes is unclear. This was a preliminary study to examine the phenotype of mice heterozygous for the genes *Chd7* and *Tbx1*, for the first time with μMRI.

Appendix 2: Overview

The introduction to this thesis mentions the use of diffusion tensor imaging (DTI) in providing a non-invasive characterisation of tissue microstructure, particularly in the brain. While there have been some previous studies utilising DTI in the characterisation of the mouse embryo, these have been restricted to studies of the embryo head only, with a low number of diffusion directions. In Appendix 2, a novel, contrast enhanced method is described that enables the whole-body phenotyping of mid-gestation embryos using 42-direction DTI.

Appendix A:

Phenotyping a Novel Double-heterozygous Model of Congenital Heart Disease Using micro-MRI

This work was presented at the meeting of the Society for Cardiovascular Magnetic Resonance, Phoenix AZ 2010.

A.1 Introduction

CHARGE and DiGeorge syndromes are conditions with incidences of 1 in 10,000 and 1in 4000 and are strongly associated with haploinsufficiency of specific genes (*CHD7* and *TBX1*). Both conditions are characterised by cardiovascular defects. Knockout mouse models are an important tool for the identification and characterisation of genes implicated in congenital heart conditions. Micro-MRI is an emerging technique for high resolution cardiac phenotyping in a reduced time compared to conventional histology, enabling the acquisition of 3D images of multiple embryos in a single scan (Cleary et al., 2009).

A.2 Purpose

Given the phenotypic overlap of these conditions this investigation sought to examine the effect on cardiac morphology in double-heterozygous mouse embryos ($Chd7^{+/-}$ $Tbx1^{+/-}$) (Randall et al., 2009), performing an initial assessment of these mice using MRI.

A.3 Methods

Study Design: 18 embryos (1 wild-type, 7 $Chd7^{+/-}$, 2 $Tbx1^{+/-}$ and 8 $Chd7^{+/-}Tbx1^{+/-}$) were imaged and examined for cardiac abnormalities. Embryo Preparation: 16.5dpc embryos were fixed for at least 2 weeks in a solution of 4% formaldehyde-PBS with 8mM Gd-DTPA (Bayer-Schering AG) and then embedded in 1% agarose gel (doped with 8mM Gd-DTPA) in 50ml centrifuge tubes.

Imaging: Performed on a Varian 9.4T VNMRS system with 33mm quadrature birdcage coil (RAPID Biomedical GmbH), using a 3D gradient echo sequence (TE/TR/FA/NSA=9/20/60/7, FOV=27x27x27mm^3, voxel size=52x52x52μm^3).

Image analysis: Datasets were zero-filled to 26x26x26μm^3 and reviewed in Amira (v5.2, Visage Imaging Inc.).

Histology: Embryos identified with abnormal hearts by MRI, were then histologically examined by H&E staining.

A.4 Results

Of the 18 embryos scanned for MR analysis, abnormal (thin or patent) ventricular septa (VSDs) were identified in 6 embryos. Of these, 1 was a *Chd7*$^{+/-}$ heterozygote (an incidence of 1/7 in this study, see Figure A.1).

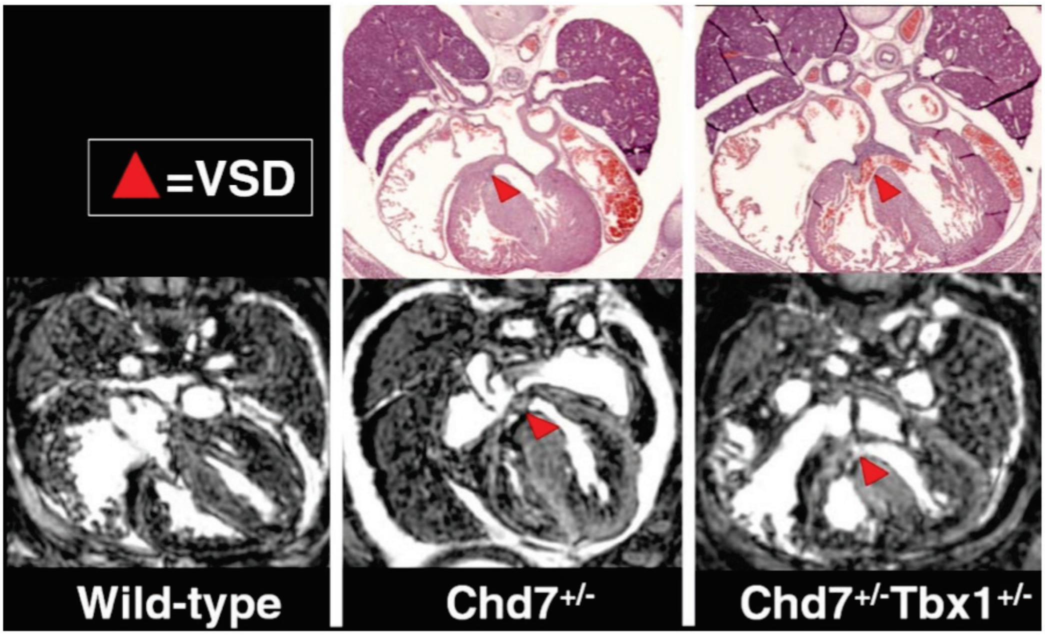

Figure A.1 *Axial sections through example embryo datasets showing the presence of ventricular septal defects (indicated by red triangles) in both Chd7*$^{+/-}$ *embryos and double Chd7*$^{+/-}$*Tbx1*$^{+/-}$ *heterozygotes.*

VSDs were seen in 5/8 *Chd7*$^{+/-}$*Tbx1*$^{+/-}$ embryos (Figure A.2a). In one double heterozygote an interrupted aortic arch was also observed, in addition to a VSD, which was readily seen by MRI (Figure A.2b).

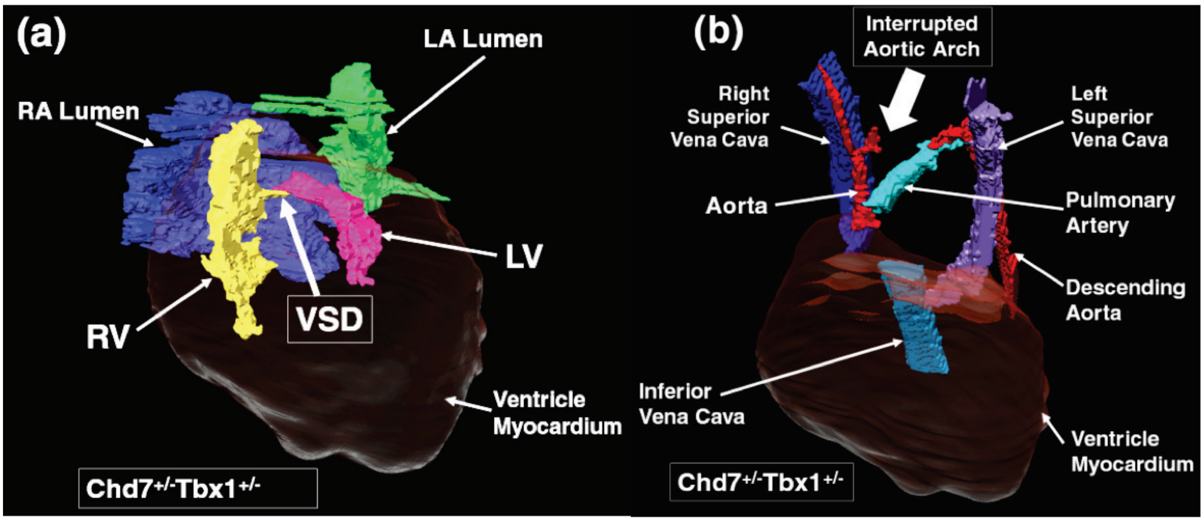

Figure A.2 ***(a)*** *Volume rendering of a heart of a Chd7*$^{+/-}$*Tbx1*$^{+/-}$ *double heterozygous embryo. (RA: right atrium, RV: right ventricle, LA: left atrium, LV: left ventricle) A clear ventricular septal defect can be seen between left and right ventricles.* ***(b)*** *Volume rendering of the same embryo showing great vessel structures only. An interrupted aortic arch was identified in this embryo (arrow).*

A.5 Conclusion

Using micro-MRI, cardiac abnormalities were successfully identified in genetically-modified embryos. A single *Chd7*$^{+/-}$ embryo was found to have an abnormal ventricular septum. A relatively high incidence of VSDs was observed in *Chd7*$^{+/-}$*Tbx1*$^{+/-}$ compared to *Chd7*$^{+/-}$ mice, indicating possible interaction of these two genes. An interrupted aortic arch was identified in one *Chd7*$^{+/-}$*Tbx1*$^{+/-}$ embryo. All abnormal findings were later confirmed by histology, which indicates that micro-MRI is an effective technique for cardiac phenotyping.

Appendix B:

Contrast-enhanced Micro-diffusion Tensor Imaging for Mouse Embryo Phenotyping

This work was presented at the meeting of the British Chapter of the International Society for Magnetic Resonance in Medicine, Nottingham 2010, and was a joint project between myself and Bernard Siow (CABI/CMIC, UCL). Mouse embryos were provided by Nicholas Greene (UCL Institute of Child Health).

B.1 Introduction

Mouse embryos are widely used as models for the study of human congenital abnormalities such as spina bifida, which is one of the most common birth defects. Morphological phenotyping of these embryos is still heavily reliant on histological sectioning: a destructive process that is time-consuming and operator dependent. Diffusion-tensor imaging (DTI) is a powerful technique that can explore tissue structure non-invasively, providing microstructural information such as the direction of tissue fibres. DTI techniques are particularly useful where traditional anatomical MR contrast is limited, such as in the developing foetal brain (Mori et al., 2001). In the mouse embryo, DTI can characterise brain development (Mori et al., 2001) as well as examine phenotype in mutant animals (Zhang et al., 2003). However, these studies have imaged only the brain in mid-gestation embryos, with a modest number of diffusion directions (typically 6) and long acquisition times (~10 hours). Gadolinium chelates, such as Gd-DTPA, are commonly used in the fixation of embryos for MR microscopy**,** to reduce T_1 and boost SNR (Cleary et al., 2009). While the use of Gd-DTPA is common in anatomical embryo imaging, its use has been limited in embryo DTI studies (Aggarwal et al., 2010). This study describes the development of a contrast-enhanced technique for whole-body DTI of mid-gestation embryos, comparing embryo preparation, pulse sequences and resolution. Subsequently, this methodology was applied to investigate the phenotype of the *splotch* mouse model of spina bifida, which carries a mutation in the gene *Pax3 (Greene et al., 2009)* a transcription factor implicated in the condition.

B.2 Methods

15.5dpc embryos (C57BL/6 background), were dissected from the mother and fixed for 2 weeks in a solution of 4% formal-PBS doped with 2mM Gd-DTPA. Later they were moved to a solution of PBS+2mM Gd-DTPA for at least 2 weeks. Imaging was performed on a Varian VNMRS system using a 26mm volume coil (RAPID Biomedical GmbH) and 3D spin-echo (3D-SE) and fast-spin-echo (3D-FSE) diffusion sequences (diffusion parameters: G=50G/cm, ∂=3.5ms, Δ=8ms, 42 directions+6 b0 images), with parameters chosen to maintain sample temperature during the acquisition: SE: TR=500ms, TE=15.3ms, b≈1550s/mm^2; FSE: TR=500ms, TE$_1$=14.75ms, ESP=5.75ms, ETL=4, b≈1660s/mm^2. Voxel size: 100x100x100μm^3 and 75x75x75μm^3 isotropic. 3D-SE T$_1$ and T$_2$ map data were also acquired. Sample temperature was 19±1°C. Images were corrected for movement by global registration (Ourselin et al., 2001). Direction encoded colour (DEC) maps were visualised in MedINRIA (Asclepios Project); FA value calculation and tractography was performed in MRtrix (Tournier et al., 2007).

B.3 Results

After rehydration in PBS+Gd-DTPA, mean whole-body T$_2$ increased from 14 to 25ms, giving improved SNR in the subsequent diffusion images (typically 39 vs. 22, 100μm SE data). DEC maps and values were similar between 3D-SE and FSE datasets (resulting 75μm DEC maps from FSE data are shown in Figure B.1). Subsequently, wild-type and *splotch* mutant mice were imaged, identifying differences in brain structure, in addition to spinal cord phenotype (Figure B.2).

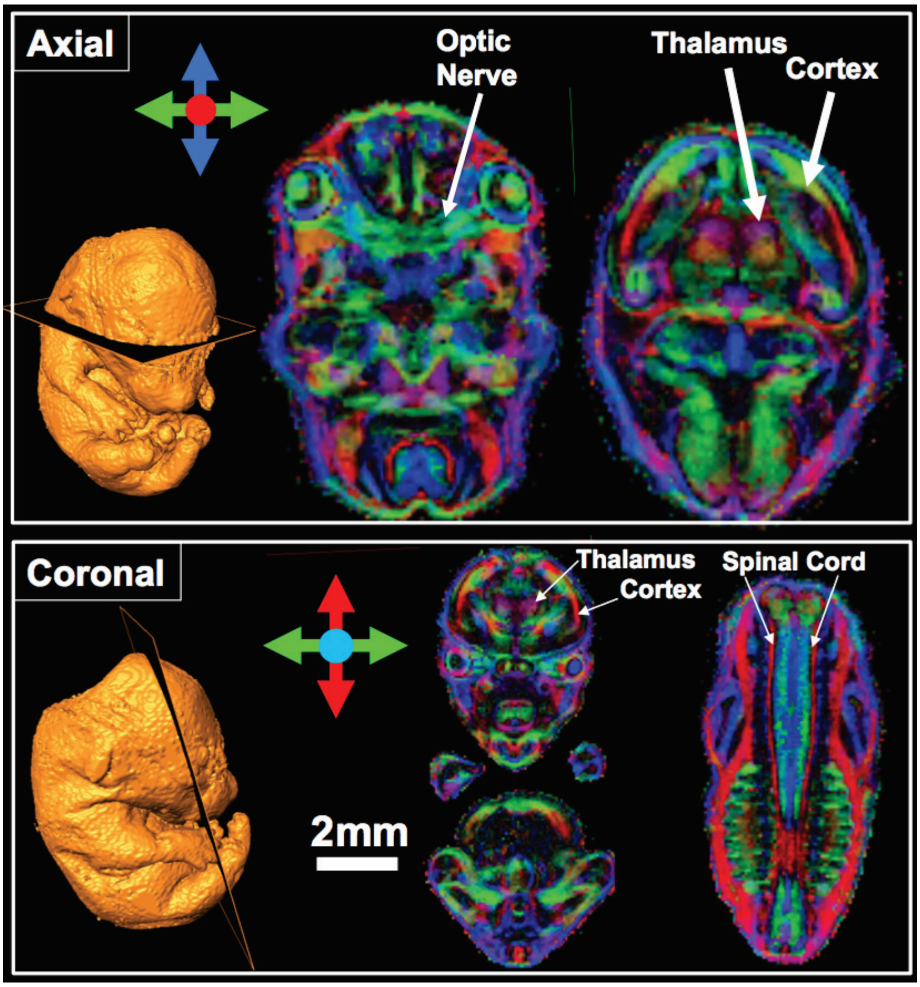

Figure B.1 *Axial and coronal DEC maps of a C57BL/6 wild-type embryo, imaged using the 75µm-FSE protocol, showing well-defined CNS anatomy and corresponding tissue directionality. (Arrows indicate principal eigenvector direction)*

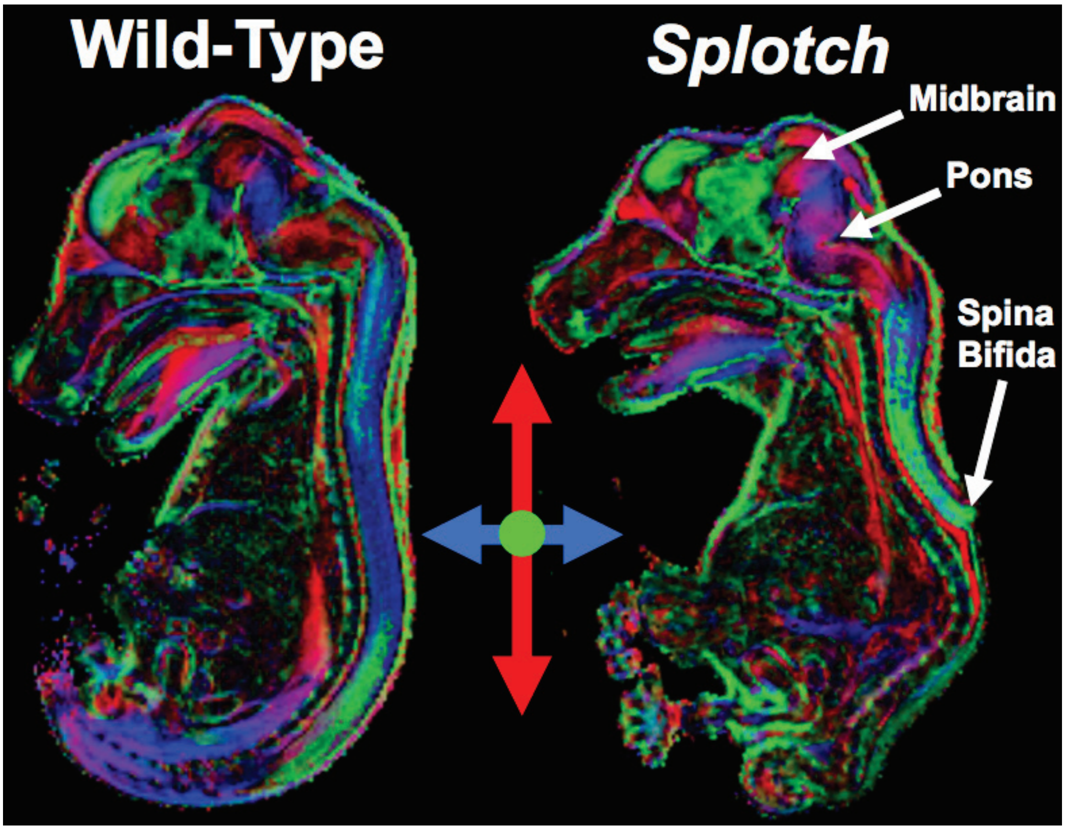

Figure B.2 *Similar mid-sagittal DEC maps through wild-type and splotch homozygous embryos. Although the primary defect is the spina bifida indicated, clear differences may also be seen in overall brain size and regions demarcated by principal eigenvector, such as in the pons and midbrain. (Arrows indicate direction of principal eigenvector)*

B.4 Conclusion

This study has shown that whole-body μDTI is able to delineate a number of anatomical brain regions according to diffusion directionality. 42 directions were used in this embryo study, achieving high-resolution (75μm) and a moderately high b-value (1660s/mm^2) in a 19h scan. Although this study concentrated on achieving high quality diffusion data for tractography through the acquisition of 48 images per scan, resorting to the minimum of 7 would give a total scan time of ~2.75 hours per embryo, improving throughput. As the final part of this study, the phenotype of the *splotch* model of spina bifida has been described for the first time with MR, characterising changes in brain structure and their relation to spinal cord phenotype. It is hoped that this methodology may enable wider adoption of DTI to embryo studies, which may offer new insights into new and existing congenital disease models.

References

Acevedo-Arozena, A., Wells, S., Potter, P., Kelly, M., Cox, R.D., Brown, S.D.M., 2008. ENU mutagenesis, a way forward to understand gene function. Annu Rev Genomics Hum Genet 9, 49-69.

Aggarwal, M., Mori, S., Shimogori, T., Blackshaw, S., Zhang, J., 2010. Three-dimensional diffusion tensor microimaging for anatomical characterization of the mouse brain. Magn Reson Med 64, 249-261.

Aldridge, K., Reeves, R.H., Olson, L.E., Richtsmeier, J.T., 2007. Differential effects of trisomy on brain shape and volume in related aneuploid mouse models. Am J Med Genet A 143A, 1060-1070.

Amunts, K., Malikovic, A., Mohlberg, H., Schormann, T., Zilles, K., 2000. Brodmann's areas 17 and 18 brought into stereotaxic space-where and how variable? NeuroImage 11, 66-84.

Ashburner, J., Friston, K.J., 2000. Voxel-based morphometry--the methods. NeuroImage 11, 805-821.

Badea, A., Ali-Sharief, A.A., Johnson, G.A., 2007a. Morphometric analysis of the C57BL/6J mouse brain. NeuroImage 37, 683-693.

Badea, A., Johnson, G.A., Williams, R.W., 2009. Genetic dissection of the mouse brain using high-field magnetic resonance microscopy. NeuroImage 45, 1067-1079.

Badea, A., Nicholls, P.J., Johnson, G.A., Wetsel, W.C., 2007b. Neuroanatomical phenotypes in the reeler mouse. NeuroImage 34, 1363-1374.

Balling, R., 2001. ENU mutagenesis: analyzing gene function in mice. Annu Rev Genomics Hum Genet 2, 463-492.

Baloch, S., Verma, R., Huang, H., Khurd, P., Clark, S., Yarowsky, P., Abel, T., Mori, S., Davatzikos, C., 2009. Quantification of brain maturation and growth patterns in C57BL/6J mice via computational neuroanatomy of diffusion tensor images. Cereb Cortex 19, 675-687.

Bamforth, S.D., Bragança, J., Farthing, C.R., Schneider, J.E., Broadbent, C., Michell, A.C., Clarke, K., Neubauer, S., Norris, D., Brown, N.A., Anderson, R.H., Bhattacharya, S., 2004. Cited2 controls left-right patterning and heart development through a Nodal-Pitx2c pathway. Nat Genet 36, 1189-1196.

Beacher, F., Daly, E., Simmons, A., Prasher, V., Morris, R., Robinson, C., Lovestone, S., Murphy, K., Murphy, D.G.M., 2010. Brain anatomy and ageing in non-demented adults with Down's syndrome: an in vivo MRI study. Psychol Med 40, 611-619.

Beck, J.A., Lloyd, S., Hafezparast, M., Lennon-Pierce, M., Eppig, J.T., Festing, M.F., Fisher, E.M., 2000. Genealogies of mouse inbred strains. Nat Genet 24, 23-25.

Bellin, M.-F., 2006. MR contrast agents, the old and the new. Eur J Radiol 60, 314-323.

Bentham, J., Bhattacharya, S., 2008. Genetic mechanisms controlling cardiovascular development. Ann N Y Acad Sci 1123, 10-19.

Benveniste, H., Blackband, S.J., 2006. Translational neuroscience and magnetic-resonance microscopy. Lancet Neurol 5, 536-544.

Benveniste, H., Kim, K., Zhang, L., Johnson, G.A., 2000. Magnetic resonance microscopy of the C57BL mouse brain. NeuroImage 11, 601-611.

Berrios-Otero, C.A., Wadghiri, Y.Z., Nieman, B.J., Joyner, A.L., Turnbull, D.H., 2009. Three-dimensional micro-MRI analysis of cerebral artery development in mouse embryos. Magn Reson Med 62, 1431-1439.

Blake, K.D., Prasad, C., 2006. CHARGE syndrome. Orphanet J Rare Dis 1, 34.

Blamire, A.M., Rowe, J.G., Styles, P., McDonald, B., 1999. Optimising imaging parameters for post mortem MR imaging of the human brain. Acta Radiol 40, 593-597.

Bloembergen, N., 1957. Proton relaxation times in paramagnetic solutions. The Journal of Chemical Physics 27, 572.

Bock, N.A., Kovacevic, N., Lipina, T.V., Roder, J.C., Ackerman, S.L., Henkelman, R.M., 2006. In vivo magnetic resonance imaging and semiautomated image analysis extend the brain phenotype for cdf/cdf mice. J Neurosci 26, 4455-4459.

Boone, J.M., Velazquez, O., Cherry, S.R., 2004. Small-animal X-ray dose from micro-CT. Mol Imaging 3, 149-158.

Boretius, S., Kasper, L., Tammer, R., Michaelis, T., Frahm, J., 2009. MRI of cellular layers in mouse brain in vivo. NeuroImage 47, 1252-1260.

Bosman, E.A., Penn, A.C., Ambrose, J.C., Kettleborough, R., Stemple, D.L., Steel, K.P., 2005. Multiple mutations in mouse Chd7 provide models for CHARGE syndrome. Human Molecular Genetics 14, 3463-3476.

Bottomley, P.A., Foster, T.H., Argersinger, R.E., Pfeifer, L.M., 1984. A review of normal tissue hydrogen NMR relaxation times and relaxation mechanisms from 1-100 MHz: dependence on tissue type, NMR frequency, temperature, species, excision, and age. Med Phys 11, 425-448.

Brodmann, K., 1909. Vergleichende Lokalisationslehre der Grosshirnrinde. Barth-Verlag, Leipzig.

Brown, S.D., 1998. Mouse models of genetic disease: new approaches, new paradigms. J Inherit Metab Dis 21, 532-539.

Brown, S.D.M., Chambon, P., de Angelis, M.H., Consortium, E., 2005. EMPReSS: standardized phenotype screens for functional annotation of the mouse genome. Nat Genet 37, 1155.

Callaghan, P., Forde, L., Rofe, C., 1994. Correlated susceptibility and diffusion effects in NMR microscopy using both phase-frequency encoding and phase-phase encoding. Journal of Magnetic Resonance.

Calmon, G., Roberts, N., 2000. Automatic measurement of changes in brain volume on consecutive 3D MR images by segmentation propagation. Magn Reson Imaging 18, 439-453.

Capecchi, M.R., 2001. Generating mice with targeted mutations. Nat Med 7, 1086-1090.

Caplen, N.J., Parrish, S., Imani, F., Fire, A., Morgan, R.A., 2001. Specific inhibition of gene expression by small double-stranded RNAs in invertebrate and vertebrate systems. Proc Natl Acad Sci USA 98, 9742-9747.

Caravan, P., 2007. Physicochemical Principles of MR Contrast Agents. In: Modo, M.M., Bulte, J.W. (Eds.), Molecular and Cellular MR Imaging. CRC Press, Boca Raton, pp. 13-36.

Carroll, J.B., Lerch, J.P., Franciosi, S., Spreeuw, A., Bissada, N., Henkelman, R.M., Hayden, M.R., 2011. Natural history of disease in the YAC128 mouse reveals a discrete signature of pathology in Huntington disease. Neurobiol Dis.

Castrop, H., 2010. Genetically modified mice-successes and failures of a widely used technology. Pflugers Arch 459, 557-567.

Chapon, C., Franconi, F., Roux, J., Marescaux, L., 2002. In utero time-course assessment of mouse embryo development using high resolution magnetic resonance imaging. Anatomy and ….

Chen, X.J., Kovacevic, N., Lobaugh, N.J., Sled, J.G., Henkelman, R.M., Henderson, J.T., 2006. Neuroanatomical differences between mouse strains as shown by high-resolution 3D MRI. NeuroImage 29, 99-105.

Choi, S., Tang, X., Cory, D., 1997. Constant time imaging approaches to NMR microscopy. International Journal of Imaging System Technology.

Cleary, J.O., Modat, M., Norris, F.C., Price, A.N., Jayakody, S.A., Martinez-Barbera, J.P., Greene, N.D.E., Hawkes, D.J., Ordidge, R.J., Scambler, P.J., Ourselin, S., Lythgoe, M.F., 2010. Magnetic resonance virtual histology for embryos: 3D atlases for automated high-throughput phenotyping. NeuroImage.

Cleary, J.O., Price, A.N., Thomas, D.L., Scambler, P.J., Kyriakopoulou, V., McCue, K., Schneider, J.E., Ordidge, R.J., Lythgoe, M.F., 2009. Cardiac phenotyping in ex vivo murine embryos using microMRI. NMR Biomed 22, 857-866.

Cleary, J.O., Wiseman, F.K., Norris, F.C., Price, A.N., Choy, M., Tybulewicz, V.L.J., Ordidge, R.J., Brandner, S., Fisher, E.M.C., Lythgoe, M.F., 2011. Structural correlates of active-staining following magnetic resonance microscopy in the mouse brain. NeuroImage.

Collins, D.L., 1994. 3D Model-based segmentation of individual brain structures from magnetic resonance imaging data. McGill University, Montreal.

Counsell, S.J., Kennea, N.L., Herlihy, A.H., Allsop, J.M., Harrison, M.C., Cowan, F.M., Hajnal, J.V., Edwards, B., Edwards, A.D., Rutherford, M.A., 2003. T2 relaxation values in the developing preterm brain. AJNR Am J Neuroradiol 24, 1654-1660.

Crawley, J.N., Belknap, J.K., Collins, A., Crabbe, J.C., Frankel, W., Henderson, N., Hitzemann, R.J., Maxson, S.C., Miner, L.L., Silva, A.J., Wehner, J.M., Wynshaw-Boris, A., Paylor, R., 1997. Behavioral phenotypes of inbred mouse strains: implications and recommendations for molecular studies. Psychopharmacology (Berl) 132, 107-124.

Crick, F., Jones, E., 1993. Backwardness of human neuroanatomy. Nature 361, 109-110.

Crum, W.R., Griffin, L.D., Hill, D.L.G., Hawkes, D.J., 2003. Zen and the art of medical image registration: correspondence, homology, and quality. NeuroImage 20, 1425-1437.

Crusio, W.E., Genthner-Grimm, G., Schwegler, H., 1986. A quantitative-genetic analysis of hippocampal variation in the mouse. J Neurogenet 3, 203-214.

Czeizel, A.E., Dobó, M., Vargha, P., 2004. Hungarian cohort-controlled trial of periconceptional multivitamin supplementation shows a reduction in certain congenital abnormalities. Birth Defects Res Part A Clin Mol Teratol 70, 853-861.

Dattani, M.T., Martinez-Barbera, J.P., Thomas, P.Q., Brickman, J.M., Gupta, R., Mårtensson, I.L., Toresson, H., Fox, M., Wales, J.K., Hindmarsh, P.C., Krauss, S., Beddington, R.S., Robinson, I.C., 1998. Mutations in the homeobox gene HESX1/Hesx1 associated with septo-optic dysplasia in human and mouse. Nat Genet 19, 125-133.

Dattani, M.T., Martinez-Barbera, J.P., Thomas, P.Q., Brickman, J.M., Gupta, R., Wales, J.K., Hindmarsh, P.C., Beddington, R.S., Robinson, I.C., 1999. HESX1: a novel gene implicated in a familial form of septo-optic dysplasia. Acta Paediatr Suppl 88, 49-54.

Dawe, R.J., Bennett, D.A., Schneider, J.A., Vasireddi, S.K., Arfanakis, K., 2009. Postmortem MRI of human brain hemispheres: T2 relaxation times during formaldehyde fixation. Magn Reson Med 61, 810-818.

de Angelis, M., Chapron, C., Brown, S., 2006. Standards of Mouse Model Phenotyping. WIley-VCH, Weinheim.

de Graaf, R.A., Brown, P.B., McIntyre, S., Nixon, T.W., Behar, K.L., Rothman, D.L., 2006. High magnetic field water and metabolite proton T1 and T2 relaxation in rat brain in vivo. Magn Reson Med 56, 386-394.

Deans, A.E., Wadghiri, Y.Z., Berrios-Otero, C.A., Turnbull, D.H., 2008. Mn enhancement and respiratory gating for in utero MRI of the embryonic mouse central nervous system. Magn Reson Med 59, 1320-1328.

Degenhardt, K., Wright, A.C., Horng, D., Padmanabhan, A., Epstein, J.A., 2010. Rapid 3D phenotyping of cardiovascular development in mouse embryos by micro-CT with iodine staining. Circ Cardiovasc Imaging 3, 314-322.

Dhenain, M., Ruffins, S., Jacobs, R., 2001. Three-dimensional digital mouse atlas using high-resolution MRI. Dev Biol.

Dice, L., 1945. Measures of the Amount of Ecologic Association Between Species. Ecology 26, 297-302.

Donahue, K.M., Burstein, D., Manning, W.J., Gray, M.L., 1994. Studies of Gd-DTPA relaxivity and proton exchange rates in tissue. Magn Reson Med 32, 66-76.

Dorr, A.E., Lerch, J.P., Spring, S., Kabani, N., Henkelman, R.M., 2008. High resolution three-dimensional brain atlas using an average magnetic resonance image of 40 adult C57Bl/6J mice. NeuroImage 42, 60-69.

Edelstein, W.A., Glover, G.H., Hardy, C.J., Redington, R.W., 1986. The intrinsic signal-to-noise ratio in NMR imaging. Magn Reson Med 3, 604-618.

Ehling, U.H., 1966. Dominant Mutations Affecting the Skeleton in Offspring of X-Irradiated Male Mice. Genetics 54, 1381-1389.

Elbashir, S.M., Harborth, J., Lendeckel, W., Yalcin, A., Weber, K., Tuschl, T., 2001. Duplexes of 21-nucleotide RNAs mediate RNA interference in cultured mammalian cells. Nature 411, 494-498.

Ellegood, J., Pacey, L.K., Hampson, D.R., Lerch, J.P., Henkelman, R.M., 2010a. Anatomical phenotyping in a mouse model of fragile X syndrome with magnetic resonance imaging. NeuroImage 53, 1023-1029.

Ellegood, J., Pacey, L.K., Hampson, D.R., Lerch, J.P., Henkelman, R.M., 2010b. Anatomical phenotyping in a mouse model of fragile X syndrome with magnetic resonance imaging. NeuroImage.

Epstein, F.H., Mugler, J.P., Brookeman, J.R., 1996. Spoiling of transverse magnetization in gradient-echo (GRE) imaging during the approach to steady state. Magn Reson Med 35, 237-245.

Feil, R., Wagner, J., Metzger, D., Chambon, P., 1997. Regulation of Cre recombinase activity by mutated estrogen receptor ligand-binding domains. Biochem Biophys Res Commun 237, 752-757.

Fischer, A., Steidl, C., Wagner, T.U., Lang, E., Jakob, P.M., Friedl, P., Knobeloch, K.-P., Gessler, M., 2007. Combined loss of Hey1 and HeyL causes congenital heart defects because of impaired epithelial to mesenchymal transition. Circ Res 100, 856-863.

Fox, N.C., Crum, W.R., Scahill, R.I., Stevens, J.M., Janssen, J.C., Rossor, M.N., 2001. Imaging of onset and progression of Alzheimer's disease with voxel-compression mapping of serial magnetic resonance images. Lancet 358, 201-205.

Fraenkel-Conrat, H., Olcott, H.S., 1948. The reaction of formaldehyde with proteins; cross-linking between amino and primary amide or guanidyl groups. J Am Chem Soc 70, 2673-2684.

Galante, M., Jani, H., Vanes, L., Daniel, H., Fisher, E.M.C., Tybulewicz, V.L.J., Bliss, T.V.P., Morice, E., 2009. Impairments in motor coordination without major changes in cerebellar plasticity in the Tc1 mouse model of Down syndrome. Human molecular genetics 18, 1449-1463.

Gardiner, K., Costa, A.C.S., 2006. The proteins of human chromosome 21. American journal of medical genetics Part C, Seminars in medical genetics 142C, 196-205.

Gates, W.H., 1925. The Japanese Waltzing Mouse, Its Origin and Genetics. Proc Natl Acad Sci USA 11, 651-653.

Genovese, C.R., Lazar, N.A., Nichols, T., 2002. Thresholding of statistical maps in functional neuroimaging using the false discovery rate. NeuroImage 15, 870-878.

Gerlai, R., 1996. Gene-targeting studies of mammalian behavior: is it the mutation or the background genotype? Trends Neurosci 19, 177-181.

Goddeeris, M.M., Rho, S., Petiet, A., Davenport, C.L., Johnson, G.A., Meyers, E.N., Klingensmith, J., 2008. Intracardiac septation requires hedgehog-dependent cellular contributions from outside the heart. Development 135, 1887-1895.

Gordon, J.W., Scangos, G.A., Plotkin, D.J., Barbosa, J.A., Ruddle, F.H., 1980. Genetic transformation of mouse embryos by microinjection of purified DNA. Proc Natl Acad Sci USA 77, 7380-7384.

Greene, N.D.E., Massa, V., Copp, A.J., 2009. Understanding the causes and prevention of neural tube defects: Insights from the splotch mouse model. Birth Defects Res Part A Clin Mol Teratol 85, 322-330.

Hardman, M., Sisi, P., Banbury…, D., 1998. Patterned acquisition of skin barrier function during development. Development.

Hattori, M., Fujiyama, A., Taylor, T.D., Watanabe, H., Yada, T., Park, H.S., Toyoda, A., Ishii, K., Totoki, Y., Choi, D.K., Groner, Y., Soeda, E., Ohki, M., Takagi, T., Sakaki, Y., Taudien, S., Blechschmidt, K., Polley, A., Menzel, U., Delabar, J., Kumpf, K., Lehmann, R., Patterson, D., Reichwald, K., Rump, A., Schillhabel, M., Schudy, A., Zimmermann, W., Rosenthal, A., Kudoh, J., Schibuya, K., Kawasaki, K., Asakawa, S., Shintani, A., Sasaki, T., Nagamine, K., Mitsuyama, S., Antonarakis, S.E., Minoshima, S., Shimizu, N., Nordsiek, G., Hornischer, K., Brant, P., Scharfe, M., Schon, O., Desario, A., Reichelt, J., Kauer, G., Blocker, H., Ramser, J., Beck, A., Klages, S., Hennig, S., Riesselmann, L., Dagand, E., Haaf, T., Wehrmeyer, S., Borzym, K., Gardiner, K., Nizetic, D., Francis, F., Lehrach, H., Reinhardt, R., Yaspo, M.L., consortium, C.m.a.s., 2000. The DNA sequence of human chromosome 21. Nature 405, 311-319.

Haug, F.M., Blackstad, T.W., Simonsen, A.H., Zimmer, J., 1971. Timm's sulfide silver reaction for zinc during experimental anterograde degeneration of hippocampal mossy fibers. J Comp Neurol 142, 23-31.

Henkelman, R.M., 2010. Systems Biology Through Mouse Imaging Centers: Experience and New Directions. Annual review of biomedical engineering.

Hernandez, D., Mee, P.J., Martin, J.E., Tybulewicz, V.L., Fisher, E.M., 1999. Transchromosomal mouse embryonic stem cell lines and chimeric mice that contain freely segregating segments of human chromosome 21. Human molecular genetics 8, 923-933.

Hof, P.R., Young, W.G., Bloom, F.E., Belichenko, P.V., Celio, M.R., 2000. Comparative cytoarchitectonic atlas of the C57BL/6 and 129/Sv mouse brains. Elsevier, Amsterdam.

Hoffman, J.I.E., Kaplan, S., 2002. The incidence of congenital heart disease. J Am Coll Cardiol 39, 1890-1900.

Holdsworth, D., Thornton, M., 2002. Micro-CT in small animal and specimen imaging. Trends in Biotechnology 20, S34-S39.

Holmes, C.J., Hoge, R., Collins, L., Woods, R., Toga, A.W., Evans, A.C., 1998. Enhancement of MR images using registration for signal averaging. J Comput Assist Tomogr 22, 324-333.

Huang, S., Liu, C., Dai, G., Kim, Y.R., Rosen, B.R., 2009. Manipulation of tissue contrast using contrast agents for enhanced MR microscopy in ex vivo mouse brain. NeuroImage 46, 589-599.

Ingalls, A.M., Dickie, M.M., Snell, G.D., 1950. Obese, a new mutation in the house mouse. J Hered 41, 317-318.

International Mouse Knockout Consortium, Collins, F.S., Rossant, J., Wurst, W., 2007. A mouse for all reasons. Cell 128, 9-13.

Ishihara, K., Amano, K., Takaki, E., Shimohata, A., Sago, H., Epstein, C.J., Yamakawa, K., 2010. Enlarged brain ventricles and impaired neurogenesis in the Ts1Cje and Ts2Cje mouse models of Down syndrome. Cereb Cortex 20, 1131-1143.

Jacobs, R.E., Ahrens, E.T., Dickinson, M.E., Laidlaw, D., 1999. Towards a microMRI atlas of mouse development. Comput Med Imaging Graph 23, 15-24.

Jahid, S., Lipkin, S., 2010. Mouse models of inherited cancer syndromes. Hematol Oncol Clin North Am 24, 1205-1228.

Jiang, Y., Johnson, G.A., 2010. Microscopic diffusion tensor imaging of the mouse brain. NeuroImage 50, 465-471.

Johnson, G.A., Ali-Sharief, A., Badea, A., Brandenburg, J., Cofer, G., Fubara, B., Gewalt, S., Hedlund, L.W., Upchurch, L., 2007. High-throughput morphologic phenotyping of the mouse brain with magnetic resonance histology. NeuroImage 37, 82-89.

Johnson, G.A., Badea, A., Brandenburg, J., Cofer, G., Fubara, B., Liu, S., Nissanov, J., 2010. Waxholm Space: An image-based reference for coordinating mouse brain research. NeuroImage.

Johnson, G.A., Cofer, G.P., Fubara, B., Gewalt, S.L., Hedlund, L.W., Maronpot, R.R., 2002a. Magnetic resonance histology for morphologic phenotyping. J Magn Reson Imaging 16, 423-429.

Johnson, G.A., Cofer, G.P., Gewalt, S.L., Hedlund, L.W., 2002b. Morphologic phenotyping with MR microscopy: the visible mouse. Radiology 222, 789-793.

Johnson, J.T., Hansen, M.S., Wu, I., Healy, L.J., Johnson, C.R., Jones, G.M., Capecchi, M.R., Keller, C., 2006. Virtual histology of transgenic mouse embryos for high-throughput phenotyping. PLoS Genet 2, e61.

Kale, S.C., Chen, X.J., Henkelman, R.M., 2009. Trading off SNR and resolution in MR images. NMR Biomed 22, 488-494.

Kaufman, M.H., 1992. The Atlas of Mouse Development. Academic Press, London.

Keller, M., Watson, C., Richards, K., Buckley, R., Kurniawan, N., Beare, R., Vukovic, J., Wang, D., Yang, S., Zhao, P., Faggian, N., Paxinos, G., Petrou, S., Egan, G., Bartlett, P., Galloway, G., Reutens, D., 2010. A new approach to mouse brain mapping. Proc. Intl. Soc. Mag. Reson. Med. 18, Stockholm, p. 3140.

Kempermann, G., Brandon, E.P., Gage, F.H., 1998. Environmental stimulation of 129/SvJ mice causes increased cell proliferation and neurogenesis in the adult dentate gyrus. Curr Biol 8, 939-942.

Kim, S., Pickup, S., Hsu, O., Poptani, H., 2009. Enhanced delineation of white matter structures of the fixed mouse brain using Gd-DTPA in microscopic MRI. NMR Biomed 22, 303-309.

Kingsley, P., 1995. Product operators, coherence pathways, and phase cycling. Part III: phase cycling. Concepts in Magnetic Resonance.

Kosaka, K., Toida, K., Aika, Y., Kosaka, T., 1998. How simple is the organization of the olfactory glomerulus?: the heterogeneity of so-called periglomerular cells. Neurosci Res 30, 101-110.

Kovacević, N., Henderson, J.T., Chan, E., Lifshitz, N., Bishop, J., Evans, A.C., Henkelman, R.M., Chen, X.J., 2005. A three-dimensional MRI atlas of the mouse brain with estimates of the average and variability. Cereb Cortex 15, 639-645.

Lange, A.W., Rothermel, B.A., Yutzey, K.E., 2005. Restoration of DSCR1 to disomy in the trisomy 16 mouse model of Down syndrome does not correct cardiac or craniofacial development anomalies. Dev Dyn 233, 954-963.

Layman, W.S., Hurd, E.A., Martin, D.M., 2010. Chromodomain proteins in development: lessons from CHARGE syndrome. Clin Genet 78, 11-20.

Layman, W.S., McEwen, D.P., Beyer, L.A., Lalani, S.R., Fernbach, S.D., Oh, E., Swaroop, A., Hegg, C.C., Raphael, Y., Martens, J.R., Martin, D.M., 2009. Defects in neural stem cell proliferation and olfaction in Chd7 deficient mice indicate a mechanism for hyposmia in human CHARGE syndrome. Human molecular genetics 18, 1909-1923.

Lebenberg, J., Hérard, A.-S., Dubois, A., Dauguet, J., Frouin, V., Dhenain, M., Hantraye, P., Delzescaux, T., 2010. Validation of MRI-based 3D digital atlas registration with histological and autoradiographic volumes: an anatomofunctional transgenic mouse brain imaging study. NeuroImage 51, 1037-1046.

Lejeune, J., Turpin, R., Gautier, M., 1959. [Mongolism; a chromosomal disease (trisomy).]. Bull Acad Natl Med 143, 256-265.

Lerch, J.P., Carroll, J.B., Spring, S., Bertram, L.N., Schwab, C., Hayden, M.R., Henkelman, R.M., 2008. Automated deformation analysis in the YAC128 Huntington disease mouse model. NeuroImage 39, 32-39.

Lerch, J.P., Yiu, A.P., Martinez-Canabal, A., Pekar, T., Bohbot, V.D., Frankland, P.W., Henkelman, R.M., Josselyn, S.A., Sled, J.G., 2010. Maze training in mice induces MRI detectable brain shape changes specific to the type of learning. NeuroImage.

Li, T.-Q., van Gelderen, P., Merkle, H., Talagala, L., Koretsky, A.P., Duyn, J., 2006. Extensive heterogeneity in white matter intensity in high-resolution T2*-weighted MRI of the human brain at 7.0 T. NeuroImage 32, 1032-1040.

Lints, T.J., Parsons, L.M., Hartley, L., Lyons, I., Harvey, R.P., 1993. Nkx-2.5: a novel murine homeobox gene expressed in early heart progenitor cells and their myogenic descendants. Development 119, 419-431.

Livet, J., Weissman, T.A., Kang, H., Draft, R.W., Lu, J., Bennis, R.A., Sanes, J.R., Lichtman, J.W., 2007. Transgenic strategies for combinatorial expression of fluorescent proteins in the nervous system. Nature 450, 56-62.

Livy, D.J., Wahlsten, D., 1991. Tests of genetic allelism between four inbred mouse strains with absent corpus callosum. J Hered 82, 459-464.

Ma, Y., Hof, P.R., Grant, S.C., Blackband, S.J., Bennett, R., Slatest, L., McGuigan, M.D., Benveniste, H., 2005. A three-dimensional digital atlas database of the adult C57BL/6J mouse brain by magnetic resonance microscopy. Neuroscience 135, 1203-1215.

MacKenzie-Graham, A., Lee, E.-F., Dinov, I.D., Bota, M., Shattuck, D.W., Ruffins, S., Yuan, H., Konstantinidis, F., Pitiot, A., Ding, Y., Hu, G., Jacobs, R.E., Toga, A.W., 2004. A multimodal, multidimensional atlas of the C57BL/6J mouse brain. J Anat 204, 93-102.

Maguire, E.A., Gadian, D.G., Johnsrude, I.S., Good, C.D., Ashburner, J., Frackowiak, R.S., Frith, C.D., 2000. Navigation-related structural change in the hippocampi of taxi drivers. Proc Natl Acad Sci USA 97, 4398-4403.

Mathur-De Vré, R., Lemort, M., 1995. Invited review: biophysical properties and clinical applications of magnetic resonance imaging contrast agents. Br J Radiol 68, 225-247.

McRobbie, D.W., Moore, E.A., Graves, M.J., 2003. MRI from picture to proton. Cambridge University Press.

Miot-Noirault, E., Barantin, L., Akoka, S., Le Pape, A., 1997. T2 relaxation time as a marker of brain myelination: experimental MR study in two neonatal animal models. J Neurosci Methods 72, 5-14.

Modat, M., Ridgway, G.R., Taylor, Z.A., Lehmann, M., Barnes, J., Hawkes, D.J., Fox, N.C., Ourselin, S., 2010. Fast free-form deformation using graphics processing units. Comput Methods Programs Biomed 98, 278-284.

Morgan, H., Beck, T., Blake, A., Gates, H., Adams, N., Debouzy, G., Leblanc, S., Lengger, C., Maier, H., Melvin, D., Meziane, H., Richardson, D., Wells, S., White, J., Wood, J., Consortium, E., de Angelis, M.H., Brown, S.D.M., Hancock, J.M., Mallon, A.-M., 2010. EuroPhenome: a repository for high-throughput mouse phenotyping data. Nucleic Acids Res 38, D577-585.

Mori, S., Itoh, R., Zhang, J., Kaufmann, W.E., van Zijl, P.C., Solaiyappan, M., Yarowsky, P., 2001. Diffusion tensor imaging of the developing mouse brain. Magn Reson Med 46, 18-23.

Morice, E., Andreae, L.C., Cooke, S.F., Vanes, L., Fisher, E.M.C., Tybulewicz, V.L.J., Bliss, T.V.P., 2008. Preservation of long-term memory and synaptic plasticity despite short-term impairments in the Tc1 mouse model of Down syndrome. Learn Mem 15, 492-500.

Mouse Genome Sequencing Consortium, Waterston, R.H., Lindblad-Toh, K., Birney, E., Rogers, J., Abril, J.F., Agarwal, P., Agarwala, R., Ainscough, R., Alexandersson, M., An, P., Antonarakis, S.E., Attwood, J., Baertsch, R., Bailey, J., Barlow, K., Beck, S., Berry, E., Birren, B., Bloom, T., Bork, P., Botcherby, M., Bray, N., Brent, M.R., Brown, D.G., Brown, S.D., Bult, C., Burton, J., Butler, J., Campbell, R.D., Carninci, P., Cawley, S., Chiaromonte, F., Chinwalla, A.T., Church, D.M., Clamp, M., Clee, C., Collins, F.S., Cook, L.L., Copley, R.R., Coulson, A., Couronne, O., Cuff, J., Curwen, V., Cutts, T., Daly, M., David, R., Davies, J., Delehaunty, K.D., Deri, J., Dermitzakis, E.T., Dewey, C., Dickens, N.J., Diekhans, M., Dodge, S., Dubchak, I., Dunn, D.M., Eddy, S.R., Elnitski, L., Emes, R.D., Eswara, P., Eyras, E., Felsenfeld, A., Fewell, G.A., Flicek, P., Foley, K., Frankel, W.N., Fulton, L.A., Fulton, R.S., Furey, T.S., Gage, D., Gibbs, R.A., Glusman, G., Gnerre, S., Goldman, N., Goodstadt, L., Grafham, D., Graves, T.A., Green, E.D., Gregory, S., Guigó, R., Guyer, M., Hardison, R.C., Haussler, D., Hayashizaki, Y., Hillier, L.W., Hinrichs, A., Hlavina, W., Holzer, T., Hsu, F., Hua, A., Hubbard, T., Hunt, A., Jackson, I., Jaffe, D.B., Johnson, L.S., Jones, M., Jones, T.A., Joy, A., Kamal, M., Karlsson, E.K., Karolchik, D., Kasprzyk, A., Kawai, J., Keibler, E., Kells, C., Kent, W.J., Kirby, A., Kolbe, D.L., Korf, I., Kucherlapati, R.S., Kulbokas, E.J., Kulp, D., Landers, T., Leger, J.P., Leonard, S., Letunic, I., Levine, R., Li, J., Li, M., Lloyd, C., Lucas, S., Ma, B., Maglott, D.R., Mardis, E.R., Matthews, L., Mauceli, E., Mayer, J.H., McCarthy, M., McCombie, W.R., McLaren, S., McLay, K., McPherson, J.D., Meldrim, J., Meredith, B., Mesirov, J.P., Miller, W., Miner, T.L., Mongin, E., Montgomery, K.T., Morgan, M., Mott, R., Mullikin, J.C., Muzny, D.M., Nash, W.E., Nelson, J.O., Nhan, M.N., Nicol, R., Ning, Z., Nusbaum, C., O'Connor, M.J., Okazaki, Y., Oliver, K., Overton-Larty, E., Pachter, L., Parra, G., Pepin, K.H., Peterson, J., Pevzner, P., Plumb, R., Pohl, C.S., Poliakov, A., Ponce, T.C., Ponting, C.P., Potter, S., Quail, M., Reymond, A., Roe, B.A., Roskin, K.M., Rubin, E.M., Rust, A.G., Santos, R., Sapojnikov, V., Schultz, B., Schultz, J., Schwartz, M.S., Schwartz, S., Scott, C., Seaman, S., Searle, S., Sharpe, T., Sheridan, A., Shownkeen, R., Sims, S., Singer, J.B., Slater, G., Smit, A., Smith, D.R., Spencer, B., Stabenau, A., Stange-Thomann, N., Sugnet, C., Suyama, M., Tesler, G., Thompson, J., Torrents, D., Trevaskis, E., Tromp, J., Ucla, C., Ureta-Vidal, A., Vinson, J.P., Von Niederhausern, A.C., Wade, C.M., Wall, M., Weber, R.J., Weiss, R.B., Wendl, M.C., West, A.P., Wetterstrand, K., Wheeler, R., Whelan, S., Wierzbowski, J., Willey, D., Williams, S., Wilson, R.K., Winter, E., Worley, K.C., Wyman, D., Yang, S., Yang, S.-P., Zdobnov, E.M., Zody, M.C., Lander, E.S., 2002. Initial sequencing and comparative analysis of the mouse genome. Nature 420, 520-562.

MRC Vitamin Study Research Group, 1991. Prevention of neural tube defects: results of the Medical Research Council Vitamin Study. . Lancet 338, 131-137.

Mulkern, R.V., Wong, S.T., Winalski, C., Jolesz, F.A., 1990. Contrast manipulation and artifact assessment of 2D and 3D RARE sequences. Magn Reson Imaging 8, 557-566.

Nagy, A., 2003. Manipulating the mouse embryo: a laboratory manual. books.google.com.

Natt, O., Watanabe, T., Boretius, S., Frahm, J., Michaelis, T., 2003. Magnetization transfer MRI of mouse brain reveals areas of high neural density. Magn Reson Imaging 21, 1113-1120.

Neumann, E., Schaefer-Ridder, M., Wang, Y., Hofschneider, P.H., 1982. Gene transfer into mouse lyoma cells by electroporation in high electric fields. EMBO J 1, 841-845.

Nieman, B.J., Flenniken, A.M., Adamson, S.L., Henkelman, R.M., Sled, J.G., 2006. Anatomical phenotyping in the brain and skull of a mutant mouse by magnetic resonance imaging and computed tomography. Physiol Genomics 24, 154-162.

Nieman, B.J., Lerch, J.P., Bock, N.A., Chen, X.J., Sled, J.G., Henkelman, R.M., 2007. Mouse behavioral mutants have neuroimaging abnormalities. Hum Brain Mapp 28, 567-575.

Nieman, B.J., Szulc, K.U., Turnbull, D.H., 2009. Three-dimensional, in vivo MRI with self-gating and image coregistration in the mouse. Magn Reson Med 61, 1148-1157.

Nolan, P.M., Peters, J., Strivens, M., Rogers, D., Hagan, J., Spurr, N., Gray, I.C., Vizor, L., Brooker, D., Whitehill, E., Washbourne, R., Hough, T., Greenaway, S., Hewitt, M., Liu, X., McCormack, S., Pickford, K., Selley, R., Wells, C., Tymowska-Lalanne, Z., Roby, P., Glenister, P., Thornton, C., Thaung, C., Stevenson, J.A., Arkell, R., Mburu, P., Hardisty, R., Kiernan, A., Erven, A., Steel, K.P., Voegeling, S., Guenet, J.L., Nickols, C., Sadri, R., Nasse, M., Isaacs, A., Davies, K., Browne, M., Fisher, E.M., Martin, J., Rastan, S., Brown, S.D., Hunter, J., 2000. A systematic, genome-wide, phenotype-driven mutagenesis programme for gene function studies in the mouse. Nat Genet 25, 440-443.

Null, B., Liu, C.W., Hedehus, M., Conolly, S., Davis, R.W., 2008. High-resolution, in vivo magnetic resonance imaging of Drosophila at 18.8 Tesla. PLoS ONE 3, e2817.

O'Doherty, A., Ruf, S., Mulligan, C., Hildreth, V., Errington, M.L., Cooke, S., Sesay, A., Modino, S., Vanes, L., Hernandez, D., Linehan, J.M., Sharpe, P.T., Brandner, S., Bliss, T.V.P., Henderson, D.J., Nizetic, D., Tybulewicz, V.L.J., Fisher, E.M.C., 2005. An aneuploid mouse strain carrying human chromosome 21 with Down syndrome phenotypes. Science 309, 2033-2037.

Oest, M.E., Jones, J.C., Hatfield, C., Prater, M.R., 2008. Micro-CT evaluation of murine fetal skeletal development yields greater morphometric precision over traditional clear-staining methods. Birth Defects Res B Dev Reprod Toxicol 83, 582-589.

Olson, L.E., Roper, R.J., Sengstaken, C.L., Peterson, E.A., Aquino, V., Galdzicki, Z., Siarey, R., Pletnikov, M., Moran, T.H., Reeves, R.H., 2007. Trisomy for the Down syndrome 'critical region' is necessary but not sufficient for brain phenotypes of trisomic mice. Human molecular genetics 16, 774-782.

Ordidge, R.J., Helpern, J.A., Qing, Z.X., Knight, R.A., Nagesh, V., 1994. Correction of motional artifacts in diffusion-weighted MR images using navigator echoes. Magn Reson Imaging 12, 455-460.

Otis, E.M., Brent, R., 1954. Equivalent ages in mouse and human embryos. Anat Rec 120, 33-63.

Ourselin, S., Roche, A., Subsol, G., Pennec, X., Ayache, N., 2001. Reconstructing a 3D structure from serial histological sections. Image Vision Comput 19, 25-31.

Panizzo, R.A., Kyrtatos, P.G., Price, A.N., Gadian, D.G., Ferretti, P., Lythgoe, M.F., 2009. In vivo magnetic resonance imaging of endogenous neuroblasts labelled with a ferumoxide-polycation complex. NeuroImage 44, 1239-1246.

Parnell, S.E., O'Leary-Moore, S.K., Godin, E.A., Dehart, D.B., Johnson, B.W., Allan Johnson, G., Styner, M.A., Sulik, K.K., 2009. Magnetic resonance microscopy defines ethanol-induced brain abnormalities in prenatal mice: effects of acute insult on gestational day 8. Alcohol Clin Exp Res 33, 1001-1011.

Pechhold, K., Chakrabarty, S., Harlan, D.M., 2007. Cytotoxic T cell-mediated diabetes in RIP-CD80 transgenic mice: autoantigen peptide sensitivity and fine specificity. Ann N Y Acad Sci 1103, 132-142.

Pelc, N.J., 1993. Optimization of flip angle for T1 dependent contrast in MRI. Magn Reson Med 29, 695-699.

Petiet, A., Hedlund, L., Johnson, G.A., 2007. Staining methods for magnetic resonance microscopy of the rat fetus. J Magn Reson Imaging 25, 1192-1198.

Petiet, A.E., Kaufman, M.H., Goddeeris, M.M., Brandenburg, J., Elmore, S.A., Johnson, G.A., 2008. High-resolution magnetic resonance histology of the embryonic and neonatal mouse: a 4D atlas and morphologic database. Proc Natl Acad Sci USA 105, 12331-12336.

Pfefferbaum, A., Sullivan, E.V., Adalsteinsson, E., Garrick, T., Harper, C., 2004. Postmortem MR imaging of formalin-fixed human brain. NeuroImage 21, 1585-1595.

Phillips, W., Morton, A.J., Barker, R.A., 2005. Abnormalities of neurogenesis in the R6/2 mouse model of Huntington's disease are attributable to the in vivo microenvironment. J Neurosci 25, 11564-11576.

Phoon, C.K.L., Turnbull, D.H., 2003. Ultrasound biomicroscopy-Doppler in mouse cardiovascular development. Physiol Genomics 14, 3-15.

Pinter, J.D., Eliez, S., Schmitt, J.E., Capone, G.T., Reiss, A.L., 2001. Neuroanatomy of Down's syndrome: a high-resolution MRI study. Am J Psychiatry 158, 1659-1665.

Prajapati, S.I., Kilcoyne, A., Samano, A.K., Green, D.P., McCarthy, S.D., Blackman, B.A., Brady, M.M., Zarzabal, L.A., Tatiparthy, A.K., Sledz, T.J., Duong, T., Ohshima-Hosoyama, S., Giles, F.J., Michalek, J.E., Rubin, B.P., Keller, C., 2010. MicroCT-Based Virtual Histology Evaluation of Preclinical Medulloblastoma. Molecular imaging and biology : MIB : the official publication of the Academy of Molecular Imaging.

Price, J.L., Powell, T.P., 1970. The morphology of the granule cells of the olfactory bulb. J Cell Sci 7, 91-123.

Purea, A., Webb, A.G., 2006. Reversible and irreversible effects of chemical fixation on the NMR properties of single cells. Magn Reson Med 56, 927-931.

Purger, D., McNutt, T., Achanta, P., Quiñones-Hinojosa, A., Wong, J., Ford, E., 2009. A histology-based atlas of the C57BL/6J mouse brain deformably registered to in vivo MRI for localized radiation and surgical targeting. Phys Med Biol 54, 7315-7327.

Pykett, I.L., Rosen, B.R., Buonanno, F.S., Brady, T.J., 1983. Measurement of spin-lattice relaxation times in nuclear magnetic resonance imaging. Phys Med Biol 28, 723-729.

Rader, K.A., 2001. "The Mouse People": Murine genetics work at the Bussey Institution, 1909-1936. J Hist Biol 31, 327-354.

Randall, V., McCue, K., Roberts, C., Kyriakopoulou, V., Beddow, S., Barrett, A.N., Vitelli, F., Prescott, K., Shaw-Smith, C., Devriendt, K., Bosman, E., Steffes, G., Steel, K.P., Simrick, S., Basson, M.A., Illingworth, E., Scambler, P.J., 2009. Great vessel development requires biallelic expression of Chd7 and Tbx1 in pharyngeal ectoderm in mice. J Clin Invest 119, 3301-3310.

Reeves, R.H., Irving, N.G., Moran, T.H., Wohn, A., Kitt, C., Sisodia, S.S., Schmidt, C., Bronson, R.T., Davisson, M.T., 1995. A mouse model for Down syndrome exhibits learning and behaviour deficits. Nat Genet 11, 177-184.

Riegler, J., Cheung, K.K., Man, Y.F., Cleary, J.O., Price, A.N., Lythgoe, M.F., 2010. Comparison of segmentation methods for MRI measurement of cardiac function in rats. J Magn Reson Imaging 32, 869-877.

Rivkees, S.A., 2003. Rest-activity patterns in children with hypopituitarism. Pediatrics 111, e720-724.

Robbins, S., Evans, A.C., Collins, D.L., Whitesides, S., 2004. Tuning and comparing spatial normalization methods. Med Image Anal 8, 311-323.

Rosenthal, N., Brown, S., 2007. The mouse ascending: perspectives for human-disease models. Nat Cell Biol 9, 993-999.

Rueckert, D., Sonoda, L.I., Hayes, C., Hill, D.L., Leach, M.O., Hawkes, D.J., 1999. Nonrigid registration using free-form deformations: application to breast MR images. IEEE Trans Med Imaging 18, 712-721.

Russell, W.L., Kelly, E.M., Hunsicker, P.R., Bangham, J.W., Maddux, S.C., Phipps, E.L., 1979. Specific-locus test shows ethylnitrosourea to be the most potent mutagen in the mouse. Proc Natl Acad Sci USA 76, 5818-5819.

Sajedi, E., Gaston-Massuet, C., Signore, M., Andoniadou, C.L., Kelberman, D., Castro, S., Etchevers, H.C., Gerrelli, D., Dattani, M.T., Martinez-Barbera, J.P., 2008. Analysis of mouse models carrying the I26T and R160C substitutions in the transcriptional repressor HESX1 as models for septo-optic dysplasia and hypopituitarism. Dis Model Mech 1, 241-254.

Sauer, B., 1998. Inducible gene targeting in mice using the Cre/lox system. Methods 14, 381-392.

Sauer, B., Henderson, N., 1988. Site-specific DNA recombination in mammalian cells by the Cre recombinase of bacteriophage P1. Proc Natl Acad Sci USA 85, 5166-5170.

Savolainen, S.M., Foley, J.F., Elmore, S.A., 2009. Histology atlas of the developing mouse heart with emphasis on E11.5 to E18.5. Toxicol Pathol 37, 395-414.

Sawiak, S.J., Wood, N.I., Williams, G.B., Morton, A.J., Carpenter, T.A., 2009a. Use of magnetic resonance imaging for anatomical phenotyping of the R6/2 mouse model of Huntington's disease. Neurobiol Dis 33, 12-19.

Sawiak, S.J., Wood, N.I., Williams, G.B., Morton, A.J., Carpenter, T.A., 2009b. Voxel-based morphometry in the R6/2 transgenic mouse reveals differences between genotypes not seen with manual 2D morphometry. Neurobiol Dis 33, 20-27.

Sawiak, S.J.W., Nigel I.; Williams, Guy B.; Morton, A. J.; Carpenter, Thomas Adrian, 2009. SPMMouse: A New Toolbox for SPM in the Animal Brain. 17th Meeting of the International Society for Magnetic Resonance in Medicine, Honolulu, HI, p. 1086.

Schneider, J.E., Bamforth, S.D., Farthing, C.R., Clarke, K., Neubauer, S., Bhattacharya, S., 2003a. High-resolution imaging of normal anatomy, and neural and adrenal malformations in mouse embryos using magnetic resonance microscopy. J Anat 202, 239-247.

Schneider, J.E., Bamforth, S.D., Farthing, C.R., Clarke, K., Neubauer, S., Bhattacharya, S., 2003b. Rapid identification and 3D reconstruction of complex cardiac malformations in transgenic mouse embryos using fast gradient echo sequence magnetic resonance imaging. J Mol Cell Cardiol 35, 217-222.

Schneider, J.E., Bamforth, S.D., Grieve, S.M., Clarke, K., Bhattacharya, S., Neubauer, S., 2003c. High-resolution, high-throughput magnetic paragraph sign resonance imaging of mouse embryonic paragraph sign anatomy using a fast gradient-echo sequence. MAGMA 16, 43-51.

Schneider, J.E., Bhattacharya, S., 2004. Making the mouse embryo transparent: identifying developmental malformations using magnetic resonance imaging. Birth Defects Res C Embryo Today 72, 241-249.

Schneider, J.E., Böse, J., Bamforth, S.D., Gruber, A.D., Broadbent, C., Clarke, K., Neubauer, S., Lengeling, A., Bhattacharya, S., 2004. Identification of cardiac malformations in mice lacking Ptdsr using a novel high-throughput magnetic resonance imaging technique. BMC Dev Biol 4, 16.

Sebrié, C., Chabert, C., Ledru, A., Guedj, F., Po, C., Smith, D.J., Rubin, E., Rivals, I., Beloeil, J.-C., Gillet, B., Delabar, J.-M., 2008. Increased dosage of DYRK1A and brain volumetric alterations in a YAC model of partial trisomy 21. Anat Rec (Hoboken) 291, 254-262.

Sharief, A.A., Johnson, G.A., 2006. Enhanced T2 contrast for MR histology of the mouse brain. Magn Reson Med 56, 717-725.

Sharpe, J., 2003. Optical projection tomography as a new tool for studying embryo anatomy. J Anat 202, 175-181.

Sharpe, J., 2004. Optical projection tomography. Annual review of biomedical engineering 6, 209-228.

Sharpe, J., Ahlgren, U., Perry, P., Hill, B., Ross, A., Hecksher-Sørensen, J., Baldock, R., Davidson, D., 2002. Optical projection tomography as a tool for 3D microscopy and gene expression studies. Science 296, 541-545.

Shepherd, G.M., Chen, W.R., Willhite, D., Migliore, M., Greer, C.A., 2007. The olfactory granule cell: from classical enigma to central role in olfactory processing. Brain research reviews 55, 373-382.

Shepherd, T.M., Ozarslan, E., King, M.A., Mareci, T.H., Blackband, S.J., 2006. Structural insights from high-resolution diffusion tensor imaging and tractography of the isolated rat hippocampus. NeuroImage 32, 1499-1509.

Shepherd, T.M., Thelwall, P.E., Stanisz, G.J., Blackband, S.J., 2009. Aldehyde fixative solutions alter the water relaxation and diffusion properties of nervous tissue. Magn Reson Med 62, 26-34.

Shmueli, K., de Zwart, J.A., van Gelderen, P., Li, T.-Q., Dodd, S.J., Duyn, J.H., 2009. Magnetic susceptibility mapping of brain tissue in vivo using MRI phase data. Magn Reson Med 62, 1510-1522.

Silva, A.C., Lee, J.H., Wu, C.W.-H., Tucciarone, J., Pelled, G., Aoki, I., Koretsky, A.P., 2008. Detection of cortical laminar architecture using manganese-enhanced MRI. J Neurosci Methods 167, 246-257.

Smith, B.R., Johnson, G.A., Groman, E.V., Linney, E., 1994. Magnetic resonance microscopy of mouse embryos. Proc Natl Acad Sci USA 91, 3530-3533.

Smith, B.R., Linney, E., Huff, D.S., Johnson, G.A., 1996. Magnetic resonance microscopy of embryos. Comput Med Imaging Graph 20, 483-490.

Solomon, I., 1955. Relaxation Processes in a System of Two Spins. Phys. Rev. 99, 559.

Spring, S., Lerch, J.P., Wetzel, M.K., Evans, A.C., Henkelman, R.M., 2010. Cerebral asymmetries in 12-week-old C57Bl/6J mice measured by magnetic resonance imaging. NeuroImage 50, 409-415.

Stanisz, G.J., Henkelman, R.M., 2000. Gd-DTPA relaxivity depends on macromolecular content. Magn Reson Med 44, 665-667.

Stuckey, D.J., Carr, C.A., Martin-Rendon, E., Tyler, D.J., Willmott, C., Cassidy, P.J., Hale, S.J.M., Schneider, J.E., Tatton, L., Harding, S.E., Radda, G.K., Watt, S., Clarke, K., 2006. Iron particles for noninvasive monitoring of bone marrow stromal cell engraftment into, and isolation of viable engrafted donor cells from, the heart. Stem Cells 24, 1968-1975.

Studholme, C., Hill, D., Hawkes, D., 1999. An overlap invariant entropy measure of 3D medical image alignment. Pattern Recognition 32, 71-86.

Takeda, T., Momose, A., Hirano, K., Haraoka, S., Watanabe, T., Itai, Y., 2000. Human carcinoma: early experience with phase-contrast X-ray CT with synchrotron radiation--comparative specimen study with optical microscopy. Radiology 214, 298-301.

Thayyil, S., Cleary, J.O., Sebire, N.J., Scott, R.J., Chong, K., Gunny, R., Owens, C.M., Olsen, O.E., Offiah, A.C., Parks, H.G., Chitty, L.S., Price, A.N., Yousry, T.A., Robertson, N.J., Lythgoe, M.F., Taylor, A.M., 2009. Post-mortem examination of human fetuses: a comparison of whole-body high-field MRI at 9.4 T with conventional MRI and invasive autopsy. Lancet 374, 467-475.

Tournier, J.-D., Calamante, F., Connelly, A., 2007. Robust determination of the fibre orientation distribution in diffusion MRI: non-negativity constrained super-resolved spherical deconvolution. NeuroImage 35, 1459-1472.

Tovi, M., Ericsson, A., 1992. Measurements of T1 and T2 over time in formalin-fixed human whole-brain specimens. Acta Radiol 33, 400-404.

Tweedle, M.F., 1997. The ProHance story: the making of a novel MRI contrast agent. Eur Radiol 7 Suppl 5, 225-230.

Tyszka, J.M., Readhead, C., Bearer, E.L., Pautler, R.G., Jacobs, R.E., 2006. Statistical diffusion tensor histology reveals regional dysmyelination effects in the shiverer mouse mutant. NeuroImage 29, 1058-1065.

Uematsu, H., Takahashi, M., Hatabu, H., Chin, C.-L., Wehrli, S.L., Wehrli, F.W., Asakura, T., 2007. Changes in T1 and T2 observed in brain magnetic resonance imaging with delivery of high concentrations of oxygen. J Comput Assist Tomogr 31, 662-665.

Ullmann, J.F.P., Cowin, G., Kurniawan, N.D., Collin, S.P., 2010. A three-dimensional digital atlas of the zebrafish brain. NeuroImage 51, 76-82.

Van Leemput, K., Maes, F., Vandermeulen, D., Suetens, P., 1999. Automated model-based tissue classification of MR images of the brain. IEEE Trans Med Imaging 18, 897-908.

Walls, J.R., Coultas, L., Rossant, J., Henkelman, R.M., 2008. Three-dimensional analysis of vascular development in the mouse embryo. PLoS ONE 3, e2853.

Wengenack, T.M., Jack, C.R., Garwood, M., Poduslo, J.F., 2008. MR microimaging of amyloid plaques in Alzheimer's disease transgenic mice. Eur J Nucl Med Mol Imaging 35 Suppl 1, S82-88.

Weninger, W.J., Geyer, S.H., Mohun, T.J., Rasskin-Gutman, D., Matsui, T., Ribeiro, I., Costa, L.d.F., Izpisúa-Belmonte, J.C., Müller, G.B., 2006. High-resolution episcopic microscopy: a rapid technique for high detailed 3D analysis of gene activity in the context of tissue architecture and morphology. Anat Embryol 211, 213-221.

Weninger, W.J., Mohun, T., 2002. Phenotyping transgenic embryos: a rapid 3-D screening method based on episcopic fluorescence image capturing. Nat Genet 30, 59-65.

Wetzel, M.K., Naska, S., Laliberté, C.L., Rymar, V.V., Fujitani, M., Biernaskie, J.A., Cole, C.J., Lerch, J.P., Spring, S., Wang, S.-H., Frankland, P.W., Henkelman, R.M., Josselyn, S.A., Sadikot, A.F., Miller, F.D., Kaplan, D.R., 2008. p73 regulates neurodegeneration and phospho-tau accumulation during aging and Alzheimer's disease. Neuron 59, 708-721.

Wiseman, F.K., Alford, K.A., Tybulewicz, V.L.J., Fisher, E.M.C., 2009. Down syndrome--recent progress and future prospects. Human molecular genetics 18, R75-83.

Wright, A.C., Song, H.K., Wehrli, F.W., 2000. In vivo MR micro imaging with conventional radiofrequency coils cooled to 77 degrees K. Magn Reson Med 43, 163-169.

Yutzey, K.E., Robbins, J., 2007. Principles of genetic murine models for cardiac disease. Circulation 115, 792-799.

Zamayadi, M., 2010. Group-wise 3D MR Image Registration of Mouse Embryos. University of Toronto.

Zamyadi, M., Baghdadi, L., Lerch, J.P., Bhattacharya, S., Schneider, J.E., Henkelman, R.M., Sled, J.G., 2010. Mouse embryonic phenotyping by morphometric analysis of MR images. Physiological genomics.

Zamyadi, M., Henkelman, RM, Bhattacharya, S, Schneider, JE, Sled, JG, 2008. Registration of 3D MR images of the mouse embryos. Proceedings of the ISMRM 17th Annual Meeting, Honolulu, p. 3099.

Zhang, J., Peng, Q., Li, Q., Jahanshad, N., Hou, Z., Jiang, M., Masuda, N., Langbehn, D.R., Miller, M.I., Mori, S., Ross, C.A., Duan, W., 2010a. Longitudinal characterization of brain atrophy of a Huntington's disease mouse model by automated morphological analyses of magnetic resonance images. NeuroImage 49, 2340-2351.

Zhang, J., Richards, L.J., Yarowsky, P., Huang, H., van Zijl, P.C.M., Mori, S., 2003. Three-dimensional anatomical characterization of the developing mouse brain by diffusion tensor microimaging. NeuroImage 20, 1639-1648.

Zhang, X., Schneider, J.E., Portnoy, S., Bhattacharya, S., Henkelman, R.M., 2010b. Comparative SNR for high-throughput mouse embryo MR microscopy. Magn Reson Med 63, 1703-1707.

Zhang, Y., Proenca, R., Maffei, M., Barone, M., Leopold, L., Friedman, J.M., 1994. Positional cloning of the mouse obese gene and its human homologue. Nature 372, 425-432.

Zilles, K., Amunts, K., 2010. Centenary of Brodmann's map--conception and fate. Nat Rev Neurosci 11, 139-145.